Polymer 52 (2011) vii–xii

Contents lists available at ScienceDirect

Polymer

journal homepage: www.elsevier.com/locate/polymer

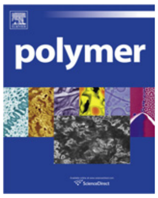

Polymer Vol. 52, No. 6, 10 March 2011

Contents

POLYMER PAPERS

A comprehensive study of the bicontinuous epoxy–silica hybrid polymers: I. Synthesis, characterization and glass transition **pp 1345–1355**

Adeel Afzal*, Humaira M. Siddiqi

Department of Chemistry, Quaid-i-Azam University, Islamabad 45320, Pakistan

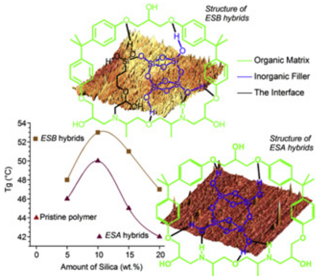

Synthesis of 'ready-to-adsorb' polymeric nanoshells for magnetic iron oxide nanoparticles via atom transfer radical polymerization **pp 1356–1366**

Nikorn Pothayee[a], S. Balasubramaniam[b], R.M. Davis[a], J.S. Riffle[a,*], M.R.J. Carroll[b], R.C. Woodward[b], T.G. St. Pierre[b]

[a] *Macromolecules and Interfaces Institute, Virginia Polytechnic Institute and State University, Blacksburg, VA 24061, United States*
[b] *School of Physics, The University of Western Australia, 35 Stirling Hwy, Crawley, WA 6009, Australia*

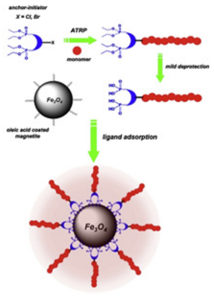

Thermosensitivity control of polyethlyenimine by simple acylation **pp 1367–1374**

Heejin Kim[a], Seonju Lee[a], Minwoo Noh[a], So Hyun Lee[a], Yeongbong Mok[a],
Geun-woo Jin[a], Ji-Hun Seo[b], Yan Lee[a,*]

[a] *Department of Chemistry, Seoul National University, 599 Gwanak-ro, Gwanak-gu,
Seoul 151 747, Republic of Korea*
[b] *Department of Materials Engineering, The University of Tokyo, 7-3-1 Hongo, Bunkyo-ku,
Tokyo 113 8656, Japan*

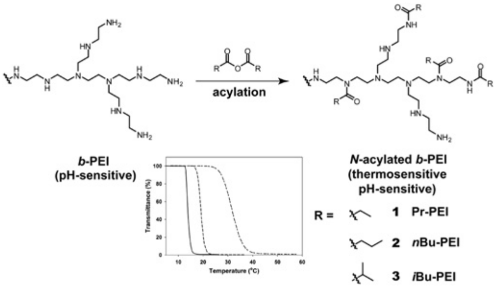

Characterization and conversion determination of stable PEDOT latex nanoparticles synthesized by emulsion polymerization **pp 1375–1384**

Chieh-Han Wu[a], Trong-Ming Don[b], Wen-Yen Chiu[a,c,d,*]

[a] *Institute of Polymer Science and Engineering, National Taiwan University, Taipei 106, Taiwan*
[b] *Department of Chemical and Materials Engineering, Tamkang University, Tamsui, Taipei county 251, Taiwan*
[c] *Department of Chemical Engineering, National Taiwan University, Taipei 106, Taiwan*
[d] *Department of Materials Science and Engineering, National Taiwan University, Taipei 106, Taiwan*

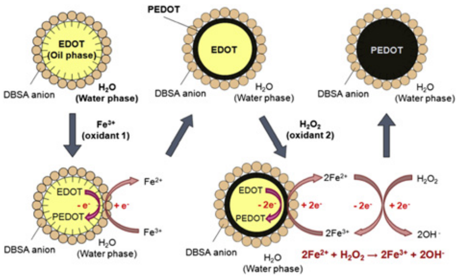

Memory effect in polymer brushes containing pendant carbazole groups **pp 1385–1390**

Yuyan Wei[a], Dazhi Gao[a], Liang Li[a,c,*], Songming Shang[b,**]

[a] *Key Laboratory for Green Chemical Process of Ministry of Education, School of Materials Science and Engineering, Wuhan Institute of Technology, Wuhan 430073, PR China*
[b] *Institute of Textiles and Clothing, Hong Kong Polytechnic University, Hong Kong, PR China*
[c] *State Key Laboratory of Coordination Chemistry, Nanjing University, Nanjing 210093, PR China*

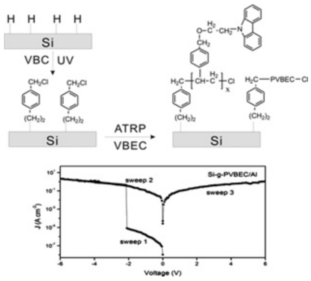

Structure, mechanical properties and degradation behaviors of the electrospun fibrous blends of PHBHHx/PDLLA **pp 1391–1401**

Mei-Ling Cheng[a], Po-Ya Chen[a], Chin-Hung Lan[a], Yi-Ming Sun[a,b,c,*]

[a] *Department of Chemical Engineering and Materials Science, Yuan Ze University, Chung-Li 320, Taiwan, ROC*
[b] *Graduate School of Biotechnology and Bioengineering, Yuan Ze University, Chung-Li 320, Taiwan, ROC*
[c] *R&D Center for Membrane Technology, Chung Yuan University, Chung-Li 320, Taiwan, ROC*

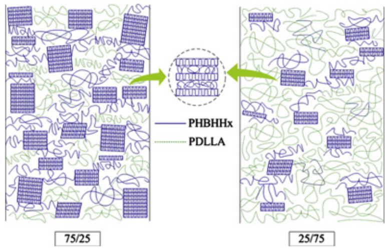

Large amplitude oscillatory shear rheology for nonlinear viscoelasticity in hectorite suspensions containing poly(ethylene glycol) pp 1402–1409

Weixiang Sun, Yanrui Yang, Tao Wang, Xinxing Liu, Chaoyang Wang, Zhen Tong*

Research Institute of Materials Science, South China University of Technology, Guangzhou 510640, China

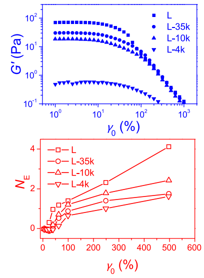

NMR relaxation reveals modifications in rubber phase dynamics during long-term degradation of high-impact polystyrene (HIPS) pp 1410–1416

Francisco Vilaplana[a,b], Sigbritt Karlsson[a], Amparo Ribes-Greus[b], Christian Schade[c], Nikolaus Nestle[c,*]

[a] *Department of Fibre and Polymer Technology, School of Chemical Science and Engineering, KTH – Royal Institute of Technology, Teknikringen 56-58, SE-10044 Stockholm, Sweden*
[b] *Instituto de Tecnología de Materiales (ITM), Universidad Politécnica de Valencia, Camino de Vera s/n, E-46022 Valencia, Spain*
[c] *BASF SE, 67056 Ludwigshafen, Germany*

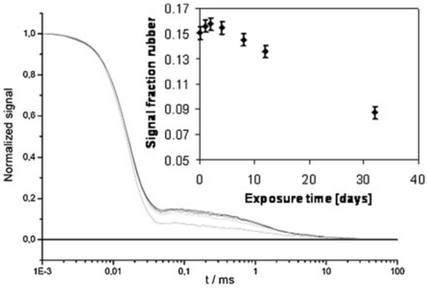

Morphology, thermal behavior and mechanical properties of binary blends of compatible biosourced polymers: Polylactide/polyamide11 pp 1417–1425

G. Stoclet*, R. Seguela*, J.-M. Lefebvre

Unité Matériaux Et Transformations, CNRS UMR 8207, Université de Lille1, Cité Scientifique, Batiment C6, 59655 Villeneuve d'Ascq, France

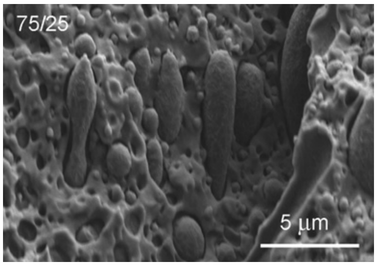

Structural characterization of the δ-clathrate forms of syndiotactic polystyrene with *n*-alkanes pp 1426–1435

Oreste Tarallo*, Maria Maddalena Schiavone, Vittorio Petraccone

Dipartimento di Chimica "Paolo Corradini", Università degli Studi di Napoli Federico II, Complesso di Monte S. Angelo, via Cintia, 80126 Napoli, Italy

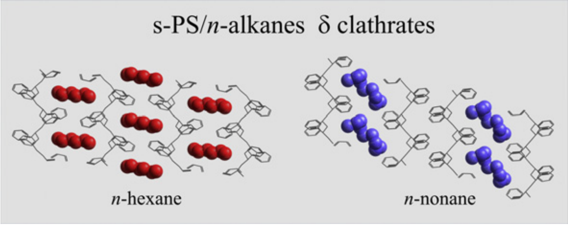

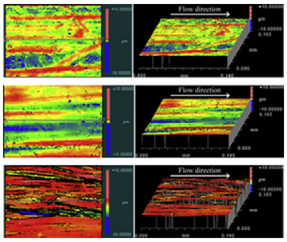
Flow direction
Flow direction
Flow direction

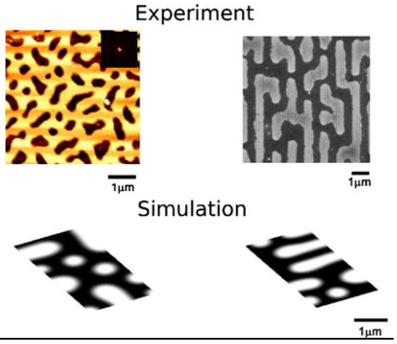
Experiment
1µm
1µm
Simulation
1µm

Structure of polymer–acid complexes in solution and crystal-solvate phases of rigid-rod heterocyclic polymer - poly (p-phenylene benzobisoxasole) **pp 1458–1468**

N.V. Lukasheva

Institute of Macromolecular Compounds, Russian Academy of Sciences, Bol'shoi pr. 31,
St. Petersburg 199004, Russia

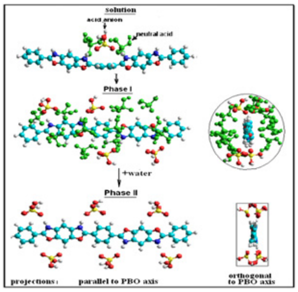

*Corresponding author

Abstracted/indexed in: AGRICOLA, Beilstein, BIOSIS Previews, CAB Abstracts, Chemical Abstracts. Current Contents: Life Sciences, Current Contents: Physical, Chemical and Earth Sciences, Current Contents Search, Derwent Drug File, Ei compendex, EMBASE/Excerpta Medica, Medline, PASCAL, Research Alert, Science Citation Index, SciSearch. Also covered in the abstract and citation database SCOPUS®. Full text available on ScienceDirect®

ISSN 0032-3861

ELSEVIER

Author Index

Polymer 52 (2011) 1345–1355

Contents lists available at ScienceDirect

Polymer

journal homepage: www.elsevier.com/locate/polymer

A comprehensive study of the bicontinuous epoxy–silica hybrid polymers: I. Synthesis, characterization and glass transition

Adeel Afzal*, Humaira M. Siddiqi

Department of Chemistry, Quaid-i-Azam University, Islamabad 45320, Pakistan

A R T I C L E I N F O

Article history:
Received 20 November 2010
Received in revised form
14 January 2011
Accepted 21 January 2011
Available online 1 February 2011

Keywords:
Epoxy resin
Sol–gel
AFM

A B S T R A C T

This paper presents a novel two-stage chronological procedure developed for the synthesis of bicontinuous epoxy–silica hybrid polymers. The epoxy–silica polymers are produced by solvent-free hydrolysis of tetraethylorthosilicate into the liquid epoxy resin, followed by the crosslinking of epoxide groups with a diamine curing agent. The two types of bicontinuous epoxy–silica hybrid polymers prepared in this way contain 0–30 wt.% silica and differ only in the absence or presence of (3-glycidoxypropyl)trimethoxysilane (*GLYMO*); minimal amount of which is used for the *in situ* functionalization of silica. *GCMS* and *DSC* analyses provide an insight into the reaction mechanism, and reveal that total conversion of silanes as well as epoxy groups is feasible in this way. The free-standing epoxy–silica polymer films are subsequently characterized by the attenuated total reflectance *FTIR* spectroscopy and *AFM*. The *AFM* micrographs exhibit a very fine dispersion of nanoscale silica into the organic matrix that is further enhanced on addition of *GLYMO*. The presence of *GLYMO* substantially affects the particle size and distribution, augments the adhesion of the two phases, and inhibits the macroscopic phase separation. The glass transition temperatures of epoxy–silica polymers are also improved by 20.4%; which is attributed to the formation of entangled epoxy–silica networks.

1. Introduction

The privileged physical characteristics of the epoxy resins, for example, superior strength, stiffness and toughness, good chemical and heat resistance, excellent adhesion and low shrinkage properties; have instituted them as the foremost choice off raw materials for the high performance composite or hybrid matrices. The silica- (silicone-, silicate-, or siloxane-) reinforced epoxy networks have found applications in the fields of coatings, tooling, encapsulation, adhesives, filament winding, laminates and several others. The epoxy–silica nanocomposite and hybrid materials are respectively synthesized by direct blending of the inorganic silica nanoparticles with the epoxy monomers or by preparing a dedicated copolymer from the epoxide and silane precursors. The former procedure offers little or no crosslinking between the organic and inorganic constituents with the result that phase separation often occurs, which is usually detrimental to one or more properties of the nanocomposites. The latter procedure often involves the sol–gel process to derive silica in the epoxy based hybrid materials, and the interphase crosslinking in this case is better and can be further improved by the use of suitable reagents [1].

The sol–gel process [2] is an efficient method for preparing inorganic networks at low temperature. It offers several benefits, for instance, the micro- and macro-structure of the hybrid polymer can be controlled by optimizing the synthetic conditions such as concentration, water/alkoxide ratio, temperature, *pH*, the type of catalyst and solvent. The sol–gel epoxy–silica hybrid polymers have been studied extensively during the past [3] & *Ref. therein*. Matějka et al. [4] prepared sol–gel epoxy–silica hybrids using either the *one-stage process* i.e. all reaction components including water were mixed and reacted simultaneously, or the *two-stage simultaneous process* i.e. *TEOS* was pre-hydrolyzed with an acid catalyst for 1 h and mixed with the organic components to start simultaneous formation of organic and inorganic phases. A *two-stage sequential process* was also developed and used by some scientist [5,6]; in which preformed epoxy-amine network was swollen for several hours in the mixture of *TEOS*, water, catalyst and solvent.

Over the years, several authors employed similar procedures with little variation to synthesize different kinds of sol–gel epoxy–silica hybrid polymers [7–9]. All these methods are primarily based on the solution processing of epoxy–silica

---

* Corresponding author. Present address: Dipartimento di Chimica, Università degli Studi di Bari, via E. Orabona 4, Bari 70126, Italy. Tel.: +39 80 544 2030; fax: +39 80 544 2026.

E-mail address: adeel.afzal@uniba.it (A. Afzal).

0032-3861/$ – see front matter © 2011 Elsevier Ltd. All rights reserved.
doi:10.1016/j.polymer.2011.01.046

polymers; which is not practical, for example, in the manufacturing of epoxy molding compounds and related applications. Additionally, a major drawback of the traditional sol–gel process is the shrinkage of the xerogel by evaporation of the co-solvent, excess water and hydrolysis by-products such as alcohol during the drying or curing steps [10].

Nonetheless, it is well known that the eventual properties of hybrid polymers are controlled and strongly influenced by the size, nature and strength of the interface, which can easily be tailored through the sol–gel process [6–9]. The stronger interphase interactions lead to more uniform morphology of the hybrids with superior physical properties [4]. Pertinent literature suggests that amine-cured epoxy–silica hybrids, presented in this study, own better compatibility due to stronger physical interactions such as hydrogen bonds between amino groups and prehydrolyzed siloxane networks [11,12]. However various chemicals such as the organo-functional silanes can significantly improve compatibility via chemical interactions i.e. by covalently binding the organic and inorganic constituents; thus so-called as the coupling agents [7]. (3-Glycidoxypropyl)trimethoxysilane (*GLYMO*) is one of the most popular coupling agents [13,14]; which can serve as a bridging unit by forming interphase links through the hydrolysis and condensation of trialkoxysilane moiety, and the polymerization of epoxy group simultaneously.

In addition to the interface effects, the ultimate performance of the sol–gel epoxy–silica hybrid polymers is substantially influenced by the experimental conditions and the processing technique. The present article describes the synthesis of the bicontinuous epoxy–silica hybrid polymers via a customized, solvent-free *two-stage chronological process*. The first-stage involved the sol–gel reaction carried out within the epoxy monomers. Once the sol–gel process was complete, silica-containing epoxy monomers were cured with a diamine in the next-stage. The two types of hybrid polymers synthesized in this way contained 0–30 wt.% silica, and differed from each other solely in the absence or presence of *GLYMO*; the amount of which was fixed at 5wt.% of the total silica content. Thin free-standing epoxy–silica polymer films are subsequently characterized by various advance analytical techniques. It is believed that the chronological addition and polymerization of the inorganic and organic precursors, their relative amount, the type of interphase interactions, and the experimental conditions employed herein would profoundly influence the ultimate properties such as the glass transition temperature of the epoxy–silica hybrid polymers.

2. Experimental

2.1. Materials

The sol–gel epoxy–silica hybrids were produced as optically transparent and thin free-standing polymer films on Teflon-coated glass plates. For this purpose, a high purity bisphenol A diglycidyl ether, D.E.R.™ 332 liquid epoxy resin with an epoxide equivalent weight of 175 g/eq, was chosen to assure uniform performance, and to provide very low viscosity in the absence of solvents. A low viscosity polyetheramine i.e. poly(oxypropylene)diamine (Jeffamine® D-400) with an amine-hydrogen equivalent weight of 107 g/eq, was employed as the curing agent for epoxy monomer. Liquid epoxy resin and polyetheramine were purchased from Dow chemical company and Huntsman Corporation, respectively. The SiO_2 networks were generated *in situ* by the hydrolysis and condensation of tetraethylorthosilicate (*TEOS*), which was obtained from Huls America Inc. (3-Glycidoxypropyl)trimethoxysilane (*GLYMO*) was received from Aldrich, and it was utilized in minimal concentration to enhance phase bicontinuity. Both of the silica precursors, *TEOS* and *GLYMO*, were obtained in the highest available purity, and were used as received.

Table 1
Composition of the pristine epoxy-amine and *ESA* hybrid polymers with respect to total SiO_2 content.

Specimen code	Total SiO_2 (wt.%)	Epoxy (g)	Jeffamine (g)	*TEOS* (g)	Water (g)
ES0R	0	6.206	3.794	-	-
ES5A	5	5.895	3.605	1.742	0.45
ES10A	10	5.585	3.415	3.483	0.90
ES15A	15	5.275	3.225	5.225	1.35
ES20A	20	4.965	3.035	6.967	1.80
ES25A	25	4.654	2.846	8.708	2.25

2.2. Polymer composition

A very simple nomenclature was devised to identify different types of epoxy–silica polymers, and it will be thoroughly used herein (see Tables 1 and 2). The first two letters of each specimen code are '*ES*' representing epoxy and silica system; followed by a '*number*' that stands for the total silica content (in wt.%) in the end-product. Finally an alphabet '*A*' or '*B*' is used to discriminate between the two series of hybrid polymers on the basis of absence or presence of *GLYMO*. The two types of hybrid polymer films and their constituents are represented as follows;

ESA hybrid polymers: constructed from epoxy-amine, and *TEOS*

ESB hybrid polymers: constructed from epoxy-amine, *TEOS*, and *GLYMO*

A pristine epoxy-amine polymer, designated by *ES0R*, was also prepared as a reference material to facilitate relative performance evaluation of the hybrid polymers. Amount of *TEOS* added to the organic matrix was calculated by the reaction stoichiometry in order to prepare hybrid materials with 5, 10, 15, 20, 25, and 30 wt.% SiO_2. Similarly, the amount of *GLYMO* was calculated according to reaction stoichiometry in order to derive 5wt.% of the total SiO_2 content from *GLYMO* during synthesis of bicontinuous *ESB* hybrid polymers. In view of the fact that a part of epoxide and silica in the *ESB* end-products originates from *GLYMO*, the amounts of epoxy monomer and *TEOS* were consequently adjusted to attain the right stoichiometry. Tables 1 and 2 summarize the precise quantities of reagents required to produce 10.0 g of thin epoxy–silica polymer films. After synthesis, all bicontinuous epoxy–silica hybrid polymers reflected the mass of end-product (the yield) within the pre-calculated range, exclusive of 2% experimental error.

Maximum amount of silica to be integrated into the organic matrix via sol–gel mechanism was decided experimentally by monitoring the macroscopic phase separation that led the SiO_2 network to be visible to the naked-eye (see Fig. 1). Light transmitted photographs of pristine and hybrid polymers were taken with a digital camera by placing thin films on a printed-piece of paper. The translucent as well as opaque morphology can evidently be examined for these films. Fig. 1 demonstrates that phase separation between organic matrix and inorganic network transpires at 25 and

Table 2
Composition of the *ESB* hybrid polymers with respect to total SiO_2 content.

Specimen code	Total SiO_2 (wt.%)	Epoxy (g)	Jeffamine (g)	*TEOS* (g)	*GLYMO* (g)	Water (g)
ES5B	5	5.311	3.605	1.654	0.114	0.447
ES10B	10	5.417	3.415	3.309	0.228	0.894
ES15B	15	5.023	3.225	4.963	0.342	1.341
ES20B	20	4.628	3.035	6.618	0.456	1.788
ES25B	25	4.233	2.836	8.272	0.570	2.235
ES30B	30	3.839	2.656	9.927	0.684	2.682

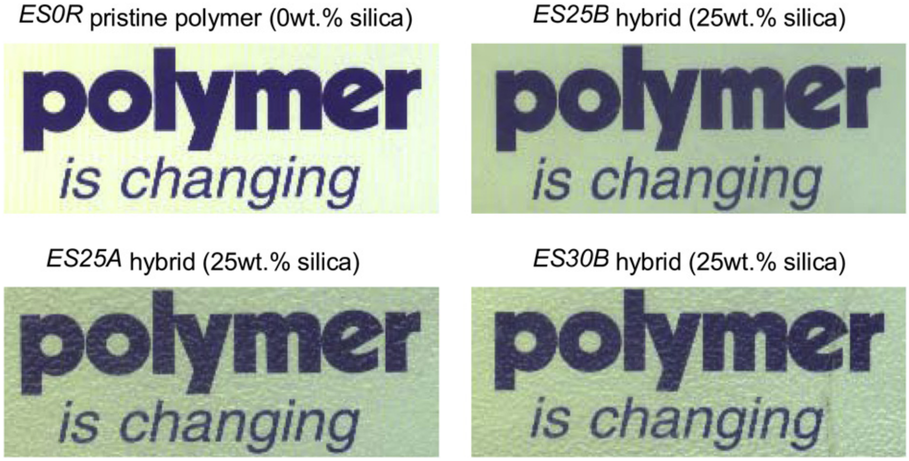

Fig. 1. Photographs of the pristine epoxy polymer and different epoxy–silica hybrids signifying the optical transparency or opaqueness of thin films.

30 wt.% SiO_2 loadings for *ESA* and *ESB* hybrid polymers, respectively. Consequently, epoxy–silica hybrid polymers with silica loadings higher than reported herein were not studied.

2.3. *Synthesis*

2.3.1. *Pristine epoxy-amine polymer: the reference*

Pristine epoxy-amine polymer was prepared by mixing calculated amounts of the epoxy and amine monomers in a 30 mL PFA beaker made with Teflon® resin. The ratio of epoxide group and amine-hydrogen was set to be 1.0 in all experiments i.e. ($C_{Ep}/C_{NH} = 1.0$). The mixture was stirred vigorously for 1 h at room temperature using a magnetic stirrer bar. To prepare thin polymer film on Teflon-coated glass plates of dimensions (6 × 6 inches), a simple and inexpensive method was employed. An especially designed preparative TLC (thin layer chromatography) applicator was used to spread the viscous liquid matrix on Teflon-coated glass plates in order to deliver polymer films with a uniform thickness of 0.15 mm. Prior to deposition, the mixture was kept under vacuum for 10 min to remove entrapped gases and air bubbles, if any. After matrix deposition, the plates were carefully placed on a leveled surface inside an oven pre-heated to 100 °C. The polymer was cured initially for 5 h at 100 °C, and subsequently for 1 h at 120 °C. The apparatus utilized in the synthesis and deposition of polymers were properly cleaned and dried according to standard procedures in order to remove organic contaminants and dust particles.

2.3.2. *Bicontinuous epoxy–silica hybrid polymers*

Hereby the exact recipe to synthesize various kinds of hybrid polymers is described, while the precise amounts of ingredients are given in Table 1 and 2. The epoxy–silica hybrid polymers containing 5–30 wt.% silica were also produced as thin polymer sheets on the Teflon-coated glass surfaces. For this purpose, epoxy monomer was first mixed with the calculated amounts of silane under absolute anhydrous conditions, and stirred vigorously with a magnetic stirrer bar for 2 h at 25 °C in order to attain a homogeneous mix of epoxy and silane monomers. *ESA* hybrid polymers contained only *TEOS*; while in *ESB* type of hybrid polymers the ratio of *TEOS* and *GLYMO* was regulated so that 5 wt.% of the total silica content is derived from *GLYMO* (see Table 2). After thorough mixing, calculated amount of water brought to $pH = 2$ with the help of an inorganic acid was added to the mixture. According to the well established stoichiometry between water and different silica precursors [15,16]; they were mixed in the following ratios; (i) water and *TEOS* = 3: 1, (ii) water and *GLYMO* = 2.25: 1. The *in situ* hydrolysis and condensation of silica precursors was carried out by continuous stirring of the mixture initially at 25 °C for 1 h, and subsequently at 60 °C for 5 h. Polyetheramine was then added to the mixture and it was further stirred for 1 h at room temperature

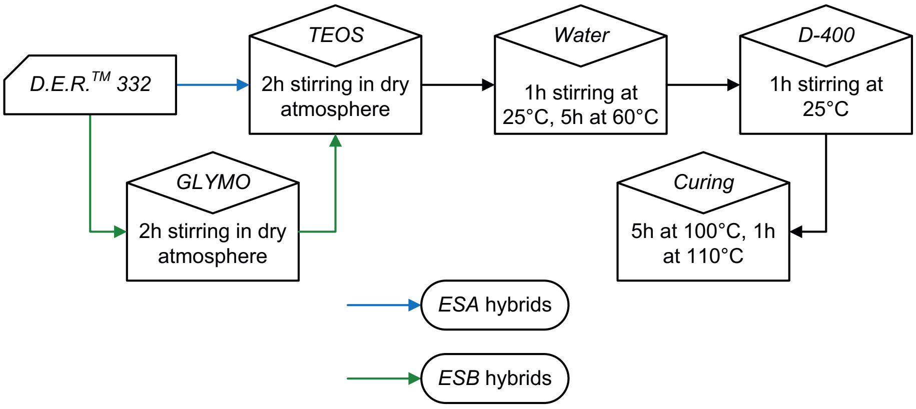

Fig. 2. Flowchart representation of the procedure adapted for the synthesis of different types of bicontinuous epoxy–silica hybrid polymers.

before the deposition and subsequent curing process. Similar procedure was employed for matrix-silica deposition on Teflon-coated glass plates and for its curing as described earlier. Fig. 2 presents a flowchart illustrating the detailed procedure for the synthesis of *ESA* and *ESB* hybrid polymer films.

2.4. Characterization

2.4.1. FTIR spectroscopy

Fourier transform infrared (*FTIR*) spectroscopy was used to characterize the pristine and hybrid polymer films, and to confirm the polymerization of silanes as well as the crosslinking of epoxy monomer with amine. The PerkinElmer system 2000 series *FTIR* spectrometer was used to examine thin polymer films via the attenuated total reflectance (*ATR*) method. The infrared spectra were recorded in the range of 4000–600 cm^{-1}.

2.4.2. Gas chromatography mass spectrometry (GCMS)

Gas chromatography mass spectrometry (*GCMS*) was used to estimate the amount of unreacted silanes and residual volatiles so as to measure the extent of sol–gel reaction. The specimen was tested on the Agilant 6890GC (version N.05.05) instrument coupled with the Agilant 5973 N mass selective detector (MSD) via a heated transfer capillary (heated to 250 °C). The instrument was operated by the Agilant C1701DA GC/MSD chem-station software. Headspace method was used for the analysis, and the volatile gases were injected in a split-less mode with the help of a 2.5 mL headspace syringe MSH 02–00B. Before injection, the specimen was incubated for 15 min at 150 °C. Helium (He) was used as the career gas with a constant flow rate of 2 mL/min.

2.4.3. Gravimetric analysis

As a confirmation of the results obtained from *GCMS* and to determine the precise amount of silica produced during the *in situ* sol–gel process, weighed amount of epoxy–silica polymers were burnt at 1000 °C inside an autoclave in regular air atmosphere. After burning, the amount of silica (in wt.%) was calculated from the char residue and the average data obtained from at least four specimens were reported.

2.4.4. Differential scanning calorimetry (DSC)

Differential scanning calorimetry (*DSC*) was used to examine the conversion of epoxy groups as well as the glass transition temperature (T_g) of fully cured specimen. It was performed with the PerkinElmer *DSC* 7 instrument by heating approximately 10 mg of the specimen in a sealed aluminum pan under inert (N_2) atmosphere. The instrument was ramped at 5 °C/min from −50 °C to 350°C, but no rate was specified for initial cooling and it was brisk. For completely cured specimen, a second *DSC* scan was also run from 0 °C to 110 °C in order to estimate the correct T_g.

2.4.5. Atomic force microscopy (AFM)

Surface characterization of the pristine polymer and epoxy–silica hybrid polymers was carried out with the help of an atomic force microscope (*AFM*). A Multimode Digital Instruments Nanoscope™ dimension IIIa *AFM*, equipped with PPP-NCLR tapping mode probe, Nanosensors™ Switzerland, was used to scan the surface of $\sim$ 10 mm^2 specimen. The *AFM* images were recorded under ambient conditions using the tapping-mode *AFM*. The scanning probe was equipped with a triangular cantilever with a pyramidal tip made of silicon nitride. The *AFM* micrographs were analyzed on the scanning probe microscopy (*SPM*) software WSxM 3.0 Beta v. 8.1, by Nanotec Electronica S.L. The micrographs shown herein have *x*- and *y*- resolution of 5 × 5 μm, unless otherwise specified; while *z*-axis height varies from 10 nm to a few 100 nm depending upon the surface roughness.

3. Results

3.1. Formation of epoxy–silica polymers

This section presents results obtained from *FTIR*, *GCMS*, and simple gravimetric analyses.

3.1.1. FTIR spectroscopy

Attenuated total reflectance (*ATR*) *FTIR* spectra of *ES15B* polymer before its deposition for curing and after completion of the cure cycle are shown in Fig. 3. It must be noted that only densely populated regions from the two spectra are separately shown herein (Fig. 3a,b) in order to clearly identify the absorption peaks and to specify the differences. The spectra of other bicontinuous polymers look alike, and there was no significant peculiarity recorded. It is because of the intricate nature of epoxy–silica polymers, in which multiple absorption peaks overlap and consequently it is difficult to distinguish between different types of hybrid polymers from their *IR* spectra.

Nonetheless, *ATR FTIR* spectra reveal significant information about the formation of silica–epoxy networks. As reported earlier

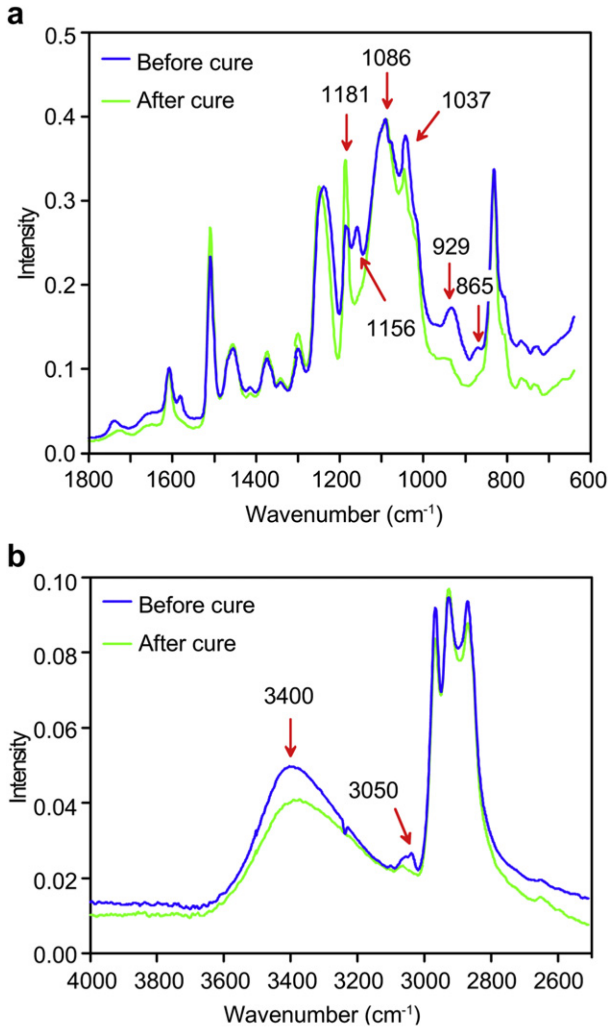

Fig. 3. Attenuated total reflectance *FTIR* spectra of *ES15B* polymer before and after curing.

[16–18], the characteristic Si–O–Si stretching is observed in the range of 1095–1075 cm^{-1}; herein the ATR spectrum shows an intense peak at 1086 cm^{-1} with a shoulder at ~1100 cm^{-1}, which confirms the formation of SiO_2 network. The characteristic O–H stretching, appeared as a broad peak closer to 3400 cm^{-1}, may be attributed to the silanol (Si-OH) groups present on the surface of silica [17]. It might well be assigned to the secondary hydroxyl groups formed as a result of epoxide ring opening during the crosslinking reaction [18]. However, an anomalous decrease in the intensity of this peak corresponds to the evaporation of side-products of the sol–gel reaction e.g. methanol, ethanol etc during the cure.

The formation of epoxy networks was verified by either weakening or disappearance of certain peaks inherent to the epoxide, and amino functional groups. Before curing, the intrinsic *IR* absorptions for epoxy groups are observed at 3050 cm^{-1} for epoxide C–H and 929 cm^{-1} and 865 cm^{-1} for C–O–C respectively before curing. After curing for 6 h, however, these peaks are diminished suggesting the approximate completion of crosslinking reaction. Further evidence came from the examination of N–C stretching frequencies of *pri*-, *sec*- and *ter*-amine, which appear in the range of 1070–1020 cm^{-1}, 1190–1130 cm^{-1}, and 1210–1150 cm^{-1} respectively [17]. Herein the peaks at 1037, 1156 and 1180 cm^{-1} are correspondingly designated to *pri*-, *sec*- and *ter*-amine groups. ATR IR spectra in Fig. 3 reveal a decrease in the intensity of *pri*-amine peak, the disappearance of *sec*-amine peak, and a significant increase in the intensity of *ter*-amine peak during the course of curing, suggesting the crosslinking of amino groups with epoxide. The absorption at 1037 cm^{-1}, observed in fully cured film with sizeable intensity, implies that some unreacted *pri*-amino groups are still present in the matrix, which might be due to absorption of amine hardener on the siloxane domains, as observed in [19].

3.1.2. Gas chromatography mass spectrometry

The extent of sol–gel reaction was monitored with the help of headspace *GCMS* analysis of bulk matrix during the course of *in situ* hydrolysis–condensation process. A few milligrams of the bulk sample were obtained from the *ES15A* reaction mixture after 1, 2, 3, 4 and 5 h of continuous stirring, and analyzed. The *ES15A* system was chosen for this study because of the presence of sufficient amount of *TEOS* and the absence of *GLYMO*. The absence of *GLYMO* ensures that *GCMS* results show peaks only for *TEOS* and the products of its hydrolysis i.e. ethanol, and oligomers of *TEOS*. The samples were incubated at 150 °C in a thermal agitator for 15 min before the injection of volatile gases into the GC column. *GCMS* results are depicted in Fig. 4; showing the abundance of unreacted *TEOS* along with other products of hydrolysis at different intervals of reaction.

Evidently a significant amount of unreacted *TEOS* was present in the bulk matrix after the first hour of stirring at 25 °C. An evenly considerable amount of the dimer hexaethoxydisiloxane (*HEDSi*) was also observed, which indicated that the sol–gel reaction had been initiated at 25 °C. The trimers and higher oligomers were not detected by *GCMS* during any stage of the sol–gel process, which may be attributed to the relatively higher boiling points of these oligomers. *GCMS* analyses of the mixture after 2 and 3 h of stirring at 60 °C showed no evidence of the existence of unreacted *TEOS*, which implies that all the *TEOS* molecules were hydrolyzed during this interval. These results are in harmony with the acid-catalyzed mechanism for the gelation of silica in pure sol–gel reactions in which the hydrolysis is very fast and condensation is the rate determining step [20].

The amount of *HEDSi* in the matrix increased significantly during the first half of sol–gel reaction. After 5 h stirring at 60 °C, however, only a minimal quantity of *HEDSi* was seen in the matrix indicating the formation of larger condensates i.e. polysiloxanes as a consequence of the total hydrolysis and condensation of *TEOS* and higher oligomers. These results not only verify the end-point of the sol–gel process, but also provide an insight into the characteristics of acidic hydrolysis *in situ*.

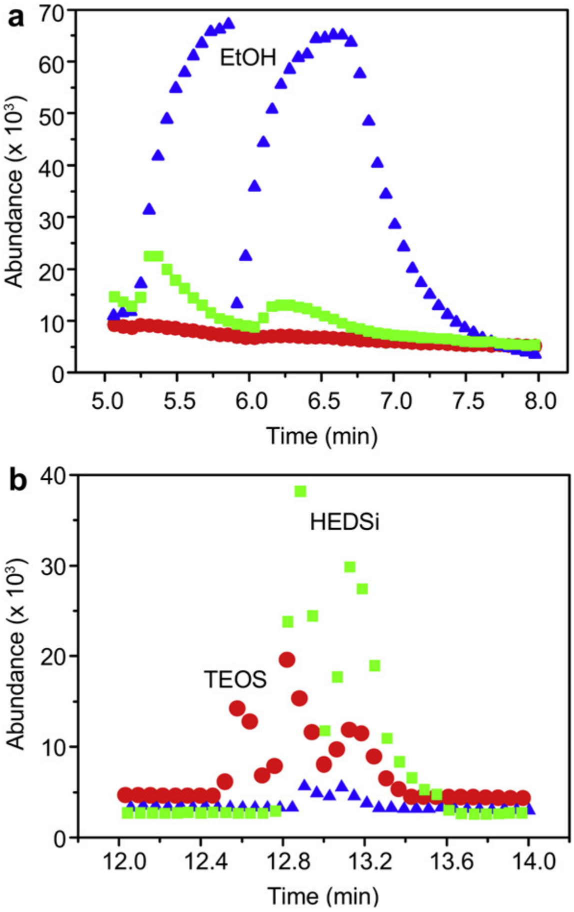

Fig. 4. Headspace *GCMS* analysis of *ES15A* bulk matrix after (○) 1 h, (□) 3 h, and (△) 5 h of *in situ* hydrolysis of *TEOS*.

3.1.3. Gravimetric analysis

The amount of silica actually formed by the *in situ* sol–gel reaction was calculated from the mass of char residue obtained after burning pre-weighed specimen at 1000 °C in air. The data are reported in Table 3. These experiments provided a good estimation of the actually formed silica, and revealed that in most cases the sol–gel reaction was ≥99% complete.

3.2. Morphology of epoxy–silica polymers

The microstructure and surface morphology of the bicontinuous epoxy–silica hybrid polymers was studied by *AFM*. *AFM* offers high

Table 3
The amount of silica (in wt.%) actually formed by the *in situ* sol–gel process.

ESA polymers	Amount of SiO_2		*ESB* polymers	Amount of SiO_2	
	wt.%	Dev.		wt.%	Dev.
ES0R	-	-	*ES5B*	5.0	0.1
ES5A	4.9	0.1	*ES10B*	9.7	0.2
ES10A	9.8	0.2	*ES15B*	14.8	0.3
ES15A	14.7	0.3	*ES20B*	19.7	0.2
ES20A	19.6	0.2	*ES25B*	24.6	0.3

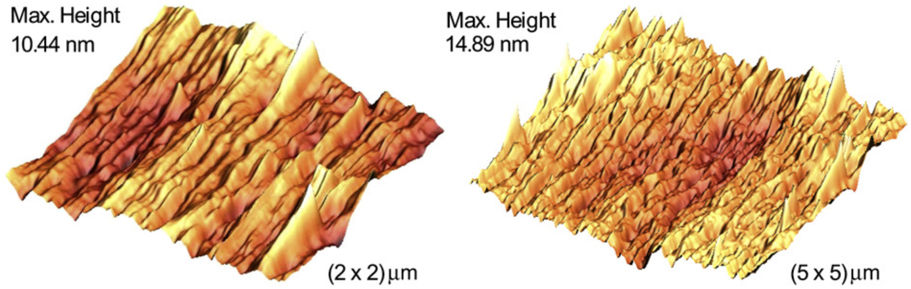

Fig. 5. The 3D *AFM* images of the pristine epoxy-amine polymer film at different *xy*-resolution.

resolution mapping of the topography of material surface at the sub-nanometer scale. For instance, *3D* (three dimensional) *AFM* images of the pristine epoxy-amine polymer films are shown in Fig. 5 with a vertical (*z*-) resolution of 10–15 nm only. These images demonstrate that pristine polymer has rather uniform surface with the *RMS* roughness of 1.68 nm. The *RMS* roughness (R_q) is defined as the square root or the standard deviation of the height distribution of points within the *AFM* image, and is given by Eq. (1) [21];

$$R_q = \sqrt{\frac{1}{N^2}\sum_{i=1}^{N}\sum_{j=1}^{N} Z_{i,j}^2} \qquad (1)$$

where $Z_{i,j}$ is the height data at position (i.j)

The surface properties of the pristine epoxy and hybrid epoxy–silica polymers calculated from their respective *3D AFM* images are furnished in Tables 4 and 5. It is evident that the RMS roughness and average height of thin film surfaces are increased with the increase in the integrated amount of silica in the hybrid polymers.

The *in situ* hydrolysis of silanes yields silica networks homogeneously distributed into the matrix and it is evident from the *AFM* images of epoxy–silica hybrid polymers. Fig. 6 shows the *AFM* images of the two types of epoxy–silica thin films with 5wt.% silica. The morphology of the *ES5A* and *ES5B* polymer surface is specified by several height points (peaks) on the *xy*-plane, designated as silica nanoparticles. These micrographs demonstrate the characteristics of a bicontinuous hybrid polymer, where *3D* organic and inorganic networks are rather uniformly distributed and interpenetrated into each other. The *RMS* roughness increases as compared to the *ES0R* due to the incorporation of silica.

The *AFM* images of other hybrids were also examined in *3D*. Fig. 7 presents the micrographs of epoxy–silica hybrids with 10wt.% silica. The surface of *ES10A* polymer shows intense peaks of silica nanoparticles and their aggregates. The distribution of peaks is uniform except for the appearance of a few nanoscale clusters of silica created in consequence of aggregation of the nanoparticles. In the *AFM* image of *ES10B* polymer, the number of peaks increases with a much lower maximum height and greater homogeneity. This kind of difference in the morphology of two hybrids may be attributed to the presence of 5wt.% *GLYMO*, which mutually holds the organic and inorganic constituents together.

The *AFM* images of 15wt.% epoxy–silica hybrid polymers are shown in Fig. 8. Again a fair distribution of height points in *ES15A* with a maximum height data of 153 nm can be observed. It is obvious that the clusters grow bigger and their number is also increased as compared to that of *ES10A* polymer. The *AFM* image of *ES15B* polymer does not show a significant increase in the height data, and the distribution of silica is excellent with no agglomeration. The silica nanoparticles are preferentially concentrated and do not form larger aggregates, Hence *3D* micrograph of *ES15B* polymer does not show any discernible structures like that of *ES15A*, again signifying the formation of bicontinuous epoxy–silica hybrid.

The *AFM* images of *ES20A* and *ES20B* polymers are presented in Fig. 9. The micrograph of *ES20A* polymer shows the surface concentrated with fairly huge clusters of silica particles. The microscopic phase separation might have originated at this stage as could be seen by the poor distribution of silica in the matrix, and a dramatic increase in the *RMS* roughness. In case of *ES20B*, the phase interlinking through covalent bonds leads to yet superior distribution and segregation of silica nanoparticles, and delays the phase separation. Also, the increase in RMS roughness is not as remarkable as that of *ES20A*, which may be attributed to the steady influence of greater strength and bicontinuity of the interphase in *ES20B* polymer.

3.3. *Differential scanning calorimetry*

The objective of *DSC* studies was to monitor the conversion of epoxy groups with time, and to determine the glass transition temperature (T_g) of the properly cured specimen. The specimen for *DSC* analysis were obtained after mixing of amine and stirring it for 10 min at 0 °C (at 0 h), after stirring the mixture for 1 h at 25 °C (1′h), and after 1, 2, 3, 4, 5, and 6 h of curing at different temperatures in order to establish the complete profile of curing process. Fig. 10 shows a typical *DSC* scan of *ES0R* and *ES10B* polymers after 5 h of curing at 100 °C. The inset shows the residual exotherms obtained from the first *DSC* scan of *ES0R* at different intervals during the mixing and curing steps. It is evident that enthalpy of reaction decreases regularly with the cure time until epoxy monomers are fully consumed, and it becomes insignificant after 6 h of curing. The residual heat of reaction (ΔH_r) is estimated by integrating the area of exothermic peak [22]. The total heat of reaction (ΔH_T) is calculated in the same way from the *DSC* thermogram at 0 h. The average values of ΔH_T for *ES0R*, *ES10A* and *ES10B* were recorded as 106.4, 99.6 and 101.2 kJ/mol, respectively. The fractional conversion (x) of epoxy groups can be calculated from the residual enthalpy (ΔH_r) of

Table 4
Roughness analysis of pristine epoxy and *ESA* hybrid polymers.

Surface properties	*ES0R*	*ES5A*	*ES10A*	*ES15A*	*ES20A*	*ES25A*
RMS roughness (nm)	1.68	2.31	3.05	7.14	12.55	23.79
Average height (nm)	5.95	6.93	11.61	20.38	28.03	38.91

Table 5
Roughness analysis of *ESB* hybrid polymers.

Surface properties	*ES5B*	*ES10B*	*ES15B*	*ES20B*	*ES25B*
RMS roughness (nm)	2.85	4.41	7.23	9.20	19.09
Average height (nm)	15.99	14.87	22.82	24.12	31.34

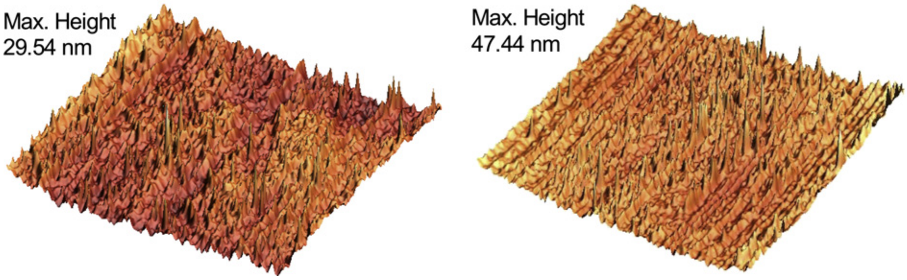

Fig. 6. The 3D atomic force micrographs (5 × 5 μm) of *ES5A* polymer (left), and *ES5B* polymer (right).

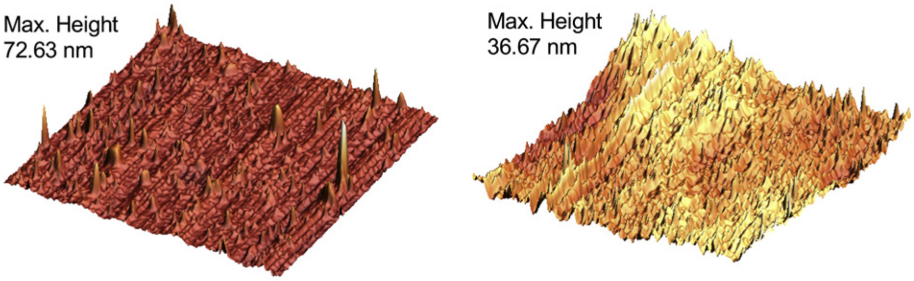

Fig. 7. The 3D atomic force micrographs (5 × 5 μm) of *ES10A* polymer (left), and *ES10B* polymer (right).

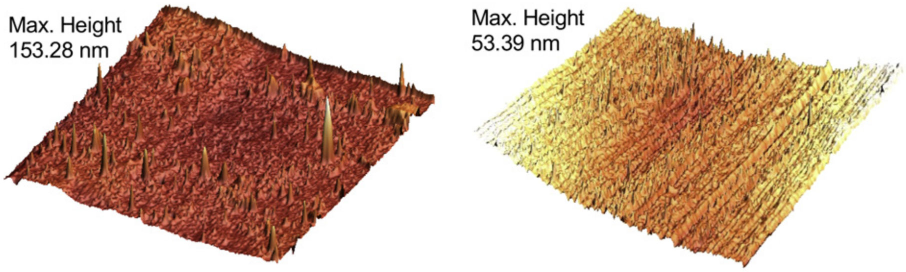

Fig. 8. The 3D atomic force micrographs (5 × 5 μm) of *ES15A* polymer (left), and *ES15B* polymer (right).

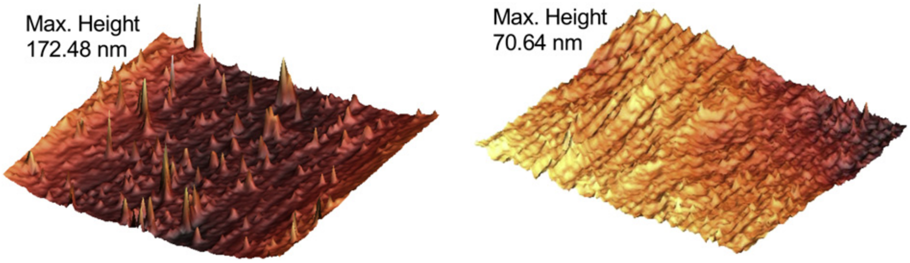

Fig. 9. The *3D* atomic force micrographs (5 × 5 μm) of *ES20A* polymer (left), and *ES20B* polymer (right).

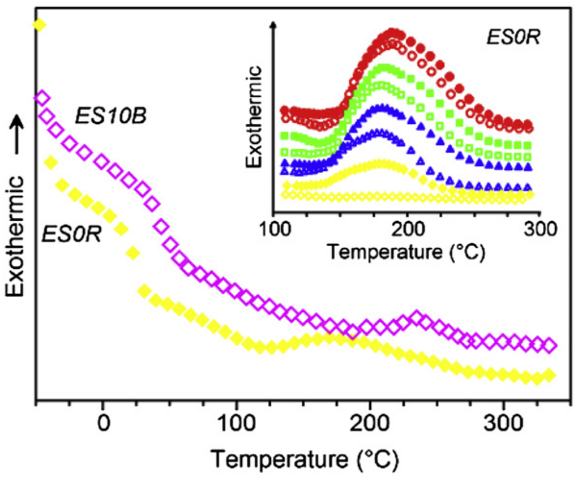

Fig. 10. A typical *DSC* scan of *ES0R* and *ES10B* after curing for 5 h at 100 °C. The inset shows residual exotherms of the epoxy and amine crosslinking reaction at (●) 0 h and (○) 1′h of mixing, and at (■) 1 h (□) 2 h (▲) 3 h (△) 4h (◆) 5 h and (◇) 6 h of curing at different temperatures.

the partially cured specimen and the total enthalpy of reaction (ΔH_T) corresponding to unreacted specimen according to Eq. (2);

$$x = (\Delta H_T - \Delta H_r)/\Delta H_T \quad (2)$$

The fractional conversion of epoxy groups (x) in pristine epoxy polymer and epoxy–silica hybrids with 10wt.% SiO_2 is plotted as a function of cure time in Fig. 11a. An increase in the total conversion with time is evident; the magnitude of which is enhanced in the later stages of cure owing to the self-catalysis by the hydroxyl groups produced in consequence of the epoxide ring opening reaction. The value of x obtained after 6 h is 0.97 (corresponding to $\Delta H_r = 3.3$ kJ/mol) for pristine epoxy-amine system (*ES0R*), signifying that 97% of the epoxide groups have reacted effectively during the cure cycle.

On the other side, the residual enthalpy after 6 h of curing is almost unmeasureable in case of hybrid polymers that verifies the total conversion of epoxy groups during the cure. It is important to note that the presence of silanol groups in *ES10A* polymer significantly enhances the rate of crosslinking reaction [23]; and the value of x reaches 0.97 after 5 h of curing at 100 °C. No residual activity is therefore observed after curing at 121 °C for the final hour. The total conversion of epoxy groups is also evident in case of *ES10B* polymer, though the rate of crosslinking reaction is significantly reduced upon introduction of 5wt.% *GLYMO*. This may be attributed to the steric hindrance caused by the glycidoxypropyl moiety in such a way that lesser silanol groups are available for the activation of epoxide ring.

The glass transition temperature (T_g) of pristine polymer and epoxy–silica hybrids with 10wt.% SiO_2 is plotted as a function of cure time in Fig. 11b. A substantial increase in T_g is detected owing to increase in the network crosslink density as the cure proceeds; also reported in *Ref.* [24–26]. In *ES0R*, T_g of the matrix is associated to x, the fractional conversion of epoxy groups. The T_g of epoxy–silica hybrids is lower as compared to that of pristine polymer in the first half of cure, while increases considerably in the second half. This kind of dual behavior is ascribed to the presence of by-products of sol–gel reaction e.g. ethanol in the first half of cure cycle, which are certainly evaporated after curing for 2–3 h at 100 °C. In addition, better cure kinetics and greater conversion leads to higher crosslinking density and improved T_g as the cure proceeds further. The final T_g of *ES10B* polymer is slightly superior to that of *ES10A* polymer indicating supplementary enhancement in the phase interlinking of matrix-silica components due to covalent bonding. In order to further elaborate these points, T_g *vs.* x plot is given in Fig. 11c. The effect of physical and chemical phase

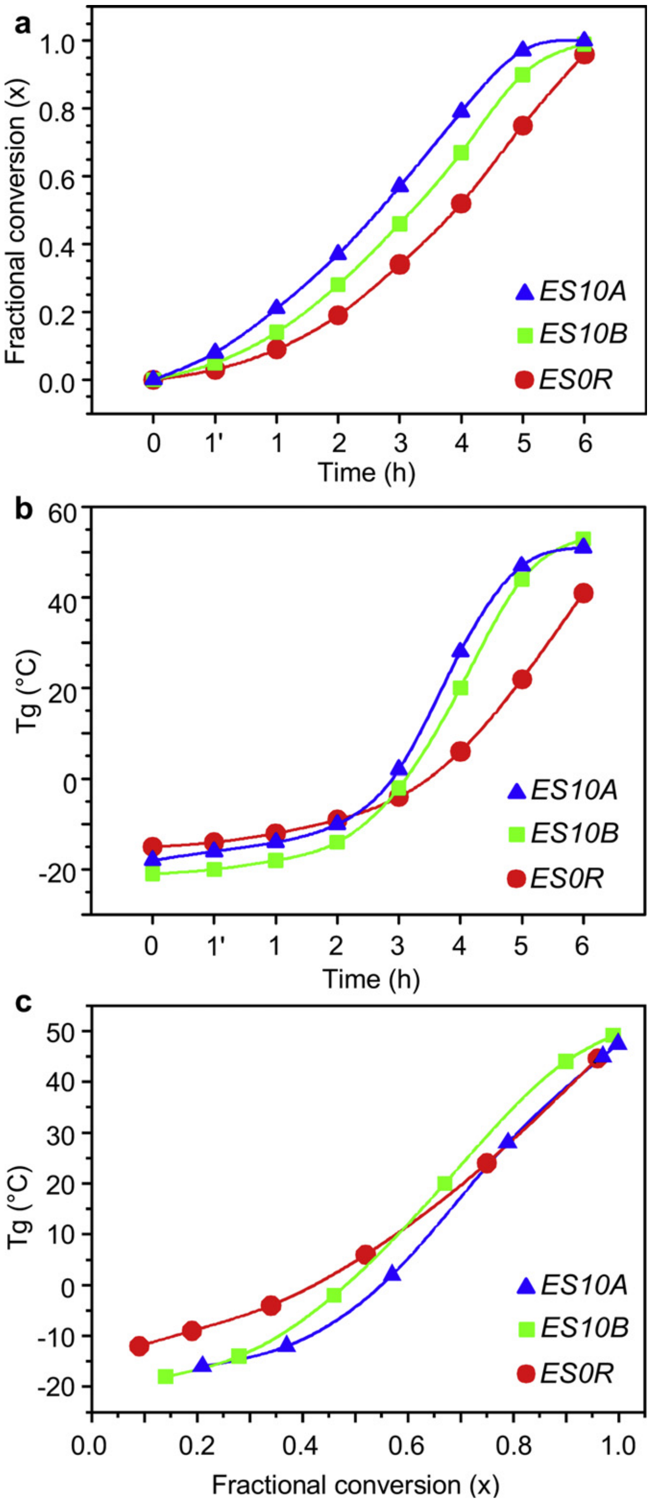

Fig. 11. (a) The fractional conversion (x) of epoxy groups, and (b) the glass transition temperature, T_g, as a function of time for the mixing (1 h at 25 °C) and curing (5 h at 100 °C & 1 h at 110 °C), and (c) T_g as a function of x in pristine epoxy-amine and epoxy–silica hybrids with 10wt.% SiO_2.

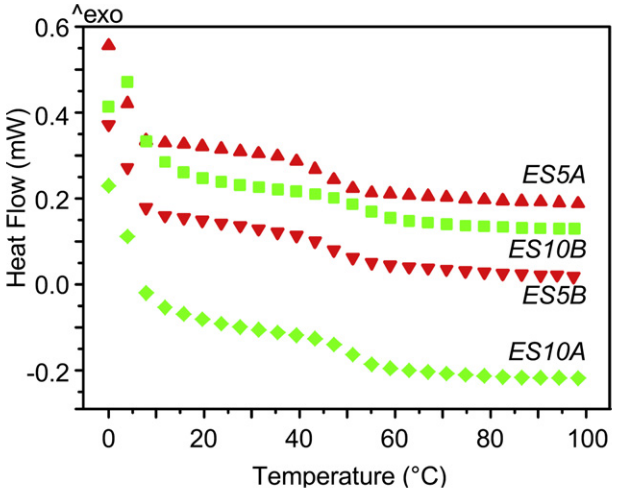

Fig. 12. Second *DSC* scans of epoxy–silica polymers after completion of the cure cycle.

interlinks is clearly depicted in this plot i.e. at same *x* values, *ES10B* shows a higher T_g as compared to *ES10A* owing to the presence of additional chemical crosslinks between two phases.

The final T_g of pristine and hybrid polymers are determined from the second *DSC* scan of specimen cured properly for 6 h at different temperatures. Fig. 12 shows the second *DSC* scans of *ESA* and *ESB* hybrids with 5 and 10wt.% silica. The T_g of these specimen increases with the integrated amount of silica owing to the strong inhibition of the movement of polymer chains, a phenomenon already observed in [27]. Overall, 13.6% and 20.4% increase in T_g is observed for *ESA* and *ESB* polymers respectively. The final T_g of different polymers are plotted as a function of SiO_2 loading in Fig. 13. The degree of improvement in T_g is greater in case of *ESB* hybrids due to interface bicontinuity and crosslinking, which resists polymer chain flow by stitching together the organic and inorganic networks and extends glass transition. A noticeable decrease in T_g at higher silica loading, however, is obvious especially in *ESA* polymers that can be described on the account of considerable increase in the polymer free-volume, more pronounced homopolymerization, and greater degree of phase segregation at higher silica loadings (see discussion).

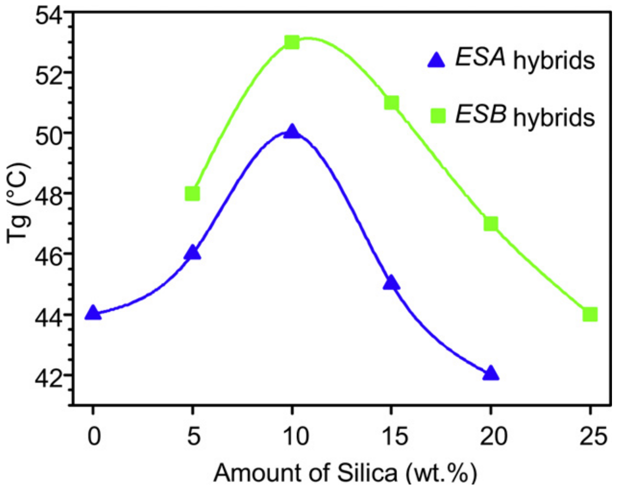

Fig. 13. The glass transition temperature, T_g, of different polymers as a function of silica content.

4. Discussion

A customized two-stage chronological procedure was used to synthesize bicontinuous epoxy–silica hybrid polymers with and without 5wt.% *GLYMO*. In the first step, acid-catalyzed sol–gel process was carried out into the liquid epoxy monomer. It is well known that epoxy ring is resistant to such hydrolysis conditions [28–30] provided that water is not used in large excess. This step was directly monitored via *GCMS*, and the analysis (in Fig. 4) revealed that the entire *TEOS* monomers had been hydrolyzed and condensed to form dimers and higher oligomers following 2 h of stirring at 60 °C. This kind of speedy hydrolysis means that total conversion of silanes into silica (or oligosiloxanes) is quite certain; also verified by the gravimetric measurements (Table 3). These results are consistent with the known growth mechanism of silica via low *pH* sol–gel process [31].

Reports suggest more open, extended coil-like, ramified silica nanostructures are formed as a result of acid-catalyzed sol–gel reaction [32,33]. The microscopic (*AFM*) analyses of epoxy–silica polymers reveal that nanosized silica particles are well-distributed into epoxy networks (Figs. 6–9). In *ESA* hybrids, the size of individual silica nanoparticles increases with the concentration of *TEOS* owing to the formation of a large number of tiny particles at relatively higher concentration of *TEOS*, which can subsequently approach surrounding species with a greater ease resulting in particle growth during the aging period. On the other hand, the size variations are little in case of *ESB* polymers, corresponding to better scattering of nanoscale clusters due to their inherent covalent crosslinks with the matrix. Addition of *GLYMO* reduces the size of nanoparticles by keeping the tiny clusters apart from each other, and obviously by steric capping of the relatively small nanoparticles. Thus it prevents particle growth even at higher concentrations of silica, and affects the overall dispersion of nanoscale silica.

Fig. 14 displays a representative of the kind of interactions among the organic and inorganic constituents, and the structure of hybrid polymers hence constructed. Only hydrogen bonds are shown as the interphase links between organic and inorganic components in *ESA* hybrids, while the two components are interlinked through covalent bonds in addition to hydrogen ones suggesting phase bicontinuous structure in *ESB* hybrids. Though, physical crosslinks such as hydrogen bonding [8] contribute toward improved dispersion of silica, hereby they do not prevent the aggregation of silica nanoparticles, if present in quantities >15wt.%, and hence the phase separation. Conversely, *GLYMO* leads to better mixing of the components at the molecular level and results in increased uniformity within the polymer film. In *ES20B* (Fig. 9), for instance, sharp peaks are transformed into broader heaps indicating particle growth phenomenon to some extent; the overall morphology remains reasonably consistent in the *xy*-plane owing to the stronger association between polymer and particles.

The second step in the preparation of epoxy–silica hybrids involved crosslinking of epoxy with a diamine curing agent. It is important to note that the extent of crosslinking of epoxide is greatly influenced by the silanol groups, and is sufficiently higher in the epoxy–silica hybrids as compared to the pristine epoxy polymer (see Figs. 10 and 11a). This result is contrary to the findings of Mahrholz et al. [34]; but is fairly in agreement with the work of other scientists [35–37]. It was also found that *GLYMO* has a propensity to reduce the rate of cure possibly due to the steric capping of silanol groups. The T_g of pristine and hybrid polymers are also plotted as a function of cure time and fractional conversion in Fig. 11b,c respectively. In case of pristine polymer, T_g increases as the cure proceeds showing a direct relationship with the fractional conversion of epoxy groups, as the crosslink density is thereby

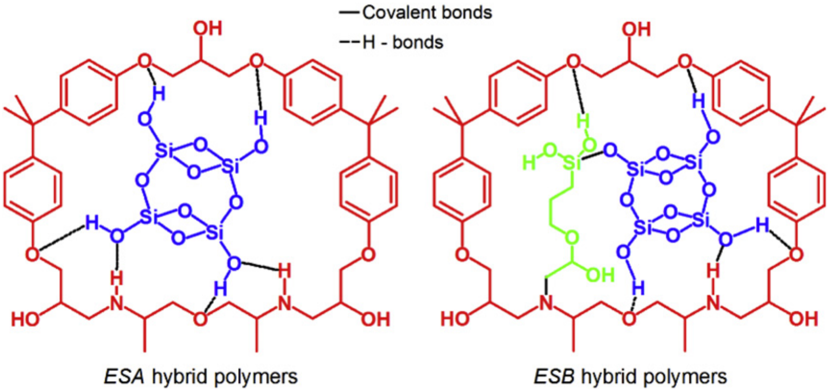

Fig. 14. A representative of the likely structure and interface linking in the two types of epoxy–silica hybrid polymers.

increased. The *ESA* and *ESB* hybrid polymers show a reduced T_g in the first half of cure, which might well be attributed to the presence of alcohol liberated during the sol–gel process. However, a huge increase in T_g is observed in the latter stages of cure owing to the greater conversion of epoxide fractions and evaporation of the liberated alcohols.

The T_g of epoxy–silica hybrid polymers increase greatly in the presence of 5wt.% *GLYMO* (Figs. 12 and 13). An increase in T_g is believed to be due to the formation of highly immobilized and thin interface layer that is developed near the surface of silica particles. The conformational entropy and the chain kinetics are greatly altered within the interface region, and the polymer chains experience sufficient constrains [27]. It is these constraining forces which in consequence shift T_g to higher temperature. In contrast, the T_g of hybrid polymers decreases significantly at higher silica loadings, which could be described on different accounts. Mascia et al. [11,19] reported that amino-functional curing agents have a tendency to adsorb on the surface of siloxane oligomers and as a result epoxy monomers homopolymerize, which eventually reduced crosslink density and T_g. It seems plausible in this study as a significant amount of primary amine was found unreacted after the completion of cure (Fig. 3). In addition an increase in the filler content may also increase the free-volume owing to the much loosened packing of the polymer chains, which in consequence assists the segmental motion of the polymer on a larger scale [38]. The greater degree of phase segregation at higher silica loading might also play a role in reducing T_g. An extensive decline in T_g at higher filler concentration has been recorded in epoxy–silica hybrids as well as in other polymers [39–42]. Nonetheless, a decrease in T_g of a hybrid polymer is inevitable at higher silica loadings due to several opposing factors.

Eventually it is evident that the sol–gel epoxy–silica hybrid polymers can effectively be prepared using a solvent-free two-stage chronological process. The size, nature and distribution of silica are excellent in these polymers and further improved on addition of *GLYMO*, which manifest the suitability of these hybrid polymers for various applications. These polymers also exhibit higher stability at elevated temperatures, and greater strength as well as material toughness [43]. Further investigations into the toughening mechanism and their behavior under stress are being carried out currently and would be a part of the next contribution on the subject.

5. Conclusion

The paper presents a comprehensive study of the epoxy–silica hybrid polymers synthesized via the two-stage chronological process. The polymers, thus produced as thin free-standing films, were fully characterized using advance analytical methods. The *in situ* sol–gel process results in the formation of small-sized silica networks, which are well-distributed into the organic matrix. The hydroxylated-nature and ramified-structure essentially allow them to interact with the polymer in a better way, resulting in the formation of phase bicontinuous hybrids. The addition of *GLYMO* supplements the interface interactions through chemical crosslinks between the organic and inorganic constituents, and enhances bicontinuity of the phases. It also affects the size and distribution of silica and inhibits phase separation. The T_g of epoxy–silica hybrid polymers thus increase significantly reaching a maximum of 13.6% and 20.4% for *ES10A* and *ES10B* hybrids respectively. A decrease in T_g is inevitable though at higher concentration of silica due to more profound negative effects of free-volume increase, homopolymerization, and phase separation.

Acknowledgments

The financial support by the University Research Fund of Quaid-i-Azam University, Islamabad 45320, Pakistan is gratefully acknowledged. The authors wish to thank Dr. Adnan Mujahid and Mr. Naseer Iqbal (Uni. Wien, Austria) for support of the experimental work, as well as Prof. Dr. Franz L. Dickert (Uni. Wien, Austria) for providing the AFM facility.

References

[1] Novak BM. Advanced Materials 1993;5:422–33.
[2] Brinker CJ, Scherer GW. Sol–gel science. London: Academic Press, Inc.; 1990 [Chapter 3].
[3] Matejka L. POSS and other hybrid epoxy polymers. In: Pascault JP, Williams RJJ, editors. Epoxy polymers: new materials and innovation. Weinheim,Germany: Wiley–VCH Verlag GmbH & Co; 2010. doi:10.1002/9783527628704.ch8.
[4] Matejka L, Plestil J, Dusek K. Journal of Non-Crystalline Solids 1998;226:114–21.
[5] Bauer BJ, Liu DW, Jackson CL, Barnes JD. Polymers for Advanced Technologies 1996;7:333–9.
[6] Matějka L, Dukh O, Kolarik J. Polymer 2000;41:1449–59.
[7] Ochi M, Takahashi R. Journal of Polymer Science B 2001;39:1071–84.
[8] Davis SR, Brough AR, Atkinson A. Journal of Non-Crystalline Solids 2003;315:197–205.
[9] Prezzi L, Mascia L. Advances in Polymer Technology 2005;24:91–102.
[10] Lu SR, Zhang HL, Zhao CX, Wang XY. Journal of Materials Science 2005;40:1079–85.
[11] Mascia L, Tang T. Journal of Materials Chemistry 1998;8:2417–21.
[12] Mascia L, Prezzi L, Wilcox GD, Lavorgna M. Progress in Organic Coatings 2006;56:13–22.
[13] Ivankovic M, Brnardic I, Ivankovic H, Huskic M, Gajovic A. Polymer 2009;50:2544–50.
[14] Spirkova M, Brus J. Progress in Organic Coatings 2008;61:145–55.
[15] Wein J, Breiner JM, Mark JE. Polymer 1998;39:5483–93.
[16] Nazir T, Afzal A, Siddiqi HM, Ahmad Z, Dumon M. Progress in Organic Coatings 2010;69:101–6.

[17] Coates J. Interpretation of infrared spectra, a practical approach. In: Meyers RA, editor. Encyclopedia of analytical chemistry. Chichester: John Wiley & Sons Ltd; 2000. p. 10815–37.
[18] Stuart BH. Infrared spectroscopy: fundamentals and applications. Chichester: John Wiley & Sons Ltd; 2004 [Chapter 4].
[19] Mascia L, Prezzi L, Haworth B. Journal of Materials Science 2006;41: 1145–55.
[20] Pope EJA, Mackenzie JD. Journal of Non-Crystalline Solids 1986;87:185–98.
[21] DeGarmo EP, Black JT, Kohser RA. Materials and processes in manufacturing. 9th ed. Chichester: John Wiley & Sons Ltd; 2004. p. 223.
[22] Yinghua W, Lixin Z, Zhiduan HE, Wei KE. Chinese Journal of Materials Research 2001;15:686–92.
[23] Ghaemy M, Nasab SMA, Barghamadi M. Journal of Applied Polymer Science 2007;104:3855–63.
[24] Macan J, Ivankovic H, Ivankovic M, Mencer HJ. Thermochimica Acta 2004;414:219–25.
[25] Huang GC, Lee JK. Composites: Part A 2010;41:473–9.
[26] Park WH, Lee JK, Kwon KJ. Polymer Journal 1996;28:407–11.
[27] Ash BJ, Schadler LS, Siegel RW. Material Letters 2002;55:83–7.
[28] Riegel B, Blittersdorf S, Kiefer W, Hofacker S, Muller M, Schottner G. Journal of Non-Crystalline Solids 1998;226:76–84.
[29] Xue G. Die Angewandte Makromolekulare Chemie 1987;151:85–93.
[30] Innocenzi P, Brusatin G, Gugliemi M, Bertani R. Chemistry of Materials 1999;11:1672–9.
[31] Iler RK. The chemistry of silica: solubility, polymerization, colloid and surface properties, and biochemistry. New York: John Wiley and Sons Ltd.; 1979.
[32] Matějka L, Dukh O, Hlavatà D, Meissner B, Brus J. Macromolecules 2001;34: 6904–14.
[33] Landry CJT, Coltrain BK, Brady BK. Polymer 1992;33:1486–95.
[34] Mahrholz T, Stangle J, Sinapius M. Composites: Part A 2009;40:235–43.
[35] Rosso P, Ye L. Macromolecular Rapid Communications 2007;28:121–6.
[36] Liu YL, Li SH. Journal of Applied Polymer Science 2005;95:1237–45.
[37] Altmann N, Halley PJ, Cooper-White J, Lange J. Macromolecular Symposia 2001;196:171–7.
[38] Bershtein VA, Egorova LM, Yakushev PN, Pissis P, Sysel P, Brozova L. Journal of Polymer Science: Part B 2002;40:1056–69.
[39] Preghenella M, Pegoretti A, Migliaresi C. Polymer 2005;46:12065–72.
[40] Zhang H, Zhang Z, Friedrich K, Eger C. Acta Materialia 2006;54:1833–42.
[41] Chen C, Justice RS, Schaefer DW, Baur JW. Polymer 2008;49:3805–15.
[42] Sun YY, Zhang ZQ, Moon KS, Wong CP. Journal of Polymer Science: Part B 2004;42:3849–58.
[43] Afzal A, Siddiqi HM, Saeed S, Ahmad Z. Unpublished data: “A comprehensive study of the bicontinuous epoxy–silica hybrid polymers: II. Thermal and mechanical properties”; 2011.

Polymer 52 (2011) 1356–1366

Contents lists available at ScienceDirect

Polymer

journal homepage: www.elsevier.com/locate/polymer

Synthesis of ‘ready-to-adsorb’ polymeric nanoshells for magnetic iron oxide nanoparticles via atom transfer radical polymerization

Nikorn Pothayee[a], S. Balasubramaniam[b], R.M. Davis[a], J.S. Riffle[a,*], M.R.J. Carroll[b], R.C. Woodward[b], T.G. St. Pierre[b]

[a] *Macromolecules and Interfaces Institute, Virginia Polytechnic Institute and State University, Blacksburg, VA 24061, United States*
[b] *School of Physics, The University of Western Australia, 35 Stirling Hwy, Crawley, WA 6009, Australia*

ARTICLE INFO

Article history:
Received 7 December 2010
Received in revised form
18 January 2011
Accepted 22 January 2011
Available online 4 February 2011

Keywords:
Poly(N-isopropylacrylamide)
Magnetite
Phosphonate

ABSTRACT

Polymer–magnetite nanoparticle complexes that respond to both magnetic fields and to temperature have been demonstrated. Novel alkyl halide-functional bis(diethylphosphonate) esters were prepared and utilized as initiators for polymerizing N-isopropylacrylamide by controlled atom transfer radical polymerization. The phosphonate esters were removed after polymerization to afford poly(N-isopropylacrylamide) with a bis(phosphonic acid) moiety precisely placed at one terminus. The bis(phosphonic acid) endgroups were adsorbed onto magnetite nanoparticles to yield nanoscale complexes that were stable against any polymer desorption and that were colloidally-stable in physiological media. Thus, the bis(phosphonate) endgroup provides a robust anchoring moiety onto the magnetite. Hydrodynamic sizes of the complexes were predicted with a density distribution model and using the measured sizes of the magnetite cores. Good agreement between the measured and predicted hydrodynamic sizes suggested that the complexes were primarily discrete, non-agglomerated nanoparticles. The complexes exhibited thermosensitive aggregation behavior near the lower critical solution temperature of the poly(N-isopropylacrylamide) component.

1. Introduction

Magnetic nanoparticles coated with macromolecules, and especially magnetite (Fe_3O_4) because of its biocompatibility, are of great interest due to a wide range of potential biomedical applications including drug delivery, treatment of detached retinas, cell separations and contrast enhancement agents for MRI [1–7]. Magnetite is a highly magnetic iron oxide with a cubic inverse spinel structure. One-third of the iron atoms are tetrahedrally coordinated with oxygen (Fe^{III}) and two-thirds are octahedrally coordinated (equal amounts of Fe^{II} and Fe^{III}) [8]. Hydrophilic macromolecules such as poly(ethylene oxide) and dextran have been widely used coatings for magnetite nanoparticles since they afford water solubility and biocompatibility for *in vivo* applications [1,9–11].

One of the main challenges of designing polymer-coated magnetic nanoparticles is a need to ensure the binding stability of the polymer to the magnetite surface so that the materials will remain intact in physiological media [11]. Functional anchor groups on polymers aid in their adsorption onto the surface of magnetite. Polymeric dispersion stabilizers containing carboxylate and alkylammonium anchor groups to complex with magnetite nanoparticles have been previously reported by our group and others [3–7,9,10]. Over the past decade, significant effort in our laboratories has been devoted to the development of strong anchor moieties for magnetite/polymer complexes [11]. Recently, catechols such as dopamine have been reported as anchor groups for linking PEO to the magnetite surface [12,13]. However, Shultz et al. have reported that the reactive nature of dopamine and iron ions on magnetite surfaces leads to the formation of dopamine quinones that are cytotoxic and facilitate degradation of the nanoparticles, so this may be a concern if the materials are to be used for *in vivo* biomedical applications [14]. We have previously reported that ammonium phosphonate zwitterions provide a robust anchor for binding PEO onto magnetite and that remarkably high surface densities can be achieved [11]. The capacity for phosphonates to form bidentate and tridentate ligands for adsorbing with high affinity onto metal and metal oxides has been described [15,16].

It has also been shown that certain cellular interactions with nanomaterials are specific and unique with regard to the structure and composition of the materials. For example, Kabanov et al. reported that the pathways of intracellular uptake of amphiphilic block copolyethers (selected Pluronics™) are sensitive and governed

---

* Corresponding author. Tel.: +1 540 231 8214.
E-mail address: judyriffle@aol.com (J.S. Riffle).

0032-3861/$ – see front matter © 2011 Elsevier Ltd. All rights reserved.
doi:10.1016/j.polymer.2011.01.047

by the hydrophilic–hydrophobic balance of the polymers [17,18]. Our work regarding the rate of cellular uptake of polyelectrolyte complexes also suggests that particles are internalized faster into phagocytic cells when they are amphiphilic rather than hydrophilic [19]. Moreover, polymeric coatings can be used to control the release of therapeutic agents from nanocarriers. Yavuz et al. demonstrated “smart” polymer nanoreservoirs with precisely controlled release from a combination of photothermal effects from gold nanocages and thermoresponsive polymeric coatings [20]. Therefore, besides the size and shape of the nanoparticle cores, the chemical compositions and solution characteristics of the polymer coatings can also offer advantages for biotechnological applications of the nanoparticles.

Herein we describe ammonium bis(phosphonate) moieties for coating other macromolecules beyond polyethers onto magnetite. The aim of our work is to develop a modular approach for engineering magnetic nanoparticles with tunable polymeric shells and flexibility of chemical functionalization. We have employed atom transfer radical polymerization (ATRP) as a tool due to its flexibility to allow a large pool of monomers to be polymerized in a controlled fashion [21–23]. This technique also offers halide endgroups that can enable further chain extension to form block copolymers or to functionalize the polymer endgroups with bioactive molecules [24–26]. Zwitterionic bis(phosphonate) functional initiators were designed to initiate macromolecules bearing ammonium bis(phosphonate) endgroups via ATRP, and these readily adsorb onto magnetite (Fig. 1).

Poly(N-isopropylacrylamide) (PNIPAM) was chosen as the polymeric shell due to its attractive thermoresponsive properties. Aqueous solutions of PNIPAM exhibit a lower critical solution temperature (LCST) around 33 °C [27]. As the temperature is raised through this region, PNIPAM undergoes a sharp coil-to-globule transition and becomes insoluble in water [28]. The polymer chains experience volume loss due to expulsion of water molecules

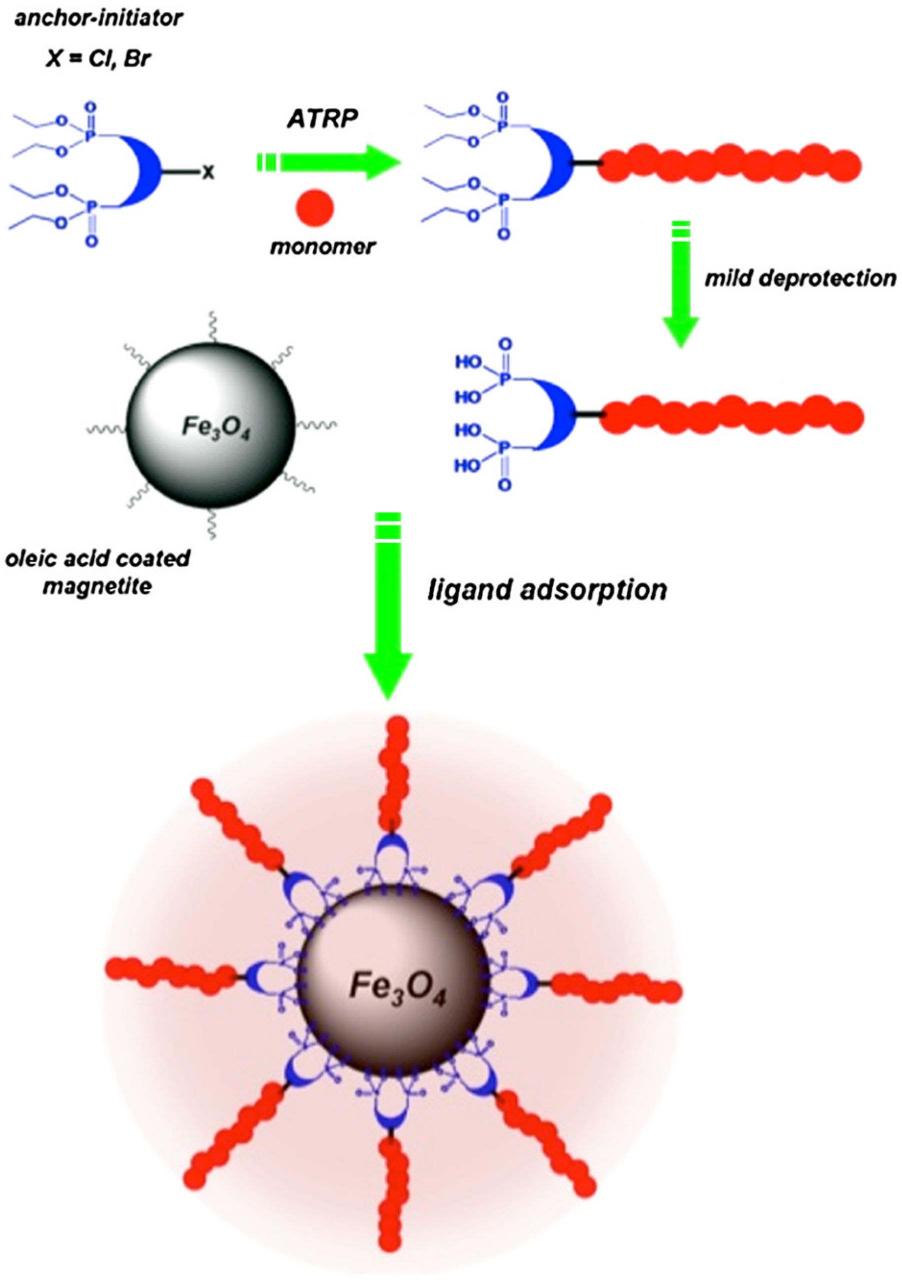

Fig. 1. Preparation of well-defined ‘ready-to-adsorb’ polymeric shells for iron oxide nanoparticles.

resulting from hydrogen bond disruption. When cooled below the LCST, the hydrogen bonds reform and the polymer re-expands in solution. Thus, a thermally-induced hydrophilic–hydrophobic "switch" can be reversibly introduced into the structure. In this work, PNIPAM was synthesized via ATRP using a unimolecular anchor-initiator that contains a protected amino bis(phosphonate) functional group. After mild deprotection, the polymer with a bis(phophonic acid) endgroup was bound to magnetite to afford well-defined polymer-metal oxide nanoparticles (Figs. 2 and 3). Physicochemical and dispersion properties in solution as well as thermosensitivity of these particles were examined.

2. Experimental

2.1. Materials

Benzyl alcohol (>98%), diethyl ether, diethyl vinylphosphonate (97%), hexanes (HPLC grade), iron (III) acetylacetonate ($Fe(acac)_3$), trimethylsilyl bromide (TMSBr, 97%), oleic acid (90%, technical grade), 2-bromoisobutyryl bromide, 2-chloropropionyl chloride, and 3-amino-1-propanol were purchased from Aldrich. N-isopropylacrylamide (NIPAM) was recrystallized twice from hexane. Tris[2-(dimethylamino)ethylamine] (Me_6TREN) was synthesized and purified according to a previously-reported method [29]. Dichloromethane (anhydrous) and acetone (HPLC grade) were purchased from Fisher Scientific and used as received. Dialysis tubing (25,000 and 3500 g mol^{-1} MWCO) was obtained from Spectra/Por. Phosphate buffered saline 10 × (PBS) was obtained from Mediatech and diluted to appropriate concentrations. The permanent magnet utilized in Fig. 18 was purchased from K and J Magnetics. It was a NdFeB permanent magnet with a diameter of 11/16" and a thickness of 1/4". It was axially magnetized with a surface field of 3880 Gauss.

2.2. Characterization

^{1}H and ^{31}P NMR spectral analyses of compounds were performed using a Varian Unity 400 NMR or a Varian Inova 400 NMR operating at 399.8 or 161.9 MHz respectively. Parameters utilized for the ^{31}P were a 45° observation pulse and 1 s relaxation delay with 256 scans.

Size exclusion chromatography (SEC) was performed on a liquid chromatograph equipped with a Waters 1515 isocratic HPLC pump, Waters Autosampler, Waters 2414 refractive index detector and Viscotek 270 RALLS/viscometric dual detector. The mobile phase was N-methylpyrrolidone containing 0.05 M LiBr. A Waters Styragel HR-1 + HR-3 + HR-4 column set maintained at 60 °C because of the viscous nature of NMP was used. Both the solvent and the sample solution were filtered before introduction into the SEC system. Absolute molecular weights were determined with a Universal Calibration that was based on polystyrene standards.

Thermogravimetric analysis (TGA) was used to determine the polymer loading for each complex. TGA measurements were carried out on the PNIPAM-magnetite nanoparticles using a TA Instruments TGA Q500 to determine the fraction of polymer in each complex. Each sample was first held at 110 °C for 10 min to drive off any excess moisture. The sample (10–15 mg) was then equilibrated at 100 °C and heated in a nitrogen atmosphere up to 600 °C at a rate of 10 °C min^{-1}. The mass remaining was recorded throughout the experiment. The mass remaining at 600 °C was taken as the fraction of magnetite in the complex corrected for the char yield of ~10 wt% from PNIPAM.

Inductively coupled plasma atomic emission spectroscopy (ICP-AES) was performed on a SPECTRO ARCOS 165 ICP spectrometer (SPECTRO Analytical Instruments, Germany). The particles (10 mg) were dispersed in Millipore DI water (5 mL). The dispersion (1 mL) was mixed with 4 mL of concentrated nitric acid to digest magnetite and release free iron. The mixture was reacted for 5 days at room temperature and diluted with DI water to a concentration of 0.02 mg mL^{-1} prior to measurement. The reported results are the mean of three measurements.

Dynamic light scattering (DLS) measurements on the magnetite/PNIPAM complexes were performed with a Zetasizer NanoZS particle analyzer (Malvern Instruments Ltd., Malvern, U.K.) equipped with a solid-state He–Ne laser ($\lambda = 633$ nm) and 173° backscatter detection. The autocorrelation function of the scattered intensity was fitted using cumulants analysis to extract the average translational diffusion coefficient and the hydrodynamic diameter was determined through the Stokes–Einstein relation. Intensity-average diameters were converted to volume- and number-average diameters using the Zetasizer Nano 4.2 software. Samples were dispersed in de-ionized water at a concentration of 1 mg mL^{-1}, sonicated in an ultrasonic bath sonicator (VWR 75T, 45 kHz) for 5 min and passed through a 1.0 μm PTFE filter before measurements.

Transmission electron microscopy was performed on a Philips EM-420 field emission gun TEM operating at an acceleration voltage of 100 kV. Samples were prepared by casting a drop of a dilute aqueous solution of PNIPAM-coated magnetite nanoparticles onto amorphous carbon-coated copper grids. Images were acquired at a magnification of 96,000×, corresponding to a resolution of 3.88 pixels nm^{-2}. The sizes of over 2400 particles from different regions of the grid were measured using Reindeer Graphics' Fovea Pro 4 plug-in for Adobe Photoshop 7.0®.

The sample magnetization (M) as a function of applied field (H) (M–H curve) was measured at 300 K and 5 K using

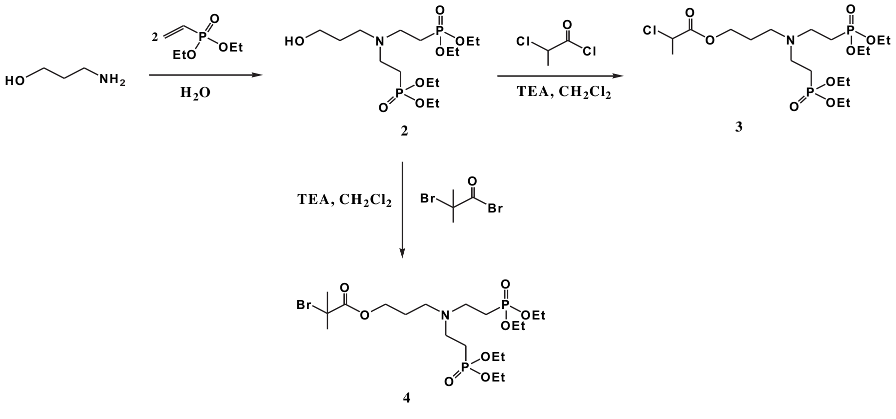

Fig. 2. Synthesis of ammonium bis(phosphonate)-functional ATRP initiators.

a superconducting quantum interference device (SQuID) magnetometer (MPMS XL, Quantum Design) in the range of ±7 T.

2.3. Synthesis

2.3.1. Synthesis of magnetite nanoparticles

Magnetite nanoparticles were synthesized using a slightly modified method of that previously reported [11]. Fe(acac)$_3$ (2.14 g, 8.4 mmol) and benzyl alcohol (45 mL, 0.43 mol) were charged to a 250-mL, three-neck, round-bottom flask equipped with a water condenser and nitrogen inlet and placed in a Belmont metal bath with an overhead stirrer with thermostatic (± 1 °C) control. The solution was held at 110 °C for 1 h under N$_2$, then the temperature was raised to 205 °C and maintained for 40 h. The reaction was cooled to room temperature and the particles were collected by centrifugation (4000 rpm, 30 min). The magnetite nanoparticles were washed 3 times with acetone (100 mL each), then were dispersed in chloroform (20 mL) containing oleic acid (0.3 g). The solvent was removed under vacuum at room temperature, and the oleic acid-stabilized magnetite nanoparticles were washed 3× with acetone (100 mL each) to remove excess oleic acid. The particles were dried under vacuum for 24 h at 25 °C.

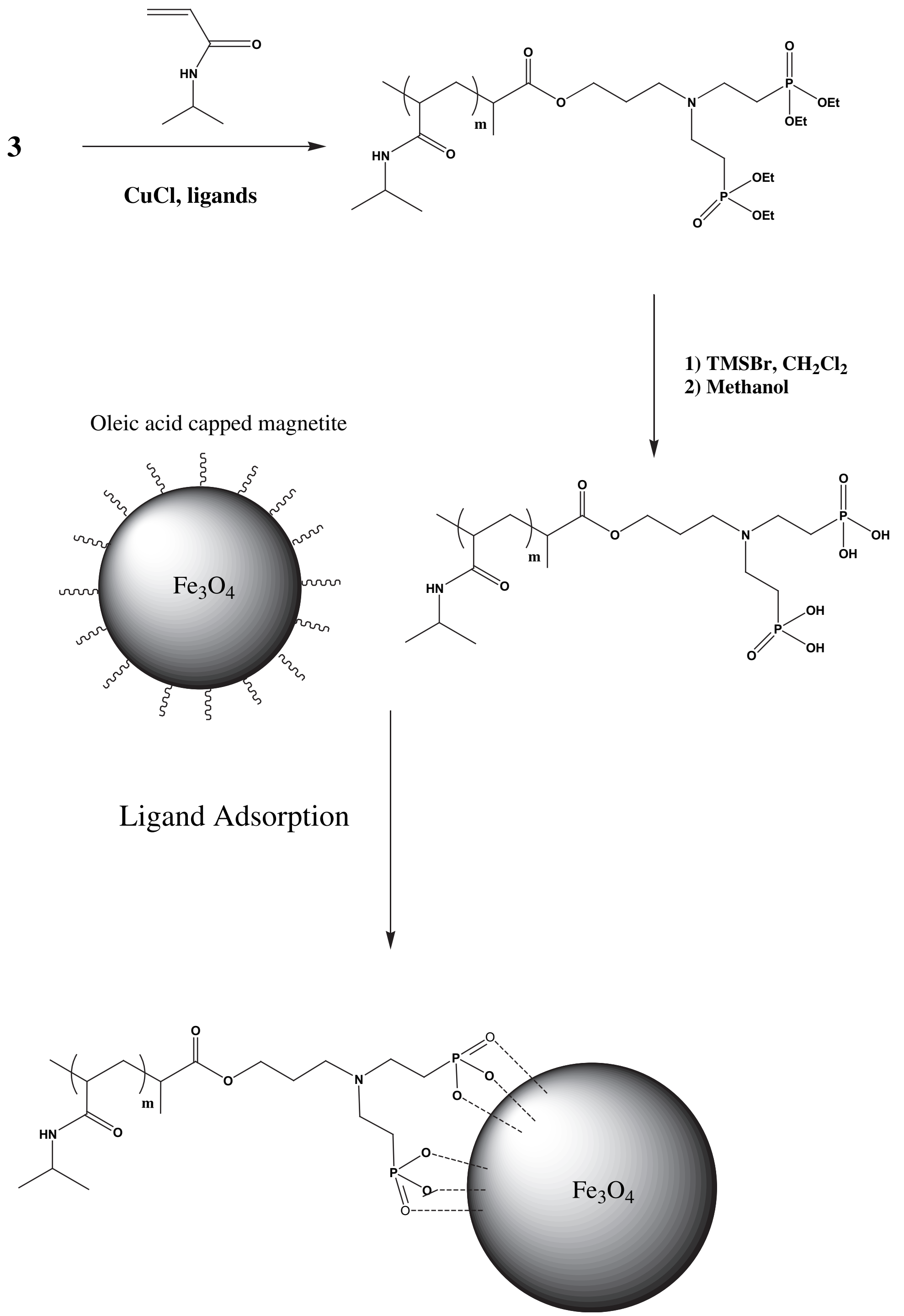

Fig. 3. Synthesis of ammonium bis(phosphonate) terminated macromolecules via ATRP and adsorption onto magnetite surfaces.

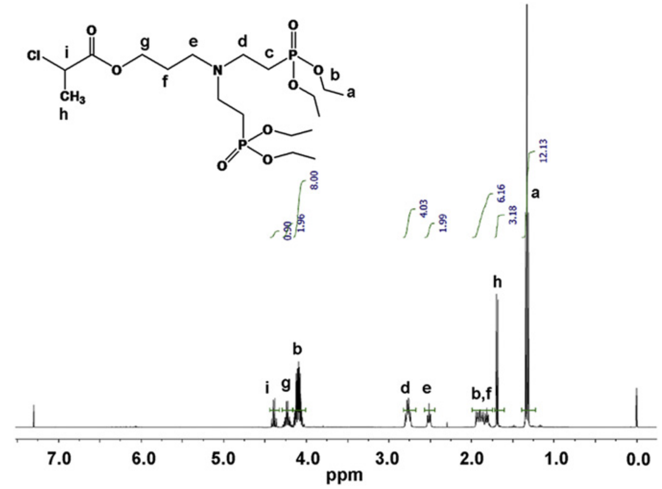

Fig. 4. ^{1}H NMR spectrum in $CDCl_3$ of initiator 3.

2.3.2. Synthesis of an amino bis(phosphonate) initiator for ATRP

3-Amino-1-propanol (**1**, 12.0 g, 0.160 mol), diethyl vinylphosphonate (53.0 g, 0.323 mol), and DI water (260 mL) were added into a 500-mL round-bottom flask equipped with a magnetic stir bar. The solution was placed into an oil bath and stirred at 50 °C for 24 h. After cooling, the pH was adjusted to ~11 with 5 N NaOH and the aqueous solution was extracted with dichloromethane (5 × 120 mL). The organic layers were combined and dried with sodium sulfate, filtered and dried under vacuum to give a clear liquid product (**2**, 62 g, 95% yield) and used without further purification. To add a halogen atom for ATRP, **2** (10.0 g, 2.48×10^{-2} mol) and triethylamine (4.0 g, 3.97×10^{-2} mol) were dissolved in anhydrous dichloromethane (150 mL) in a flame-dried, 250-mL, round-bottom flask equipped with a magnetic stir bar. After cooling in an ice bath, 2-chloropropionyl chloride (5.0 g, 3.95×10^{-2} mol) was added slowly via syringe and the reaction mixture was allowed to warm to room temperature and stirred for 24 h. The mixture was washed with 0.1 N NaOH (3 × 30 mL), saturated NaCl solution (2 × 50 mL), and DI water (50 mL). The organic solution was dried with sodium sulfate, filtered and the solvent was evaporated. A clear orange-brown viscous oil (**3**, 12.0 g, 83% yield) was obtained after drying in vacuo at 40 °C. An initiator containing a bromoalkane functional group was synthesized by reacting **2** with 2-bromoisobutyryl bromide in a similar procedure.

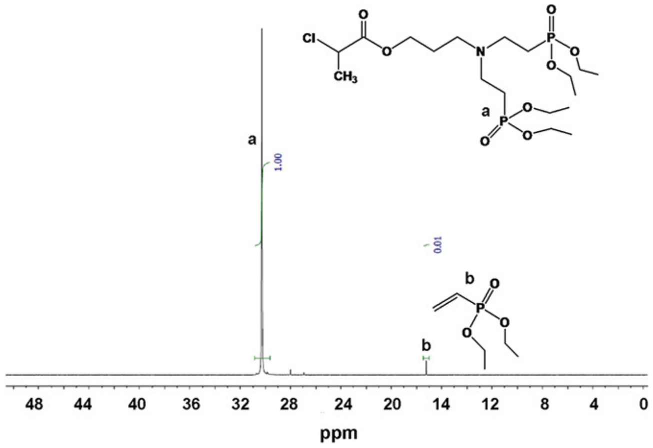

Fig. 5. ^{31}P NMR spectrum in $CDCl_3$ of initiator 3.

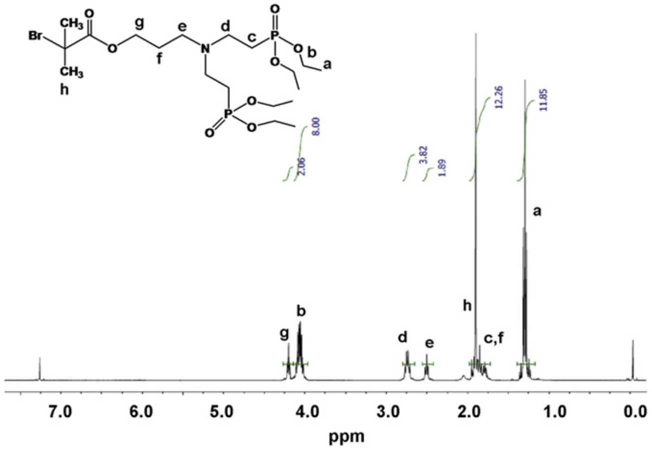

Fig. 6. ^{1}H NMR spectrum in $CDCl_3$ of initiator 4.

2.3.3. Synthesis of an ammonium bis(phosphonate) functional PNIPAM via ATRP

Synthesis of ammonium bis(phosphonate)-PNIPAM (**3**) was carried out using the alkyl chloride initiator and CuCl/Me_6TREN as the metal activator and ligand. The initiator (0.32 g, 6.48×10^{-4} mol), NIPAM (4.6 g, 4.07×10^{-2} mol), CuCl (65 mg, 6.48×10^{-4} mol), Me_6TREN (190 μL, 6.48×10^{-4} mol), and a DMF:H_2O mixture (v:v 3:1, 8 mL) were added to a 25-mL Schlenk flask. After it was degassed by three freeze-pump-thaw cycles, the flask was kept under a slight pressure of N_2. The reaction mixture was immersed in an oil bath at 25 °C for polymerization. After 60 min, the reaction was stopped by diluting it with THF (20 mL), and the mixture was passed through an alumina column to remove the copper catalyst. The polymer was purified by precipitation in n-hexane twice, collected by filtration, and dried in a vacuum oven at 30 °C for 24 h.

To remove the ethyl ester groups from the initiator, bis(phosphonate)-PNIPAM (1.10 g, 1.53×10^{-4} mol) was dissolved in anhydrous dichloromethane (30 mL). Trimethylsilyl bromide (0.190 g, 1.22×10^{-3} mol) was slowly added dropwise to the mixture under a dry N_2 atmosphere. The solution was allowed to stir at room temperature for 24 h, then the solvent and excess TMSBr were removed under vacuum at room temperature. Anhydrous methanol (5 mL) was added to the resultant polymer and the mixture was stirred for 4 h. Bis(phosphonic acid)-PNIPAM was recovered by precipitation into hexane and dried in vacuo at 40 °C.

2.3.4. Synthesis of polymer–magnetite complexes

A representative method for preparing a targeted composition of 67:33 wt:wt polymer:magnetite complex is provided. Oleic

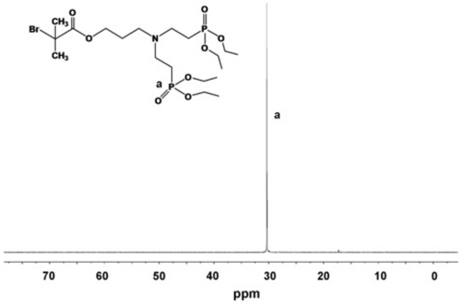

Fig. 7. ^{31}P NMR spectrum in $CDCl_3$ of initiator 4.

Table 1
Molecular weights and polydispersities of PNIPAM[a].

Initiator	Time (min)	M_n (NMR)[b] g mol^{-1}	M_n (SEC) g mol^{-1}	PDI
Chloride-functional bis(phosphonate)	60	7900	11,000	1.07
Choride-functional bis(phosphonate)	180	7300	13,000	1.17
Bromide-functional bis(phosphonate)	60	7200	12,000	1.43

[a] DMF:water = 3:1 v:v, $T_{reaction}$ = 25 °C, $[M]_o/[I]_o/[CuCl]_o/[ligand]_o$ = 60:1:1:1, ligand = Me_6TREN.

[b] Calculated from the integration ratio of the resonances of the methine protons from the polymer backbones (peak b in Fig. 10, 3.8 ppm) to the combined methylenes from the phosphonate esters and the ester endgroup methylene (peaks m and h in Fig. 10, 4.0 ppm).

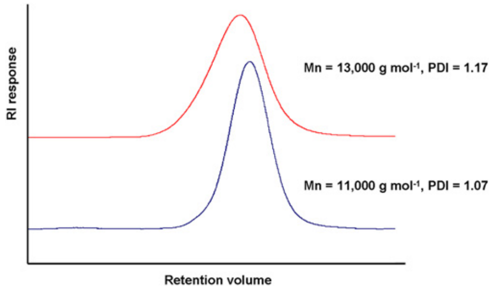

Fig. 8. SEC traces of PNIPAM initiated by the chloride-functional bis(phosphonate) as shown in Fig. 3: reacted for 60 min (bottom) and 180 min (top).

acid-stabilized magnetite nanoparticles (33.0 mg) were dispersed in chloroform (10 mL) and charged to a 50-mL round-bottom flask. An ammonium bis(phosphonate) functional PNIPAM (67.0 mg) was dissolved in DMF (10 mL) and added to the dispersion. The reaction mixture was sonicated in a VWR 75T sonicator for 2 h under N_2, and then stirred at rt for 24 h. The nanoparticles were precipitated in hexanes (300 mL). A permanent magnet was utilized to collect the magnetite nanoparticles and free oleic acid was decanted with the supernatant. The particles were dried under vacuum overnight and dispersed in DI water (20 mL) using sonication for 30–60 s. The complexes were dialyzed against DI water (1 L) for 24 h in a 25,000 g mol^{-1} MWCO dialysis bag to remove free polymer, then freeze-dried to obtain a black-brown solid product.

3. Results and discussion

3.1. Synthesis of an ammonium bis(phosphonate) functional ATRP initiator

One of the key features of our design is having ammonium bis(phosphonate) moieties at the end of the polymer without further post-polymerization functionalization. The effort focused on preparing initiators that contained phosphonate zwitterions. Vinyldiethylphosphonate was reacted with an aminoalcohol through a double aza-Michael reaction to afford hydroxy γ-amino(bisphosphonate). However, in common organic solvents, it is known that aza-Michael reactions are sluggish without a use of elevated temperature and a catalyst [30]. Double-fold addition of an amine onto weakly-active Michael acceptors such as vinylphosphonate, therefore, is even more difficult. Recently, organic reactions in water have received much attention due to their enhanced rate of reaction [31,32]. The catalytic activity of water molecules was described by the formation of a chair-like intermediate involving the Michael donor and acceptor [33]. In our case, double addition of an amine onto vinylphosphonates in water was found to be smooth and marked with very high yields of >95%. The intermediates could be used without purification since no side reactions were observed. Integration of the two resonances in the ^{31}P NMR spectrum was

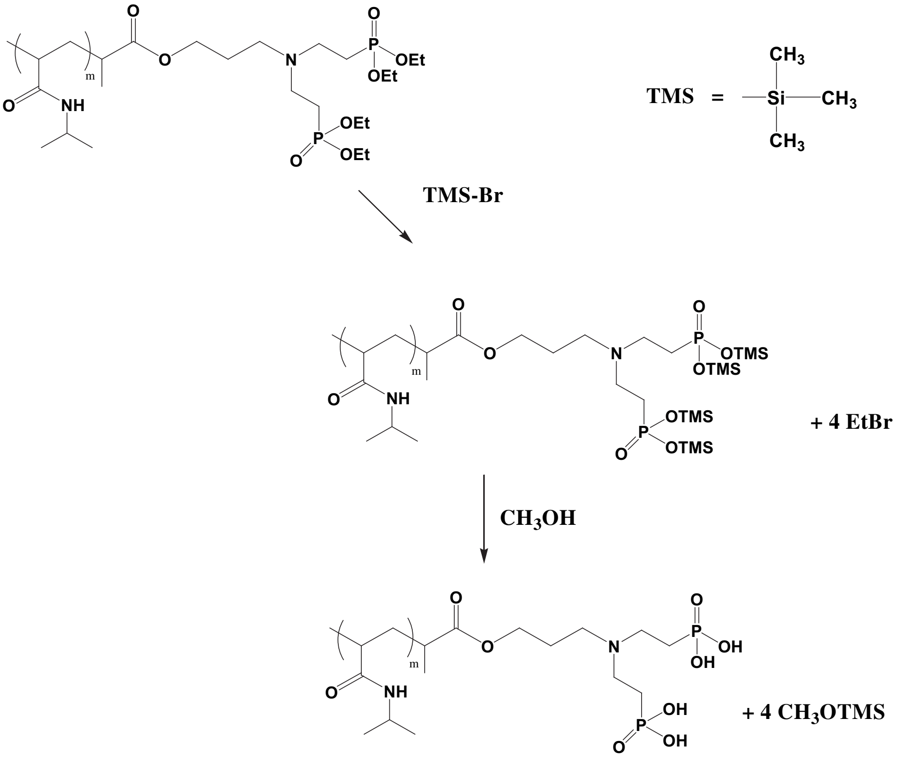

Fig. 9. Selective deprotection of ethylphosphonate esters.

99:1, indicating that almost all of the crude product was the targeted compound. The hydroxyalkylamino bis(diethylphosphonate) intermediate was reacted with either chloropropionyl chloride or bromoisobutyryl bromide to obtain ATRP initiators. Purification processes of the initiators were simple and required no chromatography. The overall yields of the products exceeded ~70% after repetitive washing and extraction followed by drying in vacuo. The initiator structures were confirmed by both ^{1}H and ^{31}P NMR (Figs. 4–7).

3.2. Synthesis of ammonium bis(phosphonate) functional macromolecules

Polymerization of NIPAM through ATRP is complicated by challenges which include 1) occurrence of slow deactivation in conjunction with fast activation, 2) the loss of halogen endgroups attributed to a cyclization reaction involving nucleophilic displacement of the halogen endgroup by amide nitrogens from monomers, and 3) copper catalyst complexation with amide groups [34]. Several catalyst systems have been employed to circumvent such problems. Most NIPAM polymerizations using linear amine or bipyridine based ligands generally result in low conversions [35,36]. Masci et al. was the first to report the successful use of ATRP for polymerizing NIPAM with good control and high conversion by using Me_6TREN as a ligand, chloride-functional endgroups, and a DMF/water mixture as a solvent [37]. Hydrogen-bonding between the solvent and amide groups of monomers and the polymer chain markedly reduces both their catalyst association and chain-end termination. Similar observations were also reported by Stover et al. who reported that alcohol solvents in conjunction with chloride-functional endgroups, could be employed to polymerize NIPAM with high conversion and narrow dispersions of molecular weight through ATRP [38].

In the work reported herein, we have investigated bis(phosphonate)-containing chloride and bromide initiators. As expected based on previous reports, the chloride initiator in conjunction with Me_6TREN provided better control [37,38]. This is likely at least partially attributable to better retention of the chloride (relative to bromide) due to improved resistance against substitution by amides during the polymerization. The polydispersity index (PDI) decreased from 1.43 to 1.07 (Table 1) when changing from the bromide to chloride initiator in conjunction with cuprous bromide or cuprous chloride respectively. High conversions (>95%) were observed within 60 min of reaction under the specified conditions. Table 1 shows number-average molecular weights calculated from compositions determined by NMR with the assumption that there was one initiator fragment per chain. Number-average molecular weights derived from SEC using a universal calibration showed somewhat higher molecular weights. It is not clear why this is the case. The NMR spectrum (Fig. 4) of the chloride-functional initiator shows that within error of the measurement, the initiator is Quantitatively functionalized. Thus, it is suggested that the higher molecular weights than expected derived from SEC could result

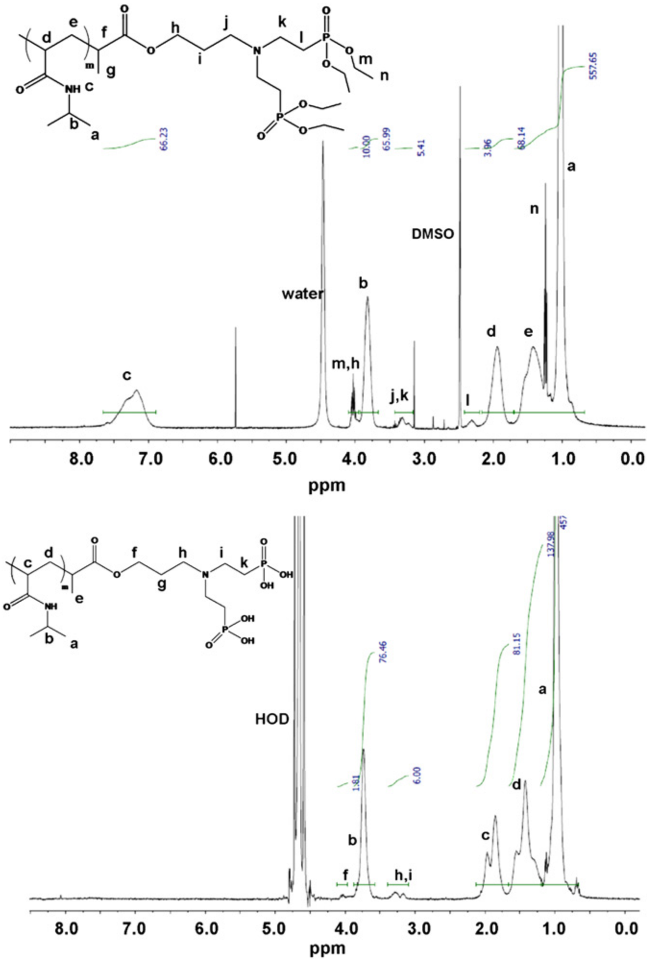

Fig. 10. ^{1}H NMR spectra of the bis(diethylphosphonate)-PNIPAM in d_6-DMSO prior to removal of the diethyl esters (top), and ^{1}H NMR spectra of the bis(phosphonic acid)-PNIPAM in D_2O after removal of the diethyl esters (bottom).

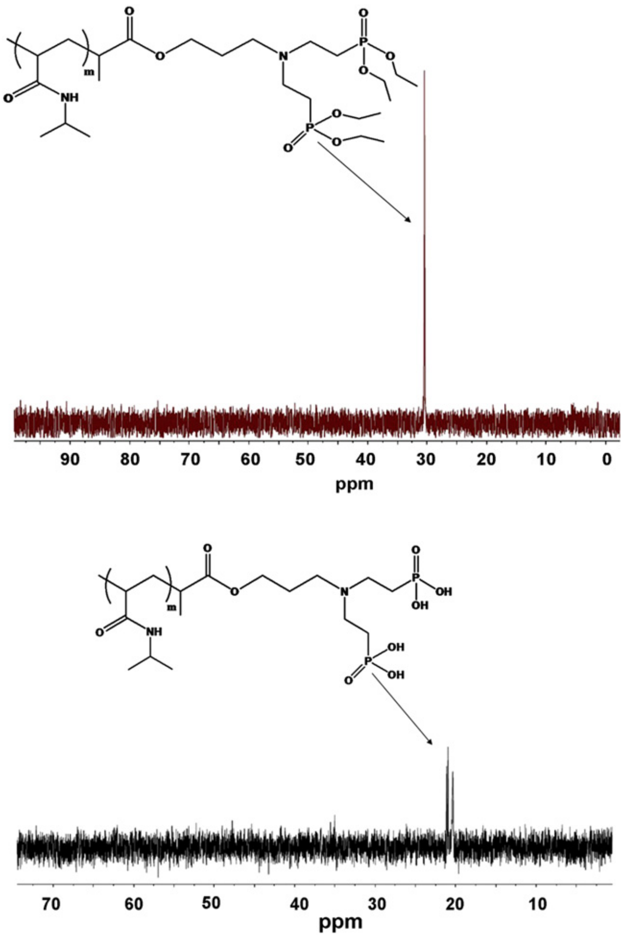

Fig. 11. ^{31}P NMR spectra of PNIPAM-bis(diethylphosphonate) in d_6-DMSO (top), and ^{31}P NMR spectra of PNIPAM-bis(phosphonic acid) in D_2O (bottom).

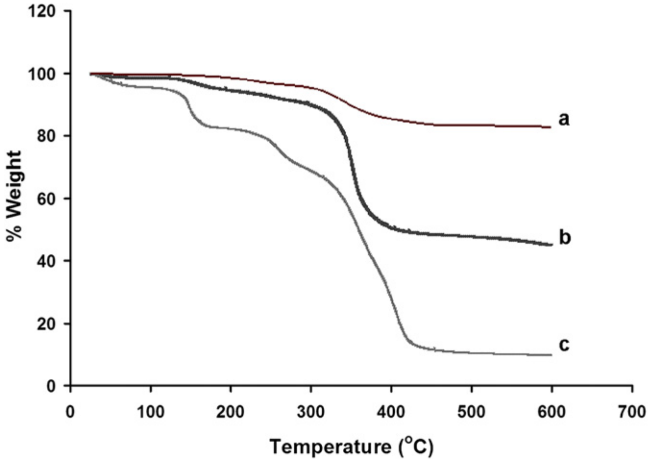

Fig. 12. TGA of a) oleic acid-coated magnetite, b) magnetite-PNIPAM and c) PNIPAM.

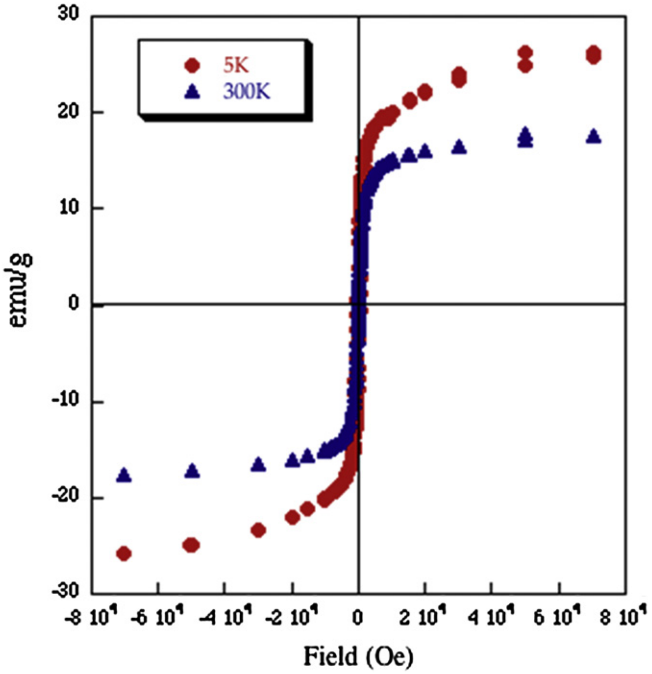

Fig. 13. Hysteresis loop of magnetite-PNIPAM measured by SQuID.

from some inactivation of the chains, possibly by halide displacement, during polymerization and/or some radical–radical coupling. Table 1 shows an increase in molecular weight with longer times at high conversions with the development of a high molecular weight tail on the SEC chromatogram (Fig. 8), and this could reflect more coupling. ^{1}H and ^{31}P NMR revealed that the aminoalkyl bis(phosphonate) endgroup was retained throughout the course of polymerization. The ethyl ester groups were then removed to afford the corresponding bis(phosphonic acid) prior to immobilization on the surface of magnetite. To prevent non-selective cleavage of the ester linkage between PNIPAM and the aminoalkyl bis(phosphonate) initiator moiety, trimethylsilyl bromide (TMSBr) was used as the silylating agent followed by mild removal of silyl ester groups via methanolysis (Fig. 9).

Since an excess of TMSBr was used to ensure quantitative deprotection, the residual TMSBr must be removed prior to methanolysis to avoid any generation of HBr that might cleave the ester linkage between the bis(phosphonate) initiator and the PNIPAM. It is also important that PNIPAM must be completely dry during this step to prevent side reactions. To ensure this, PNIPAM was dissolved in dichloromethane and dried with sodium sulfate, filtered, precipitated in hexane, and dried under vacuum at 70 °C for 24 h prior to the deprotection step. Realizing that the ester bond may be vulnerable to hydrolysis, future efforts will improve upon stability by incorporating a more stable amide linkage.

The complete disappearance of the resonance peaks at chemical shifts of 1.2 and 4.1 ppm indicated that the ethyl ester groups were quantitatively removed (Fig. 10). The resonance signal in the ^{31}P NMR spectrum also shifted from approximately 30 to 21 ppm upon removing the ethyl groups (Fig. 11).

3.3. Adsorption of ammonium bis(phosphonate) functional PNIPAM on magnetite nanoparticles

ATRP has been employed for surface modification of magnetic nanoparticles via a “grafting from” method that propagates polymer chains from nanoparticle surfaces. Most anchor groups on the ligand/initiators have been carboxylates or silanes [39–42]. We have shown that polyethers that are bound to magnetite through one to three carboxylates desorb significantly when the complexes are exposed to phosphate ions in phosphate buffers [11], so the integrity of the carboxylate-magnetite anchor is a concern for biotechnological applications. Silanol coupling may provide a more stable covalent linkage [40]. Another concern regarding a “grafting from” approach is that several heavy metal ions including copper have been shown to efficiently bind with iron oxide through formation of inner sphere complexes, and this raises potential contamination and toxicity issues for biomedical applications [43,44].

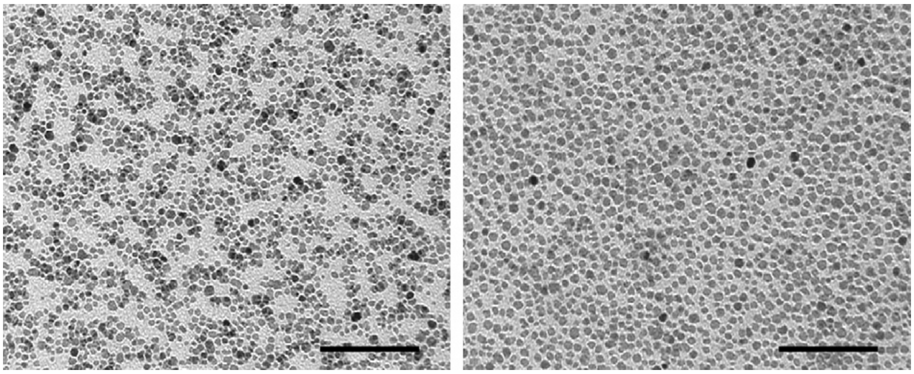

Fig. 14. TEM images of oleic acid-coated magnetite cast from hexane (left) and PNIPAM-coated magnetite cast from DI water (right). Scale bar = 100 nm.

We chose to form the polymer through ATRP first, remove the copper catalyst from a solution of the polymer, then adsorb it onto the magnetite surface through robust phosphonate anchoring moieties. We previously demonstrated that high brush densities could be achieved using homogeneous ligand adsorption [11,45]. Ligand adsorption was employed to link the bis(phosphonate)-PNIPAM to the magnetite nanoparticles. This process requires that the polymer and nanoparticles are homogeneously dissolved/dispersed in the solvent. While poly(ethylene oxide) with ammonium phosphonate endgroups can be efficiently adsorbed onto magnetite from chloroform [11], attempts to use chloroform as a solvent for PNIPAM adsorption resulted in less polymer coverage and poor dispersibility of the particles in aqueous media. This was attributed to poor solubility of the PNIPAM-bis(phosphonic acid) in chloroform. Using a mixed solvent of 1:1 DMF and chloroform, wherein the PNIPAM forms a transparent colorless solution, circumvents this issue. After adsorption, the particles were precipitated into hexane, which is a non-solvent for the PNIPAM but a good dispersant for oleic acid-coated magnetite nanoparticles. Any unbound polymer was removed by dialysis against DI water. TGA results (Fig. 12) indicated that the composition of the PNIPAM-magnetite complex was 65 wt% polymer (corrected with the approximately 10% char yield of PNIPAM) and this was in close agreement with the targeted 67 wt% polymer composition. ICP-AES results following digestion with nitric acid showed 66.3 wt% polymer. These results were consistent with our previous work showing that high concentrations of phosphonate-functional polymers can be adsorbed onto magnetite. These PNIPAM-magnetite nanoparticles were dispersible in water.

The magnetic properties of the magnetite nanoparticles were analyzed by SQuID magnetometry. The magnetization (M) versus applied field (H) curves of the magnetite-PNIPAM nanoparticles at 300 K and 5 K are depicted in Fig. 13. The sample was fully superparamagnetic at 300 K with a saturation magnetization (M_S) of 18 emu g^{-1} at an applied field of 70 kOe. This corresponds to an M_S of ~55 emu g^{-1} for the magnetite nanoparticle core. The decrease in saturation magnetization compared to the value of bulk magnetite can be attributed to spin canting caused by reduced coordination and broken exchange at the particle surface and/or broken symmetry associated with crystalline disorder [46–49].

There have been several reports of magnetite nanoparticles coated with PNIPAM. Most of this research utilized conventional solution free radical polymerization in the presence of magnetite. The efforts led to particle and aggregate sizes ranging from approximately 100–600 nm in diameter [50–52]. Alternatively, as demonstrated in this work, adsorption of PNIPAM with one bis(phosphonate) functional group precisely positioned at one end onto discrete nanoparticles from a homogeneous dispersion resulted in dispersed particles without significant aggregation (Fig. 14).

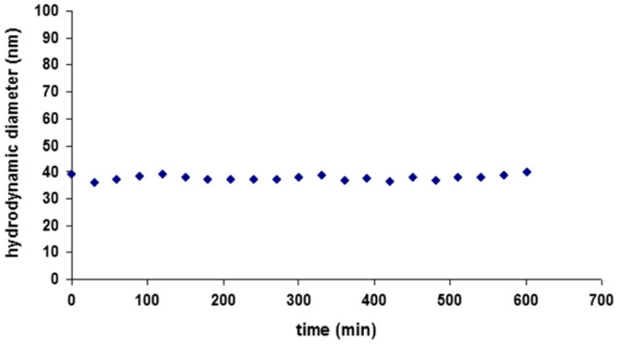

Fig. 15. Colloidal stability of the nanoparticles in phosphate buffered saline (0.14 M NaCl, pH 7.4, 13 mM phosphate) assessed by measurements of intensity average hydrodynamic diameter using DLS at 25 °C.

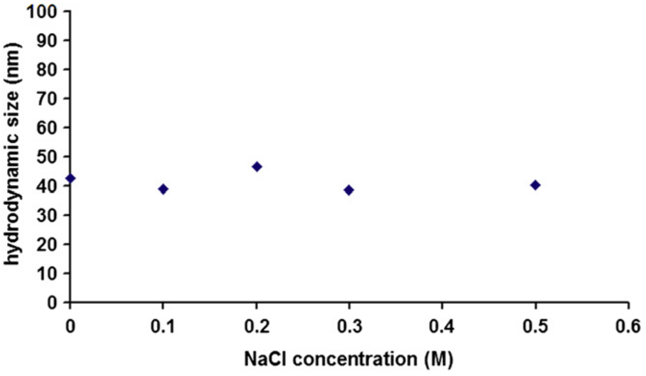

Fig. 16. Intensity average hydrodynamic diameters of magnetite-PNIPAM complexes in NaCl solutions. Complex concentration was 1 mg mL^{-1}.

The PNIPAM-coated magnetite nanoparticles were readily dispersible in aqueous media at room temperature due to the hydrophilic nature of the PNIPAM shell.

The intensity- and volume-average hydrodynamic diameters of the magnetite nanoparticles coated with PNIPAM (65 wt% polymer, M_n = 13000 g mol^{-1}) measured by DLS were 38 and 28 nm respectively. The relatively narrow size distribution of the complexes was evident from the low polydispersity indices (<0.15). To determine if the polymer–magnetite complexes consisted mostly of dispersed primary particles or of aggregates, the average sizes of the polymer–magnetite complexes were estimated using a modified density distribution model [53] which predicts the thickness of the polymer brush around the magnetite core using a theory developed originally for star polymers. This modified model was used previously to predict the sizes of magnetite stabilized with polyethers in water [11] and polydimethylsiloxane in chloroform [54]. For well-defined polymer–magnetite complexes, the model can predict the size to within 7% without any adjustable parameters. The measured sizes of ~2400 particles by TEM (Fig. 14) were used to fit a two-parameter Weibull distribution of magnetite cores with a mean radius of 4.04 ± 1.16 nm. The chain stiffness of the PNIPAM in water at 25 °C is characterized by the statistical segment length, or Kuhn length, of 1.34 nm (given by the product of the characteristic ratio, $C_\infty = 10.6$ and the virtual bond length, $l_o = 0.126$ nm) [55]. The polymer–solvent interaction is characterized by the Flory exponent, $\nu = 0.518$ (25 °C in water) [56]. Using the above parameters in the density distribution model, the number-average diameter of the complexes was estimated to be 29.4 nm, which corresponds to a brush thickness of ~11 nm. The predicted volume- and intensity-average diameters are

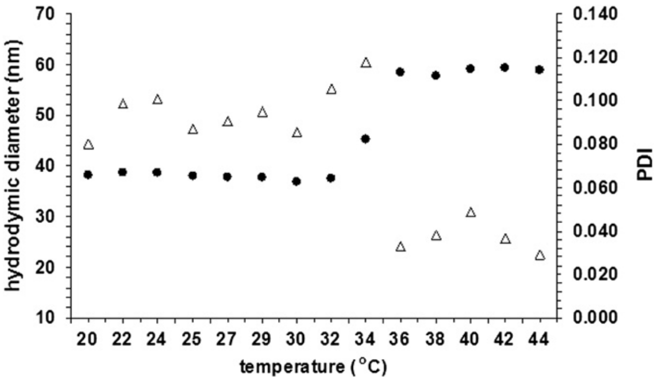

Fig. 17. DSL study of magnetite nanoparticle-PNIPAM complexes at a concentration of 2 mg mL^{-1} in DI water. Intensity average hydrodynamic diameter (black circles) and polydispersity index, PDI (open triangles), were monitored as a function of temperature.

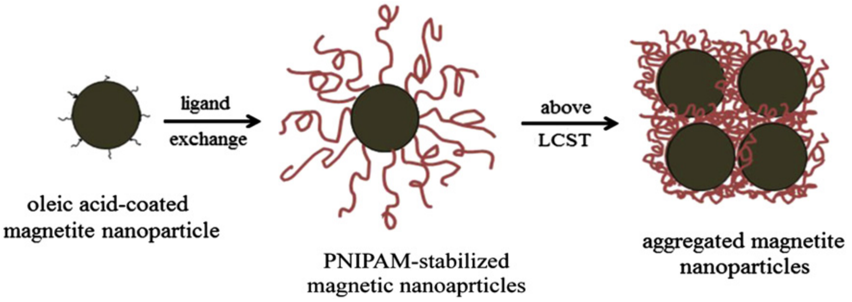

Fig. 18. Schematic illustration of the LCST-induced aggregation of PNIPAM-stabilized magnetite nanoparticles.

31.4 nm and 32.4 nm respectively. Comparison of the predicted sizes with the D_v and D_i measured by DLS indicates that the complexes consisted mostly of dispersed particles.

3.4. *Stability of particles*

The stability of the bis(phosphonate) anchor group in binding to the magnetite surface was evaluated in media of different ionic strengths and also in the presence of competitive phosphate ions in PBS. As shown in Fig. 15, the intensity average hydrodynamic diameter of the PNIPAM-coated magnetite nanoparticles remained virtually unchanged in the presence of 0.14 M NaCl with 13 mM phosphate, and this was the case up to 0.5 M NaCl, a 3.5-fold higher ionic strength relative to physiological media and body fluid. Furthermore, the particles exhibited good colloidal stability in PBS (0.14 M, pH 7.4) without noticeable aggregation (Fig. 16).

Dispersions of the particles were dialyzed against PBS for 24 h to measure any polymer desorption that might be caused by displacement by salts or phosphate ions in the medium. The dispersions were subsequently dialyzed against water for an additional 24 h to remove any desorbed polymer and salts. After freeze-drying, TGA was used to determine the polymer loadings of the particles before and after this process to investigate anchor group stabilities in the presence of phosphate salts in the medium. Any desorption of the polymer from the magnetite surface in PBS should be indicated by a decrease in polymer loading. The amount of polymer after dialysis in PBS was 63 wt%, indicating no significant loss of PNIPAM. Based on this study, it was reasoned that bis(phosphonate) anchor groups would likely have good stability in physiological media, and thus be suitable candidates for biomedical applications.

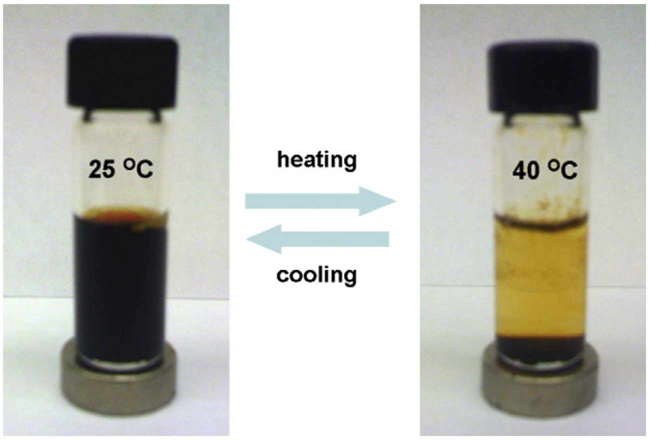

Fig. 19. Magnetic field-induced reversible flocculation of PNIPAM-magnetite nanoparticles. Concentration of nanoparticles is 20 mg mL^{-1} in DI water.

3.5. *Thermosensitive properties of PNIPAM-magnetite nanoparticles*

PNIPAM was chosen as a brush for the magnetite nanoparticles because of its thermoresponsive properties close to body temperature. DLS was used to monitor the temperature-induced change in hydrodynamic size of the PNIPAM-coated magnetite in the range of 20–44 °C. A dispersion (2 mg mL^{-1}) of the complexes was equilibrated at 20 °C for 10 min, then the initial size was measured by DLS. Subsequently, the temperature was increased in 2 °C increments, equilibrated for 10 min at each step, and the sizes were remeasured. Results shown in Fig. 17 revealed that there is an onset of particle size increase at ~33 °C, which is in reasonable range of the reported LCST of PNIPAM. This indicates that there is an aggregation of particles since PNIPAM shells dehydrate and become more hydrophobic, thus causing the agglomeration of particles (as illustrated in Fig. 18). The complex diameter was 60 nm at 34 °C and remained stable at this size, without sedimentation, as the temperature was increased up to 44 °C. The increase in hydrodynamic size and formation of nanoclusters were accompanied by a marked drop in the particle polydispersity index (PDI) measured by DLS. Evidently, above 33 °C, the formation of clusters occurs uniformly throughout the sample as indicated by very low PDI values of 0.05–0.02. These results are encouraging and suggest the possibility of engineering controlled magnetic nanoclusters, which may lead to enhanced performance in some biomedical applications [57,58]. More detailed investigations with respect to the thermally-induced formation of nanoclusters are currently in progress.

PNIPAM-coated magnetite nanoparticles were dispersible in water at room temperature and exhibited good colloidal stability even at high concentrations of ~20 mg mL^{-1}. No sedimentation was observed when a vial containing the dispersion was placed on top of a Nd–Fe–B permanent magnet. By contrast, when heated above the LSCT (Fig. 19), there was a sharp increase in turbidity and the particles could be collected with the permanent magnet. The dispersibility of the complexes could be fully restored by cooling the dispersions down to room temperature. Therefore, the thermoresponsive behavior of the PNIPAM shell enables reversible flocculation of the nanoparticles by a combination of thermal and magnetic effects.

4. Conclusion

We have reported the synthesis and characterization of a new bis(phosphonate) functional initiator for the polymerization of thermoresponsive PNIPAM through ATRP. In three simple and efficient reaction steps, bis(phosphonate) initiators can be synthesized for the polymerization of NIPAM. After mild deprotection of the phosphonic acid moieties, adsorption of bis(phosphonic acid)-PNIPAM onto magnetite affords well-defined, water-dispersible and thermoresponsive nanoparticles. Combining a thermosensitive polymeric shell with a magnetic core paves the way for multi-stimuli-responsive nanoparticles for biomedical applications. As a continuing effort of our group on investigating nanoparticle–cell interactions and structure–relaxivity relationships of magnetic nanoparticles, we envision that this methodology can be modularly extended and applied to polymerize other monomers to create a library of polymeric shells for magnetic iron oxide nanoparticles.

Acknowledgments

The authors gratefully acknowledge the support of the National Science Foundation under contracts DMR 0909065 and DMR 0805179 and the Australian Research Council's Discovery Projects funding scheme (project DP0985848).

References

[1] Hafeli U, Schutt W, Teller J, Zborowski M, editors. Scientific and clinical applications of magnetic carriers. NY: Plenum Press; 1997.
[2] Jung CW, Jacobs P. Magn Reson Imaging 1995;13(5):661–74.
[3] Mefford OT, Carroll MRJ, Vadala ML, Goff JD, Mejia-Ariza R, Saunders M, et al. Chem Mater 2008;20(6):2184–91.
[4] Mefford OT, Vadala ML, Goff JD, Carroll MRJ, Mejia-Ariza R, Caba BL, et al. Langmuir 2008;24(9):5060–9.
[5] Thunemann ASD, Kaufner L, Pison U, Mohwald H. Langmuir 2006;22:2351–7.
[6] Wilson KS, Goff JD, Riffle JS, Harris LA, St. Pierre TG. Polym Adv Technol 2005;16(2–3):200–11.
[7] Harris LA, Goff JD, Carmichael AY, Riffle JS, Harburn JJ, St. Pierre TG, et al. Chem Mater 2003;15(6):1367–77.
[8] Schwertmann U, Cornell RM. Iron oxides in the laboratory. In: Preparation and characterization. 2nd ed. NY: Wiley-VCH; 2000.
[9] Vadala ML, Thompson MS, Ashworth MA, Lin Y, Vadala TP, Ragheb R, et al. Biomacromolecules 2008;9(3):1035–43.
[10] Huffstetler PP, Miles WC, Goff JD, Reinholz CM, Carroll MRJ, Woodward RC, et al. Polymer 2008;49(2):1103–4.
[11] Goff JD, Huffstetler PP, Miles WC, Pothayee N, Reinholz CM, Ball S, et al. Chem Mater 2009;21(20):4784–95.
[12] Xu C, Xu K, Gu H, Zheng R, Liu H, Zhang X, et al. J Am Chem Soc 2004;126 (32):9938–9.
[13] Xie J, Xu C, Xu Z, Hou Y, Young KL, Wang S, et al. Chem Mater 2006;18 (23):5401–3.
[14] Shultz MD, Reveles JU, Khanna SN, Carpenter EE. J Am Chem Soc 2007;129 (9):2482–7.
[15] Traina CA, Schwartz J. Langmuir 2007;23(18):9158–61.
[16] Daou TJ, Grenech JM, Pourroy G, Buathong S, Derory A, Ulhaq-Bouillet C, et al. Chem Mater 2008;20(18):5869–75.
[17] Sahay G, Batrakova EV, Kabanov AV. Bioconjug Chem 2008;19(10):2023–9.
[18] Batrakova EV, Li S, Brynskikh AM, Sharma AK, Li Y, Boska M, et al. J Controlled Release 2010;143(3):290–301.
[19] Ranjan A, Pothayee N, Seleem MN, Sriranganathan N, Kasimanickam R, Makris M, et al. Antimicrob Agents Chemother 2009;53(9):3985–8.
[20] Yavuz MS, Cheng Y, Chen J, Cobley CM, Zhang Q, Rycenga M, et al. Nat Mater 2009;8(12):935–9.
[21] Matyjaszewski K, Xia J. Chem Rev 2001;101(9):2921–90.
[22] Matyjaszewski K. Macromolecules 1998;31(15):4710–7.
[23] Lee SB, Russell AJ, Matyjaszewski K. Biomacromolecules 2003;4(5):1386–93.
[24] Lele BS, Murata H, Matyjaszewski K, Russell AJ. Biomacromolecules 2005;6 (6):3380–7.
[25] Gao H, Matyjaszewski K. J Am Chem Soc 2007;129(20):6633–9.
[26] Golas PL, Matyjaszewski K. Chem Soc Rev 2010;39(4):1338–54.
[27] Wei H, Cheng SX, Zhang XZ, Zhuo RX. Prog Polym Sci 2009;34:893–910.
[28] Wu C, Wang X. Phys Rev Lett 1998;80:4029–94.
[29] Xia J, Gaynor SG, Matyjaszewski K. Macromolecules 1998;31(17):5958–9.
[30] Bartoli G, Bosco M, Marcantoni E, Petrini M, Sambri L, Torregiani E. J Org Chem 2001;66:9052–5.
[31] Azizi N, Saidi MR. Org Lett 2005;7(17):3649–51.
[32] Khatik GL, Kumar R, Chakraborti AK. Org Lett 2006;8(11):2433–6.
[33] Ranu BC, Banerjee S. Tetrahedron Lett 2007;48:141–3.
[34] Rademacher JT, Baum M, Pallack ME, Brittain WJ. Macromolecules 2000;22 (2):284–8.
[35] Teodorescu M, Matyjaszewski K. Macromolecules 1999;32:4826–31.
[36] Rademacher JT, Baum M, Pallack ME, Brittain WJ, Simonsick WJ. Macromolecules 2000;33:284–8.
[37] Masci G, Giacomelli L, Crescenzi V. Macromol Rapid Commun 2004;25(4):559–64.
[38] Xie Y, Yin X, Burke NAD, Stöve HDH. Macromolecules 2005;38(14):5937–43.
[39] Vestal CR, Zhang ZJ. J Am Chem Soc 2002;124(48):14312–3.
[40] Hu F, Neoh KG, Cen L, Kang ET. Biomacromolecules 2006;7(3):809–16.
[41] Fan QL, Neoh KG, Kang ET, Shuter B, Wang SC. Biomaterials 2007;28(36): 5426–33.
[42] Marutani E, Yamamoto S, Ninjbadgar T, Tsujii Y, Fukuda T, Takano M. Polymer 2004;45:2231–5.
[43] Puttamraju P, SenGupta AK. Ind Eng Chem Res 2006;45(22):7737–42.
[44] Ebner AD, Ritter JA, Navrati JD. Ind Eng Chem Res 2001;40(7):1615–23.
[45] Miles WC, Goff JD, Huffstetler PP, Reinholz CM, Pothayee N, Caba BL, et al. Langmuir 2009;25(2):803–13.
[46] Kodama RH, Berkowitz AE, McNiff EJ, Foner S. Phys Rev Lett 1996;77(2): 384–97.
[47] Morup S. J Magn Magn Mater 2003;266(1–2):110–8.
[48] Li D, Teoh WY, Woodward RC, Cashion JD, Selomulya C, Amal R. J Phys Chem C 2009;11328:12040–7.
[49] Morales MP, Veintemillas-Verdaguer S, Montero MI, Serna CJ, Roig A, Casas L, et al. Chem Mater 1999;11(11):3058–64.
[50] Rubio-Retama J, Zafeiropoulos NE, Serafinelli C, Rojas-Reyna R, Voit B, Cabarcos EL, et al. Langmuir 2007;23(20):10280–5.
[51] Regmi R, Bhattarai SR, Sudakar C, Wani AS, Cunningham R, Vaishnava PP, et al. J Mater Chem 2010;23:6158–63.
[52] Herrera AP, Rodríguez M, Torres-Lugo M, Rinaldi C. J Mater Chem 2008;18: 855–8.
[53] Vagberg LJM, Cogan KA, Gast AP. Macromolecules 1991;24(7):1670–7.
[54] Miles WC, Goff JD, Huffstetler PP, Mefford OT, Riffle JS, Davis RM. Polymer 2010;51(2):482–91.
[55] Fang Z, Zhen T, Sato T. Sci China B 1999;42(3):290–7.
[56] Hirotsu S. J Chem Phys 1991;94:3949–57.
[57] Carroll MR, Woodward RC, House MJ, Teoh WY, Amal R, Hanley TL, et al. Nanotechnology 2010;21(3). 035103(1–7).
[58] Lin JJ, Chen JS, Huang SJ, Ko JH, Wang YM, Chen TL, et al. Biomaterials 2009;30 (28):5114–24.

Polymer 52 (2011) 1367–1374

Contents lists available at ScienceDirect

Polymer

journal homepage: www.elsevier.com/locate/polymer

Thermosensitivity control of polyethlyenimine by simple acylation

Heejin Kim [a,1], Seonju Lee [a,1], Minwoo Noh [a,1], So Hyun Lee [a], Yeongbong Mok [a], Geun-woo Jin [a], Ji-Hun Seo [b], Yan Lee [a,*]

[a] Department of Chemistry, Seoul National University, 599 Gwanak-ro, Gwanak-gu, Seoul 151 747, Republic of Korea
[b] Department of Materials Engineering, The University of Tokyo, 7-3-1 Hongo, Bunkyo-ku, Tokyo 113 8656, Japan

A R T I C L E I N F O

Article history:
Received 7 December 2010
Received in revised form
20 January 2011
Accepted 22 January 2011
Available online 1 February 2011

Keywords:
Acylation
Polyethylenimine
Thermosensitivity

A B S T R A C T

Branched polyethylenimine (*b*-PEI), an amine-rich polymer, can obtain thermosensitivity by a simple acylation reaction. The resulting *N*-acylated *b*-PEI derivatives showed a similar lower critical solution temperature (LCST) transition as their linear correspondent, poly(*N*-alkyloxazoline). Three acyl groups (propionyl, and isobutyryl, and *n*-butyryl) were introduced and resulted in LCSTs ranging from 10 °C to 90 °C depending on the structure and environment. The hydrophobicity of *N*-acylated *b*-PEI can be controlled by varying the acyl group and degree of acylation. Because the LCST transition is determined by the delicate balance between the hydrophobicity and hydrophilicity of the polymers, an increase of the hydrophobicity in *N*-acylated *b*-PEI lowers the transition temperature. Also, *N*-acylated *b*-PEI contains tertiary amines as well as unacylated primary or secondary amines which can be protonated during acidification from a pH of 7.4 to a pH of 5.5. The LCST transition was observed at elevated temperatures due to the increase of hydrophilicity by the protonation in the acidic environment. The LCST was also influenced by the salt concentration. A decrease of the LCST was observed as the NaCl concentration increased, probably due to the dominance of the salting-out effect. The very simple introduction of thermosensitivity into pre-existing polymers can be easily applied for the development of various dual or multiple signal-sensitive polymer systems.

1. Introduction

Due to the recent rapid growth of biological and medical uses of polymers, the application of smart polymers whose physicochemical properties change in response to biosignals such as ionic concentration, pH, glutathione concentration, light, and temperature change are being increasingly developed [1,2]. Among the biosignals, physical signals including light and temperature change are easily controllable. For example, temperature change, which may be induced by inflammation or activated metabolism in a biosystem, can also be generated externally by a heat pad or illumination [3]. The time- and site-specific control of a physical signal will attract considerable attention to temperature-responsive polymers considering that the variety of light-responsive polymers is still limited.

Most temperature-responsive polymers, also known as thermosensitive polymers, show a hydrophilic to hydrophobic phase transition above a certain temperature known as the lower critical solution temperature (LCST). Due to the negative entropy change (ΔS) during the solvation of thermosensitive polymers, they form insoluble aggregates in aqueous solutions when the Gibbs free energy of hydration ($\Delta G = \Delta H - T\Delta S$) becomes positive above the LCST [4]. After the LCST transition of poly(*N*-isopropylacrylamide) (PNIPAAM) was discovered [5], the thermosensitivity of other poly(*N*-substituted acrylamide)s [6], poly(*N*-alkyloxazoline)s [7], amphiphilic block copolymers [8], and polypeptides [9], has been intensively investigated. Of course, polymers that show a LCST transition in the biologically tolerable temperature range of 20–40 °C are more attractive for biomedical uses such as in hydrogel [10], tissue engineering [11], and drug/gene delivery [12] applications.

Moreover, the integration of thermosensitivity and other signal sensitivity into one polymer system enables it to be used in more sophisticated applications. Polyethylenimine (PEI) has a high density of amine residues in its backbone which can be protonated or deprotonated in a pH-dependent manner. When PEI is cross-linked with a thermosensitive polymer such as PNIPAAM, the cross-linked polymer can form a hydrogel with both thermo- and pH-sensitivity [13]. In addition, considering that PEI demonstrates outstanding gene delivery efficiency due to its pH-sensitivity [14], the control of gene delivery by a temperature signal can be achieved by the grafting of

---

[*] Corresponding author. Tel.: +82 2 880 4344; fax: +82 2 871 2496.
E-mail address: gacn@snu.ac.kr (Y. Lee).
[1] These authors contributed equally to this work.

0032-3861/$ – see front matter © 2011 Elsevier Ltd. All rights reserved.
doi:10.1016/j.polymer.2011.01.045

PNIPAAM on the surface of PEI [15]. However, the synthetic procedures of dual-sensitive polymers are relatively complicated such that a simpler and faster procedure is often required.

In the structure of thermosensitive polymers, the hydrophilicity of the polar moiety is delicately counter-balanced by the hydrophobicity of the nonpolar moiety. Therefore, the introduction of appropriate hydrophobic groups into a hydrophilic polymer can endow a thermosensitive nature to the polymer. The surface amines of dendrimers have been successfully modified with several hydrophobic groups to introduce thermosensitivity [16,17].

In this paper, we describe the introduction of thermosensitivity on branched PEI by a simple acylation. Inspired by the result that poly(*N*-alkyloxazoline), a thermosensitive polymer, synthesized by careful ring-opening polymerization of *N*-alkyloxazoline monomer, can be hydrolyzed to produce linear PEI (*l*-PEI) [18], we hypothesized that branched PEI (*b*-PEI), which is synthesized by acid catalyzed ring-opening polymerization of aziridine [19], can also obtain thermosensitivity by *N*-acylation of its amine groups (Fig. 1). Because the resulting *N*-acylated *b*-PEI derivatives contain multiple tertiary amine groups which are not acylated, they can maintain the pH-sensitivity of the original *b*-PEI. The thermosensitivity can be controlled by the hydrophobicity of the acyl groups and the degree of acylation. The dependence of the thermosenstivity on pH and ionic concentration is also discussed in detail in this paper.

2. Experimental

2.1. Materials

Branched polyethylenimine (*b*-PEI) ($M_w = 25{,}000$, PD (M_w/M_n) = 2.5) was purchased from Aldrich (USA). Methanol and triethylamine (TEA) were purchased from Daejung (Korea). Isobutyric anhydride and *n*-butyric anhydride were purchased from Kasei (Japan). Propionic anhydride was purchased from Acros (USA). All reagents were used without further purification.

2.2. Synthesis of N-acylated polyethylenimine (Fig. 1)

b-PEI (500 mg; 11.4 mmol of total amine residues) was dissolved in 15 mL of methanol and TEA was added to the solution. After the solution was chilled on ice, each anhydride was added dropwise to the solution under vigorous stirring. The molar feed ratios (moles of anhydride/moles of reactive amines in *b*-PEI) for achieving appropriate degrees of acylation are summarized in Table 1. Generally, the same molar equivalent of TEA relative to the anhydride was used as a proton quencher during the acylation reaction. The reaction mixture was subsequently stirred overnight at room temperature.

The acylated PEI was purified by dialysis. The reaction mixture was dialyzed using ethanol (×2) and deionized water (×3) using a dialysis membrane (Spectrum Laboratories, Inc. (USA); M.W.C.O = 6000–8000) in order to remove the low-molecular weight impurities. The v/v ratio of the mixture solution: ethanol or deionized water is 1:100. The final purified acylated PEI can be obtained as a pale-yellow powder or viscous jelly after lyophilization. The degree of acylation of each polymer was calculated from the ^{1}H NMR spectra and the results are summarized in Table 1. All of the NMR spectra were recorded using a Bruker DPX-300 NMR spectrometer (300 MHz). The chemical shift was reported in terms of ppm downfield from tetramethlylsilane (TMS). The NMR spectra of the acylated PEI derivatives are shown in Fig. 2 and in the Supporting material.

2.3. Measurement of LCST

The LCST phase transition was monitored by measuring the light turbidity at a wavelength of 600 nm. The turbidity change of each sample solution (2 mg/mL) was measured by a Jasco (Japan) V-650 UV–vis spectrophotometer equipped with a STR-707 water thermostatted cell holder and stirrer. For these measurements, the heating rate was set at 0.5 °C/min. The LCST was defined as the temperature corresponding to the initial break points in the resulting transmittance versus temperature curve.

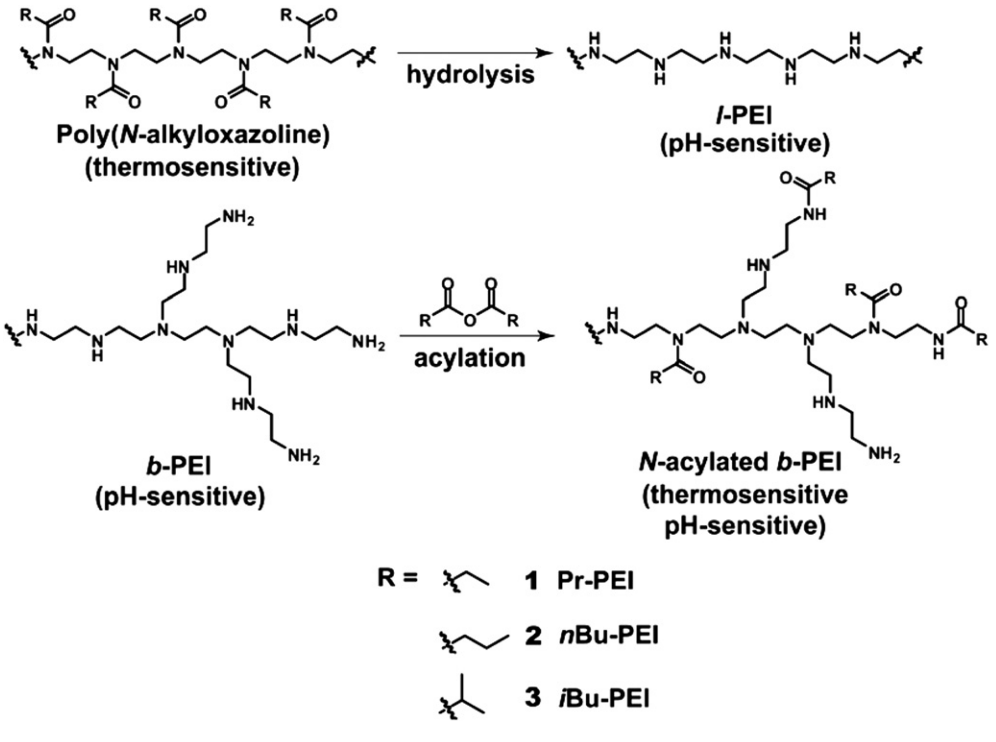

Fig. 1. Synthetic scheme of thermosensitive *N*-acylated *b*-PEI derivatives.

Table 1
Feed ratios, acylation degrees and transition temperatures of acylated *b*-PEI derivatives.

	Anhydride (eq)	Acylation degree (%)[a]	pH 7.4 (150 mM NaCl)		pH 7.4 (75 mM NaCl)		pH 7.4 (0 mM NaCl)		pH 5.5 (150 mM NaCl)		pH 9.3 (150 mM NaCl)	
			T_{cp}[b] (°C)	T_{50}[b] (°C)	T_{cp}[b] (°C)	T_{50}[b] (°C)	T_{cp}[b] (°C)	T_{50}[b] (°C)	T_{cp}[b] (°C)	T_{50}[b] (°C)	T_{cp}[b] (°C)	T_{50}[b] (°C)
Pr-PEI	0.50	51.32	65.02	71.48	56.49	68.52	76.48	87.10	N.D.	N.D.	–	–
	0.75	78.78	61.00	67.48	63.05	70.50	72.53	81.50	N.D.	N.D.	–	–
	5.00	94.85	52.52	53.98	52.48	53.50	56.48	57.39	86.37	88.54	–	–
*n*Bu-PEI	0.65	55.00	24.02	31.52	27.02	37.46	37.02	50.53	44.98	64.45	19.50	24.46
	0.86	75.10	16.54	19.02	18.93	22.93	23.50	28.46	25.93	30.96	15.51	17.56
	3.00	91.20	12.59	13.96	12.46	13.52	14.98	15.95	18.94	20.54	12.49	13.48
*i*Bu-PEI	0.70	49.31	51.49	53.48	57.50	60.52	65.98	69.06	–	–	–	–
	1.00	80.60	22.00	22.42	23.48	24.53	21.02	25.94	37.48	41.55	23.03	23.50
	7.00	90.30	15.48	17.41	11.94	19.02	22.02	22.92	–	–	–	–

[a] Acylation degree (%) was determined by ^{1}H NMR.
[b] The polymer concentration was fixed at 2.0 mg/mL.

2.4. Titration of N-acylated polyethylenimine

An acid–base titration was performed to compare the buffering capacity of the *N*-acylated polyethylenimine derivatives. In this assay, each derivative was dissolved in 10 mL of water at a concentration of 10 μM. Then, about 100 μL of 1 N NaOH was added to each solution to adjust the initial pH to the alkaline range. In the titration, HCl standard solution (0.100 N) was used as the titrant to lower the pH to acidic conditions.

3. Results and discussion

3.1. Acylation of polyethylenimine

Various acylated derivatives of *b*-PEI were produced by the reaction with acyl anhydrides including propionic anhydride (**1**), *n*-butyric anhydride (**2**), and *iso*butyric anhydride (**3**). The ^{1}H NMR spectrum of the *n*-butyryl *b*-PEI derivative is shown in Fig. 2. The downshift of the neighboring methylene protons near nitrogen (from *b* to *a*) is caused by the acylation. Because only primary and secondary amines can react with acyl anhydrides, the exact primary:secondary:tertiary amine ratio in *b*-PEI should be known for the calculation of the degree of acylation. The amine ratio can be measured from the inverted gate (INVGATE) ^{13}C NMR spectrum of *b*-PEI, which is shown in Fig. S1 in the Supporting material [20,21]. Based on the primary:secondary:tertiary amine ratio of 1.2179:1.6789:1.0000 obtained from Fig. S1 and the integration (*I*) ratio of the ^{1}H NMR spectra in Fig. 2, Figs. S2 and S3, the degrees of acylation (*x*) can be calculated from the formula shown below.

$$\frac{I_a}{1.6789\times 2\times x+1.2179\times 1\times x}=\frac{I_b}{1.0000\times 3\times 1+1.6789\times 2\times(1-x)+1.2179\times 1\times(1-x)}$$
$$=\frac{I_c}{1.6789\times x+1.2179\times x}=\frac{I_d}{1.6789\times x+1.2179\times x}=\frac{I_e}{1.5\times(1.6789\times x+1.2179\times x)}$$

The degrees of acylation of the various *b*-PEI derivatives are summarized in Table 1. The degree of acylation of a derivative is expressed as a subscript following the acyl notation. For example, *n*Bu$_{75}$-PEI corresponds to *n*-butyryl *b*-PEI with a degree of acylation of 75%. Because of the high content (~26%) of tertiary amines in *b*-PEI, a derivative with a degree of acylation of 100% still possesses unreacted tertiary amines which can be protonated during the acidification process. The thermosensitive characteristics of the synthesized *N*-acylated *b*-PEI derivatives were examined in detail in this study.

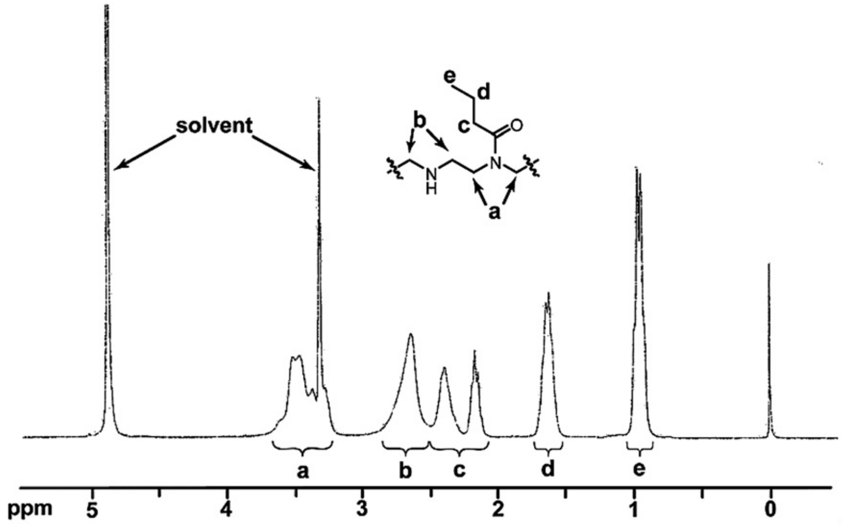

Fig. 2. ^{1}H NMR spectrum of *n*Bu$_{75}$-PEI in CD_3OD.

3.2. Degree of acylation–LCST relationship

b-PEI obtained thermosensitivity by the *N*-acylation described above. Fig. 3 shows the LCST transition of *n*Bu$_{91}$-PEI, an *N*-acylated *b*-PEI derivative. The solution of *n*Bu$_{91}$-PEI in phosphate buffered saline (PBS) was transparent at temperatures below 12 °C, and became turbid when heated above 15 °C. The entropy loss (ΔS) of water molecules near the hydrophobic *n*-butyryl group become dominant compared to the enthalpy gains (ΔH) of the polymer solvation over the LCST and the polymer molecules start to form large aggregates over several hundred nanometers, which scatter visible light. Therefore, the relationship between the temperature and the turbidity or transmittance of the polymer solutions can be a reasonable estimate of the LCST transition [16,17,22].

Fig. 4 shows the transmittance change of the *n*Bu-PEI derivatives (**2**) solution as a function of temperature. In order to describe the LCST transition, two different temperatures were defined: the cloud-point temperature (T_{cp}) corresponding to a 1.0% decrease in the transmittance and the half-transmittance temperature (T_{50}) corresponding to a 50% decrease in the transmittance (Table 1). Based on the difference between the two temperatures (ΔT), the sharpness of the transition could be estimated.

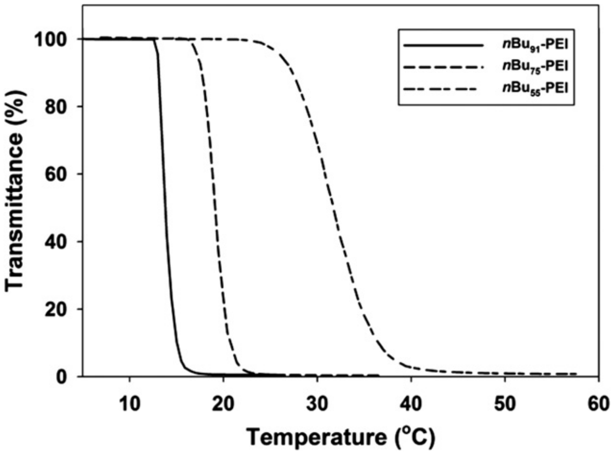

Fig. 4. Effect of acylation degree on LCST of *n*Bu-PEI in 10 mM PBS (pH 7.4, 150 mM NaCl). The concentration of *n*Bu-PEI was 2.0 mg/mL.

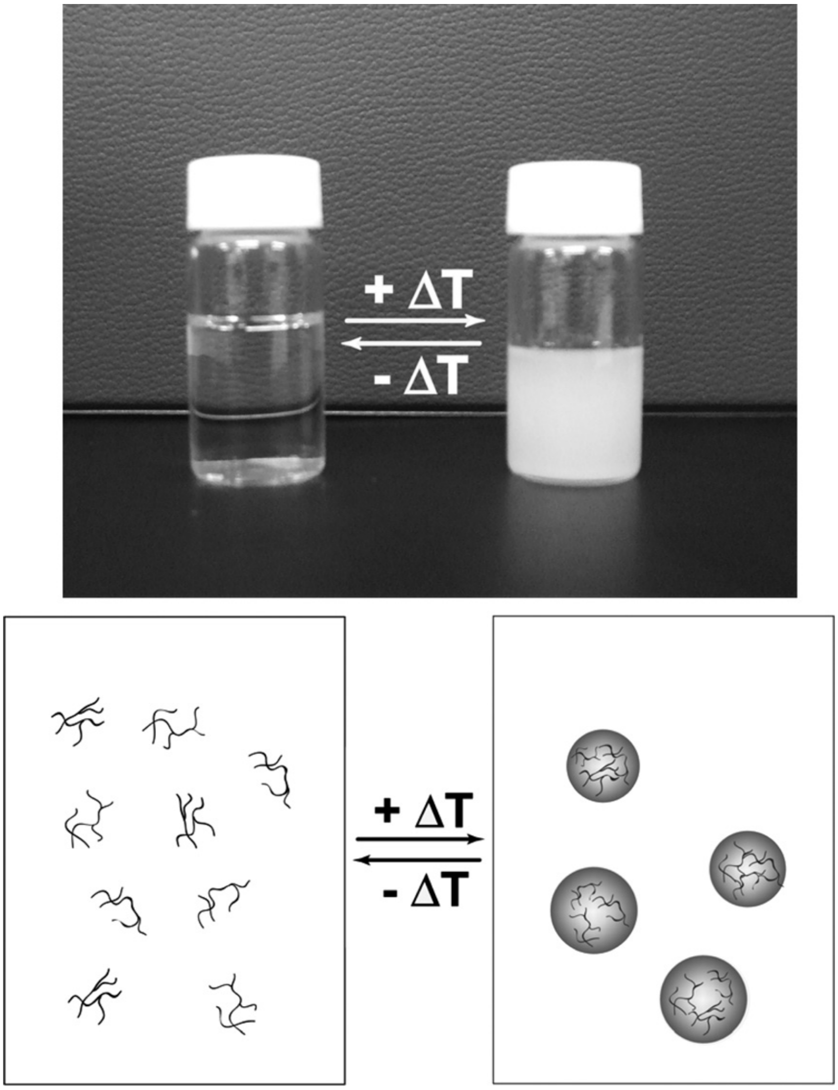

Fig. 3. LCST transition of *n*Bu$_{91}$-PEI and schematic illustration of the transition. *n*Bu$_{91}$-PEI solution in 10 mM PBS (pH 7.4, 150 mM NaCl) below 12 °C (left) and over 15 °C (right). The concentration of *n*Bu$_{91}$-PEI was 2.0 mg/mL.

The transition temperature can be effectively decreased by the degree of butyrylation, which determines the entropy loss. The T_{cp} of *n*Bu-PEI was slightly lowered from 24.02 °C to 12.59 °C as the degree of butyrylation was increased from 55.00% to 91.20%. On the other hand, T_{50} had a larger decrease from 31.52 °C to 13.96 °C, with the same change of the degree of butyrylation. Even after each *n*-butyryl moiety in the polymer started to exclude water molecules from its neighbor at a certain temperature (T_{cp}), the hydrophobic moieties should get together to form large aggregates resulting in significant turbidity. The aggregation kinetics was dependent upon the density of the hydrophobic moieties. Therefore, an *n*Bu-PEI derivative with a high density of *n*-butyryl groups showed a sharp LCST transition with a smaller ΔT value (for *n*Bu$_{91}$-PEI, $\Delta T = 1.37$ °C), whereas a less-butyrylated derivative showed a relatively gradual transition curve with a larger ΔT value (for *n*Bu$_{55}$-PEI, $\Delta T = 7.50$ °C).

3.3. Acyl group–LCST relationship

The LCST of *N*-acylated *b*-PEI can vary based on the type of acyl group. The LCST transitions of propionic *b*-PEI (Pr-PEI; **1**) and isobutyric *b*-PEI (*i*Bu-PEI; **3**) are shown in Fig. 5A and Fig. 5B, respectively. Over the broad range of the transition temperatures (10–70 °C), the LCST of *b*-PEI can be controlled by the choice of the acyl group as well as its degree of acylation. Acetylated *b*-PEI derivatives were also synthesized and tested, but no LCST transition was observed (data not shown). The T_{cp}s of Pr-PEI derivatives ranged from 52 °C to 65 °C as a function of degree of acylation, which ranged from 51.32% to 94.85%, whereas the T_{cp}s of *i*Bu-PEI derivatives ranged from 15 °C to 52 °C as the degree of acylation increased from 49.31% to 90.30%. In particular, *i*Bu-PEI showed an outstandingly sharp transition with a ΔT less than 2.0 °C over the various degree of acylation.

The difference between the T_{cp}s of Pr-PEI and Bu-PEI can easily be rationalized considering that the entropy loss (ΔS) of Bu-PEI during the solvation was higher than that of Pr-PEI. Acetyl group, which is less hydrophobic than propionyl group, cannot provide enough entropy loss during solvation to show LCST transition up to 100 °C, the boiling point of water. Meanwhile, the T_{cp}s' trends of *n*Bu-PEI and *i*Bu-PEI require a more detailed discussion. Although it has been claimed that the hydrophobicity of the isobutyryl group is somewhat higher than that of the *n*-butyiric group [23], other previously obtained results support the opposite behavior. The T_{cp} of poly(*n*-propyloxazoline) (P*n*PrOx), a linear PEI derivative of *n*Bu-PEI, showed a lower T_{cp} than poly(isopropyloxazoline) (P*i*PrOx), a linear PEI derivative of *i*Bu-PEI [24]. In addition, poly(*N*-propylacrylamide) showed a lower T_{cp} than PNIPAAM with a *N*-isopropyl side chain [25]. In our results, *n*Bu-PEI also showed the LCST transition at a lower T_{cp} than *i*Bu-PEI, which also confirmed this trend.

Generally, acylated *b*-PEI derivatives have shown lower T_{cp}s than linear PEI derivatives. The T_{cp}s of Pr$_{95}$-PEI, *n*Bu$_{91}$-PEI, and *i*Bu$_{90}$-PEI were 52.02 °C, 12.59 °C, and 15.48 °C, whereas those of the corresponding linear PEI derivatives, poly(ethyloxazoline) (PEtOx), P*n*PrOx, and P*i*PrOx, were 75.1 °C, 23.8 °C, and 38.7 °C, respectively [24]. Considering that acylated *b*-PEI containing unreacted tertiary amine groups is less hydrophobic than the corresponding linear PEI derivatives, the lowering of the T_{cp} is probably due to the highly branched structure of the *b*-PEI backbone. Because the entropy loss of branched polymers during aggregation is smaller than that of linear polymers, the acylated *b*-PEI derivatives can form aggregates at lower transition temperatures.

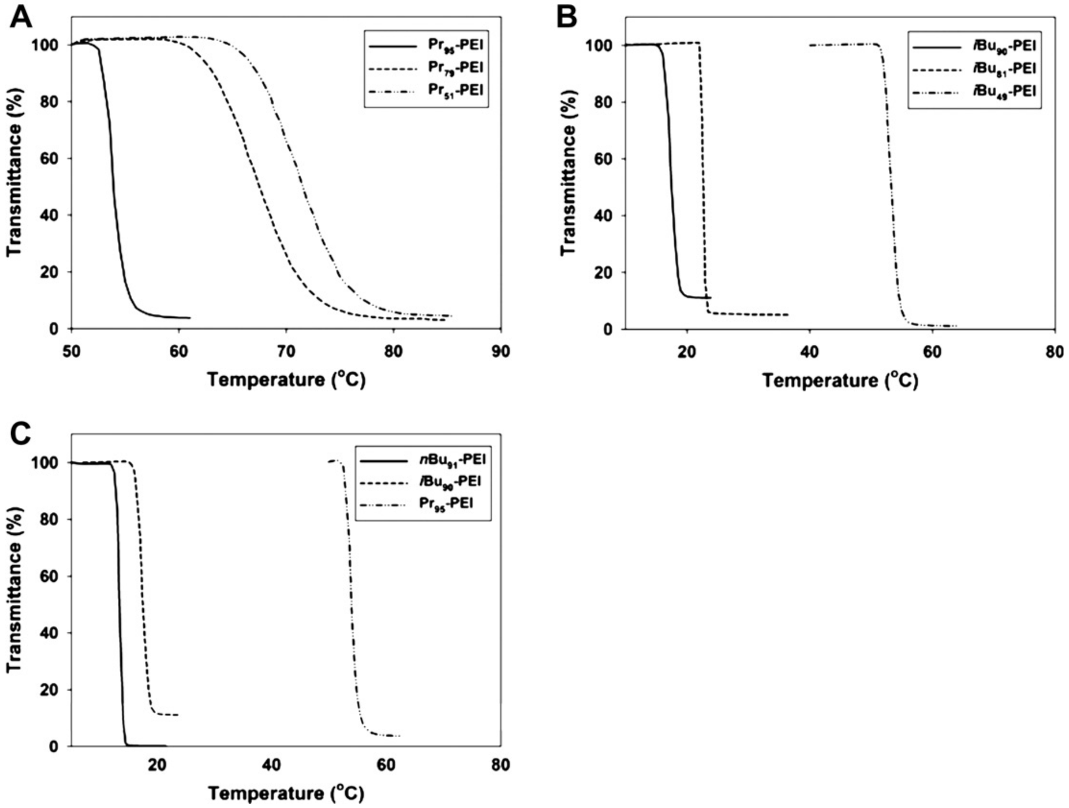

Fig. 5. LCST–acyl group relationship of *N*-acylated *b*-PEI. LCST transition of (A) Pr-PEI, (B) *i*Bu-PEI with different acylation degrees, and (C) comparison of LCST transition of *N*-acylated *b*-PEI derivatives with different acyl groups. The concentration of *N*-acylated *b*-PEI was 2.0 mg/mL in 10 mM PBS (pH 7.4, 150 mM NaCl).

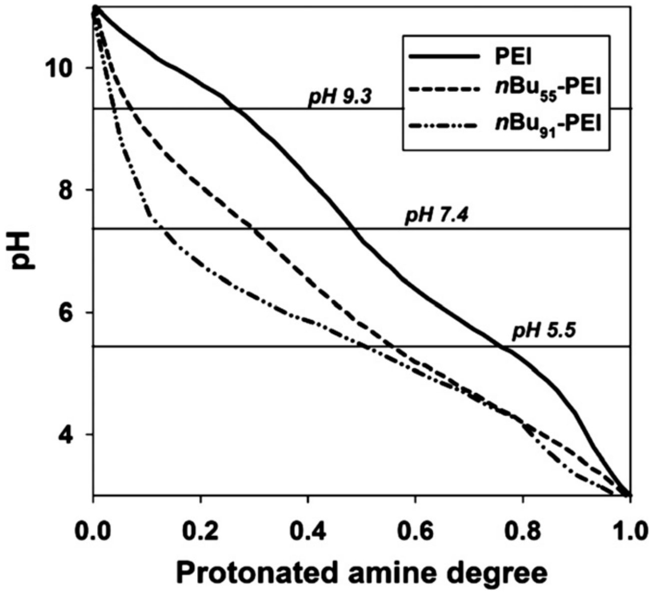

Fig. 6. Comparison of buffering capacity of *b*-PEI, $n\mathrm{Bu}_{55}$-PEI, and $n\mathrm{Bu}_{91}$-PEI at varying pH values.

3.4. Buffering capacity of acylated b-PEI

The pH-sensitivity of PEI is caused by the pH-dependent protonation–deprotonation of its amine groups. As the primary and secondary amine groups of *b*-PEI are consumed to form amides by acylation, it is expected that the buffering behavior of acylated *b*-PEI is quite different than the original polymer. The $\mathrm{p}K_\mathrm{a}$ values of amine groups in *b*-PEI varied over the pH ranges of 4–10, demonstrating its broad buffering behavior. Primary and secondary amines (∼74%) tend to be protonated at higher pH values, and tertiary amines (∼26%) in the interior of the *b*-PEI structure are protonated at a more acidic pH [26]. Therefore, acylated *b*-PEI derivatives are expected to lose their buffering capacity at higher pH values through the consumption of primary and secondary amines and the formation of a more hydrophobic environment.

Fig. 6 shows the titration curves of *b*-PEI and its butyrylated derivatives. According to the calculations based on the degree of acylation and the amine ratio, $n\mathrm{Bu}_{55}$-PEI possesses 57% primary/secondary amines and 43% tertiary amines. The amine groups of $n\mathrm{Bu}_{91}$-PEI are composed of 21% primary/secondary amines and 79% tertiary amines. Therefore, $n\mathrm{Bu}_{55}$-PEI showed a relatively balanced buffering capacity both at higher and lower pHs, whereas $n\mathrm{Bu}_{91}$-PEI showed effective buffering only at pH values below 6. According to the titration curves, about 50% and 71% of the amine groups of $n\mathrm{Bu}_{55}$-PEI and $n\mathrm{Bu}_{91}$-PEI can be protonated at a pH below 6, respectively. The maintenance of pH-sensitivity or buffering capacity at a pH value of around 5.5 may be a strong advantage for acylated *b*-PEI as a pH and temperature-sensitive polymer at the early endosomal pH.

3.5. pH–LCST relationship

The LCST, which is determined by the balance between hydrophilicity and hydrophobicity, can be influenced by pH changes (Fig. 7). Because the hydrophilicity of polymers can be increased by the protonation of amine groups to positively charged ammoniums (more negative ΔH of solvation), an increase of the LCST at the acidic pH value of 5.5 was generally observed. Conversely, lowering of the LCST was detected at the basic pH value of 9.3.

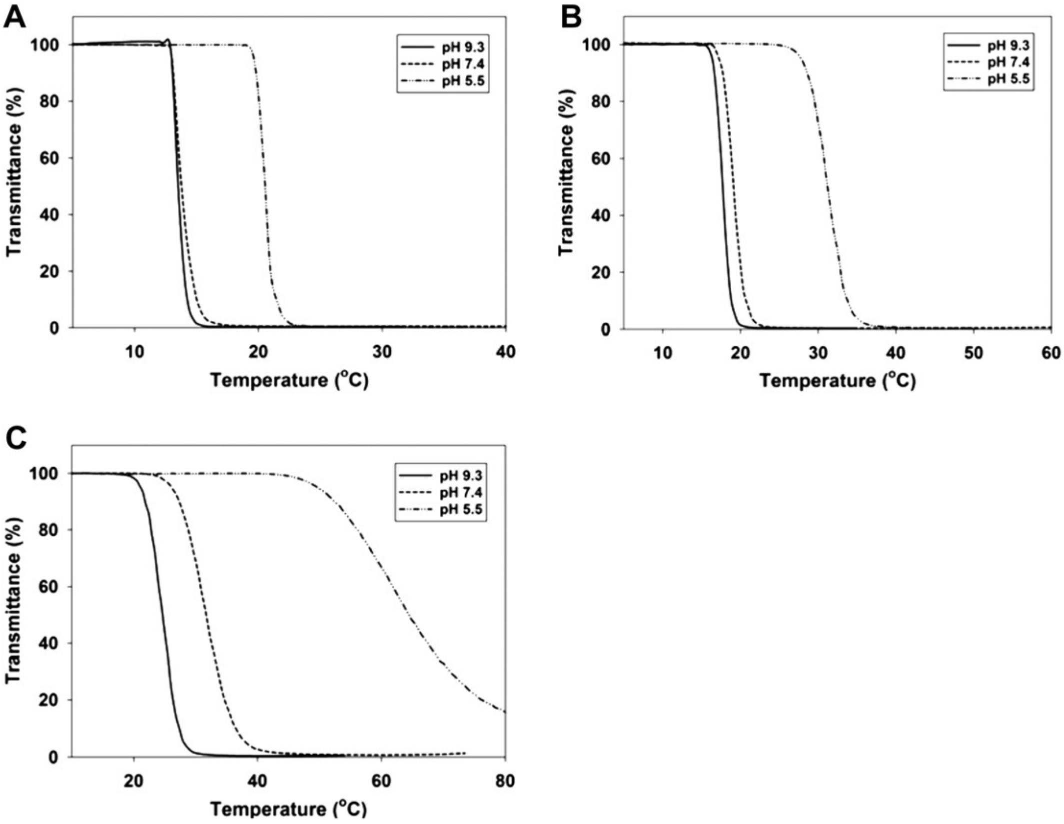

Fig. 7. Effect of pH on LCST of (A) $n\mathrm{Bu}_{91}$-PEI, (B) $n\mathrm{Bu}_{75}$-PEI, and (C) $n\mathrm{Bu}_{55}$-PEI. The concentration of *n*Bu-PEI was 2.0 mg/mL.

The LCST variation with pH is highly dependent upon the degree of acylation. With the pH change from 9.3 to 5.5, the T_{cp} of nBu$_{91}$-PEI increased by only 6.45 °C from 12.49 °C to 18.94 °C (Table 1). The T_{cp} of nBu$_{75}$-PEI increased by 10.42 °C from 15.51 °C to 25.93 °C and the T_{cp} of nBu$_{55}$-PEI increased by 25.48 °C from 19.50 °C to 44.98 °C. These results are closely related to the number of protonable amines in the polymer molecule. Less acylated *b*-PEI, which possesses more protonable amines, showed a more sensitive pH-dependence of the LCST transition.

The LCST variation of acylated *b*-PEI showed clear differences depending on the pH range. As discussed earlier (Fig. 6), *b*-PEI possessed an almost uniform buffering capacity during the acidification from a pH of 9.3 to a pH of 5.5, but the buffering capacity of acylated *b*-PEI in basic pH ranges decreased as the degree of acylation increased. Therefore, the increase of the LCST was relatively small when the pH decreased from 9.3 to 7.4, but a significant increase of the LCST was observed when the pH decreased from 7.4 to 5.5. For example, nBu$_{91}$-PEI, whose buffering capacity is concentrated in the acidic range, showed only a 0.10 °C difference of T_{cp} between a pH of 9.3 and a pH of 7.4 compared to the 6.35 °C difference observed between a pH of 7.4 and a pH of 5.5. In contrast, nBu$_{55}$-PEI, which still maintains some buffering capacity in the basic pH range, showed a 5.52 °C difference of the T_{cp} between a pH of 9.3 and a pH of 7.4. Again, the high sensitivity of the LCST in the biologically tolerable range between neutral a pH of 7.4 and a slightly acidic pH of 5.5 can be maintained even after the acylation.

3.6. *Ionic concentration–LCST relationship*

We measured the LCST transition of nBu-PEI in 10 mM phosphate buffers (pH 7.4) with different concentrations of NaCl (0 mM, 75 mM and 150 mM) (Fig. 8). A lowering of the T_{cp} was generally observed as the ionic strength increased within this range. The lowering of the T_{cp} in the nBu-PEI derivatives with lower degrees of acylation is particularly remarkable. Although the T_{cp} of nBu$_{91}$-PEI decreased by only 2.39 °C with an increase of the NaCl concentration from 0 mM to 150 mM, the T_{cp} of nBu$_{75}$-PEI decreased by 6.96 °C and that of nBu$_{55}$-PEI decreased by 13.00 °C. Similar decreases of the T_{cp} were also observed in other acylated derivatives with propionyl or isobutyryl groups (Table 1). The change of LCST was also dependent upon salt types. The T_{cp} change of nBu$_{55}$-PEI by the addition of sodium sulfate (Na_2SO_4) is shown in Fig. S4 in the Supporting material.

The change of the T_{cp} or aqueous solubility of polymers at a given temperature by the addition of salts can be interpreted as a similar phenomenon with the so-called 'salting-in' or 'salting-out' effect on the precipitation of proteins [27]. As with the salting-in effect, the hydrophilic or ionic surface moiety of polymers (*e.g.* amine or ammonium groups) is stabilized by the increased salt concentration. In contrast, the hydrophobic moiety of polymers is destabilized by the increased salt concentration. The salting-in effect results in a more negative value of the Gibbs free energy of solvation, which increases the solubility of amphiphilic polymers, whereas the salting-out effect reduces the solubility at a given temperature due to the addition of salts. Although it is difficult to predict whether a polymer shows phase separation at a certain ionic concentration and temperature by these two opposite effects, the salting-out effect is generally dominant at high salt concentrations, and the lowering of the solubility and LCST is often observed with an increased ionic strength [28]. The LCST transition of *N*-acylated PEI derivatives in NaCl solutions is also supposedly regulated by the salting-out effect, considering the decrease of T_{cp} or aqueous solubility with increased ionic strength.

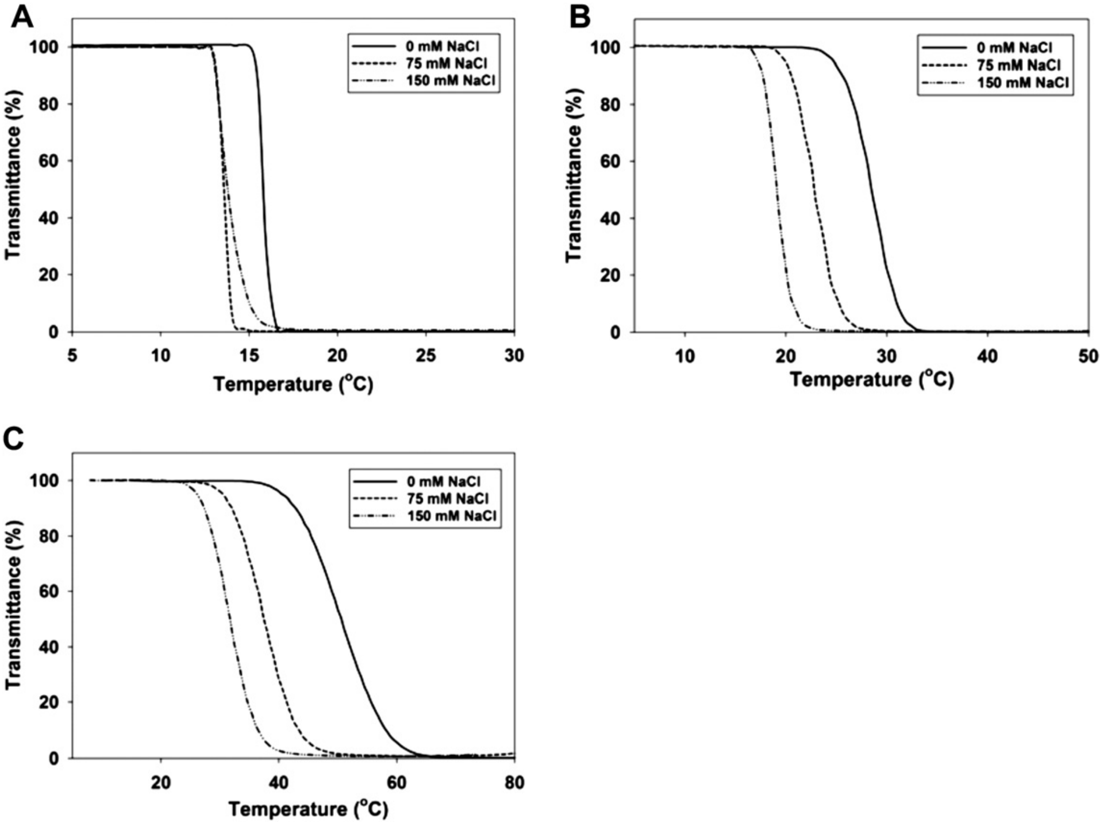

Fig. 8. Effect of NaCl concentrations on LCST of (A) nBu$_{91}$-PEI, (B) nBu$_{75}$-PEI, and (C) nBu$_{55}$-PEI. The concentration of nBu-PEI was 2.0 mg/mL. The pH of the solution was fixed at 7.4 in 10 mM phosphate buffer.

4. Conclusions

Integration of dual or multiple signal-sensitivities into a polymer system has been one of the important objectives in polymer chemistry. Moreover, biomedical applications require polymer systems whose properties can be controllable in more advanced ways with multiple variables. We synthesized a temperature- and pH-sensitive polymer via a very simple acylation method from a commercially available polymer, *b*-PEI. The LCST of the *N*-acylated *b*-PEI derivatives can be carefully controlled by the balance between the hydrophobicity and hydrophilicity of the polymer functionalities, which are determined by the acyl groups, degrees of acylation, and protonation of amine groups. In particular, *n*Bu-PEI derivatives showed a variation of the LCST transition in the temperature and pH ranges of 10–40 °C and pH 5–9, which are biologically tolerable ranges. The very simple introduction of thermosensitivity into a pre-existing polymer can be easily applied to the development of other polymer systems with different multiple signal-sensitivities.

Acknowledgments

The authors thank Prof. Kazunori Kataoka of the University of Tokyo, for his kind discussion about the research. This work is supported by the Research Settlement Fund for new faculty of Seoul National University, the grant (2010-P2-14) of Advanced Institute of Convergence Technology (AICT), and the Basic Science Research Program (2010-0007118) through the National Research Foundation of the Ministry of Education, Science and Technology of Korea.

Supplementary material

Supplementary data related to this article can be found online at doi:10.1016/j.polymer.2011.01.045.

References

[1] Liu F, Urban MW. Prog Polym Sci 2010;35:3–23.
[2] Lee Y, Kataoka K. Soft Matter 2009;5:3810–7.
[3] Pissuwan D, Valenzuela SM, Cortie MB. Trends Biotechnol 2006;24:62–7.
[4] Schild HG. Prog Polym Sci 1992;17:163–249.
[5] Scarpa JS, Mueller DD, Klotz IM. J Am Chem Soc 1967;89:6024–30.
[6] Gan LH, Gan YY, Deen GR. Macromolecules 2000;33:7893–7.
[7] Park J-S, Akiyama Y, Winnik FM, Kataoka K. Macromolecules 2004;37:6786–92.
[8] Bromberg LE, Ron ES. Adv Drug Deliv Rev 1998;31:197–221.
[9] Nowak AP, Breedveld V, Pakstls L, Ozbas B, Pine DJ, Pochan D, et al. Nature 2002;417:424–8.
[10] Jeong B, Bae YH, Kim SW. Macromolecules 1999;32:7064–9.
[11] Hirose M, Kwon OH, Yamato M, Kikuchi A, Okano T. Biomacromolecules 2000;1:377–81.
[12] Wei H, Cheng S-X, Zhang X-Z, Zhuo R-X. Prog Polym Sci 2009;34:893–910.
[13] Wang Z-C, Xu X-D, Chen C-S, Wang G-R, Cheng C-X, Zhang X-Z, et al. React Funct Polym 2009;69:14–9.
[14] Boussif O, Lezoualc'h F, Zanta MA, Mergny MD, Scherman D, Demeneix B, et al. Proc Natl Acad Sci USA 1995;92:7297–301.
[15] Türk M, Dinçer S, Yuluğ IG, Pişkin E. J Control Release 2004;96:325–40.
[16] Haba Y, Harada A, Takagishi T, Kono K. J Am Chem Soc 2004;124:12760–1.
[17] Tono Y, Kojima C, Haba Y, Takahashi T, Harada A, Yagi S, et al. Langmuir 2006;22:4920–2.
[18] Jeong JH, Song SH, Lim DW, Lee H, Park TG. J Control Release 2001;73:391–9.
[19] Fischer D, Bieber T, Li Y, Elsässer HP, Kissel T. Pharm Res 1999;16:1273–9.
[20] Lim Y-b, Kim S-M, Lee Y, Lee W-k, Yang T-g, Lee M-j, et al. J Am Chem Soc 2001;123:2460–1.
[21] Liu H, Shen Z, Stiriba S-E, Chen Y, Zhang W, Wei L. J Polym Sci Polym Chem 2006;44:4165–73.
[22] Dai F, Wang P, Wang Y, Tang L, Yang J, Liu W, et al. Polymer 2008;49:5322–8.
[23] Haba Y, Kojima C, Harada A, Kono K. Macromolecules 2006;39:7451–3.
[24] Park J-S, Kataoka K. Macromolecules 2007;40:3599–609.
[25] Ito S. Kobunshi Ronbunshu 1989;46:437–43.
[26] Suh J, Paik H-J, Hwang BK. Bioorg Chem 1994;22:318–27.
[27] Melander W, Horbath C. Arch Biochem Biophys 1977;183:200–15.
[28] Schild HG, Tirrell DA. J Phys Chem 1990;94:4352–6.

Polymer 52 (2011) 1375–1384

Contents lists available at ScienceDirect

Polymer

journal homepage: www.elsevier.com/locate/polymer

Characterization and conversion determination of stable PEDOT latex nanoparticles synthesized by emulsion polymerization

Chieh-Han Wu [a], Trong-Ming Don [b], Wen-Yen Chiu [a,c,d,*]

[a] *Institute of Polymer Science and Engineering, National Taiwan University, Taipei 106, Taiwan*
[b] *Department of Chemical and Materials Engineering, Tamkang University, Tamsui, Taipei county 251, Taiwan*
[c] *Department of Chemical Engineering, National Taiwan University, Taipei 106, Taiwan*
[d] *Department of Materials Science and Engineering, National Taiwan University, Taipei 106, Taiwan*

ARTICLE INFO

Article history:
Received 20 October 2010
Received in revised form
10 January 2011
Accepted 18 January 2011
Available online 25 January 2011

Keywords:
Emulsion polymerization
Bi-oxidant $Fe(OTs)_3/H_2O_2$ system
Conversion determination

ABSTRACT

In this research, poly(3,4-ethylenedioxythiophene) (PEDOT) latex nanoparticles with good colloidal stability were prepared by emulsion polymerization and the conversions of EDOT were determined. Two kinds of oxidants, Iron(III) *p*-toluenesulfonate $Fe(OTs)_3$ and hydrogen peroxide H_2O_2, were introduced to decrease the use of iron salt and therefore reduce the particle coagulation. The ferrous ions (Fe^{2+}) produced during the polymerization would be re-oxidized back to the reactive ferric ions (Fe^{3+}) with the help of H_2O_2. This cyclic oxidation–reduction process resulted in the sustained regeneration of Fe^{3+} ions and led to a higher conversion. A dark blue PEDOT latex with long-term dispersion stability was obtained when $Fe(OTs)_3$ and H_2O_2 were added in sequence. The results obtained from dynamic light scattering and TEM measurements showed that the sizes of nanoparticles were around 100 nm. To determine the conversion of EDOT, two methods (gravimetric analysis and UV–visible method) were used and compared. For the first time, the UV–visible method was established to quantitatively determine the conversion of EDOT monomer. From the measurement, the conversion of EDOT in this system was determined as 74–75%. The PEDOT film prepared by drying the latex solution had conductivity up to 6.3 S/cm.

1. Introduction

Since the first intrinsic conducting polymer (ICP) polyacetylene was discovered by Shirakawa et al. in 1977 [1,2], the field of conducting polymers has attracted increasing attention from scientists in the world [3–5]. Among the various families of conducting polymers, as one of polythiophene derivatives, Poly(3,4-ethylenedioxythiophene) (PEDOT) has been studied extensively because of its great thermal and environmental stability, low band gap, high conductivity, and high transparency [6–8]. PEDOT was developed by scientists at the laboratories of Bayer AG in the late 1980s [9,10] and it has been widely used in numerous applications such as electrochromics [11], light emitting diodes [12], solar cells [13], antistatic coatings [14,15], and sensors [16,17]. The electro-donating dialkoxy group of EDOT offers the stabilizing effect on lowering its oxidative doping potential, thus resulting in a stable p-doped state and better defined polymer chains [18,19].

Usually, PEDOT can be prepared by oxidative chemical or electrochemical polymerization. Electrochemical polymerization has been widely used for fabricating thin films of conducting polymers because it can be carried out with small amounts of monomers, short reaction time, and can acquire films on conducting substrates or free-standing films [20]. Nevertheless, the requirement of conducting substrates for electrochemical polymerization would restrict its applications [21]. For the purpose of mass production, PEDOT can be prepared from oxidative chemical polymerization alternatively. One method of chemical-polymerized PEDOT film as reported by de Leeuw at al. [22] has been developed via *in situ* polymerization. EDOT monomer is spin coated on a substrate first, following by utilizing the mixture of ferric (Fe^{3+}) oxidizing agent, for instances, iron(III) chloride ($FeCl_3$) or iron(III) *p*-toluenesulfonate ($Fe(OTs)_3$), and weak base imidazole to polymerize PEDOT film onto the substrate directly. In our earlier research, another co-monomer 3-thienyl ethoxybutanesulfonate (TEBS) was added to reduce the copolymerization rate, leading to the much uniform film surface which increased the conductivity [23]. However, like other conjugated polymers, pure PEDOT material is insoluble in organic solvents and water medium. To overcome this drawback, many researches focused on the enhancement of solubility to resolve its practical applications in industry [7,24].

Nowadays, a commercial product of PEDOT which is so-called “Baytron P” has been developed by the Bayer AG company of

---

* Corresponding author. Department of Materials Science and Engineering, National Taiwan University, Taipei 106, Taiwan. Tel./fax: +886 2 23623259.
E-mail address: ycchiu@ntu.edu.tw (W.-Y. Chiu).

0032-3861/$ – see front matter © 2011 Elsevier Ltd. All rights reserved.
doi:10.1016/j.polymer.2011.01.034

Germany [9]. It is an aqueous dispersion of PEDOT and poly(styrene sulfonate) (PSS), PEDOT–PSS, which is prepared by synthesizing EDOT in the presence of the water-soluble template polymer PSS. The PSS in the PEDOT–PSS complex acts as the charge balancing counter ion of PEDOT and is able to make PEDOT segments dispersed in the water phase. Although PEDOT–PSS is solution-processable for coating conductive thin films, the surface morphology and optical transparency of the films do not satisfy the requirements very well [21].

Another route to improve the processability and increase the dispersion property in water is to polymerize conjugated polymers by using steric stabilizers such as monomeric surfactants [25,26] or soluble polymers [27,28]. Among the oxidative chemical polymerization, emulsion polymerization seems to be promising because higher yield and more uniform particle size can be obtained at the same time. Recently, Im and coworkers [26] had reported the preparation of PEDOT latex via emulsion polymerization in the aqueous dodecylbenzene sulfonic acid (DBSA) solution and attained a relatively high conductivity up to 50 S/cm. As a kind of anionic surfactant for stabilizing the colloids, the sulfonate functional groups in DBSA molecules can serve as a doping agent as well. In general, typical oxidants of chemical polymerization are iron salts (*e.g.* $FeCl_3$ and $Fe(OTs)_3$) and peroxides (*e.g.* ammonium persulfate (APS) and potassium persulfate (KPS)) [7,26]. Unfortunately, the excess oxidants left in the final products would affect the optoelectronic behavior of PEDOT [29,30] and makes the post-treatments more complicated. On the other hand, the rather high content of metallic ions may adsorb onto the surface of latex particles and cause them to aggregate and precipitate.

In order to carry out the polymerization without influencing the latex stability, Yamamoto and his group [31,32] synthesized conjugated polymers by using the Fe(II)-, Fe(III)-, and Cu(II)-H_2O_2 catalyst systems. Meanwhile, similar Fe(II) or Fe(III)-H_2O_2 catalytic system was also applied to the polymerization of aniline [33–38] and thiophene [30,39–41] in numerous reports. Such catalytic system can effectively reduce the use of iron salt, because the main oxidizing ability relies on hydrogen peroxide. The introducing of hydrogen peroxide also enhances the dispersion stability of latex particles. Moreover, the waste of the main oxidant H_2O_2 is H_2O, which is much friendly than organic solvents to the environment and is easily removed from the reaction system.

In the present paper, we proposed the fabrication of stable PEDOT latex nanoparticles in the water medium by using $Fe(OTs)_3$ and H_2O_2 bi-oxidant system in the presence of surfactant DBSA. A two-stage polymerization profile was applied and the morphology change of latex particles was examined. The reaction mechanism between $Fe(OTs)_3$ and H_2O_2 was also discussed in detail in this article. Furthermore, due to its poor solubility in organic solvents, the molecular weight and monomer conversion of the PEDOT material are difficult to analyze by the conventional methods such as gel permeation chromatography (GPC). The lack of an appropriate method for measuring monomer conversion makes it hard to control and evaluate the product quality of PEDOT. By utilizing the high sensitivity of UV–visible spectrometer to the solute concentration, we were able to develop a simple and quick method for calculating the conversion of EDOT monomer quantitatively.

2. Experiments

2.1. Chemicals

Monomer 3, 4-ethylenedioxythiophene (EDOT) and Iron(III) *p*-toluenesulfonate hexahydrate ($Fe(OTs)_3 \cdot 6H_2O$) were purchased from Sigma–Aldrich Inc., and were used without further purification. Surfactant dodecylbenzene sulfonic acid (DBSA, from ACROS ORGANICS), hydrochloric acid (37%) and hydrogen peroxide solution (35 wt.%, from ACROS ORGANICS) were used as received. Deionized water was used throughout the experiments.

2.2. Preparation of PEDOT latex nanoparticles by emulsion polymerization

PEDOT nanoparticles were synthesized by emulsion polymerization under ambient conditions. Typically, surfactant DBSA (0.5 g) was dissolved in 40 mL of deionized water and followed by the addition of 0.2 mL of EDOT monomer. The mixed solution was stirred in a water bath at room temperature for 30 min. The first oxidant, 0.25 g of $Fe(OTs)_3 \cdot 6H_2O$ in 10 mL water, was added into the solution to start the first stage of polymerization. After 1 h of reaction, 0.3 g of hydrochloric acid was dripped into the solution. Then the second oxidant, hydrogen peroxide solution (0.50 g), was added into the reaction system for the second stage of polymerization. The reactant mixture was stirred for 48 h at room temperature to obtain a stable emulsion with dark blue color. The PEDOT synthesized under this two-stage polymerization is designated as PEDOT2. For comparison, different reaction conditions were also adopted, as listed in Table 1. PEDOT1 stands for the polymer synthesized by only adding $Fe(OTs)_3$ to the reaction system. PEDOT3 was prepared by adding $Fe(OTs)_3$ and H_2O_2 simultaneously to be compared with the PEDOT2, of which H_2O_2 was added at 1 h after the addition of $Fe(OTs)_3$.

2.3. Determination of conversion

The conversion of EDOT monomer after polymerization was determined by both gravimetric analysis and UV–visible method. For the gravimetric analysis, the PEDOT emulsion obtained after reaction was directly dried to a constant weight in vacuum and the monomer conversion, Conversion A (%), was then calculated according to the following equation (1),

$$\text{Conversion A}(\%) = \frac{W_R - W_{SI}}{E_0} \times 100\left(\%\right) \qquad (1)$$

where W_R is the weight of the dried PEDOT latex and W_{SI} is the weight of oven-drying product of the solution prepared by only dissolving the DBSA and $Fe(OTs)_3$ in the water with the same concentrations as the original reaction system for synthesizing PEDOT. The other method of determining the conversion of EDOT monomer, Conversion B (%), was via UV–visible method which would be discussed in detail in the text later.

2.4. Characterization

The synthesized PEDOT latex was diluted 100 times in water first, and then the size distribution and zeta potential of polymer particles were determined by dynamic light scattering (DLS) technique (Malvern Nano-ZS, Particle Size and Zeta Potential Analyzer).

Table 1
The compositions of reactants used in the emulsion polymerization.

Sample	EDOT (ml)	DBSA (g)	$Fe(OTs)_3$ (g)	H_2O_2 (g)
PEDOT1[a]	0.2	0.5	0.25	0
PEDOT2[b]	0.2	0.5	0.25	0.5
PEDOT3[c]	0.2	0.5	0.25	0.5

[a] Reaction with only $Fe(OTs)_3$.
[b] Reaction with $Fe(OTs)_3$ for 1 h in the first-stage polymerization, followed by adding H_2O_2 for the second-stage polymerization.
[c] Reaction with $Fe(OTs)_3$ and H_2O_2 simultaneously in the beginning. The total reaction time was 48 h for PEDOT1–PEDOT3.

The morphology of latex particles was observed with JOEL JEM-1230 transmission electron microscope (TEM) and Nova TM NanoSEM 230 field emission scanning electron microscope (FE-SEM). The PEDOT latex was diluted in water and then dropped onto the cooper grid coated with carbon (for TEM) and onto a plastic culture dish (for FE-SEM), drying by air evaporation.

To obtain the UV–visible absorption spectra of reactants and products in water, a Helios UV–vis spectrometer was applied. The samples withdrawn from the reactor were diluted about one thousand times in water with pipet before measurement. The quartz cell was used. The software PeakFit 4.11 was used to facilitate the peak-fitting and deconvolution when dealing with the UV–visible absorption spectra.

For the film formation, the synthesized PEDOT latex was poured into a plastic culture dish and dried in the oven at 60 °C to form the conductive PEDOT thin film. The conductivity of the PEDOT thin film, σ, was calculated by the equation $\sigma=1/Rd$, where σ is the conductivity in S/cm, R is the surface resistance in $\Omega/\square$, and d is the thickness of PEDOT film. The surface resistances of PEDOT films were measured using a standard four-point probe method, and the thickness of PEDOT film was measured with a TENCOR Alpha-Step 500 surface profiler. The FE-SEM was also used to observe the surface roughness of these PEDOT films.

3. Results and discussion

3.1. Reaction mechanism via the Fe^{3+}/H_2O_2 bi-oxidant system

Basically, the polymerization used in this study could be divided into three parts, including the partition of monomer, the first stage of polymerization, and the second stage of polymerization. In the beginning, the dissolved DBSA anions in the aqueous medium would form micelles because the concentration of DBSA in this work was higher than the critical micelle concentration (CMC, 1.6 mM for DBSA). The hydrophobic long carbon chains of the surfactant would assemble toward the center of micelle and the hydrophilic sulfonic groups ($-SO_3^{2-}$) would expose in the water phase, resulting in the negatively charged micelle surface. When the EDOT monomer (oil phase) was added into the water phase, a certain amount of monomer diffused quickly into the center of micelles and monomer-swollen micelles were formed, leading to the partition of monomer. Large monomer droplets were also formed and surrounded by DBSA anions.

In the first-stage polymerization, the first initiator, $Fe(OTs)_3$, was fed in the water phase and the ferric ions (Fe^{3+}) would tend to approach the negatively charged surfaces of both micelles and monomer droplets due to the electrostatic attraction [30]. As the ferric ions were attached to the micelle or droplet surface, EDOT monomer at the inner surface would be oxidized by Fe^{3+} ions and the polymerization was carried out from the interface of oil/water. Because of the neutralization on the micelles' surface by the attached Fe^{3+}, the colloidal stability would be affected and in some cases, coagulation of latex particles was observed. Therefore, it would be helpful to limit the amount of $Fe(OTs)_3$ added into the reaction system to increase the colloidal stability. However, the conversion would be low due to the insufficient $Fe(OTs)_3$ oxidant. Only monomers near the interface of particles were reacted and polymerized during the first stage of polymerization. Those unreacted monomers would remain in the central region of micelles or droplet particles and therefore hollow structures would be observed. Within the first stage of polymerization, Fe^{3+} ions were reduced to inactive ferrous ions (Fe^{2+}) without any further oxidative ability.

To increase the conversion, the hydrogen peroxide as the second oxidant was introduced to the system in the second stage of polymerization. When H_2O_2 encountered Fe^{2+} in the aqueous medium, Fe^{2+} would catalyze the decomposition reaction of H_2O_2 to form the hydroxyl radical ($OH^\bullet$). This typical reaction is well-known as the Fenton reaction and can be described in the following equation [42],

$$Fe^{2+} + H_2O_2 \rightarrow Fe^{3+} + OH^- + OH^\bullet \tag{2}$$

The produced $OH^\bullet$ radical is a strong oxidant, which could further oxidize Fe^{2+} ions to Fe^{3+} ions.

$$Fe^{2+} + OH^\bullet \rightarrow Fe^{3+} + OH^- \tag{3}$$

Combing equations (2) and (3), the oxidation of Fe^{2+} ions by H_2O_2 could be expressed as equation (4).

$$2Fe^{2+} + H_2O_2 \rightarrow 2Fe^{3+} + 2OH^- \tag{4}$$

According to equation (4), the ferrous ions formed in the first stage of polymerization could be transformed to the oxidative ferric ions. Because the amount of H_2O_2 added into the system was abundant, the Fe^{3+} ions thus could be regenerated continuously and the remaining EDOT monomers were allowed to polymerize without feeding additional iron salt. However, it is known that the self-redox decomposition of H_2O_2 is also catalyzed by Fe^{3+} through the following reactions,

$$Fe^{3+} + H_2O_2 \rightarrow Fe^{2+} + HO_2^\bullet + H^+ \tag{5}$$

$$Fe^{3+} + HO_2^\bullet \rightarrow Fe^{2+} + H^+ + O_2 \tag{6}$$

The self-redox decomposition of H_2O_2 can be obtained by combining equations (4)–(6), and H_2O and O_2 are eventually produced, as shown in equation (7) [40].

$$2H_2O_2 \rightarrow 2H_2O + O_2 \tag{7}$$

These side reactions would decrease the efficiency of the regeneration of Fe^{3+}, and therefore the degree of polymerization and reaction rate would be affected consequently.

To eliminate these side reactions, hydrochloric acid was externally added into the system before the addition of H_2O_2 for the second stage of polymerization. Since the Fenton reaction is sensitive to the pH value of solution, when the pH value is below one, equation (7) is negligible and equation (4) is the only reaction between Fe^{2+} and H_2O_2 [43]. Some reports also pointed out that the lower pH value could enable the Fe^{3+} to take part in the polymerization easier [26,32]. With the assistance of H_2O_2, the continuously reproduced Fe^{3+} via this cyclic oxidation–reduction reaction of Fe^{2+} and H_2O_2 thus can polymerize the monomer to a very high extent even though the iron salt is deficient stoichiometrically. The proposed synthetic mechanism for polymerization of PEDOT latex nanoparticles via the Fe^{3+}/H_2O_2 bi-oxidant system is shown in Scheme 1.

3.2. Morphology and particle size distribution

The morphology and size distribution of PEDOT latex particles could be determined from the DLS method and TEM photographs of PEDOT latexes. From the preceding measurement, after agitating the DBSA and EDOT mixture for 30 min, some monomer droplets still remained as large droplets with μm in diameters and certain portion of monomers dissolved in micelles which had diameters around 4 nm. In our experiment, large monomer droplets were further broken into smaller droplets due to the continuous agitation after the first oxidant was added. The total surface area of monomer droplets increased with agitation time as the size of

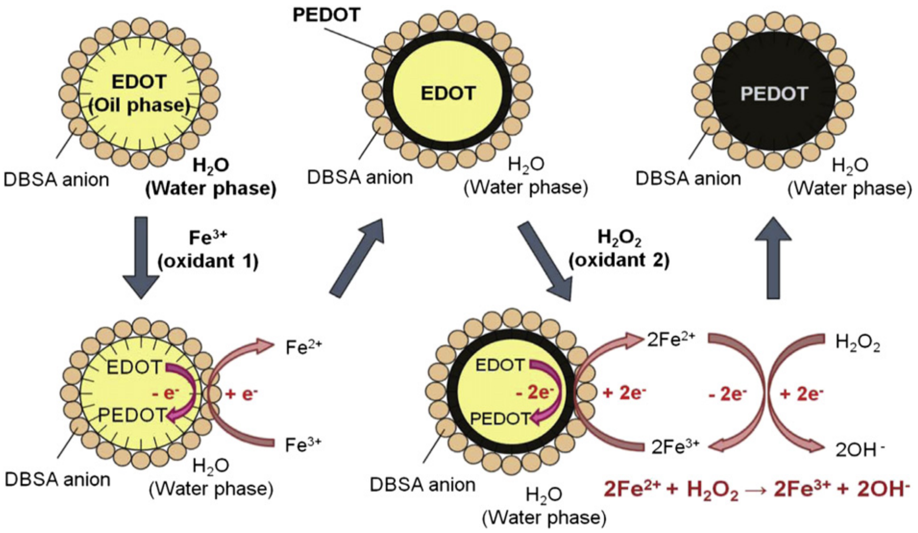

Scheme 1. Synthetic mechanism for polymerization of PEDOT latex nanoparticles via the Fe^{3+}/H_2O_2 bi-oxidant system.

droplets decreased. Furthermore, the reaction started from the interface of oil/water, both the surfaces of micelles and droplets would occur polymerization, hence micellar nucleation and droplet nucleation should be both considered.

Fig. 1 shows the TEM images of PEDOT latex particles formed under different reaction conditions. As the polymerization was initiated by the limited amount of $Fe(OTs)_3$ in the first hour (the first-stage polymerization), PEDOT was synthesized from the outer surfaces of both micelles and droplets. The polymerization in monomer-swollen micelles could reach a higher conversion in a short time compared to the monomer droplets, in which only those monomers near oil/water interface could be polymerized because of their large volumes and the limited amount of Fe^{3+} ions. During the first stage of polymerization, PEDOT polymer grew steadily and gradually solidified the micelle particles, thus forming small PEDOT solid nanoparticles. However, there were merely PEDOT thin membranes formed at the droplets' surfaces. At the same time, smaller nanoparticles formed from monomer-swollen micelles could collide with large soft droplets and thus adhere to the surface of droplets. As a result, at the end of first-stage of polymerization, solid PEDOT nanoparticles formed from micelles and vesicle-like hollow spheres with a layer of PEDOT membrane were observed, as shown in Fig. 1(a).

If the polymerization initiated only by the limited amount of $Fe(OTs)_3$ proceeded further without any additional oxidants, the PEDOT1 with the recipe listed in Table 1 would be formed after 48 h of reaction. Fig. 1(b) shows the PEDOT1 had two particle size distributions. One was in the range of 10–20 nm and the other was around 90 nm. Similar bimodal size distribution of particles was also observed in DLS measurement (Fig. 2). The smaller particles

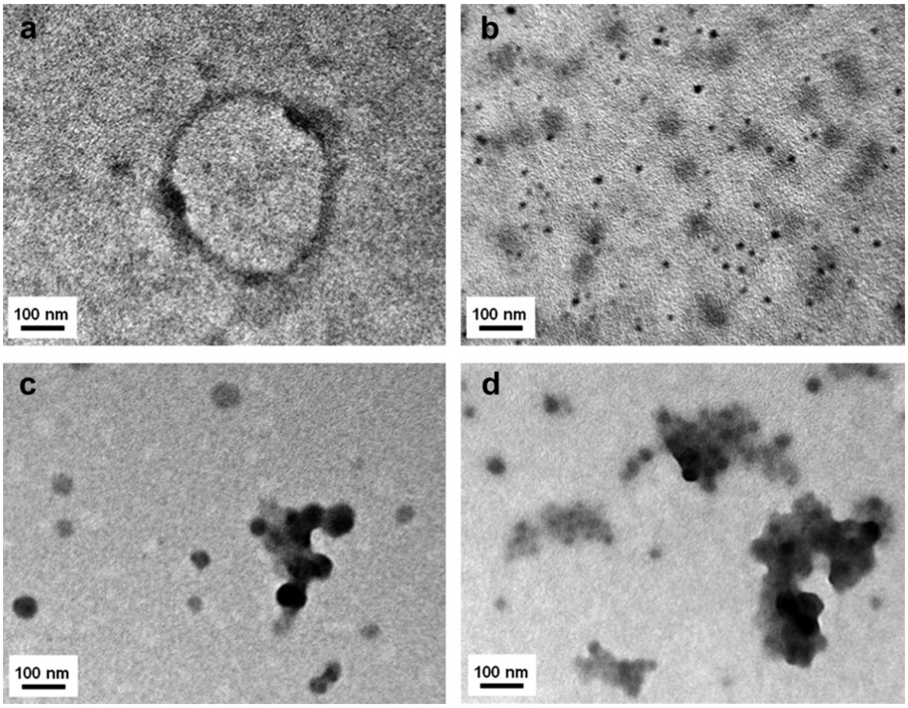

Fig. 1. TEM images of PEDOT latex nanoparticles formed under different reaction conditions (a) Reaction with only $Fe(OTs)_3$ for only 1 h, (b) PEDOT1, (c) PEDOT2, and (d) PEDOT3.

were generated from the micelles and the larger particles were originated from monomer droplets.

Unlike the PEDOT1, the PEDOT2 and PEDOT3 were prepared by using $Fe(OTs)_3$ and H_2O_2 bi-oxidant system to reach an even higher conversion. $Fe(OTs)_3$ and H_2O_2 were added simultaneously in the beginning of the reaction to produce PEDOT3, yet, a two-stage polymerization was carried out for the PEDOT2, where $Fe(OTs)_3$ was added in the beginning and the reaction was continued for 1 h before the addition of the H_2O_2 for the second-stage polymerization. Total reaction time for both systems was the same, 48 h. Although introducing H_2O_2 could help the Fe^{2+} ions back to Fe^{3+}, the newly generated Fe^{3+} ions on the particle surfaces had more powerful effect on neutralizing the negative surface charges than Fe^{2+} ions, causing some degree of coagulation among the colloidal nanoparticles. Fig. 1(c) and (d) presents the coagulation of latex particles in the PEDOT2 and PEDOT3, respectively. There was a more serious coagulation among particles in the PEDOT3 than PEDOT2, yet the size of single latex particle in the PEDOT3 was smaller than that in the PEDOT2. The SEM results in Fig. 3 presented the different degree of coagulation in the PEDOT2 and PEDOT3 as well.

The DLS results in Fig. 2 display the differences between the PEDOT2 and PEDOT3. The PEDOT3 had trimodal size distribution which centered at 40 nm, 480 nm, and 2780 nm, respectively. Since $Fe(OTs)_3$ and H_2O_2 in the PEDOT3 were added into the system simultaneously in the beginning, rapid polymerization and the Fenton reactions took place at the same time. The nucleation of polymer particles occurred rapidly from both monomer-swollen micelles and monomer droplets in a short time, accompanying with a serious coagulation among particles. On the other hand, an unimodal size distribution with an average size of 90 nm was observed for the PEDOT2 as shown in Fig. 2. The two-stage polymerization by introducing $Fe(OTs)_3$ and H_2O_2 in sequence moderated the entire polymerization rate. Lower polymerization rate in the beginning resulted in the higher coherence of droplets and micelles during the course of reaction. As a result, more uniform latex particles could be obtained in the end of polymerization.

The colloidal stability of latex particles was evaluated via zeta potential measurement. The results show that the PEDOT1 (−52 mV) and PEDOT2 (−52 mV) had higher zeta potentials than the PEDOT3 (−39 mV), indicating they had better dispersion properties. Fig. 4 compares the dispersion state of these three PEDOT latexes after resting for one week. The pictures shown in Fig. 4(a) revealed the color of PEDOT2 and PEDOT3 latexes was dark blue, yet PEDOT1 latex was sky blue due to its lower EDOT conversion. If the bottles were turned upside down, partial precipitation of PEDOT3 latex was observed at the bottom of the bottles, whereas PEDOT1 and PEDOT2 still maintained good colloidal stability. It suggests that not only the surfactant such as DBSA but also appropriate reaction conditions are required to ensure good dispersion properties of PEDOT particles in the water medium. Particularly, among three systems, the PEDOT2 latex had an excellent long-term stability even stored for several months.

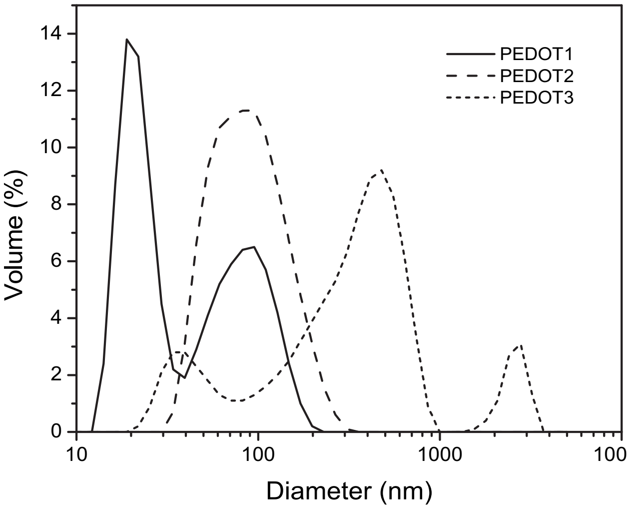

Fig. 2. Particle size distributions of PEDOT latex nanoparticles prepared from different reaction conditions.

3.3. Monomer conversions

After polymerization, the final latex product was a complex mixture, including surfactant, unreacted reactants, oligomers of EDOT, and PEDOT polymer. It is thus very difficult to determine the extent of reaction of EDOT monomer during and after polymerization especially due to the absence of a common organic solvent for PEDOT. The dialysis process by using the dialysis tube (MW cut off = 3500, flat width = 47 mm, purchased from Membrane Filtration Product Incorporation (MFPI)) had been attempted to remove substances with smaller molecular weights (unreacted monomer, EDOT oligomers, excess surfactant DBSA and $Fe(OTs)_3$). However, the residual DBSA and $Fe(OTs)_3$ doped on the PEDOT chains were not easy to be dedoped and detached from the PEDOT chains by the simple dialysis process. In this research, two different analytical methods, the gravimetric analysis and the UV–visible method, were used to determine the extent of reaction and the results were compared. In the method of gravimetric analysis, the PEDOT latex solution was dried directly in vacuum to exclude those vaporizable components such as water, unreacted monomer, and probably some DBSA and $Fe(OTs)_3$. After weighing, Conversion A, was then calculated using equation (1), as shown in Table 2. It was found that the PEDOT1 had the lowest conversion. The PEDOT2 and PEDOT3, with almost the same values, had much higher conversions than the PEDOT1. Since, the PEDOT1 was prepared by only $Fe(OTs)_3$ initiator, it suggests that hydrogen peroxide indeed participated in the polymerization and could greatly raise the conversion, even with the addition of a small amount of ferric ion.

Though gravimetric analysis could give an idea about the extent of reaction, it is a time-consuming process, which is not efficient for industrial fabrication. To determine the conversion of EDOT directly and instantly, a unique and simple method by using the technique of UV–visible spectrophotometry was developed in this research. By analyzing the spectra, quantitative analysis of monomer conversion could be achieved. In order to establish this analytical method, UV–visible absorption spectra of all components used in the emulsion polymerization system were recorded firstly, as displayed in Fig. 5. All the concentrations of species prepared in the water medium for recording their spectra were the same as those in the reaction systems except the EDOT monomer. For the EDOT monomer, the main absorption peak was located at 256 nm and was ascribed to the thiophene ring, accompanying with a weaker peak centered around 235 nm, in agreement with literature [44,45]. Both DBSA and $Fe(OTs)_3$ had the same strong absorption peak at 223 nm which was due to their substituted phenyl groups [46,47]. Only weak absorbances were observed in the range of 240–280 nm and 240–350 nm for DBSA and $Fe(OTs)_3$, respectively. On the other side, there was no obvious absorbance above 250 nm for the second oxidant H_2O_2. Thus, it can be assumed that the peak at 256 nm was mainly from the EDOT monomer and the decrease of absorbance value at 256 nm during the polymerization can be considered as the consumption of the EDOT monomer in the system.

Fig. 6 shows the UV–visible absorption spectra of reaction solutions with various concentrations of EDOT before polymerization.

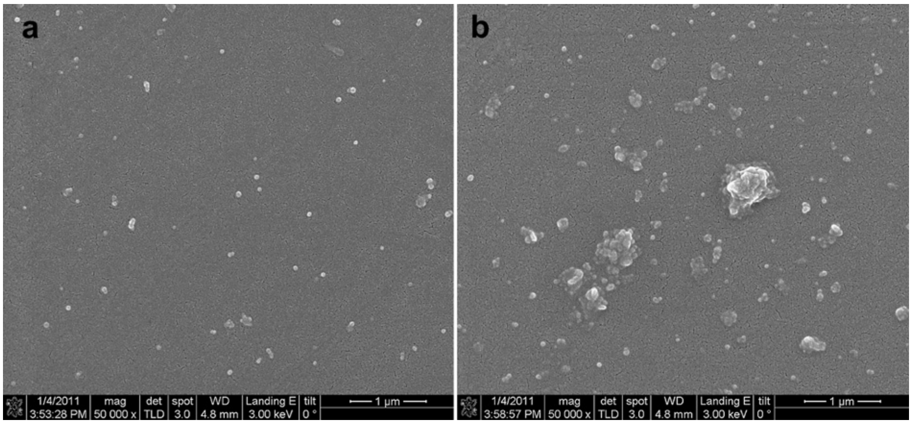

Fig. 3. The SEM images of PEDOT nanoparticles. (a) PEDOT2, (b) PEDOT3.

With the same concentrations of DBSA and Fe(OTs)$_3$, the absorbance signal at 256 nm increases linearly with the EDOT concentration from 5.8×10^{-6} M (curve 2) to 2.9×10^{-5} M (curve 6), as shown in the inset in Fig. 6. According to this monotonic increase of absorbance value at 256 nm, a calibration curve between the absorbance at 256 nm and the concentration of EDOT was then created. The overall absorbance at 256 nm could be described as follows:

$$A_{256} = A_{256}^{m} + A_{256}^{SI} \tag{8}$$

where A_{256} is the overall absorbance at 256 nm, A_{256}^{m} is the absorbance of the EDOT monomer at 256 nm, and A_{256}^{SI} is the subtotal absorbance of the surfactant (DBSA) and initiator (Fe(OTs)$_3$) at 256 nm since the weak absorbance from DBSA and Fe(OTs)$_3$ could not be excluded. Because the concentrations of surfactant and initiator (actually the OTs$^-$ counterpart) were constant during the polymerization, the decrease of absorbance at 256 nm could be referred to the decrease of monomer concentration. In other words, the slight change of monomer concentration during the polymerization can be monitored quantitatively via the UV–visible spectra with the help of the calibration curve. As long as the remaining amount of monomer was determined, the consumption amount and the conversion of the EDOT monomer were obtained.

The UV–visible absorption spectra of three final PEDOT latexes with the same dilution ratio are shown in Fig. 7. The strong absorption peaks of DBSA and Fe(OTs)$_3$ below 235 nm were cut to emphasize the intensity changes in monomer and polymer regions. Briefly, the PEDOT1 had a distinct and high absorption peak at 256 nm which means it had less monomer consumption and lower conversion than the PEDOT2 and PEDOT3. For the PEDOT2 and PEDOT3, with only weak peaks around 256 nm, broad absorption bands from 400 to 600 nm were observed, corresponding to the $\pi \rightarrow \pi^*$ electronic transition in the neutral PEDOT state [48–50]. In addition, the absorption peaks from 600 to 900 nm were characteristic of polaronic state in the doped PEDOT because of the doping of DBSA anions and p-tosylate ions [51–53]. By contrast, PEDOT1 exhibited weak absorbance over wavelength 300 nm, reflecting the lower degree of polymerization.

Since the UV–visible absorption spectra of the resulting latexes were obtained, the EDOT conversion of three latexes could be calculated via the calibration curve. However, the calculations became complicated when dealing with the PEDOT2 and PEDOT3. As seen in Fig. 7, besides the weak peak around 256 nm, a shoulder was found around 276 nm in the spectra. This shoulder might originate from other species and apparently would affect the overall signal at 256 nm, hence the equation (8) needed to be corrected while trying to calculate the conversions.

Considering the reaction products in the system, three more components might have contributed to the absorbance at 256 nm. The first and second are EDOT dimer and trimer. Numerous researches in recent years have been reported about the synthesis of dimer, trimer, and oligomers of thiophene or EDOT end-capped with mesitylthio, phenyl, or hexyl groups [54,55]. For instance, EDOT dimeric compound can be prepared via oxidative coupling of 2-lithio-ethylenedioxythiophene with CuCl$_2$ and EDOT trimeric compound was prepared through a Grignard reaction with the catalyst NiCl$_2$ [54]. EDOT dimer and trimer can also be synthesized by simply using protonic acids and some Lewis acids to catalyze an equilibrium reaction of EDOT, yielding dimer (25–50 wt.%) and trimer (5–15 wt.%) without further oxidation or polymerization [56].

Following their methods [56], we tried to synthesize the dimer and trimer and record their spectra for comparison. Fig. 8(a) shows the UV–visible spectra of the EDOT dimer and timer produced in the aqueous solution by catalyzing the EDOT with nitric acid and

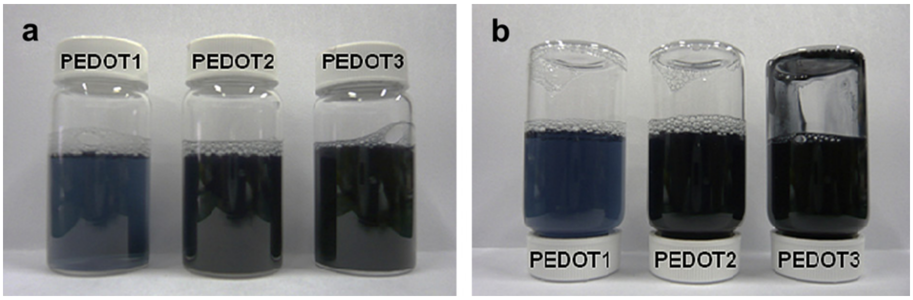

Fig. 4. The dispersion state of PEDOT latexes after resting for one week. (a) The appearance of three PEDOT latexes, (b) certain degree of precipitation occurred in the PEDOT3 latex but not in the PEDOT1 and PEDOT2 when bottles were turned upside down.

Table 2
Conversion of EDOT monomer after polymerization determined by gravimetric analysis (Conversion A) and UV–visible method (Conversion B).

Sample	Conversion A (%)	Conversion B (%)
PEDOT1	13.7	23.6
PEDOT2	77.1	75.0
PEDOT3	77.5	74.3

sulfuric acid at 4 °C for two weeks. In the acidic environment of nitric acid, partial EDOT was dimerized and trimerized, where the absorption peaks of dimer and trimer were found to be located at 303 nm and 350 nm, respectively. In the case of sulfuric acid, merely trimerized EDOT was observed and its absorbance peak was also located at 350 nm. The observed peaks of monomer (256 nm), dimer (303 nm) and trimer (350 nm) are close to the respective absorption peaks (261, 322, and 400 nm) reported in the previous literatures [44,54,57]. The blue shift in our system is caused by the differences in the surrounding medium (water instead of CH_2Cl_2) and their end-capped groups.

The third component was the oxidized EDOT monomer due to the Fe^{3+}/H_2O_2 system used in this study. In the petroleum and coal industries, the Fenton agent is widely applied in the desulphurization process [58,59]. As a good catalyst for the decomposition of H_2O_2, the Fe^{2+} can accelerate the formation of hydroxyl radical ($OH^{\bullet}$), as described in equation (2). The strong hydroxyl radical may not only oxidize the rest of Fe^{2+} but also attack the thiophene ring of EDOT. This so-called “oxidative desulphurization (ODS)” process is believed to undertake, where partial thiophene ring of EDOT in the system was oxidized into the corresponding sulfone (1,1-dioxide) product during the polymerization [60]. The oxidation reaction process of the thiophene ring can be presented as:

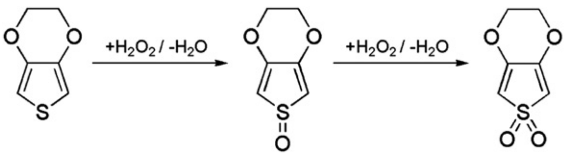

(9)

In addition, Nakayama and coworkers [61] had synthesized and isolated thiophene 1,1-dioxide successfully. It had a bimodal absorption curve in the UV–visible spectrum with $CHCl_3$ as the solvent. One peak coming from the absorption of thiophene ring was centered at 245 nm and the other peak, resulting from the sulfone structure, was centered at 288 nm. This peak of sulfone structure at 288 nm is also close to our monomer peak (256 nm). Accordingly, we believe the absorption peak caused by the oxidized thiophene ring of EDOT would need to be regarded when we modify the equation (8). Furthermore, if the thiophene ring had been oxidized to have the sulfone structure, the original planarity of thiophene ring would be hampered. Those EDOT monomers with twisted structure might participate in the polymerization and the conductivity of thus-synthesized PEDOT would be decreased.

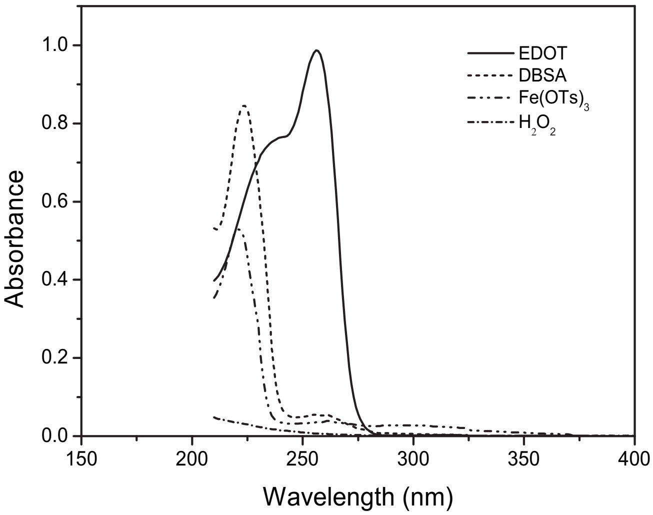

Fig. 5. UV–visible absorption spectra of all components used in the emulsion polymerization of PEDOT.

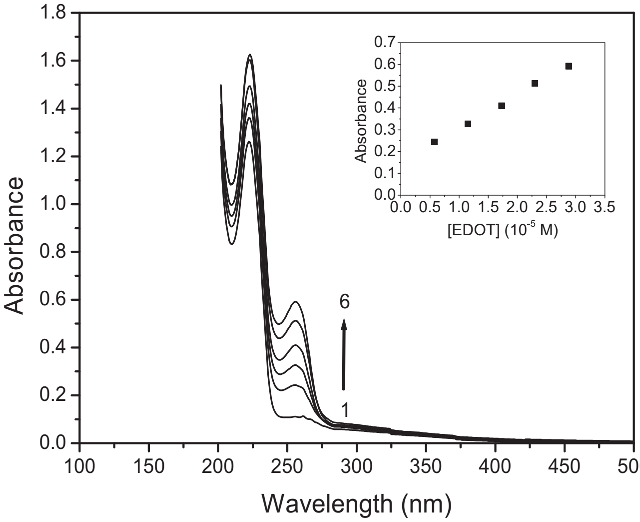

Fig. 6. UV–visible absorption spectra of the reaction solutions formulated with various amounts of EDOT monomer. The curves from 1 to 6 indicate the increasing added EDOT amount with the same concentrations of DBSA and $Fe(OTs)_3$: 1 (0 mL), 2 (0.04 mL), 3 (0.08), 4 (0.12 mL), 5 (0.16 mL), and 6 (0.2 mL). Inset shows the linear relation of the measured absorbance at 256 nm with different EDOT concentrations.

To confirm the above deduction, EDOT was treated with diluted hydrogen peroxide solution for several days to induce partial oxidation that would produce the sulfone structure. Fig. 8(b) shows the UV–visible absorption spectrum of partial oxidized EDOT

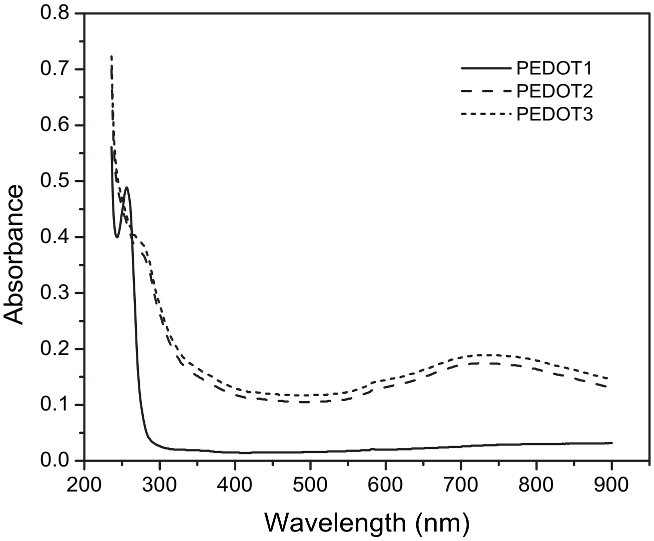

Fig. 7. UV–visible absorption spectra of PEDOT latexes prepared from different reaction conditions.

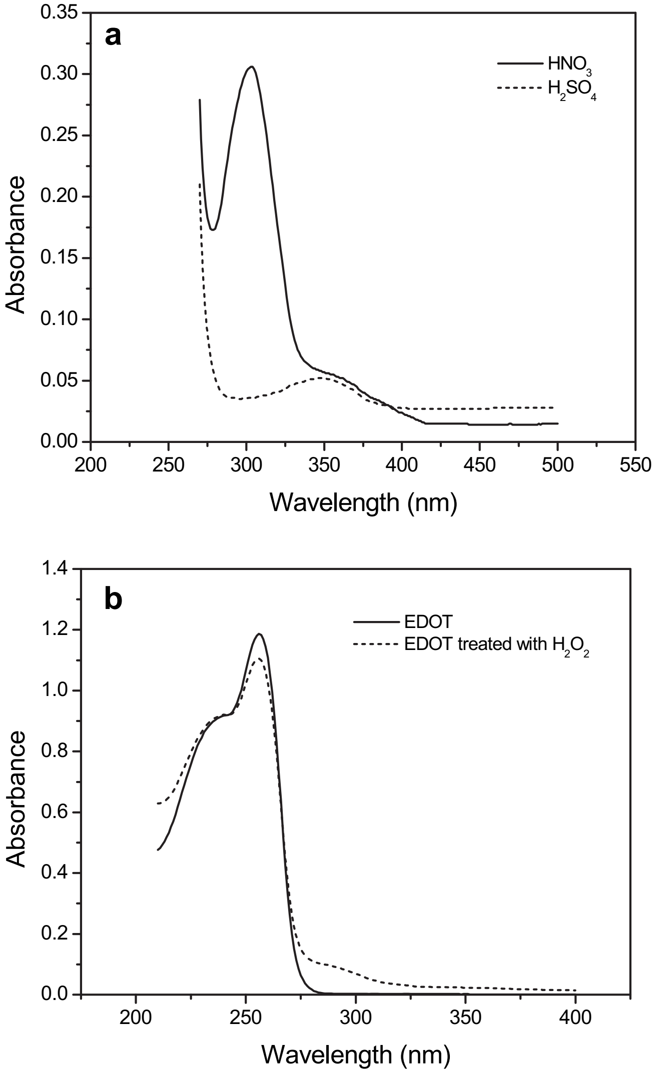

Fig. 8. UV–visible absorption spectra of (a) the EDOT dimer and trimer produced by catalyzing the EDOT with nitric acid and sulfuric acid, (b) the partial oxidized EDOT monomer.

monomer, clearly, a small peak at 276 nm was indeed observed in the spectrum, when comparing to the spectrum of pure EDOT monomer. In conclusion, Fig. 8(b) proved that some thiophene rings of EDOT monomers were oxidized into the sulfone compound in the Fe^{3+}/H_2O_2 bi-oxidant system used in this present study.

Because the UV–visible absorption peak of the dimer, trimer, and the oxidized EDOT might overlap with the absorption peak of EDOT monomer at 256 nm, the presentation of overall absorbance at 256 nm in equation (8) should be modified into a general form:

$$A_{256} = A^{m}_{256} + A^{SI}_{256} + A^{sulfone}_{256} + A^{d}_{256} + A^{t}_{256} \qquad (10)$$

Table 3
The parameters of EDOT monomer, dimer, trimer, and oxidized monomer for the simulation.

Species	Monomer	Dimer	Trimer	Oxidized monomer
Peak wavelength (nm)	236, 258.5	303	350	276
Simulated absorption range (nm)	190–285	263–343	310–390	216–336

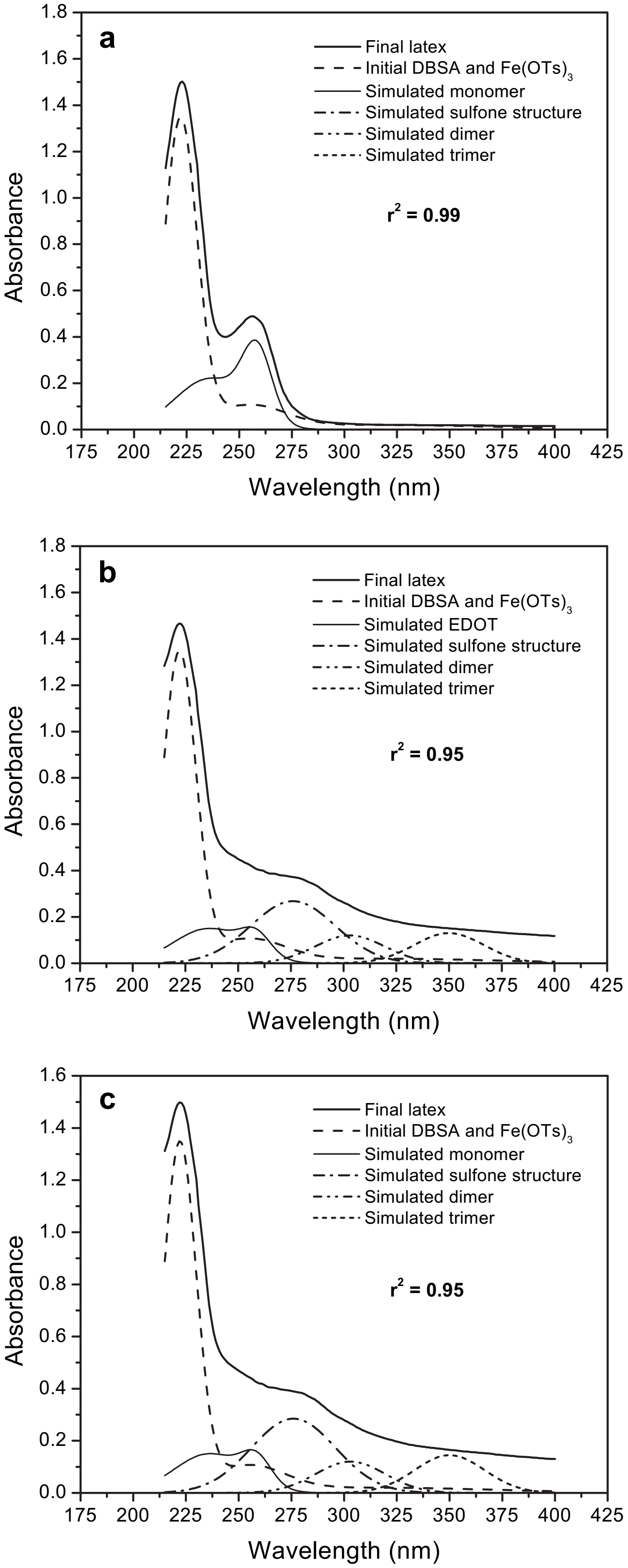

Fig. 9. Simulation of UV–visible absorption spectra of the PEDOT latexes (a) PEDOT1, (b) PEDOT2, and (c) PEDOT3. There are no dimer, trimer, and sulfone structure observed in the PEDOT1 (a).

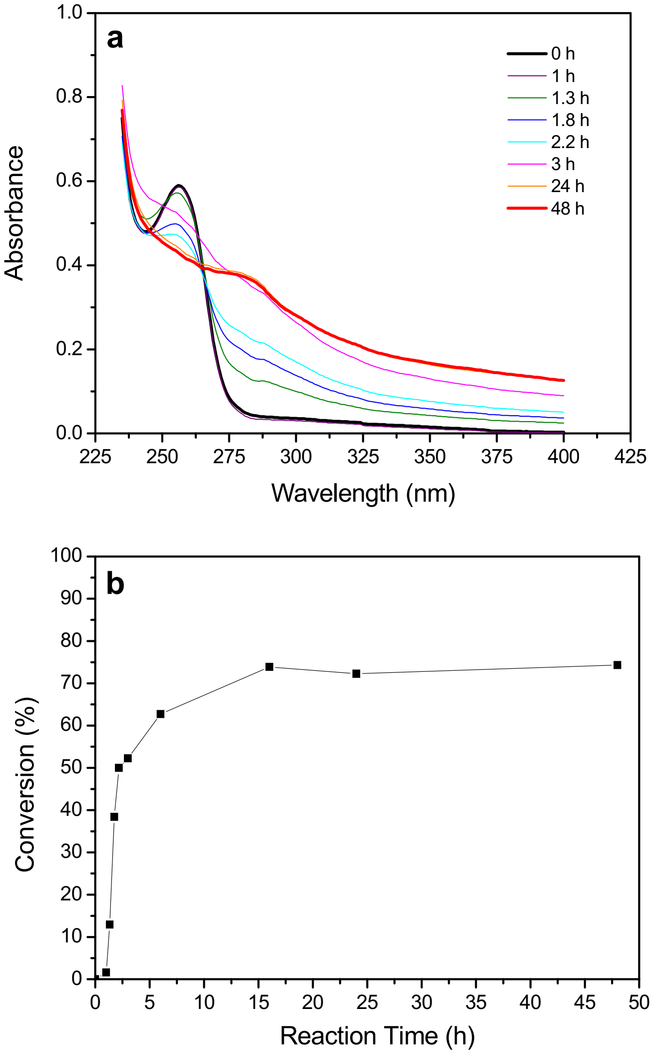

Fig. 10. The polymerization of EDOT for PEDOT2 (a) the evolution of UV–visible curve with reaction time, (b) the EDOT monomer conversion versus reaction time.

where $A^{sulfone}_{256}$ is the contribution of the absorbance at 256 nm from the sulfone group, A^{d}_{256} is the contribution from the dimer, and A^{t}_{256} is the contribution from the trimer. In order to identify the contribution of each component to the absorbance at 256 nm in equation (10), soft program PeakFit 4.11 was applied to isolate and simulate the spectra. Gaussian amplitude distribution was chosen to simulate the absorption curves for all components. According to the previous results in Figs. 5 and 8, the parameters of all components for simulation could be obtained and listed in Table 3.

Fig. 9(a)–(c) displays the computer simulations of three PEDOT latexes. The absorbances of DBSA and $Fe(OTs)_3$ were assumed unchanging during polymerization. The analyzed wavelength interval was in the range between 215 and 400 nm. The absorption curves of the residual EDOT, dimer, trimer, and oxidized thiophene ring in Fig. 9 were simulated according to the parameters in Table 3. From the simulation results in Fig. 9(a), only DBSA, $Fe(OTs)_3$, and EDOT absorptions were observed. There were no apparent dimer, trimer, and sulfone found in the PEDOT1 sample. On the other hand, besides those absorptions observed in PEDOT1, the dimer, trimer, and sulfone absorptions were observed in the spectra of PEDOT2 and PEDOT3.

From the simulation results, Fig. 9, the contribution to the absorbance at 256 nm from dimer and trimer was found negligible, thus equation (10) could be further simplified as:

$$A_{256} = A^{m}_{256} + A^{SI}_{256} + A^{sulfone}_{256} \tag{11}$$

In other words, once the $A^{sulfone}_{256}$ value was determined from simulation, the effect of sulfone structure on the A_{256} could be eliminated and the real absorption of $(A^{m}_{256} + A^{SI}_{256})$ was obtained. Thus, the remaining monomer concentration in the final latex was then found via the calibration curve (Fig. 6), and the conversion was finally calculated. For example, there is no $A^{sulfone}_{256}$ found in the PEDOT1, the ratio of monomer EDOT left in the final latex would be calculated as 76.4% by simply comparing the A_{256} with calibration curve. In other words, there are 23.6% of EDOT consumed during the polymerization, which means the conversion of PEDOT1 is 23.6%. For PEDOT2, due to the existence of $A^{sulfone}_{256}$, the real absorption $(A^{m}_{256} + A^{SI}_{256})$ for PEDOT2 is $(A_{256} - A^{sulfone}_{256})$. Comparing $(A_{256} - A^{sulfone}_{256})$, i.e. $(A^{m}_{256} + A^{SI}_{256})$, with the calibration curve, there are 25.0% of monomer left in the latex, which means the conversion of PEDOT2 is 75.0%. Similarly, the conversion of PEDOT3 is 74.3% after calculation. These conversions obtained from the UV–visible spectra, Conversion B, are listed in Table 2 and compared with the gravimetric method. Generally speaking, the trend of Conversion B values in three PEDOT samples are in good agreement with the Conversion A, verifying the efficacy of this method.

The establishment of UV–visible absorption spectra method offers a quick and easy way to determine the conversion of EDOT monomer quantitatively with good accuracy. This method can be widely applied for practical use if samples are drawn out from the

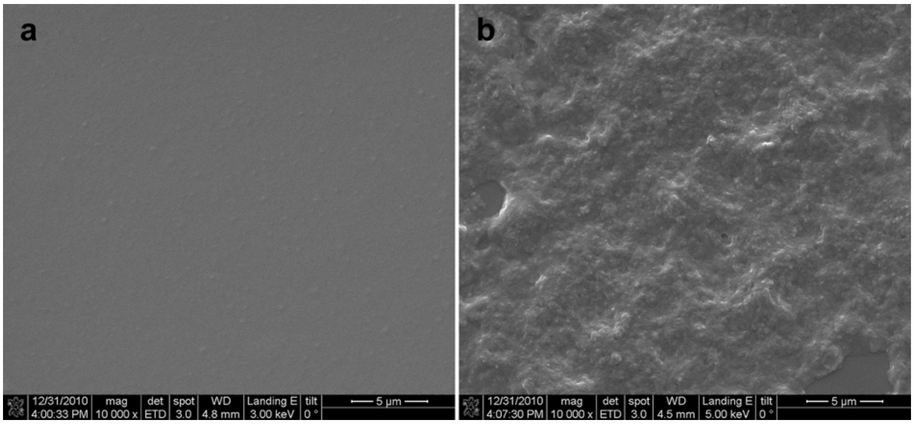

Fig. 11. The SEM images of PEDOT film. (a) PEDOT2, (b) PEDOT3.

reaction solution at different times. Fig. 10(a) showed the UV–visible spectra of the latex PEDOT2 at different reaction times. Only the wavelength ranged from 235 to 400 nm were displayed to emphasize the intensity changes near monomer region. As seen in figure, the absorbance at 256 nm did not decrease much at the first-stage polymerization, but decreased with time obviously after H_2O_2 was added (second-stage polymerization). In the mean time, when H_2O_2 was added in, the absorbance around 276 nm (sulfone structure) immediately turned up and grew with time. By using the computer simulations and comparing with calibration curve, the EDOT conversions at different reaction times were calculated, as demonstrated in Fig. 10(b). Based on the simulation results, less than 2% of EDOT were consumed in the first-stage polymerization, and the conversion began to level off after 16 h.

The conductivity of the PEDOT latex films was evaluated by a standard four-point probe method. The conductivity of the PEODT film increased significantly from 10^{-2} S/cm for PEDOT1 to 6.3 S/cm for PEDOT2 and 4.3 S/cm for PEDOT3. Without the second oxidative agent H_2O_2, cracks were observed in the PEDOT1 film and the surface was not continuous because of its low conversion and low degree of polymerization. For PEDOT2 and PEDOT3, the film integrity was greatly enhanced. Comparing PEDOT2 with PEDOT3, the more uniform particle size distribution of PEDOT2 led to a more uniform film with smoother surface, as the SEM images shown in Fig. 11. And the conductivity of PEDOT2 was higher.

4. Conclusions

In summary, conducting PEDOT latex nanoparticles were prepared by emulsion polymerization using the bi-oxidant system, $Fe(OTs)_3$ and H_2O_2. With its oxidative activity, H_2O_2 could regenerate Fe^{3+} that oxidized EDOT again and thus increased the conversion, even though the feeding amount of Fe^{3+} was insufficient. The addition of second oxidant H_2O_2 could largely decrease the added amount of iron salt, increase the conversion, and improve the colloidal stability. Stable PEDOT latex nanoparticles with diameters around 100 nm could be obtained when $Fe(OTs)_3$ and H_2O_2 were added in sequence. For determining the EDOT monomer conversion, a method based on the UV–visible absorption spectra was firstly established. By using curve-fitting to resolve the UV–visible spectrum of the final latex dispersion, individual spectrum of the respective species could be revealed, including unreacted EDOT monomer, the DBSA surfactant, the $Fe(OTs)_3$ initiator, the dimer, the trimer, and most importantly, the EDOT sulfone product produced by H_2O_2 oxidation. From the deconvolution of UV–visible spectra curves, the conversion of PEDOT latex could be calculated and found to be 74–75%. The establishment of UV–visible method offers a quick and easy approach to the quantitative determination of the EDOT conversion. Finally, the conductivity of the uniform PEDOT latex film, PEDOT2, was obtained as 6.3 S/cm.

References

[1] Shirakawa H, Louis EJ, MacDiarmid AG, Chiang CK, Heeger AJ. J Chem Soc Chem Commun 1977;16:578–80.
[2] Chiang CK, Fincher CR, Park YW, Heeger AJ, Shirakawa H, Louis EJ, et al. Phys Rev Lett 1977;39:1098–101.
[3] Li XG, Huang MR, Duan W. Chem Rev 2002;105:2925–3030.
[4] Liao YZ, Li XG, Kaner RB. ACS Nano 2010;4:5193–202.
[5] Li XG, Li A, Huang MR. Chem Eur J 2008;14:10309–17.
[6] Jonas F, Schrader L. Synth Met 1991;41:831–6.
[7] Groenendaal L, Jonas F, Freitag D, Pielartzik H, Reynolds JR. Adv Mater 2000; 12:481–94.
[8] Kirchmeyer S, Reuter K. J Mater Chem 2005;15:2077–88.
[9] Bayer AG. Eur Patent 1988;339,340.
[10] Heywang G, Jonas F. Adv Mater 1992;4:116–8.
[11] Welsh DM, Kumar A, Meijer EW, Reynolds JR. Adv Mater 1999;11:1379–82.
[12] Huang F, MacDiarmid AG. Appl Phys Lett 1997;71:2415–7.
[13] Zhang F, Mammo W, Andersson LM, Admassie S, Andersson MR, Inganäs O. Adv Mater 2006;18:2169–73.
[14] Jonas F, Krafft W, Muys B. Macromol Symp 1995;100:169–73.
[15] Jeon SS, Han SI, Jin YH, Im SS. Synth Met 2005;148:287–91.
[16] Meskers SCJ, van Duren JKJ, Janssen RAJ, Louwet F, Groenendaal L. Adv Mater 2003;15:613–6.
[17] Yoon H, Chang M, Jang J. Adv Funct Mater 2007;17:431–6.
[18] Pei Q, Zuccarello G, Ahlskog M, Inganäs O. Polymer 1994;35:1347–51.
[19] Yamamoto T, Abla M. Synth Met 1999;100:237–9.
[20] Sotzing GA, Reynolds JR, Steel PJ. Adv Mater 1997;9:795–8.
[21] Huang J, Miller PF, Wilson JS, de Mello AJ, de Mello JC, Bradley DDC. Adv Funct Mater 2005;15:290–6.
[22] de Leeuw DM, Kraakman PA, Bongaerts PFG, Mutsaers CMJ, Klaassen DBM. Synth Met 1994;66:263–73.
[23] Chen JH, Dai CA, Chiu WY. J Polym Sci Part A Polym Chem 2008;46:1662–73.
[24] Kumar A, Reynolds JR. Macromolecules 1996;29:7629–30.
[25] Lei Y, Oohata H, Kuroda SI, Sasaki S, Yamamoto T. Synth Met 2005;149:211–7.
[26] Choi JW, Han MG, Kim SY, Oh SG, Im SS. Synth Met 2004;141:293–9.
[27] Mumtaz M, Cuendias AD, Putaux JL, Cloutet E, Cramail H. Macromol Rapid Commun 2006;27:1446–53.
[28] Dai CA, Chang CJ, Chi HY, Chien HT, Su WF, Chiu WY. J Polym Sci Part A Polym Chem 2008;46:2536–48.
[29] Pron A, Genoud F, Menardo C, Nechtschein M. Synth Met 1988;24:193–201.
[30] Lee SJ, Lee JM, Cheong IW, Lee H, Kim JH. J Polym Sci Part A Polym Chem 2008;46:2097–107.
[31] Liu CF, Moon DK, Maruyama T, Yamamoto T. Polym J 1993;25:775–9.
[32] Liu CF, Maruyama T, Yamamoto T. Polym J 1993;25:363–72.
[33] Moon DK, Ezuka M, Maruyama T, Osakada K, Yamamoto T. Macromolecules 1993;26:364–9.
[34] Sun Z, Geng Y, Li J, Jing X, Wang F. Synth Met 1997;84:99–100.
[35] Sun Z, Geng Y, Li J, Wang X, Jing X, Wang F. J Appl Polym Sci 1999; 72:1077–84.
[36] Svoboda J, Bláha M, Sedláček J, Vohlídal J, Balcar H, Mav-Golež I, et al. Acta Chim Slov 2006;53:407–16.
[37] Wang H, Park SM. Anal Chem 2007;79:240–5.
[38] Ayad MM, Zaki EA. J Appl Polym Sci 2008;110:3410–9.
[39] Jung YJ, Lee JM, Cheong IW, Kim JH. Macromol Symp 2007;249-250:265–9.
[40] Jung YJ, Lee SJ, Choi SW, Kim JH. J Polym Sci Part A Polym Chem 2008;46:5968–75.
[41] Lee JM, Lee SJ, Jung YJ, Kim JH. Curr Appl Phys 2008;8:659–63.
[42] Teel AL, Finn DD, Schmidt JT, Cutler LM, Watts RJ. J Environ Eng 2007; 133:853–8.
[43] Kremer ML. J Phys Chem A 2003;107:1734–41.
[44] Turbiez M, Frère P, Allain M, Gallego-Planas N, Roncali J. Macromolecules 2005;38:6806–12.
[45] Li XG, Li J, Meng QK, Huang MR. J Phys Chem B 2009;113:9718–27.
[46] Wakizaka D, Fushimi T, Ohkita H, Ito S. Polymer 2004;45:8561–5.
[47] Smith RR, Smith AP, Stricker JT, Taylor BE, Durstock MF. Macromolecules 2006;39:6071–4.
[48] Huh PH, Kim SC, Kim YH, Kumar J, Kim BS, Jo NJ, et al. Polym Eng Sci 2007; 47:71–5.
[49] Jang J, Chang M, Yoon H. Adv Mater 2005;17:1616–20.
[50] Li XG, Li J, Huang MR. Chem Eur J 2009;15:6446–55.
[51] Sikora T, Marcilla R, Mecerreyes D, Rodriguez J, Pomposo JA, Ochoteco E. J Polym Sci Part A Polym Chem 2009;47:306–9.
[52] Nagarajan S, Kumar J, Bruno FF, Samuelson LA, Nagarajan R. Macromolecules 2008;41:3049–52.
[53] Yang Y, Jiang Y, Xu J, Yu J. Polymer 2007;48:4459–65.
[54] Turbiez M, Frère P, Roncali J. J Org Chem 2003;68:5357–60.
[55] Turbiez M, Frère P, Allain M, Videlot C, Ackermann J, Roncali J. Chem Eur J 2005;11:3742–52.
[56] H. C. Starck GmbH. Eur Patent 20021;375,560.
[57] Perepichka IF, Roquet S, Leriche P, Raimundo JM, Frère P, Roncali J. Chem Eur J 2006;12:2960–6.
[58] Hulea V, Fajula F, Bousquet J. J Catal 2001;198:179–86.
[59] Li H, Zhu W, Wang Y, Zhang J, Lu J, Yan Y. Green Chem 2009;11:810–5.
[60] Dai Y, Qi Y, Zhao D, Zhang H. Fuel Process Technol 2008;89:927–32.
[61] Nagasawa H, Sugihara Y, Ishii A, Nakayama J. Bullet Chem Soc Jpn 1999; 72:1919–26.

Polymer 52 (2011) 1385–1390

Contents lists available at ScienceDirect

Polymer

journal homepage: www.elsevier.com/locate/polymer

Memory effect in polymer brushes containing pendant carbazole groups

Yuyan Wei [a], Dazhi Gao [a], Liang Li [a,c,*], Songmin Shang [b,**]

[a] Key Laboratory for Green Chemical Process of Ministry of Education, School of Materials Science and Engineering, Wuhan Institute of Technology, Wuhan 430073, PR China
[b] Institute of Textiles and Clothing, The Hong Kong Polytechnic University, Hong Kong, PR China
[c] State Key Laboratory of Coordination Chemistry, Nanjing University, Nanjing 210093, PR China

ARTICLE INFO

Article history:
Received 25 September 2010
Received in revised form
4 January 2011
Accepted 24 January 2011
Available online 1 February 2011

Keywords:
Polymer brushes
Memory effect
Atom transfer radical polymerization

ABSTRACT

Poly(9-(2-(4-vinyl(benzyloxy)ethyl)-9H-carbazole)) (PVBEC) brushes, have been successfully prepared on the silicon surfaces via surface-initiated atom transfer radical polymerization (ATRP). Conductance switching at a voltage of about −2.1 V is observed in the memory device based on the PVBEC brushes. The fabricated device shows the good memory characteristics as the ON/OFF current ratio up to 10^5, and enduring 10^6 read cycles under −1 V pulse voltages. Compared with those of the conventional Si/PVBEC/Al device fabricated by spin-coating, the switch voltage is lower and the ON/OFF current ratio is higher in the volatile Si-g-PVBEC/Al memory device.

1. Introduction

During the decades, considerable attention has been paid to fabricate different functions of electronic devices using small molecular and polymer materials [1–3]. Several types of organic and polymeric electronics, including light-emitting diodes, thin-film transistors, lasers, photovoltaic cells, switches and memories have been realized for practical device application [4–7]. Recently, as one of the emerging memory technologies, the polymer memory device, with a typical configuration of polymer active materials sandwiched between two electrodes, has received increasing interest due to their material variety and advantageous properties such as simple structure, light weight, good scalability, low cost and large-capacity data storage [8–12]. Memory devices based on inorganic materials store and retrieve data based on the amount of charge stored in the device. However, polymer memory devices store data in another form, for instance, based on the electrical bistability in response to an applied electric field [11]. Rewritable-type memory and write-once read-many-times (WORM)-type memory based on polymeric materials have been demonstrated [13,14]. Conductive polymers doped with gold nanoparticles, polyelectrolytes, dendritic polymers, and organic donor–acceptor complexes, have been reported to fabricate the sandwich structured memory devices and exhibit good memory performances [15–18].

Compatibility at an organic–inorganic interface is particularly important for future electronic applications. Incompatibility between inorganic electrodes with organic thin films is a problem commonly encountered in the fabrication of high performance and stable photovoltaic cells and organic light-emitting devices [19,20]. It may lead to the delamination of the spin-coated or vacuum-sublimated organic layer and a high resistance in such device [21]. Until now, polymer active materials are usually deposited by ink-jet printing, spin-coating or vacuum evaporation on a variety of metal, metal oxide and inorganic substrates in the fabrication of memory devices [22–24]. Most of the researchers have focused on the improvement of the interfacial contact between the inorganic electrode and the organic film by chemisorption or covalent attachment of functional groups, such as carboxylic acid and alkanethiols, surface cleaning/pretreatment by a base or plasma, and intercalation of a thin film, such as that of poly(3,4-ethylene dioxythiophene) doped with poly(4-styrenesulfonate), between the inorganic electrode and the active organic material [25–27].

Tethering of polymer brushes on a solid substrate is an effective method of modifying the surface properties of the substrate [28–36]. Consequently, it is expected that the problems associated with the inorganic substrate/organic polymer interface should be minimized if the polymer film is covalently attached to the inorganic surface. With the progress in polymer chemistry, it is possible to prepare the graft polymer chains on various substrate surfaces by different polymerization methods. Surface-initiated polymerization has been utilized to functionalize the conducting transparent

---

* Corresponding author. Key Laboratory for Green Chemical Process of Ministry of Education, School of Materials Science and Engineering, Wuhan Institute of Technology, Wuhan 430073, PR China. Tel./fax: +86 27 87195661.
** Corresponding author. Tel./fax: +86 27 87195661.
E-mail addresses: msell08@163.com (L. Li), tcshang@inet.polyu.edu.hk (S. Shang).

0032-3861/$ – see front matter © 2011 Elsevier Ltd. All rights reserved.
doi:10.1016/j.polymer.2011.01.044

electrode, indium tin oxide (ITO) with polyvinylcarbazole brushes [37]. Among them, surface-initiated atom transfer radical polymerization (ATRP) has provided a unique tool for the preparation of well-defined polymer brushes on various substrates, in the form of well-defined polymer–inorganic hybrids, for various applications. In this work, polymer brushes containing pendant carbazole, tethered directly on the Si surface, have been prepared by surface-initiated ATRP and the memory behaviors are first observed in the polymer brushes. Conductance switching, with an ON/OFF current ratio up to 10^5, is observed in a polymer memory device fabricated from Si with surface-grafted polymer brushes with pendant carbazole.

2. Experiment

2.1. Preparation of polymer brushes

The silicon wafer doped lightly as n-type was sliced into the chips of 1 × 2 cm in size. The chips were immersed in 10 vol% HF to remove the oxide film and to leave behind a uniform H-terminated Si surface (the Si–H surface) [38,39]. According to the detailed procedure reported by Xu et al. [28], the surface initiators for ATRP were immobilized via UV-induced coupling of 4-vinylbenzyl chloride (VBC) with the Si–H surface to give rise to a covalently bonded (Si–C bonded) monolayer (the Si–VBC surface). The process is shown schematically in Fig. 1. The synthesis of the monomer, 9-(2-(4-vinyl (benzyloxy)ethyl)-9H-carbazole) (VBEC), has already been reported in the literature [40]. For the preparation of the VBEC polymer (PVBEC) brushes on the Si–VBC surface via surface-initiated ATRP, VBEC (0.5 g or 1.53 mmol), CuCl (4 mg or 0.05 mmol), $CuCl_2$ (1 mg or 0.007 mmol) and N,N,N′,N″,N″-pentamethyldiethylenetriamine (PMDETA) (50 μL or 0.24 mmol) were added to 5 mL of dry toluene in a Pyrex® tube containing the Si–VBC chip. The reaction mixture was stirred and degassed with argon for 30 min. The reaction was allowed to proceed at 100 °C for 24 h to produce a Si chip with surface-grafted PVBEC (Si-*g*-PVBEC). The Si-*g*-PVBEC chip was washed and extracted thoroughly with excess toluene and tetrahydrofuran.

2.2. Instruments

The chemical compositions of the modified Si surfaces were determined by X-ray photoelectron spectroscopy (XPS) on a Kratos AXIS Ultra spectrometer. The static water contact angles were measured by the sessile drop method, using a 3 μL water droplet, in a telescopic goniometer (Rame–Hart model 100-00230). For each angle reported, at least three measurements from different surface locations were averaged. The thickness of the polymer brushes grafted on the silicon substrate was determined by ellipsometry at incident angles of 70° and 75° in the wavelength range 200–1000 nm. For each sample, the thickness measurements were made on atleast four different surface locations. Data were recorded and processed with the WVASE32 software package. The topography of the modified Si surfaces was studied by atomic force microscope (AFM). An area of 5 × 5 μm^2 was scanned using the tapping mode. The arithmetic mean of the surface roughness (R_a) reported was calculated from the roughness profile determined by AFM.

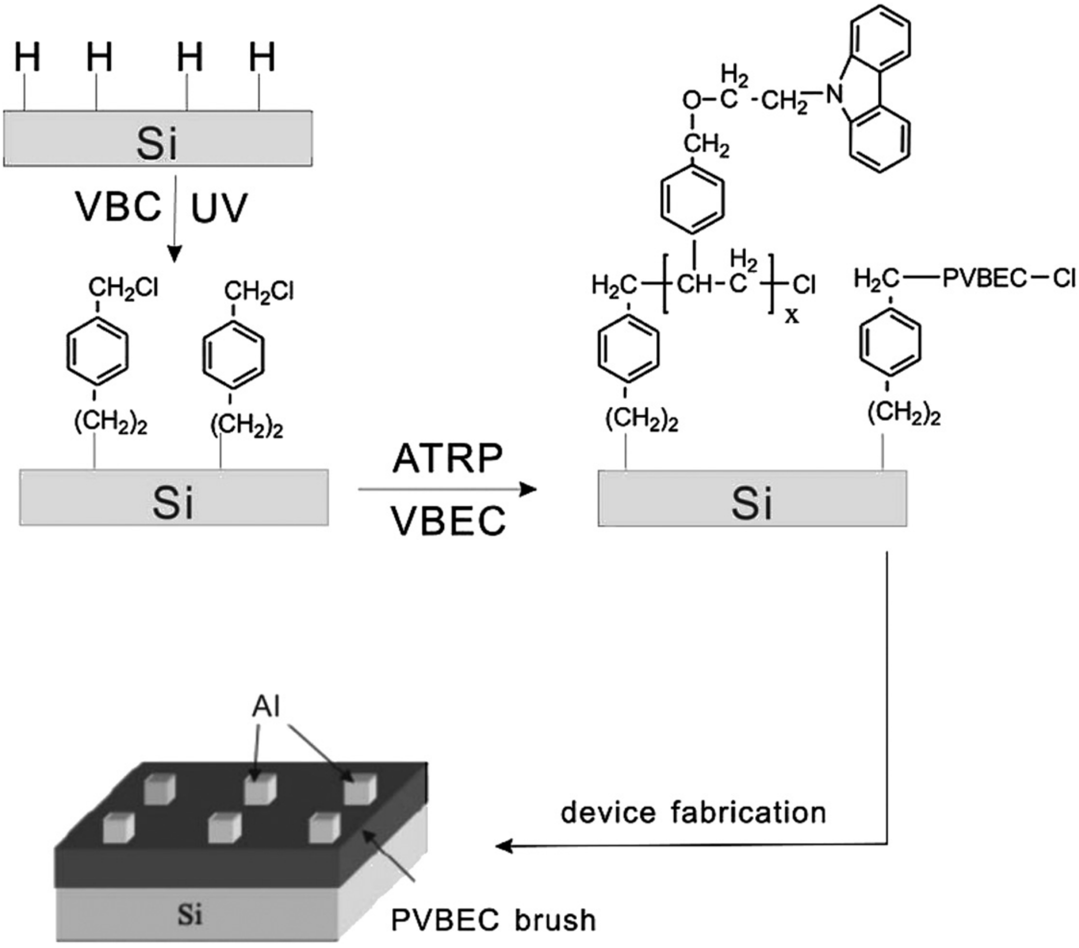

Fig. 1. Schematic diagram illustrating the preparation of the polymer device.

2.3. Fabrication of the device

Aluminum top electrodes (about 120 nm in thickness) were thermally evaporated onto the Si-*g*-PVBEC chips at about 10^{-6} Torr through a shadow mask with different area. For comparison, another device, with the structure of Si/PVBEC/Al, was prepared by spin-coating a 10 mg/ml chloroform solution of PVBEC onto a clean Si chip. All electrical measurements of the device were carried out using an HP 4145B semiconductor parameter analyzer under ambient conditions.

3. Results and discussion

The chemical composition of the silicon surfaces at various stages of surface modification is determined by XPS. No signal attributable to Cl is discernable in Cl 2p core-level spectrum of the pristine Si surface (Fig. 2a). For the preparation of polymer brushes on the silicon surface, a uniform and dense monolayer of initiators immobilized on the silicon surface is necessary. The initiators are immobilized via UV-induced coupling of VBC on the Si—H surface to give rise to a stable initiator monolayer via the Si—C bonds [28]. Fig. 2b shows the corresponding Cl 2p core-level spectrum of the Si—VBC surface. The Cl 2p core-level spectrum in Fig. 2d consists of the Cl $2p_{3/2}$ and Cl $2p_{1/2}$ peak components at the BE's of about 199.3 and 201.5 eV, respectively, attributable to the covalently bonded chlorine species [41]. The immobilization of the ATRP initiator is also accompanied by a change in static water contact angle of the Si surface. The static water contact angle of the pristine (oxide-covered) Si surface is about 20°. The water contact angles for the Si—H surface and the Si—VBC surface are about 70° and 85°, respectively.

The presence of grafted PVBEC on the Si—VBC surface is further confirmed by XPS analysis. As shown in Fig. 1c, the C 1s core-level spectrum of the Si-*g*-PVBEC surface can be curve-fitted with three peak components with BEs at about 284.6, 285.4 and 286.2 eV, attributable to the C—H, C—N, C—O species [42], respectively. Moreover, the area ratio of the above three peak components is about 16.8:2.9:2.0, which is in agreement with the theoretical ratio of 18:3.0:2.0 for PVBEC homopolymer. The appearance of a distinct N 1s signal at about 399 eV [42] in Fig. 1d is also consistent with the successful graft polymerization of VBEC from the Si—VBC surface. The thickness of the polymer brushes grafted on the Si substrates is about 20 nm after an ATRP time of 24 h. The static water contact angle of the Si-*g*-PVBEC surface is about 95°, which is comparable to that of the PVBEC homopolymer film.

The changes in topography of the Si surface after surface-initiated ATRP are investigated by AFM. Fig. 3a,b show the representative AFM images of the Si—VBC surface and the Si-*g*-PVBEC surfaces, respectively. The Si—VBC surface remains molecularly uniform with a root-mean-square surface roughness (R_a) of about 0.29 nm. After surface graft polymerization of VBEC via ATRP, the R_a value has increased slightly to about 1.5 nm. The only slight change in the R_a value indicates that the surface-initiated ATRP has proceeded uniformly on the VBC-functionalized silicon surface. As shown in Fig. 3b, the grafted PVBEC chains on the silicon surface exist as a distinctive and continuous overlayer. The process is thus suitable for the fabrication of organic electronic devices on Si chips.

The memory effect of polymer brush is demonstrated by the typical *J*—*V* curves of this Si-*g*-PVBEC/Al device (Fig. 4a). Initially, the as-fabricated device is in its low conductivity state (OFF state). The current density in the low voltage range on the first sweep is low. *J* increases progressively with the applied voltage (sweep 1).

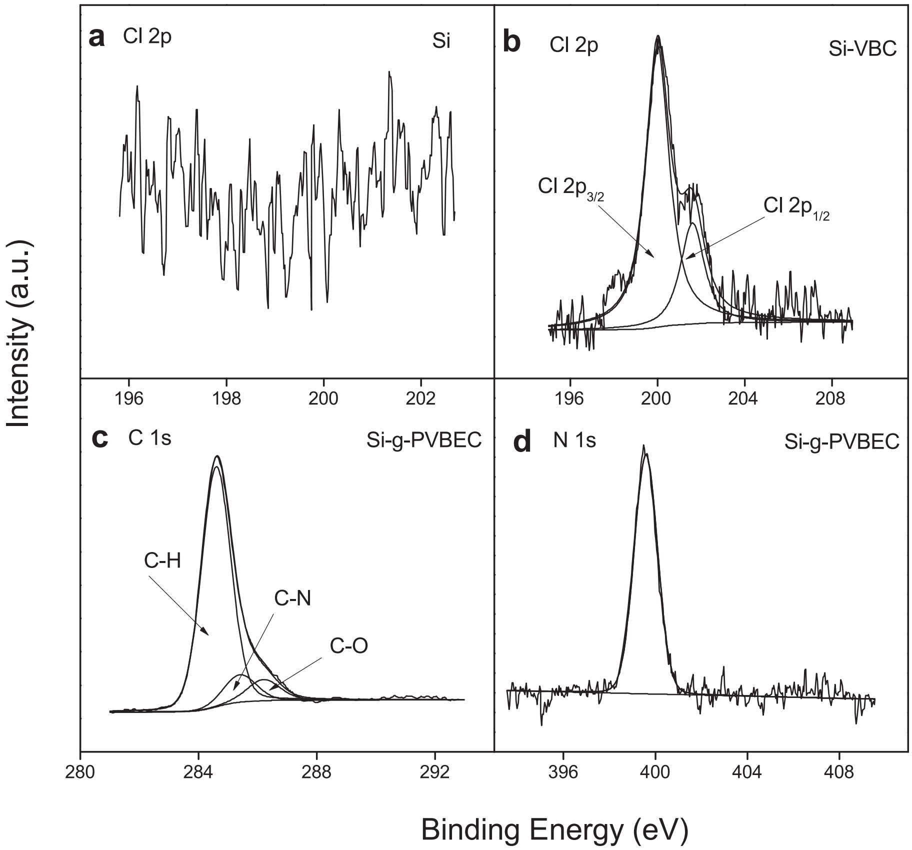

Fig. 2. Cl 2p core-level spectra of the (a) Si surface and (b) Si—VBC surface, (c) C 1s core-level spectrum and (d) N 1s core-level spectrum of Si-*g*-PVBEC.

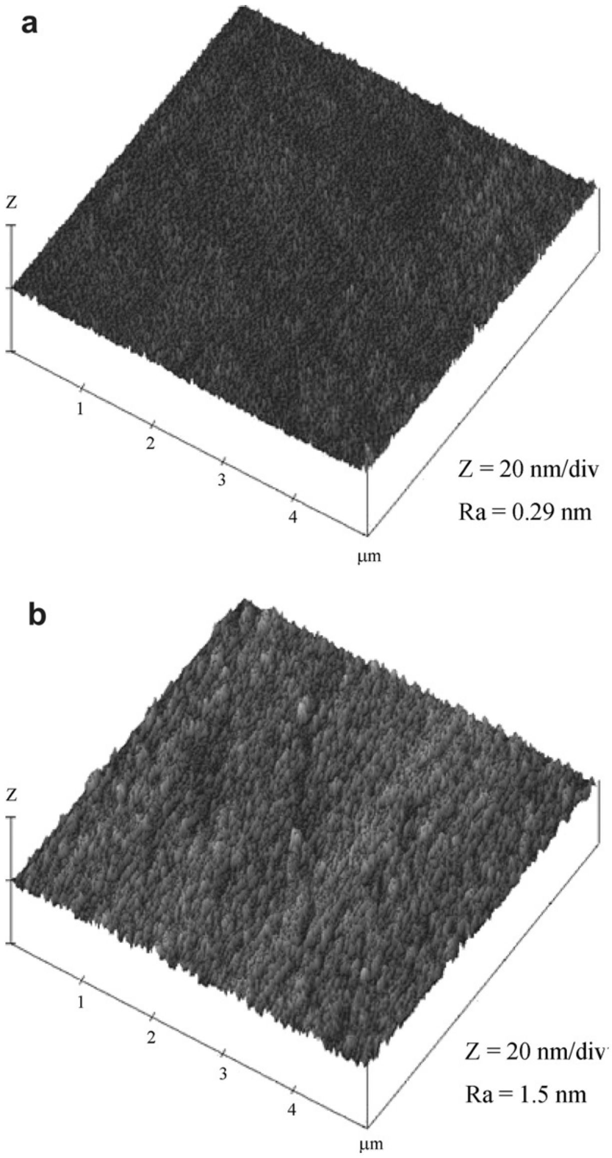

Fig. 3. AFM images of (a) the Si–VBC surface, and (b) the Si-g-PVBEC surface.

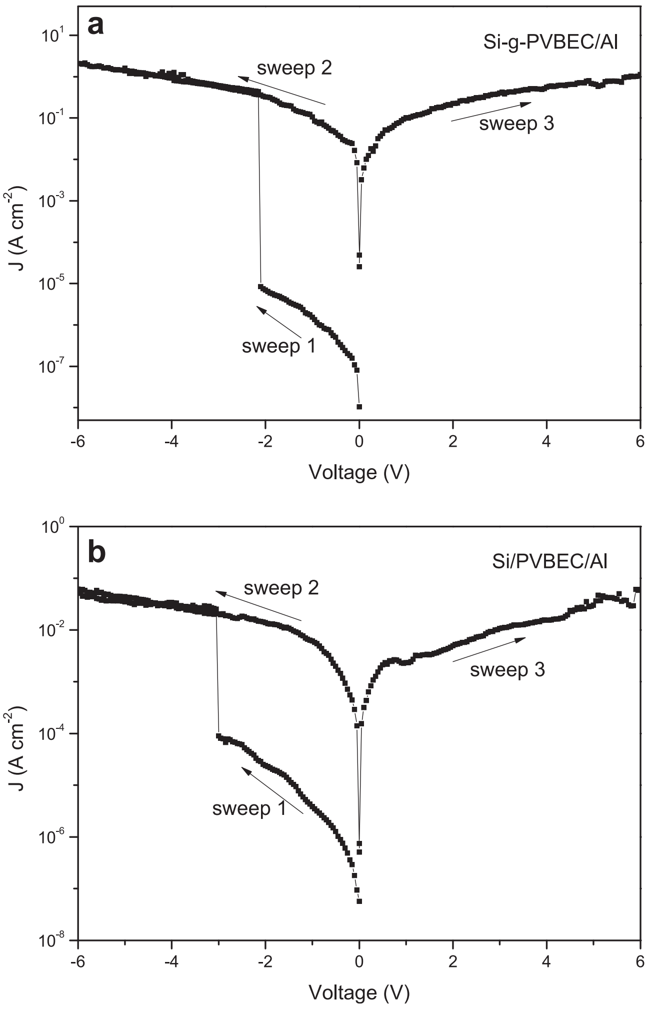

Fig. 4. Current density–voltage curves of the (a) Si-g-PVBEC/Al device and (b) Si/PVBEC/Al device.

When a switching threshold voltage of about −2.1 V is applied, an abrupt increase in J from 10^{-5}–10^{0} A/cm^2 is observed, indicating the device transition from a low conductivity state (OFF state) to a high-conductivity state (ON state). It remained in the ON state in the subsequent voltage scan (sweep 2). The memory device could not be returned to the low conductivity state by the application of a reverse bias of the same magnitude (sweep 3) after it had been switched on. Thus it is non-rewritable. The memory device was able to remain in the ON state for about 5 min after turning off the power, after which it can be switched ON again by applying the appropriate voltage. The memory effect of the device based on the polymer brush is thus volatile. The memory device is able to achieve an ON/OFF current ratio as high as 10^5, which is comparable to those of the contemporary single layer molecular switching devices [43]. The high ON/OFF current ratio also promises a low misreading rate in the two states. For comparison, a similar device based on the spin-coated PVBEC homopolymer, is also fabricated. The spin-coated PVBEC was synthesized by free-radical homopolymerization of VBEC, and had a weight-average molecular weight of about 21,000 g/mol and a polydispersity index of about 1.8. The thickness of the spin-coated film was similar to that of the polymer brush. The J–V characteristics of the Si/PVBEC/Al device are shown in Fig. 4b. Both memory devices show the similar memory behaviors. However, the Si/PVBEC/Al device switches from the OFF state to the ON state at about −3 V with an ON/OFF ratio of about 10^2–10^3.

The high-conductivity state of PVBEC may be similar to that of poly(N-vinylcarbazole) (PVK) since both polymers have the same carbazole pendant groups and a saturated main chain. The carbazole group is an electron-donor and hole-transporter [44,45], and has a tendency to form a partial or full face-to-face conformation with the neighboring carbazole groups to provide the extended electron delocalization [46]. In the region of electron delocalization, charge-carrier hopping is easier via the carbazole groups in the direction of the electric field [47]. The switching effect in the PVBEC devices probably arises from a conformation change in the polymers via rotations of the carbazole groups to result in a more regioregular arrangement [48]. Initially the carbazole pendant groups attached to the main chain via flexible C–O linkages are in random orientations, corresponding to the OFF state. When the applied voltage exceeds the threshold value, charge transfer occurs through the neighboring carbazole groups either on the same or neighboring polymer chains (intrachain or interchain hopping) [49], corresponding to the ON state. The phenyl ring and the alkyl side chain, which act as spacers between the pendant carbazole group and the

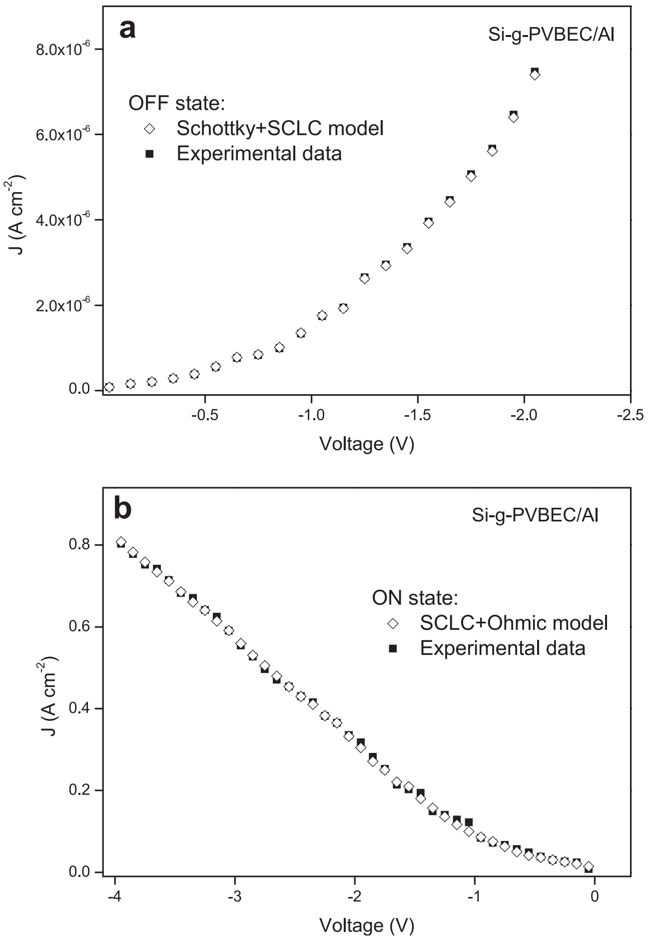

Fig. 5. Experimental and fitted current density–voltage curves of the Si-*g*-PVBEC/Al device: (a) OFF state with the Schottky emission model and (b) ON state with a combination of the space-charge-limited model and the Ohmic model (the former is predominant).

backbone of the PVBEC chain, also has a greater degree of freedom for conformation relaxation. The rotation of the carbazole and phenyl rings about the C–O bond may cause the ON state to be short-lived. When the externally applied voltage is removed, the carbazole groups in the polymer return to their original conformation (OFF state). Thus, the memory effect exhibited by the device is volatile.

The electroactive layer of well-defined and directly grafted PVBEC brushes in Si-g-PVBEC/Al device, instead of the spin-coated layer in Si/PVBEC/Al device, has resulted in a reduced switching voltage, as well as a significantly higher ON/OFF current ratio. The conductance switching in PVBEC occurs via a conformation change of the carbazole groups to extend electron delocalization [48]. Compared to the randomly arranged chains in the bulk polymer film, the more ordered polymer brushes from the ATRP process increases the ease of such transformation. Thus, a smaller applied voltage is able to provide sufficiently large electric field strength to effect the conformation change. In the high-conductivity state, the polymer brushes provide more ordered pathways for charge hopping along the face-to-face carbazole groups in the direction perpendicular to the Si substrate. In contrast, charge transport through the disordered and fragmented pathways in the bulk polymer film in the high-conductivity state is expected to be less efficient. Therefore, the ON/OFF current ratio for the Si-*g*-PVBEC/Al device is higher than that for the PVBEC spin-coated device.

To further understand the device transition from the OFF state to the ON state, the *J*–*V* curves in both states were analyzed in terms of theoretical models. For the OFF state, the *J*–*V* curve can be fitted by a combination of the Schottky emission model and space-charge-limited model:

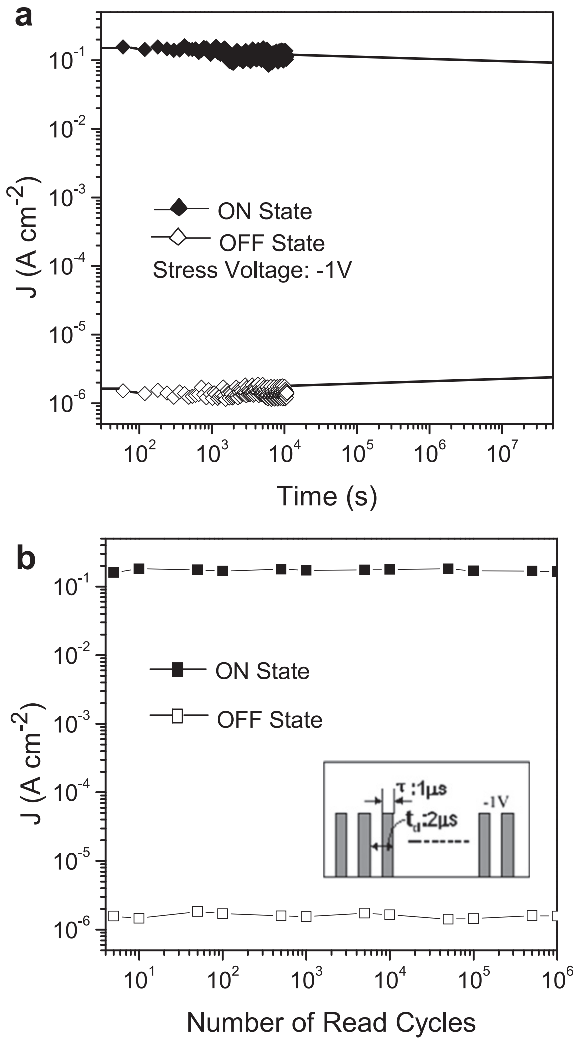

Fig. 6. (a) Stability of the Si-*g*-PVBEC/Al device in either ON or OFF state under a constant stress at −1 V. (b) Effect of read cycles on the ON and OFF states in the Si-*g*-PVBEC/Al device.

$$J = BT^2\exp\left(+a\sqrt{V}/T - q\phi_B/kT\right) + A\frac{9\varepsilon_i\mu V^2}{8d^3}$$

wherein, *T* is room temperature (298 K), $a = \sqrt{q/(4\pi\varepsilon_i d)}$, φ_B is the barrier height, ε_i is the dynamic permittivity of the insulator, *d* is the film thickness, and μ is the mobility of carriers. As shown in Fig. 5a, at the low voltage the current is dominated by Schottky emission from the electrode. As the voltage is increased, the large number of holes readily supplied by the anode results in the flow of current through the device being limited by the buildup of space charges in the PVBEC layer, and the current is a combination of the Schottky emission and space-charge-limited conduction. At the threshold voltage, there is sufficient energy for the conformation change to occur, and the charge carriers can be easily transported along aligned carbazole groups via hopping, resulting in a surge in current. For the ON state, the *J*–*V* curve can be best simulated by a combination of the space-charge-limited model and the Ohmic model as follows:

$$J = A\frac{9\varepsilon_i\mu V^2}{8d^3} + V\exp(-c/T)$$

wherein, *c* is a positive constant independent of *V* or *T*, although the *J*–*V* curve of PVK can both be fitted to the Ohmic conduction model [49]. This result may be ascribed to the presence of benzene units in the charge transport pathways, which are not as efficient at charge transportation and thus limit the current flow.

In order to assess the stability of the device based on the polymer brushes, both stress and read pulse cycles tests are conducted. The stability of the device under a constant stress of −1 V is shown in Fig. 6a. An ON/OFF current ratio of about 10^5 can be maintained and no degradation in current for the ON and OFF states is observed during the test. This characteristic promises a low misreading rate due to the precise control of the ON and OFF states. The effect of continuous read pulses (with a read voltage of −1 V) on the ON and OFF states is also investigated. As shown in Fig. 6b, more than one million read cycles are conducted on the Si-*g*-PVBEC/Al device and no current degradation is observed for the ON and OFF states. Neither the voltage stress nor the read pulses cause state transition because the applied voltage (−1.0 V) is lower than the switching threshold voltage. Thus, both states are stable under voltage stress and are insensitive to read pulses.

4. Conclusions

In summary, well-defined polymer–Si hybrids, consisting of covalently tethered polymer brushes of VBEC via surface-initiated ATRP on the Si–VBC substrates, could be readily prepared. The volatile memory behavior with an ON/OFF current ratio up to 10^5, is observed in a device fabricated from the Si-*g*-PVBEC chips. Both the ON and OFF states are stable under a constant read voltage stress of −1.0 V and even can endure 10^6 read cycles under a pulse read voltage. The switching performance of the Si-*g*-PVBEC/Al device is superior to that of the conventional spin-coated Si/PVBEC/Al device. Further investigations on effect of many factors, such as the temperature and time of surface-initiated ATRP, on the memory properties of polymer brushes are in progress. The present work suggests an alternative approach to the direct fabrication of molecular electronics and devices via surface-initiated controllable living polymerizations to meet the demand for data storage in memory devices.

Acknowledgements

The work is supported by National Natural Science Foundation of China (20904044), Scientific Research Key Project of MOE (209081), Scientific Research Foundation for Returned Overseas Chinese Scholars of MOE ([2009]1341), State Key Laboratory of Coordination Chemistry (Nanjing University), Educational Bureau of Hubei Province (Q20091508) and the Hong Kong innovation technology funding (ITS/003/09). The authors thank Prof. E. T. Kang (Department of Chemical & Biomolecular Engineering, National University of Singapore) for his kind help.

References

[1] Kim JY, Lee K, Coates NE, Moses D, Nguyen T-Q, Dante M, et al. Science 2007;317(5835):222–5.
[2] Ouyang J, Chu CW, Szmanda CR, Ma LP, Yang Y. Nat Mater 2004;3(12):918–22.
[3] Lowry MS, Goldsmith JI, Slinker JD, Rohl R, Pascal RA, Malliaras G, et al. Chem Mater 2005;17(23):5712–9.
[4] Reineke S, Lindner F, Schwartz G, Seidler N, Walzer K, Lussem B, et al. Nature 2009;459(7244):234-U216.
[5] Peumans P, Uchida S, Forrest SR. Nature 2003;425(6954):158–62.
[6] Pamuk M, Tirkes S, Cihaner A, Algi F. Polymer 2010;51(1):62–8.
[7] Hasobe T, Fukuzumi S, Kamat PV. Angew Chem Int Ed 2006;45(5):755–9.
[8] Lee TJ, Chang CW, Hahm KK, Park S, Kim DM, Kim J, et al. Nanotechnology 2009;20(13):135204.
[9] Li H, Li N, Gu H, Xu Q, Yan F, Lu J, et al. Phys Chem C 2010;114(13):6117–22.
[10] Naber RCG, Asadi K, Blom PWM, de Leeuw DM, de Boer B. Adv Mater 2010;22(9):933–45.
[11] Ling QD, Liaw DJ, Teo EYH, Zhu CX, Chan DSH, Kang ET, et al. Polymer 2007;48(18):5182–201.
[12] Liu C, Hsu J, Chen W, Sugiyama K, Hirao A. ACS Appl Mater Interfaces 2009;1(9):1974–9.
[13] Kanwal A, Chhowalla M. Appl Phys Lett 2006;89(20):203103.
[14] Li L, Ling QD, Lim SL, Tan YP, Zhu CX, Chan DSH, et al. Org Electron 2007;8(4):401–6.
[15] Chen Q, Zhao L, Li C, Shi GQ. J Phys Chem C 2007;111(49):18392–6.
[16] Moller S, Forrest SR, Perlov C, Jackson W, Taussig C. J Appl Phys 2003;94(12):7811–9.
[17] Choi S, Hong SH, Cho SH, Park S, Park SM, Kim O, et al. Adv Mater 2008;20(9):1766–70.
[18] Liu YL, Wang KL, Huang GS, Zhu CX, Tok ES, Neoh KG, et al. Chem Mater 2009;21(14):3391–9.
[19] Veinot JGC, Marks TJ. Acc Chem Res 2005;38(8):632–43.
[20] Hanson EL, Guo J, Koch N, Schwartz J, Bernasek SL. J Am Chem Soc 2005;127(28):10058–62.
[21] Armstrong NR, Carter C, Donley C, Simmonds A, Lee P, Brumbach M, et al. Thin Solid Films 2003;445(2):342–52.
[22] Moller S, Perlov C, Jackson W, Taussig C, Forrest SR. Nature 2003;426(6963):166–9.
[23] Kang SJ, Park YJ, Bae I, Kim KJ, Kim H, Bauer S, et al. Adv Funct Mater 2009;19(10):1609–16.
[24] Ling QD, Song Y, Ding SJ, Zhu CX, Chan DSH, Kwong DL, et al. Adv Mater 2005;17(4):455–9.
[25] Yan C, Zharnikov M, Gölzhäuser A, Grunze M. Langmuir 2000;16(15):6208–15.
[26] Kim JS, Ho PKH, Thomas DS, Friend RH, Cacialli F, Bao GW, et al. Chem Phys Lett 1999;315(5–6):307–12.
[27] Bernede JC, Derouiche H, Djara V. Sol Energ Mat Sol C 2005;87(1–4):261–70.
[28] Xu FJ, Song Y, Cheng ZP, Zhu XL, Zhu CX, Kang ET, et al. Macromolecules 2005;38(15):6254–8.
[29] Nystrm D, Lindqvist J, Stmark E, Antoni P, Carlmark A, Hult A, et al. ACS Appl Mater Interfaces 2009;1(4):816–23.
[30] Chen RX, Madaughlin S, Botton G, Zhu S. Polymer 2009;50(18):4293–8.
[31] Zhao B, Brittain WJ. Prog Polym Sci 2000;25(5):677–710.
[32] Brittain WJ, Minko S. J Polym Sci Part A Polym Chem 2007;45(16):3505–12.
[33] Edmondson S, Osborne VL, Huck WTS. Chem Soc Rev 2004;33(1):14–22.
[34] Pyun J, Kowalewski T, Matyjaszewski K. Macromol Rapid Commun 2003;24(18):1043–59.
[35] Barbey R, Lavanant L, Paripovic D, Schuwer N, Sugnaux C, Tugulu S, et al. Chem Rev 2009;109(11):5437–527.
[36] Ayres N. Polym Chem 2010;1(6):769–77.
[37] Fulghum TM, Taranekar P, Advincula RC. Macromolecules 2008;41(15):5681–7.
[38] Buriak JM. Chem Rev 2002;102(5):1272–308.
[39] Sieval AB, Linke R, Zuilhof H, Sudholter JR. Adv Mater 2000;12(19):1457–60.
[40] Bossmann SH, Ghatlia ND, Ottaviani MF, Turro C, Durr H, Turro NJ. Synthesis 1996;11:1313–9.
[41] Beamson G, Briggs D. High-resolution XPS of organic polymers: The Scienta ESCA300 Database. Chichester: John Wiley; 1992.
[42] Moulder JF, Stickle WF, Sobol PE, Bomben KD. In: Chastain J, editor. Handbook of X-ray photoelectron spectroscopy. Eden Prairie: Perkin-Elmer; 1992. p. 40.
[43] Bandyopadhyay A, Pal AJ. Appl Phys Lett 2003;82(8):1215–7.
[44] Morin J, Leclerc M, Ades D, Siove A. Macromol Rapid Comm 2005;26(10):761–78.
[45] Akcelrud L. Prog Polm Sci 2003;28(6):875–962.
[46] Vandendriessche J, Palmans P, Toppet S, Boens N, de Schryver FC, Masuhara H. J Am Chem Soc 1984;106(26):8057–64.
[47] Grazulevivius JV, Strohrirgl P, Pielichowski J, Pielichowski K. Prog Polym Sci 2003;28(6):1297–353.
[48] Lim SL, Ling QD, Teo EYH, Zhu CX, Chan DSH, Kang ET, et al. Chem Mater 2007;19(21):5148–57.
[49] Safoula G, Napo K, Bernede JC, Touihri S, Alimi K. Eur Polym J 2001;37(4):843–9.

Polymer 52 (2011) 1391–1401

Contents lists available at ScienceDirect

Polymer

journal homepage: www.elsevier.com/locate/polymer

Structure, mechanical properties and degradation behaviors of the electrospun fibrous blends of PHBHHx/PDLLA

Mei-Ling Cheng [a], Po-Ya Chen [a], Chin-Hung Lan [a], Yi-Ming Sun [a,b,c,*]

[a] *Department of Chemical Engineering and Materials Science, Yuan Ze University, Chung-Li 320, Taiwan, ROC*
[b] *Graduate School of Biotechnology and Bioengineering, Yuan Ze University, Chung-Li 320, Taiwan, ROC*
[c] *R&D Center for Membrane Technology, Chung Yuan University, Chung-Li 320, Taiwan, ROC*

ARTICLE INFO

Article history:
Received 4 June 2010
Received in revised form
31 December 2010
Accepted 19 January 2011
Available online 27 January 2011

Keywords:
Poly(3-hydroxybutyrate-co-3-hydroxyhexanoate)
Poly(D,L-lactic acid)
Electrospinning

ABSTRACT

Blends of poly(3-hydroxybutyrate-co-3-hydroxyhexanoate) (PHBHHx) and poly(D,L-lactic acid) (PDLLA) with different ratios were fabricated into fibrous membranes by electrospinning processes. Suggested by DSC, WAXD, and SAXS results, the molecular chains of PHBHHx and PDLLA were partially mixed in the amorphous phase, PDLLA didn't affect the growth of PHBHHx crystalline phase, and PDLLA was excluded from PHBHHx lamella stacks, i.e. in form of interstack segregation, in the blend fibrous matrix. The mechanical properties of the electrospun fibrous membranes depended on the orientation of fibers in the membranes. The electrospun membranes had higher elongation; furthermore, the tensile strength and modulus of the fibers within the membranes were higher than the corresponding cast membranes. As the content of PDLLA increased, the electrospun fibrous membranes of the blends showed higher elongation and lower tensile modulus due to the decreased number of lamellae. According to the change of molecular weight distribution, both PHBHHx and PDLLA portions in the electrospun blend membranes followed bulk erosion and PDLLA degraded faster than PHBHHx during the degradation process. The morphology change of the electrospun fibrous blends during the hydrolytic degradation indicated that the degradation behaviors were strongly influenced by the miscibility and the structural phase segregation of PHBHHx/PDLLA blend in the electrospun fibers.

1. Introduction

Electrospinning has been actively explored because it could produce ultrafine polymer fibers with diameters typically in the range of several microns down to tens of nanometers. Electrospun nanofibers have distinctive properties such as high surface area-to-volume ratio, high porosity, and enhanced specific mechanical performance [1]. Electrospun nanofibers have been used in various applications such as nano-sensors, electronic/optical industrial applications, cosmetic skin masks, military body armor, filtration media, etc.[1–3]. In order to enhance the quality and improve the functionality of the resulting of nanofiber structure, a lot of modifications have been developed in the electrospinning process. For example, aligned fibers [4,5], blend [6,7], organic–inorganic nanocomposite fibers [8,9], and core-shell bicomponent nanofiber structures using co-axial electrospinning [3,10,11] have emerged as methods of choice for the applications. Recently, many attempts in biomedical applications have been widely reported using biodegradable nanofibers, such as wound dressings, drug delivery systems [12], vascular grafts, and scaffolds for tissue engineering [13,14].

Polyhydroxyalkanoates (PHAs) are a class of biodegradable and biocompatible thermoplastic polyesters produced by various microorganisms, such as soil bacteria, blue-green algae, and some genetically modified plants [15,16]. Poly(3-hydroxybutyrate) (PHB) is the first member of the PHA family, and it has great potential in commercial applications because of its biodegradability. However, the application has been limited by some obstacles such as poor mechanical properties due to the large spherulites and high extent of secondary crystallization behavior in PHB [17]. For the purpose of industrial applications, its copolymer in various ratios, or blend with other polymers has been introduced to enhance the processing and mechanical properties of PHB [17–20]. Poly(3-hydroxybutyrate-co-3-hydroxyhexanoate) (PHBHHx) has substantially different behavior compared to PHB due to its long chain branching, which reduces the crystallinity and melting temperature, and results in a polymer with better ductile and processing properties than PHB [21]. Furthermore, PHAs were introduced to fabricate nano-structured nonwoven mesh by electrospinning process for biomedical applications [4–6].

---

* Corresponding author. Department of Chemical Engineering and Materials Science, Yuan Ze University, Chung-Li 320, Taiwan, ROC. Tel.: +886 3 4638800x2558; fax: +886 3 4559373.
E-mail address: cesunym@saturn.yzu.edu.tw (Y.-M. Sun).

0032-3861/$ – see front matter © 2011 Elsevier Ltd. All rights reserved.
doi:10.1016/j.polymer.2011.01.039

Poly(D,L-lactic acid) (PDLLA) is a mostly amorphous polyester, and it's also a biodegradable and biocompatible polymer that can be produced from renewable sources, such as corn starch [22]. This polymer shows lower strength compared to poly(L-lactic acid) due to its amorphous structure [23,24]. It is a preferred candidate for developing drug delivery vehicles and scaffolding materials for tissue regeneration [24].

Both PHBHHx and PDLLA have been studied or applied as biomedical materials in the plastics industry. The mechanical properties and biodegradability of the materials are crucial criteria in many applications. The blends of PHBHHx and PDLLA provide a simple way to modify the properties of each other for various purposes. It is well known that the apparent properties of a polymer blend depend on the miscibility between blended polymers. For the PHBHHx/PDLLA blend system, amorphous PDLLA may be segregated out of the crystalline PHBHHx domain when the solid–liquid phase separation and crystallization process occur. When polymers are crystallized from the bulk, the most obviously observable structures are spherulites [25]. According to the distance between amorphous regions in the blend, there are three kinds of segregation morphologies which can be observed: interlamellar, interfibrillar, and interspherulitic segregations [26]. However, the crystallization behavior of semi-crystalline polymeric nanofibers is particular and quite different from the bulk polymer due to the one-dimensional fiber size effect and the elongation during the electrospinning process [27–29]. In our past study, the results indicated that the crystallization of the PHBHHx nanofibers was restricted to specific crystalline planes due to the molecular orientation along the axial direction of the fibers [30]. While the polymeric nanofiber is modified by blending with other polymers, the crystalline dimensional and structure may alter depending on the miscibility of two components [31,32]. Until now, the crystallization behavior and morphology of segregation in the blended electrospun fibers are still not clear and worth a better understanding.

In this work, we blended PHBHHx and PDLLA in several selected weight ratios to fabricate biodegradable nanofibrous membranes via electrospinning. According to the literature report [33], the tensile properties of electrospun membranes would be influenced by the crystalline morphology strongly. The aim of this study is to observe the miscibility and crystalline structure of the electrospun blend in the nanofibers, develop a model of the morphological structure for the blend nanofibers based on the observation, and then correlate those properties to the mechanical properties and degradation behaviors of these nanofibrous membranes.

2. Experimental

2.1. Materials

PHBHHx was kindly provided by Procter and Gamble (West Chester, USA). The 3-hydroxyhexanoate (HHx) content of the PHBHHx copolymer was 3.9 mol% determined by ^{1}H NMR spectra.

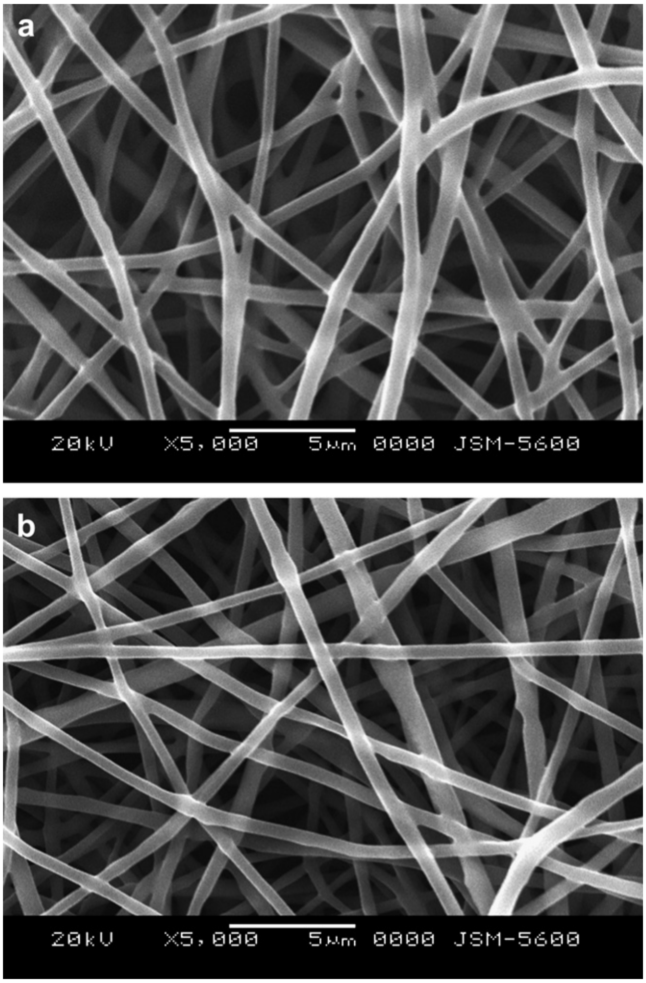

Fig. 1. The morphology of random electrospun blend fibers with the PHBHHx/PDLLA ratios of (a) 100/0 and (b) 75/25.

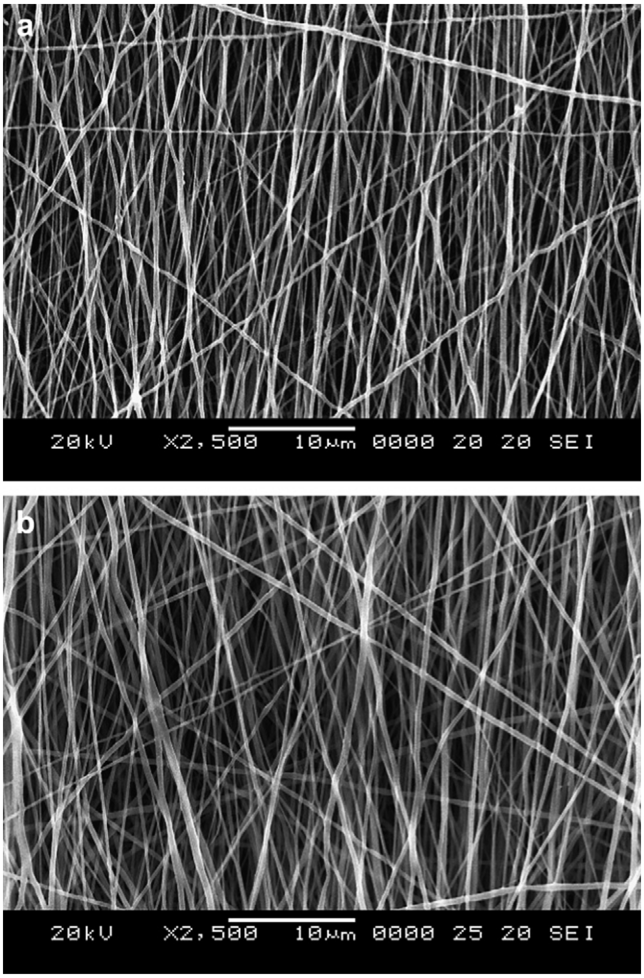

Fig. 2. The morphology of aligned electrospun blend fibers with the PHBHHx/PDLLA ratios of (a) 100/0 and (b) 75/25.

PDLLA (6300D) was obtained from NatureWorks (Blair, USA). The weight-average molecular weight ($\overline{M}_w$) of PHBHHx and PDLLA was 690,000 and 170,000; the polydispersity index (PDI) was 1.21 and 1.55, respectively, measured by GPC. Chloroform was from Mallinckrodt (Hazelwood, USA) and N,N-dimethylformamide (DMF) was from Tedia (Fairfield, USA).

2.2. Preparation of electrospun and cast membranes

The electrospinning instrument consisted of an adjustable, regulated, high-voltage power supply (up to 40 kV, You-Shang Technical Co., Taiwan), a syringe pump (Cole-Parmer, EK-74900-00, USA), and collector units. PHBHHx and PDLLA were blended with several selected weight ratios (100/0, 75/25, 50/50, 25/75, and 0/100) and dissolved in chloroform/DMF solution (80/20 w/w) at a total polymer concentration of 3 or 6 wt%. The polymer solution was filled in a 10 ml glass syringe which was connected to a blunt-ended gauge-22 needle. The syringe was then placed in a syringe pump and the needle connected to the positive end of the high-voltage power supply set at 18 kV, and the temperature was controlled at 40 °C. For the preparation of random electrospun (RES) membranes, fibers were collected onto a grounded plate which was covered by an aluminum foil with a collection distance of 25 cm, and the solution feeding rate was set at 0.5 ml/h. For the preparation of aligned electrospun (AES) membranes, fibers were collected onto a rotating drum (i.e. length and OD of the drum are 40 and 9 cm, respectively) with a 1200 rpm of rotational speed. The collection distance was fixed at 28 cm and the solution feeding rate was set at 1 ml/h. Approximate 6 h processing time would be needed to produce a nanofibrous membrane in this study. The electrospun membranes were dried in vacuum at room temperature for 48 h to remove the residual solvent completely.

As reference samples, the cast membranes were prepared from the blend solutions of 6–15 wt%. The solution was cast on a glass dish and was dried at room temperature for 48 h. Afterwards, vacuum drying was applied to completely remove remaining solvent in the membranes.

2.3. Characterization of membranes

The morphology of the collected fibers was observed by SEM (JEOL JSM-5600). Samples were sputter-coated with gold for 30 s to reduce electric charging effects. SEM was operated at 20 kV in high vacuum. Moreover, the average diameter of electrospun fibers was measured by analyzing the SEM images. First, five horizontal straight lines were drawn on a SEM picture. All the diameters of the fibers which crossed the straight lines were measured. Finally, more than 200 data points were collected for the measurement of an average diameter for a kind of electrospun fibers.

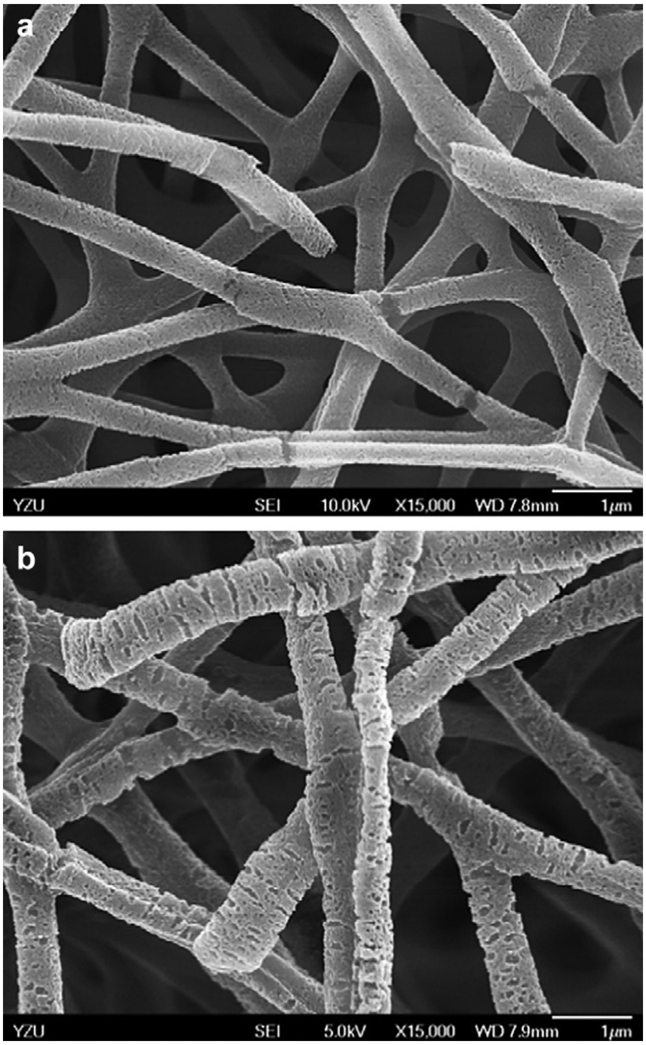

Fig. 3. The morphology of random electrospun blend fibers after alkaline-treatment with the PHBHHx/PDLLA ratios of (a) 75/25 and (b) 50/50.

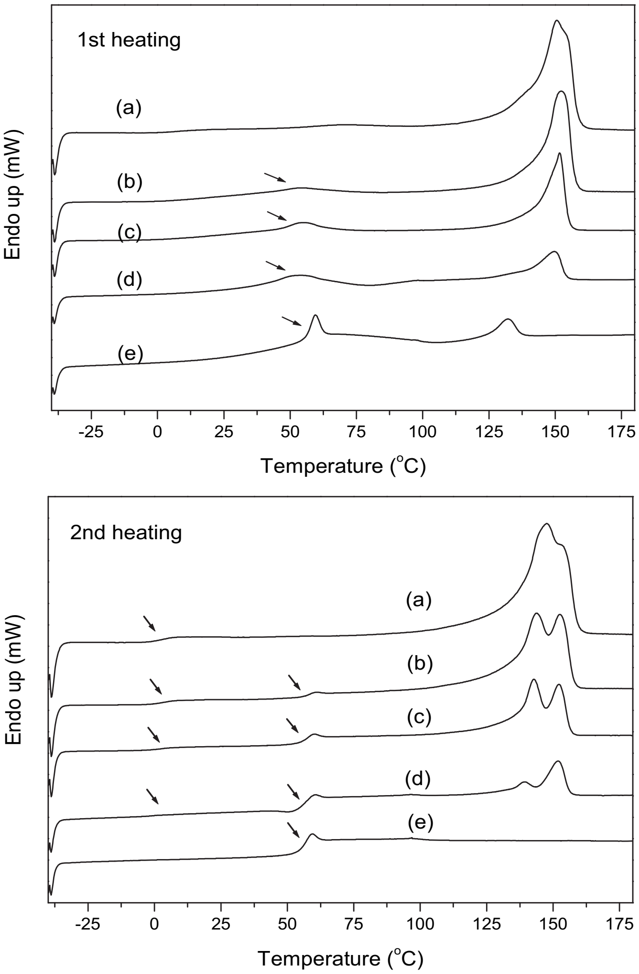

Fig. 4. DSC curves of random electrospun PHBHHx/PDLLA blend membranes: (a) 100/0, (b) 75/25, (c) 50/50, (d) 25/75, and (e) 0/100.

Table 1
Glass transition of random electrospun PHBHHx/PDLLA blend membranes (standard deviation (SD) < 2 °C, n = 3).

PHBHHx/PDLLA	T_g (°C)		T_m (°C)	
	1st heating	2nd heating	1st heating	2nd heating
100/0	–	4	151	147/153
75/25	50	5/59	153	144/153
50/50	51	6/58	153	143/152
25/75	48	4/60	151	139/152
0/100	58	58	134	–

For the observation of the phase separation of PHBHHx/PDLLA blends, the samples were immersed in 1 wt% NaOH solution at 40 °C to remove PDLLA component selectively. The etching time was adjusted depending on the PDLLA content in the fibers. After etching, the samples were washed by distilled water and dried thoroughly under vacuum, and then the samples were sputter-coated with platinum for 60 s. The morphology of treated samples was observed by field emission SEM (FE-SEM, JEOL 6701F), which was operated at 5 kV in high vacuum.

The porosity of electrospun membranes was calculated by the following equation:

$$\varepsilon(\%) = \left(1 - \frac{\rho_{\text{bulk}}}{\rho_{\text{true}}}\right) \times 100\% \tag{1}$$

where ρ_{bulk} and ρ_{true} are bulk density and true density of the membranes, respectively. The bulk density was calculated by a gravimetric method. Samples were cut into $1 \times 1\ \text{cm}^2$ and weighted by a micro-balance (AX-250R, Mettler, USA). The thickness of samples was measured by a digital micrometer (IDF-112, Mitutoyo, Japan) for determining the bulk volume. In addition, the true volume was measured by the pycnometric method. About 0.1 g of the sample was placed into the sample holder of the pycnometer (AccuPyc 1330, Micromeritics, USA) in which helium was used as the probing gas.

Thermal analysis was performed with differential scanning calorimeter (DSC7, Perkin–Elmer, USA) under nitrogen atmosphere to study the miscibility of the PHBHHx/PDLLA blends. Approximate 6 mg of samples were hermetically sealed in an aluminum pan for measurements. Under a nitrogen atmosphere, samples were heated from −40 to 180 °C with a heating rate of 10 °C/min (first run), cooled to −40 °C at the same rate (cooling run), and then heated again as that in the first run (second run).

Crystalline structure of the membranes was determined by a wide angle X-ray diffractometer (XRD-6000, Shimadzu, Japan), with Ni-filtered Cu Kα radiation ($\lambda = 1.54$ Å) generated with 40 kV and 30 mA as the X-ray source. The diffraction angle was scanned from 5° to 40° at a rate of 1°/min. The crystallinity was determined based on the percentage of the crystalline peak area in the total area under WAXD halos. Small-angle X-ray scattering (SAXS) measurements were performed with an X-Ray spectrometer (PSASA-USH-WAXS-002, Osmic Inc., USA), with Cu Kα radiation ($\lambda = 1.54$ Å) generated with 45 kV and 0.67 mA as the X-ray source. SAXS patterns were recorded in the range of $2\theta = 0–3.5°$ with an increment of 0.0025°.

Mechanical properties in terms of tensile strength, Young's modulus, elongation at break, and toughness were measured by using an Instron tester (model 4204, Instron, USA). The gauge length and crosshead speed are 50 mm and 5 mm/min, respectively. All samples were prepared in the form of standard dumbbell-shaped according to ASTM D638 by die cutting (DIN 53504-S3A, Shimadzu, Japan). The total length and neck width of the dumbbell-shaped membrane sheet are 50 and 4 mm, respectively. Obtained results were averaged over five samples for each condition.

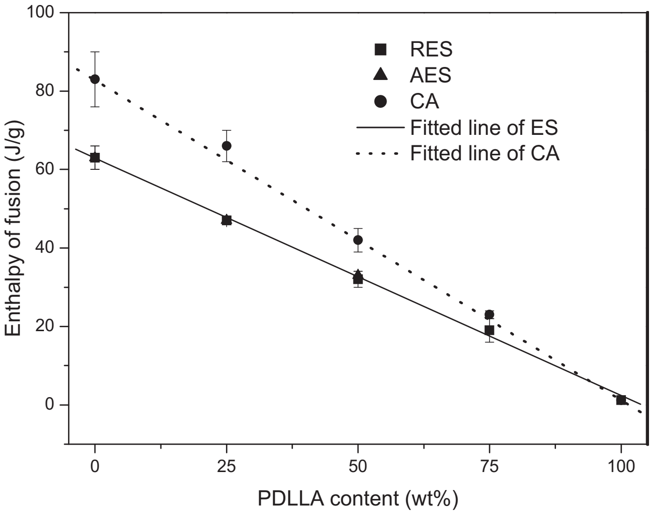

Fig. 5. The correlation between the overall enthalpy of fusion and the PDLLA content in the electrospun (ES) and cast (CA) PHBHHx/PDLLA blend membranes.

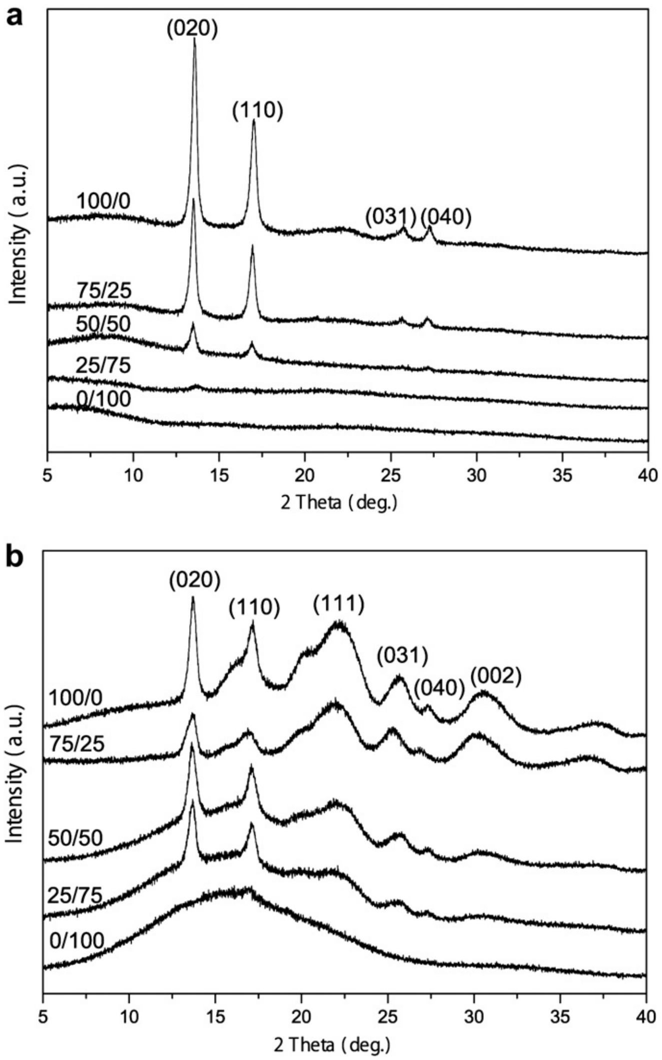

Fig. 6. XRD pattern of the (a) random electrospun membranes and (b) cast membranes in various PHBHHx/PDLLA ratios.

Table 2
The crystallite size, crystallinity, and long period value of random electrospun PHBHHx/PDLLA blend membranes (n = 3).

PHBHHx/PDLLA	$D_{(020)}$ (nm)[a]	$D_{(110)}$ (nm)[a]	$X_{c,\ overall}$ (%)[b]	$X_{c,\ PHBHHx}$ (%)[c]	L (nm)[d]
100/0	23 ± 3	20 ± 2	43	43	5.1 ± 0.2
75/25	23 ± 2	21 ± 1	31	41	5.4
50/50	24 ± 1	22 ± 1	20	40	4.7 ± 0.1
25/75	–	–	10	40	4.8 ± 0.2

[a] $D_{(hkl)}$: the apparent lateral crystallite size obtained by using Eq. (3).
[b] $X_{c,\ overall}$: the crystallinity calculated from WAXD.
[c] $X_{c,\ PHBHHx}$: the crystallinity of the PHBHHx portion in the blend based on WAXD.
[d] L: the weight-average long period which was calculated from the position of the peak maximum of the Lorentz-corrected profile and using Eq. (4).

2.4. *In vitro degradation*

Electrospun membranes were immersed in phosphate buffer solution (PBS) solution (pH = 7.4) and were hydrolyzed under shaking at 60 rpm at 37 °C. After each degradation period, the sample was washed and dried in a vacuum freeze-dryer for 48 h. The morphology, molecular weight and weight loss of hydrolyzed membranes were followed by SEM, FE-SEM, GPC, and microbalance, respectively.

3. Results and discussion

3.1. *Morphology of electrospun blend membranes*

Fibrous membranes of PHBHHx/PDLLA blends in various ratios (100/0, 75/25, 50/50, and 25/75 w/w) were fabricated successfully by the electrospinning technique. Typical images of the random electrospun (RES) membranes with smooth fibers are shown in Fig. 1. The average size (diameter) of those fibers was about 500–600 nm for the blends of PHBHHx/PDLLA with the ratios of 100/0, 75/25, and 50/50 when the feed polymer concentration was 3%, and it was about 1000 nm for the 25/75 or 0/100 blend when the feed polymer concentration was 6%. The particular feed polymer concentrations were chosen so that the solutions had sufficient viscosity to form smooth fibers. Fine alignment of the aligned electrospun (AES) membranes was observed as shown in Fig. 2. The average fiber diameter was from 200 to 400 nm. The size of AES fibers was smaller than that of RES with the similar conditions since AES fibers might be further stretched during collecting. No significant size differences exist among the fibers prepared from various PHBHHx/PDLLA ratios for both RES and AES membranes at the feed polymer concentration of 3%. The porosity of those fibrous mats was around 70–80% and didn't show much dependence on the processing conditions.

The morphology of the blend fibers was further detected by alkaline-etching since PDLLA domain could be selectively removed by short-time strong alkaline-treatment [34]. Pristine PDLLA fibers could be eroded and completely dissolved rapidly in NaOH solution; in contrast, pristine PHBHHx fibers didn't show any change in morphology as a whole fiber at the same condition after12 h treatment (data not shown). The 75/25 and 50/50 blend fibers were alkaline-etched for 60 and 30 min of etching time, respectively. As shown in Fig. 3a, the 75/25 blend fibers contained dispersed fine pore morphology as PDLLA being the discontinued phase. The 50/50 blend fibers showed mostly a bi-continuous morphology (Fig. 3b). The PDLLA component lay in isolated domains and those domains dispersed along the fibers with few tens nm distance apart. It was suspected that the morphology of the blend fibers was caused by the phase separation of PHBHHx and PDLLA over the entire composition range.

3.2. *Miscibility and thermal properties of the blends*

As shown in DSC results (Fig. 4), there was a glass transition temperature (T_g) observed in the first heating trace, which could be assigned to the T_g of PDLLA fraction, for the PHBHHx/PDLLA blend fibrous membranes. The T_g was lower than that of pristine PDLLA, however, it kept relatively constant even for blends with different ratios (Table 1). Besides, it was hard to observe the T_g of PHBHHx fraction during the first heating run due to the high crystallinity of PHBHHx. It was presumed that PHBHHx and PDLLA in the blend fibrous membranes might be partially mixed in the amorphous state. During the second heating run, two clear T_gs in the PHBHHx/PDLLA blends presented. There was no significant difference in the individual T_g of PHBHHx and PDLLA between the PHBHHx/PDLLA blends (Fig. 4 and Table 1). This result indicates that the blends

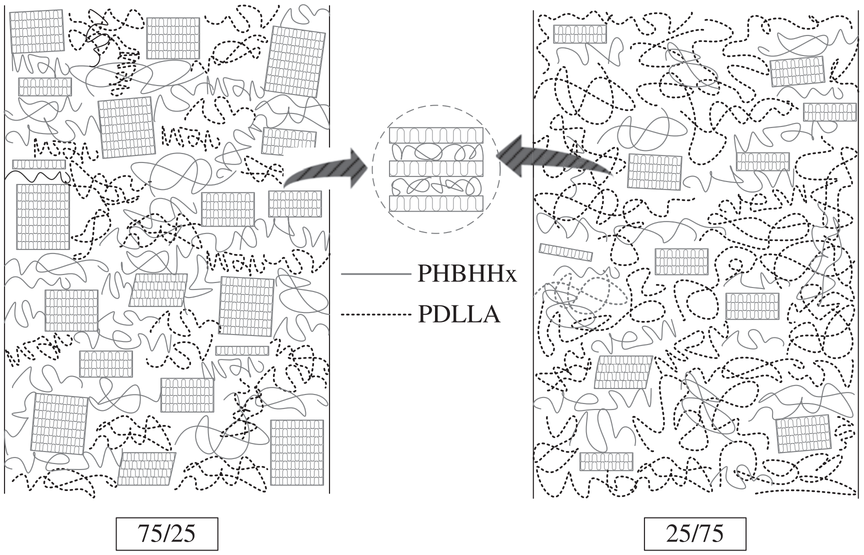

Scheme 1. The schematic arrangement of polymer chains in the electrospun PHBHHx/PDLLA blend fibers (solid lines: amorphous PHBHHx chains, dot lines: amorphous PDLLA chains, and cake: lamellar stacks of PHBHHx).

of PHBHHx and PDLLA are immiscible in the amorphous state. However, the system may not be able to completely phase separate, due to fast evaporation of solvent during the solidification process of fibers, so that some partially mixed behaviors are observed in the amorphous phase in the electrospun PHBHHx/PDLLA blended fibers. In addition, the melting points (1st heating) of the pristine PHBHHx and the blend fibrous membranes were almost constant, i.e. near 150 °C, it didn't alter while PDLLA was added. It illustrated that the crystallization of PHBHHx was not affected by the presence of PDLLA in the electrospun PHBHHx/PDLLA blended fibers.

According to the results of thermal properties, the crystallization of PHBHHx is not interfered by PDLLA. The theoretical enthalpy of fusion (melting heat) of PHBHHx/PDLLA blends can be calculated from Eq. (2):

$$\Delta H_m = \Delta H_{m,\mathrm{PHBHHx}} \times r_{\mathrm{PHBHHx}} + \Delta H_{m,\mathrm{PDLLA}} \times (1 - r_{\mathrm{PHBHHx}}) \qquad (2)$$

where $\Delta H_{m,\mathrm{PHBHHx}}$ and $\Delta H_{m,\mathrm{PDLLA}}$ are the enthalpies of fusion of pristine PHBHHx and PDLLA, respectively; ΔH_m is theoretical enthalpy of fusion of the blends, and r_{PHBHHx} is the weight fraction of PHBHHx in the blend. In our case, the PDLLA phase can slightly crystallize during the heating process and result in a melting peak ($\Delta H_m \cong 3$ J/g). The correlation between the enthalpy of fusion from first heating and PDLLA content in the blend systems can be identified (Fig. 5). The overall enthalpy of fusion (i.e. the crystallinity of the electrospun fibrous membranes) decreased with the PDLLA content and the experimental values of the enthalpy of fusion totally agreed with the predicted values (dash fitting lines in the Fig. 5). The linear relationship demonstrates that PHBHHx and PDLLA cannot co-crystallize and they may form each own domain and the corresponding crystallinity of PHBHHx portion is constant in all the blend systems. Comparing with the cast membranes, the enthalpy of fusion of the electrospun membranes was always lower with all kind of blend ratios. It was speculated that the dimension of nanofibers had a restrictive effect on the growth of spherulites so that the crystallinity was lower than that of the cast membranes [30].

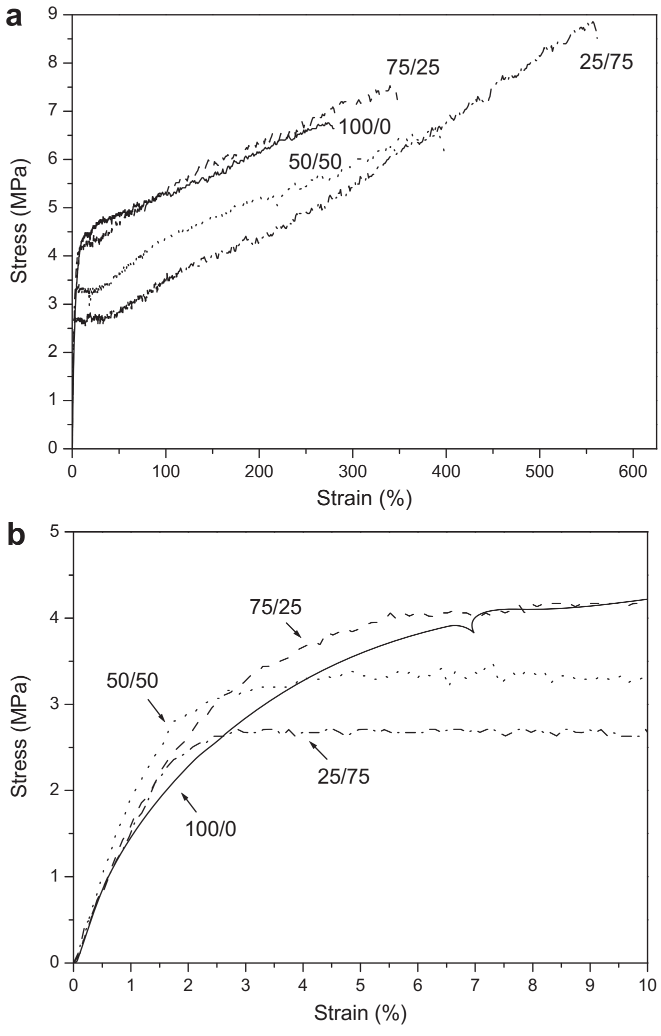

Fig. 7. Typical tensile stress–stain curves of random electrospun blend membranes in various PHBHHx/PDLLA ratios: (a) the full range up to break, and (b) the range of the initial 10% strain.

Table 3
Elongation (%) at break of cast films and electrospun PHBHHx/PDLLA blend membranes (n = 10).

PHBHHx/PDLLA	CA	RES	AES-L[a]	AES-T[b]
100/0	12 ± 3	270 ± 60	30 ± 5	430 ± 30
75/25	320 ± 70	370 ± 70	70 ± 10	380 ± 60
50/50	530 ± 80	380 ± 60	–	–
25/75	540 ± 90	540 ± 30	140 ± 10	560 ± 30

[a] AES-L: tensile force is applied to the longitudinal direction of aligned fibers.
[b] AES-T: tensile force is applied to the transverse direction of aligned fibers.

3.3. *Crystallization behaviors of blend membranes*

Fig. 6 shows the X-ray diffraction patterns of electrospun fibrous membranes and cast membranes. Electrospun fibrous membranes of neat PHBHHx exhibited distinct crystalline peaks at (020) and (110) (Fig. 6a). In the meantime, the diffraction peaks of (111) and (002) planes shown in cast membranes (Fig. 6b) disappeared completely in the diffraction patterns of electrospun fibers (Fig. 6a). Similar behaviors can also be found in other electrospun PHBHHx/PDLLA fibers. It is also noted that the (110) diffraction peak of electrospun fibers (Fig. 6a) is sharper than that of the cast membranes for neat PHBHHx (Fig. 6b). This indicates that there exists oriented chain packing in the crystalline phase of the electrospun PHBHHx fibers. The (020) and (110) planes or the c-axis of the crystal lattice of PHBHHx was parallel to the fiber direction or the electrospun membrane surface, that is, the c-axis of PHBHHx crystal was along the fiber axis of the nanofibers. Similar results have been found and discussed in a previous publication [30]. The diffraction pattern of the neat PDLLA electrospun membrane showed a broad and almost flat profile which indicated that it was a mostly amorphous matrix at room temperature without any heating history. As the fraction of amorphous PDLLA increased, the intensity of crystalline peaks gradually decreased so that the crystallinity of the membranes decreased, which was similar to the results obtained from DSC. However, it is noted that the intensity of the crystalline peaks of the electrospun PHBHHx/PDLLA blend is getting much weaker than expected based on the DSC results when

Table 4
Tensile strength and elastic modulus of cast films and electrospun PHBHHx/PDLLA blend membranes (n = 10).

PHBHHx/ PDLLA	Tensile strength (MPa)			Elastic modulus (GPa)		
	CA	RES	AES-R[a]	CA	RES	AES-R[a]
100/0	16 ± 2	6.0 ± 0.9	113 ± 20	0.61 ± 0.08	0.11 ± 0.01	1.2 ± 0.2
75/25	12 ± 2	7.1 ± 0.8	33 ± 5	0.54 ± 0.05	0.14 ± 0.01	0.7 ± 0.1
50/50	13 ± 2	6.5 ± 0.5	–	0.40 ± 0.03	0.15 ± 0.02	–
25/75	12 ± 2	8.3 ± 0.5	20 ± 3	0.30 ± 0.03	0.13 ± 0.02	0.5 ± 0.1

[a] AES-R: the true tensile strength or elastic modulus of the aligned fibers. (AES-R) = (AES-L)/(1 − ε), ε: the porosity of aligned electrospun membrane.

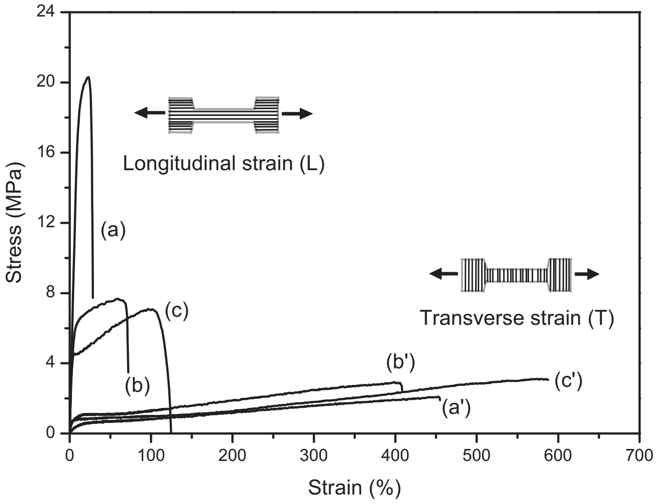

Fig. 8. Typical tensile stress–stain curves of aligned electrospun PHBHHx/PDLLA blend membranes: (a), (a′) 100/0, (b), (b′) 75/25, and (c), (c′) 25/75 ((a), (b), and (c) are AES-L; (a′), (b′), and (c′) are AES-T).

the PDLLA content is getting higher as shown in Fig. 6a. In addition, the distinct amorphous hump shown in cast membranes (Fig. 6b) became unclear in all the electrospun samples (Fig. 6a). The behavior is not well understood at this moment. It may be possibly due to a shielding effect of the disorder phase in the fibrous membranes, which reduces the intensity of diffraction peaks. Further study is required to clarify this suspect. Nevertheless, the absolute intensity of these crystalline peaks didn't affect the analysis as the crystallinity was determined based on the percentage of the crystalline peak area in the total area under WAXD halos.

From the diffraction peaks in the WAXD pattern, the apparent lateral crystallite size, D_{hkl}, could be calculated using the Scherrer equation [35]:

$$D_{\mathrm{hkl}} = \frac{K'\lambda}{\left(\beta_{1/2}\cos\theta\right)} \tag{3}$$

where $\beta_{1/2}$ is defined as the full width at the half-maximum of the diffraction peak hkl in radians, the shape factor K' is set at 0.9 for a polymer system, λ is the X-ray wavelength, and θ is the half of diffraction angle. According to Eq. (3), the lateral size of the crystallite along the (020) and (110) crystallographic planes with strong

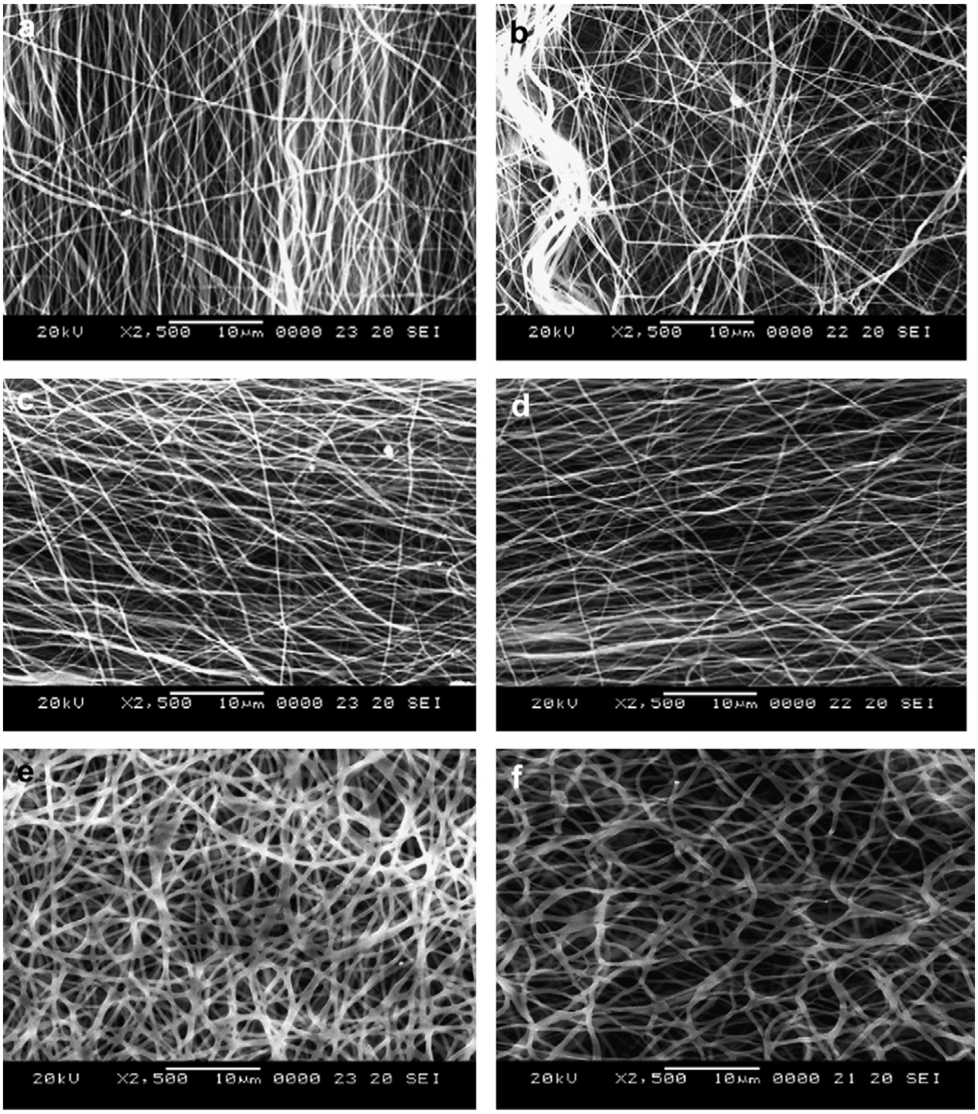

Fig. 9. The morphology of electrospun PHBHHx membranes after different strains: (a) 0% of AES-T, (b) 300% of AES-T, (c) 0% of AES-L, (d) 20% of AES-L, (e) 0% of RES, and (f) 200% of RES.

diffraction intensity was calculated and reported for electrospun nanofibers in Table 2. The position of the diffraction peaks didn't change and the lateral crystallite size of (020) and (110) didn't have significant difference within all the blend nanofibers. As described above, they indicated the PHBHHx crystalline region was not affected by PDLLA and the molecular chains of PDLLA were excluded from the PHBHHx crystalline region in the blend membranes; the PHBHHx crystallites only grew by themselves.

The crystalline lamellar structure of the electrospun membranes was observed by SAXS profile. In the lamellar stack model, the long period represents the sum of the lamella thickness (L_c) and the amorphous layer thickness (L_a). The weight-average long period (L) can be calculated from the position of the peak maximum of the Lorentz-corrected profile [36] using Bragg's equation:

$$L = \frac{2\pi}{q_{\max}} \tag{4}$$

where $q_{\max}$ is the maximum of scattering vector,$(4\pi/\lambda')\sin(\theta'/2)$; θ' and λ' are the scattering angle and the X-ray wavelength, respectively. The long period (L) values of the electrospun membranes, which represent the thickness of repeating PHBHHx lamella/PHBHHx amorphous layer, are as shown in Table 2. The small variation of the long period indicated the lamella/amorphous layer thickness didn't change significantly with increasing of PDLLA in the PHBHHx/PDLLA system. Therefore, it can be concluded this system is in form of interstack segregation, i.e. the PDLLA domain was segregated out of PHBHHx lamellar stacks. This proposition is further supported by the dispersed morphology shown in Fig. 3. When PDLLA was added into the system, the crystallinity of the electrospun membranes was proportionally decreased with the content of PDLLA (Table 2); that is, the crystallinity of PHBHHx portion was almost constant. The results were in agreement with those from the melting heat analysis in DSC study. The number of lamellae of the electrospun blend membranes with higher PDLLA content was much less than that of pristine PHBHHx electrospun membranes. Accordingly, the arrangement of polymer chains in blended system is proposed as shown in Scheme 1. In the electrospun blend fibers, PHBHHx and PDLLA are mostly phase separated from each other, PDLLA is excluded from the PHBHHx crystalline

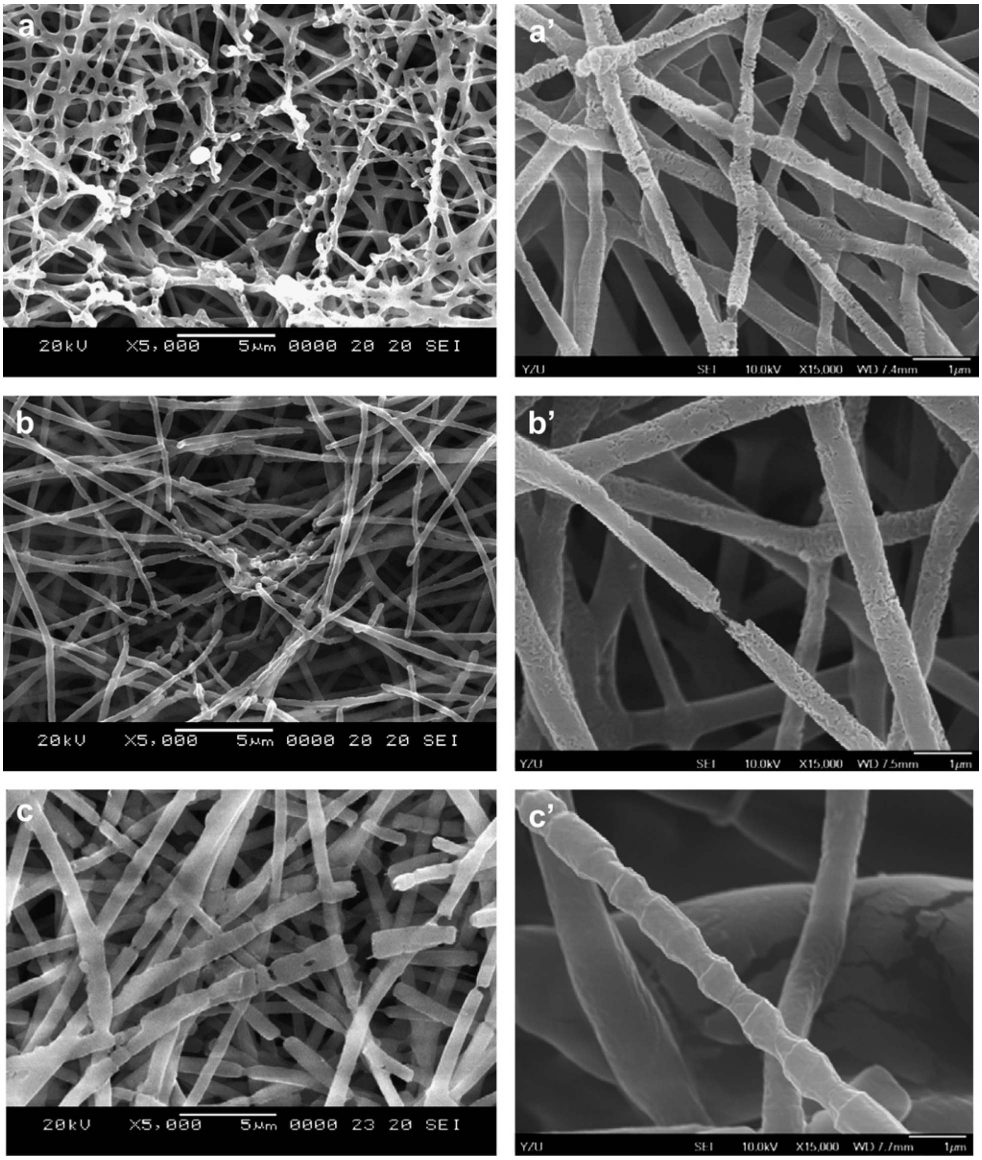

Fig. 10. The morphology of random electrospun blend PHBHHx/PDLLA membranes after hydrolysis for 24 weeks: (a), (a′) 100/0; (b), (b′) 75/25; and (c), (c′) 25/75 ((a), (b), and (c) are ×5000; (a′), (b′), and (c′) are ×15,000).

phase, and PHBHHx and PDLLA are partially mixed in the amorphous phase. Only PHBHHx can crystallize and all the lamellar stacks of PHBHHx were oriented along the axial direction of the fibers.

3.4. Mechanical properties

The mechanical properties of the electrospun blend membranes were discussed. Fig. 7 shows the stress–strain curve of the RES membranes. In the case of pristine PHBHHx system, RES membranes showed much higher elongation and lower tensile strength and modulus than cast membranes (Tables 3 and 4). It indicated RES membrane was soft and tough. As PDLLA content increased, the elongation at break of RES blend membranes increased from 270 ± 60% to 540 ± 30% and the tensile strength varied from 6 to 8 MPa as shown in Tables 3 and 4. The RES blend membranes became more flexible, tough and ductile as the PDLLA content increased because of the adding amorphous PDLLA material and the decrease of the overall crystallinity of the fibrous membranes (Table 2). Thus, the mechanical properties of PHBHHx fibrous membranes can be adjusted significantly by simple blending with PDLLA.

In fact, the true tensile properties of the fibers should be measured along the fiber axis. Aligned fibrous membranes have been fabricated via electrospinning with rotating collector in this study. Fig. 8 showed the stress–strain curve of AES membranes. With respect to the architecture of aligned fibers, the longitudinal and transverse samples were obtained from AES membranes. The longitudinal aligned electrospun (AES-L) membranes had lower elongation than transverse aligned electrospun (AES-T) and RES membranes (Fig. 8 and Table 3). After the transverse tensile test, aligned fibers in the fibrous membranes became disorder and the distance between the fibers increased, as shown in Fig. 9a and b, so that much longer elongation was measured. On the contrary, the aligned fibers became more oriented after longitudinal elongation (Fig. 9c and d). Herein, the tensile properties of the fibers which were tested along longitudinal direction were close to the true properties of fibers due to the parallel strain to the axis of nanofibers. It should be borne in mind that the measured data may slightly deviate from the true ones due to the presence of some non-aligned fibers in the matrix. In addition, the morphology of RES membranes after the tensile process showed uniformly web structure and disordered fiber matrix since it combined the morphology changes of AES-L and AES-T (Fig. 9e and f). Therefore, the elongation of RES membranes was between that of AES-L and AES-T. In other words, the apparent properties of fibrous membranes depended on the degree of the fiber orientation (architectural design).

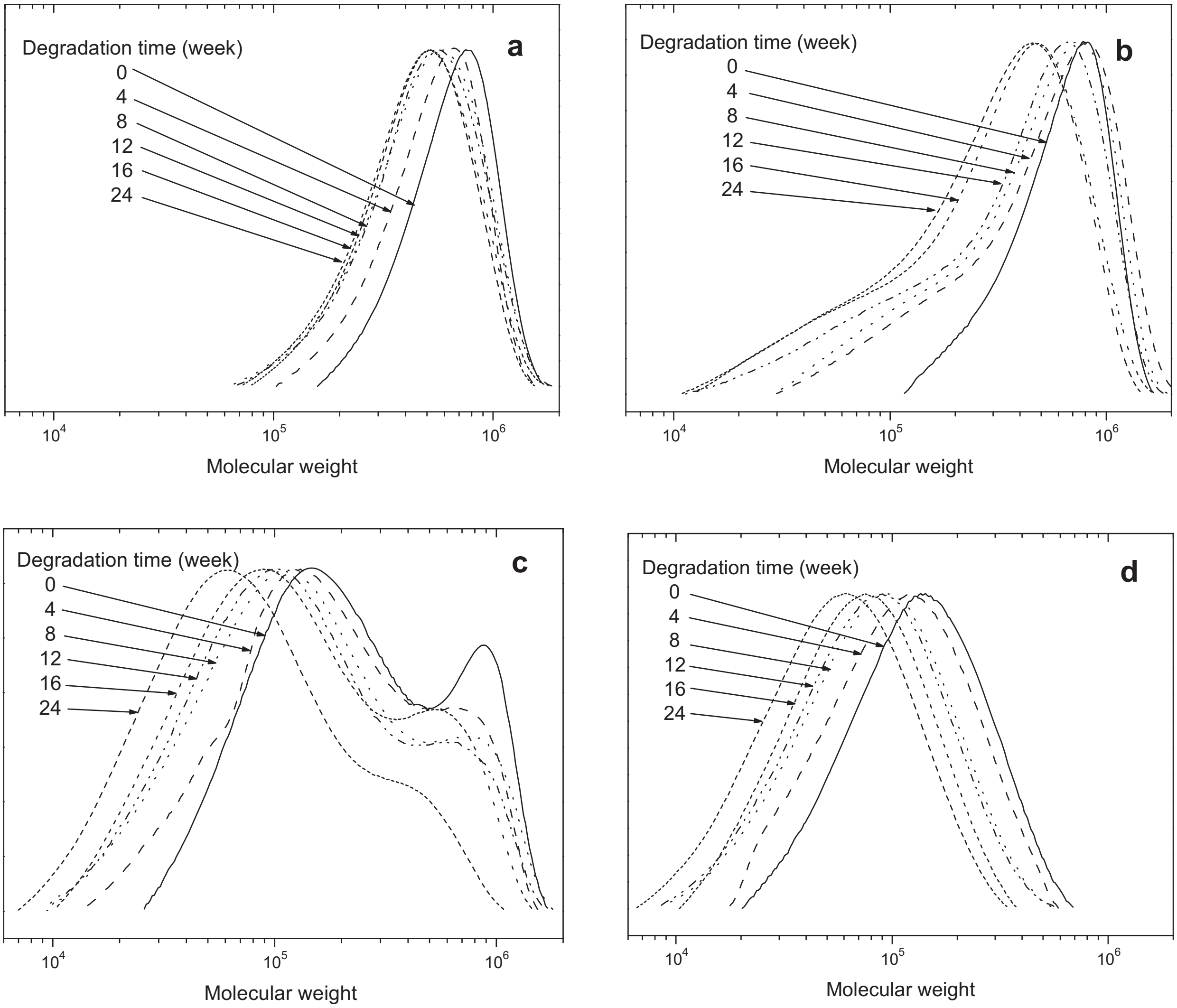

Fig. 11. The molecular weight distributions of the random electrospun blend membranes as a function of hydrolysis time with PHBHHx/PDLLA ratio: (a) 100/0, (b) 75/25, (c) 25/75, and (d) 0/100.

In order to obtain the true strength and modulus of the aligned electrospun fibers (AES-R), the porosity of membranes was considered. Before the tensile test, the porosity of fibrous membranes was measured and it was in the range of 70–90% for whole blend ratio of the fibrous membranes. Table 4 listed the tensile strength and elastic modulus of cast membranes, RES and AES-R membranes. Similar to that of the conventional melt-spun fibers, the tensile strength and elastic modulus of AES-R fibers are greater than that of cast film since the formation of connected crystalline phase along the fiber axis during the electrospinning process. The crystalline lamellae might stack along the fiber axis, as shown in Scheme 1, so that the fibers exhibited harder and stronger properties than that of bulk materials. The effect of composition on the mechanical properties of fibers is also performed similarly to the cast membranes. When amorphous PDLLA was adding into the blend fibers, the number of aligned lamellar stacks of the fibers reduced (i.e. the overall crystallinity decreased); therefore, the hardness and strength of the fibers dropped drastically.

3.5. Degradation behaviors

The *in vitro* degradation process of the PHBHHx/PDLLA electrospun blend fibrous membranes was observed by the changes of morphology, molecular weight, and weight loss during the period of 24 weeks. As shown in Fig. 10, the morphology in the 100/0 and 75/25 blend fibers was rough on the surface after 24 weeks of degradation; however, the 25/75 fibers were comparably smooth but broken down into short fibrous fragments. These changes of morphology during the degradation process were correlated to the structure of blend fibers. Upon degradation, the amorphous regions would be attacked first and degraded faster than the crystalline regions. The surface of the 100/0 blend fibers was rougher than others because there were more numbers of crystalline lamellar stacks. Fig. 11 shows the molecular weight change of the RES blend membranes versus the degradation time. During the period of degradation, the chain scission occurred and then the molecular weight decreased fast while the weight loss was still less than 3% for all kind of RES PHBHHx/PDLLA blend membranes. It indicated that both PHBHHx and PDLLA fibers underwent bulk degradation during hydrolysis. In the meantime, it was found that the molecular weight of the PDLLA (0/100) RES membranes dropped to 42% of the origin while that of the PHBHHx (100/0) RES membranes remained above 70% of the origin. The degradation rate determined by the molecular weight change of RES blend membranes was in the order of the 0/100 > 25/75 > 75/25 > 100/0, which increased with increasing content of PDLLA as expected. It was noted that the amount of PHBHHx portion in the 25/75 fibers reduced significantly with degradation time as shown in Fig. 11c. Because PDLLA formed continuous phase in the 25/75 fibers, the fibers were attacked by water molecules and broken into fragments during the degradation process; and then the dispersed PHBHHx portion surrounded by the PDLLA matrix might be lost together with the broken fragments. The phase segregation in the PDLLA-rich blends and the fiber structure seemed to accelerate the degradation of PHBHHx in the blend fibers.

4. Conclusions

Electrospun nanofibrous membranes of PHBHHx/PDLLA blends were prepared successfully. Due to limited solidification time during electrospinning, PHBHHx and PDLLA are partially mixed in the amorphous phase although they are an immiscible system. On the other hand, the unvaried lateral crystallite size and lamellar stack thickness of PHBHHx phase upon blending implied the crystallization of PHBHHx didn't interfere with PDLLA. Thus, PDLLA molecular chains were segregated outside of PHBHHx lamellar stack that was interstack segregation over the entire composition range. As results, the apparent mechanical properties of fibrous membranes were strongly influenced by the chemical composition and the architectural design, which depended on the degree of the fiber orientation. As PDLLA content increased in the blend system, the elongation and toughness of the electrospun membranes would be improved significantly. In addition, the nanofibers have stronger tensile strength and higher modulus than the thin films due to aligned lamellar stacks structure along the fiber axis. The degradation behavior of PHBHHx/PDLLA blends is directly related to the structure and morphology of the electrospun fibers. Both PHBHHx and PDLLA in the nanofibers display bulk degradation behavior which is observed by the decreased molecular weight during the degradation time. It was found that the degradation rate of PDLLA is faster than that of PHBHHx and the degradation rates is different between the crystalline and amorphous phases, so that the surface morphology of fibers with higher crystallinity was rougher after degradation for 24 weeks. In conclusion, the phase segregation and crystalline structure in the blend fibers provide a good basis to understand the mechanical properties and hydrolytic degradation behaviors of PHBHHx/PDLLA blend fibrous membranes. The stacked-lamellar structure of PHBHHx provides the mechanical strength to the blend fibers, while the amorphous PDLLA increases the hydrolytic degradation rate of the blends. The properties of the nanofibrous membranes of PHBHHx/PDLLA could be adjusted to optimize the mechanical properties and the degradation rates for some specific needs in practical applications.

Acknowledgment

This work was supported by the National Science Council of the Republic of China through the grant of NSC96-2221-E-155-074. The authors thank Dr. Isao Noda of the Procter & Gamble Co. for his kind providing PHBHHx.

References

[1] Huang Z-M, Zhang YZ, Kotaki M, Ramakrishna S. Compos Sci Technol 2003;63(15):2223–53.

[2] Li D, Xia Y. Adv Mater 2004;16(14):1151–70.

[3] Moghe AK, Gupta BS. Polym Rev 2008;48(2):353–77.

[4] Zhong S, Teo WE, Zhu X, Beuerman RW, Ramakrishna S, Yung LYL. J Biomed Mater Res A 2006;79A(3):456–63.

[5] Zong X, Bien H, Chung C-Y, Yin L, Fang D, Hsiao BS, et al. Biomaterials 2005;26(26):5330–8.

[6] Park KE, Kang HK, Lee SJ, Min B-M, Park WH. Biomacromolecules 2006;7(2):635–43.

[7] Sombatmankhong K, Suwantong O, Waleetorncheepsawat S, Supaphol P. J Polym Sci Part B Polym Phys 2006;44(19):2923–33.

[8] Sui X, Shao C, Liu Y. Polymer 2007;48(6):1459–63.

[9] Wang H, Lu X, Zhao Y, Wang C. Mater Lett 2006;60(20):2480–4.

[10] He C-L, Huang Z-M, Han X-J, Liu L, Zhang H-S, Chen L-S. J Macromol Sci Part B Phys 2006;45(4):515–24.

[11] Xu X, Zhuang X, Chen X, Wang X, Yang L, Jing X. Macromol Rapid Commun 2006;27(19):1637–42.

[12] Katti DS, Robinson KW, Ko FK, Laurencin CT. J Biomed Mater Res B 2004;70B(2):286–96.

[13] Ito Y, Hasuda H, Kamitakahara M, Ohtsuki C, Tanihara M, Kang I-K, et al. J Biosci Bioeng 2005;100(1):43–9.

[14] Li W-J, Laurencin CT, Caterson EJ, Tuan RS, Ko FK. J Biomed Mater Res 2002;60(4):613–21.

[15] Lee SY. Biotechnol Bioeng 1996;49(1):1–14.

[16] Sudesh K, Abe H, Doi Y. Prog Polym Sci 2000;25(10):1503–55.

[17] Li J, Zhu B, He Y, Inoue Y. Polym J 2003;35(4):384.

[18] de Lima JA, Felisberti MI. Eur Polym J 2006;42(3):602–14.

[19] Gunaratne LMWK, Shanks RA. Polym Eng Sci 2008;48(9):1683–92.

[20] Hu Y, Sato H, Zhang J, Noda I, Ozaki Y. Polymer 2008;49(19):4204–10.

[21] Gao Y, Kong L, Zhang L, Gong Y, Chen G, Zhao N, et al. Eur Polym J 2006;42(4):764–75.

[22] Lim LT, Auras R, Rubino M. Prog Polym Sci 2008;33(8):820–52.

[23] Chen C-C, Chueh J-Y, Tseng H, Huang H-M, Lee S-Y. Biomaterials 2003;24(7):1167–73.

[24] Nair LS, Laurencin CT. Prog Polym Sci 2007;32(8–9):762–98.
[25] Khoury F, Passaglia E. The morphology of crystalline synthetic polymers. In: Hannay NB, editor. Treatise on solid state chemistry, vol. 3. New York: Plenum Press; 1976. p. 335.
[26] Stein RS, Khambatta FB, Warner FP, Russell T, Escala A, Balizer E. J Polym Sci Polym Symp 1978;63(1):313–28.
[27] Deitzel JM, Kleinmeyer J, Harris D, Beck Tan NC. Polymer 2001;42(1):261–72.
[28] Ishii D, Lee W-K, Kasuya K-I, Iwata T. J Biotechnol 2007;132(3):318–24.
[29] Wang C, Hsu C-H, Hwang IH. Polymer 2008;49(19):4188–95.
[30] Cheng M-L, Lin C-C, Su H-L, Chen P-Y, Sun Y-M. Polymer 2008;49(2):546–53.
[31] Chen H, Liu Z, Cebe P. Polymer 2009;50(3):872–80.
[32] Tsuji H, Nakano M, Hashimoto M, Takashima K, Katsura S, Mizuno A. Biomacromolecules 2006;7(12):3316–20.
[33] Lim CT, Tan EPS, Ng SY. Appl Phys Lett 2008;92(14):141908.
[34] Park JW, Doi Y, Iwata T. Biomacromolecules 2004;5(4):1557–66.
[35] Klug HP, Alexander LE. X-ray diffraction procedures for polycrystalline and amorphous materials. New York: Wiley; 1954.
[36] Kavesh S, Schultz JM. J Polym Sci Part A Polym Chem 1970;8:243–76.

Polymer 52 (2011) 1402–1409

Contents lists available at ScienceDirect

Polymer

journal homepage: www.elsevier.com/locate/polymer

Large amplitude oscillatory shear rheology for nonlinear viscoelasticity in hectorite suspensions containing poly(ethylene glycol)

Weixiang Sun, Yanrui Yang, Tao Wang, Xinxing Liu, Chaoyang Wang, Zhen Tong*

Research Institute of Materials Science, South China University of Technology, Guangzhou 510640, China

A R T I C L E I N F O

Article history:
Received 4 November 2010
Received in revised form
7 January 2011
Accepted 22 January 2011
Available online 1 February 2011

Keywords:
Large amplitude oscillatory shear (LAOS)
Hectorite suspension
Lissajous curve

A B S T R A C T

The effect of poly(ethylene glycol) (PEG) on the nonlinear viscoelasticity of Laponite suspensions containing NaCl was investigated with large amplitude oscillatory shear rheology. The molecular weight (M_w) of PEG was 4k, 10k and 35k, and the concentration of PEG was varied from 0.063 wt% to 2.4 wt%. The dynamic strain sweep showed that the nonlinearity appeared at $\gamma_0 > 30\%$ with a stress overshoot at $\gamma_0 = 50–70\%$. The intensity ratio $I_{3/1}$ from Fourier-transform increased with γ_0 when entering the nonlinear regime and leveled off at $\gamma_0 \geq 100\%$ with higher slope and constant value for the PEG of higher M_w or lower concentration. $I_{3/1}$ revealed the structure difference in the suspensions induced by adsorbing PEG in the nonlinear regime. The minimum- and large-strain rate viscosities η_M and η_L from the Lissajous curve were found to be sensitive to the nonlinear viscoelasticity and the peak of η_M and η_L appeared at lower γ_0 with higher maximum following the same dependency as $I_{3/1}$ on PEG M_w and concentration. The overall nonlinearity parameters N_E and N_V were proposed in this paper and demonstrated to reflect the difference in the Laponite suspensions with PEG more clearly and more effectively.

1. Introduction

The synthetic hectorite clay Laponite can be exfoliated in water to monodisperse nanoplatelets of 30 nm diameter and 1 nm thickness [1,2]. A Laponite suspension will change into an isotropic soft solid after aged over time due to the electrostatic interaction of the negative charge on the surface and positive charge at the rim. The nature of this liquid to solid transition is still controversial [3]. Generally, this soft solid is considered, as a repulsive glass when pH is high and/or salt concentration is low, for the dominant interparticle force is electrostatic repulsion of the surface charge [4]. When the salt concentration is increased to screen the surface charge, the van der Waals attractive force affects the suspension together with the electrostatic interaction and the soft solid is formed through gelation of fractal aggregates of the particles [5]. In both cases, mobility and diffusion of individual particles are hindered by the growth of the aggregate structure following a nonergodic process [6]. External shear reverses the system to a fluid by partially destroying the structure during a process called rejuvenation [7].

Addition of poly(ethylene glycol) (PEG) changes the dynamics and phase behavior of the Laponite suspension. PEG adsorbed on the Laponite surface in a very close-packed manner, acting as a steric hindrance between the neighboring platelets [8–10]. The PEG of low molecular weight (M_w, but $>$ 1k) delayed the aging process of Laponite suspension more effectively [11]. The dynamic moduli in the linear viscoelastic regime for an aged Laponite suspension containing PEG depended on the PEG M_w. When the M_w was lower than 50k, the storage modulus G' decreased with increasing M_w, and then increased with further increasing M_w [12]. This reentrant phenomenon was believed to be resulted from the bridging effect of the adsorbed polymer chains over the platelets [13]. All of the progresses about the clay suspension structure with PEG have been achieved on the data under small strain deformation.

The hectorite clay is widely applied as a rheology modifier in surface coatings, paints, personal care products, adhesives etc. Due to the charged nature of the clay particles, however, the product property is sensitive to a subtle change in pH and ionic strength, which significantly limits the application of the materials. It is therefore a common technique to add polymers to the suspensions, which stabilizes the suspension by steric hindrance after adsorption and prolongs the shelf live under a wider variety of pH and ionic strength [14–16]. The effect of the adsorbed polymer on the linear viscoelastic rheology, i.e. behaviors at the small deformation limit, has been studied intensively [17–20]. However, knowledge of the nonlinear rheology for these suspensions under large shear deformation is desired to predict the flow property in the applications.

---

* Corresponding author. Tel.: +86 20 87112886; fax: +86 20 87110273.
E-mail address: mcztong@scut.edu.cn (Z. Tong).

0032-3861/$ – see front matter © 2011 Elsevier Ltd. All rights reserved.
doi:10.1016/j.polymer.2011.01.048

Several methods have been proposed to study the viscoelasticity under large shear. The large amplitude oscillatory shear (LAOS) rheology was intensively accepted during recent years in studying nonlinear behavior of complex fluids [21–23]. Furthermore, several approaches for data interpretation proposed by different authors have been known sensitive to the intricate and specific structures. Fourier-transform rheology [24], for example, extracted a series of high harmonic waves from the non-sinusoidal responsive stress. The overtone intensity ratio provided the long chain branching [25] or comb-like chain topology [26] in homopolymers, the droplet size distribution in polymer blends [27], and the shear-induced phase separation in block copolymers [28].

For such samples as colloids, emulsions, gels, however, multiple high harmonics appeared depending on the experimental conditions. In these cases, capture and comparison of the overall nonlinear viscoelasticity only by the Fourier-transform rheology becomes limited. Alternatively, four characteristic functions were assigned to describe all the non-sinusoidal responsive stress for these materials [29]. Although it was useful in understanding of specified rheology behavior from the overall nonlinear response, the arbitrariness in choosing the model functions hindered the universality of the superposed function for various materials [30]. Recently, Ewoldt et al. proposed [22] several parameters to describe the distortion of the Lissajous curve from ellipse, which were powerful in interpreting structural-function relationship of complex fluids [31].

In this work, hectorite clay suspensions containing PEG of different M_w and NaCl have been investigated in nonlinear viscoelastic regime using several methods based on the LAOS rheology. What we focus on is which method is more sensitive to detect the change in nonlinear viscoelasticity and microstructure of the clay suspension induced by adsorbing PEG of different M_w at different concentrations, which is hard to be distinguished by conventional methods in the linear regime.

2. Experimental

Synthetic hectorite clay Laponite XLG ($[Mg_{5.34}Li_{0.66}Si_8O_{20}(OH)_4]Na_{0.66}$, Rockwood Ltd.) was used after dried in vacuum at room temperature overnight. Poly(ethylene glycol) (PEG, Uni-Chem) samples of weight average molecular weight M_w 4000 (PEG-4 k), 10,000 (PEG-10 k) and 35,000 (PEG-35 k) with $M_w/M_n = 1.02–1.10$ were used after dried in vacuum at 50 °C. Water was purified by deionization and filtration with a Millipore purification apparatus (18.2 M cm). Other chemicals were all analytic grade reagents.

Laponite suspension of 3 wt% and pH 9–10 was prepared by mixing the clay powder with water under stirring for 15 min and subsequently by ultrasonic radiation for another 15 min for homogenization. PEG was dissolved in water with occasional shakes for 1 day to obtain a 10 wt% solution. The solutions for rheology measurements were prepared by mixing the Laponite suspension and PEG solution with NaCl. The final concentration of Laponite and NaCl in all the test solutions was fixed at 2 wt%, and 5 mM, respectively, while the concentration of PEG was varied. The test solution was further ultrasonicated for 15 min and aged for 48 h prior to the measurement. The samples of Laponite suspensions containing PEG of different M_w and concentrations c_p were denoted in the form of L–M_w–c_p, where L meant the Laponite

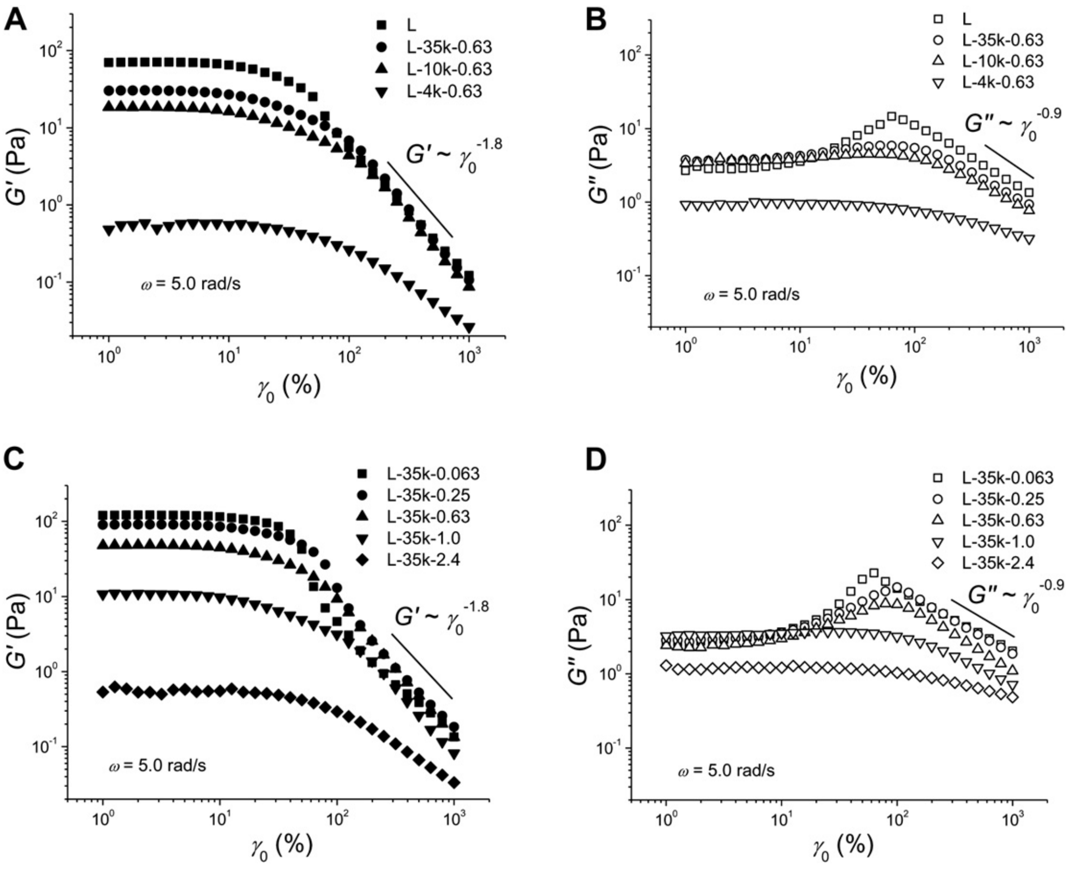

Fig. 1. Dynamic strain amplitude γ_0 sweep results of storage modulus G' and loss modulus G'' for samples with indicated M_w of PEG at 0.63 wt% (A and B) and samples with PEG-35 k at concentrations 0.063–2.4 wt%.

component, M_w the molecular weight of PEG, and c_p the concentration of PEG in wt%. For example, L denotes a sample without addition of PEG, while L-35 k-0.63 denotes a sample with 0.63 wt% of PEG-35 k.

Rheology measurements were carried out at 25 °C on a strain-controlled rheometer (ARES-RFS) using a cone-plate fixture of 50 mm diameter and cone angle of 0.04 rad. Silicon oil was laid on the rim of the fixture to prevent water evaporation. As a common practice for characterizing thixotropic samples [32], the sample was pre-sheared at 200 s^{-1} (76.4 rpm) for 200 s and left at rest for 800 s before each test in order to eliminate the deformation history and establish a reproducible initial state. Dynamic strain sweep was at an angular frequency ω of 5.0 rad/s. For the LAOS, sinusoidal strain $\gamma(t) = \gamma_0 \sin 5t$ at several oscillatory shear strain amplitudes γ_0 was applied and the responsive stress was recorded. 40 cycles were repeated for each γ_0. For the Fourier-transform, the stress was transferred from time domain to the frequency domain. The data were processed with the MITLaos program [33] for the Lissajous curve.

3. Results and discussion

3.1. Response to large amplitude oscillatory shear strain

Fig. 1 shows the storage modulus G' and loss modulus G'' at $\omega = 5.0$ rad/s as a function of shear strain amplitude γ_0 ranging from 1% to 1000% for the Laponite suspensions containing 0.63 wt% of PEG with different M_w (A and B) and PEG-35 k of different c_p (C and D). The linear viscoelasticity regime was observed at $\gamma_0 < 10\%$ for all samples. In this regime, G' decreases with decreasing PEG M_w (Fig. 1A) or with increasing PEG concentration (Fig. 1C). By comparing the results at the same concentration of 0.63 wt% (Fig. 1A and B), $G' > G''$ were observed, indicating that these samples exhibited a gel-like behavior dominated by elasticity. For these samples, G'' did not vary significantly with PEG M_w or concentration, as seen from Fig. 1B and D. In contrast, samples L-4 k-0.63 and L-35 k-2.4 were fluids macroscopically with $G' < G''$, and the values of G'' for these samples were lower than those of the gel-like samples.

Baghdadi et al. investigated the *linear* viscoelasticity behavior of the Laponite-PEO system with PEO M_w ranging from 13k to 1070k without addition of salts while allowed to stand for 80 days [12,34]. They found that with increasing M_w, the storage modulus G' first decreased and then increased until the value exceeding that of the neat Laponite suspension. Therefore, a threshold PEO molecular weight leading to the G' minimum was suggested to separate the two opposite effects of PEO M_w on the gelation and/or glass transition in Laponite suspensions: the interparticle bridging by high-MW PEO and reduction in the effective volume fraction by depletion force of low-MW PEO. Nelson et al. [8,9] reported the adsorption of PEG on the Laponite platelets in the suspension containing NaCl was enhanced for the PEG with lower M_w to inhibit the gelation. The present PEG M_w range was much narrower than that in the literature and the samples contain NaCl, therefore only a part of reported phenomena were observed. The present work will focus on the rheology behavior of the Laponite suspension with PEG and NaCl under the LAOS and does not go further to the linear regime.

All samples enter the nonlinear viscoelastic regime at $\gamma_0 > 30\%$, which is the lower boundary of LAOS measurements. From Fig. 1, it is observed that G' decreases monotonically with γ_0 when $\gamma_0 > 30\%$ for all samples. For the gel samples whose $G' > G''$ in the linear regime, G'' starts to increase as γ_0 exceeds 30%, then decreases monotonically, exhibiting a peak at about $\gamma_0 = 50–70\%$ as the yielding occurs in these samples. On the contrary, for the fluidic samples with $G' < G''$ in the linear regime, G'' directly decreases with γ_0 when $\gamma_0 > 30\%$ without any peak. Furthermore, the decay of G' and G'' at large γ_0 follows the power laws of $G' \sim \gamma_0^{-2\nu'}$ and $G'' \sim \gamma_0^{-\nu'}$, where $\nu' \approx 0.9$. The peak in G'' at the transition from linear to nonlinear regime and the subsequent power law decay of G' and G'' were also observed from the LAOS results on Laponite [1,35], hard or soft sphear colloids [36,37], block copolymer micelles [38], foams [39,40] and emulsions [41] with the decay exponential ν' varied among different systems.

Comparing the samples in Fig. 1, one can find that the PEG M_w and concentration dependence of the height of the G'' peak is the same as G' in the linear regime, i.e. the higher G' in the linear regime, the higher G'' peak appears. This peak is generally considered to come from the dissipative energy during the oscillatory deformation for destroy and rearrangement of the aggregated “house-of-cards” microstructure in the Laponite suspension. The phenomenon is understood as that when the gel structure is stronger the higher dissipative energy arises under shear destruction. However, both G' and G'' become undistinguished among different samples at high γ_0, so the method of dynamic strain sweep is not favorable for detailed study of the nonlinear viscoelasticity.

3.2. Fourier-transform rheology and Lissajous curve

More detailed study on the nonlinear viscoelasticity is allowed with the responsive stress in the LAOS experiment. Fig. 2 depicts

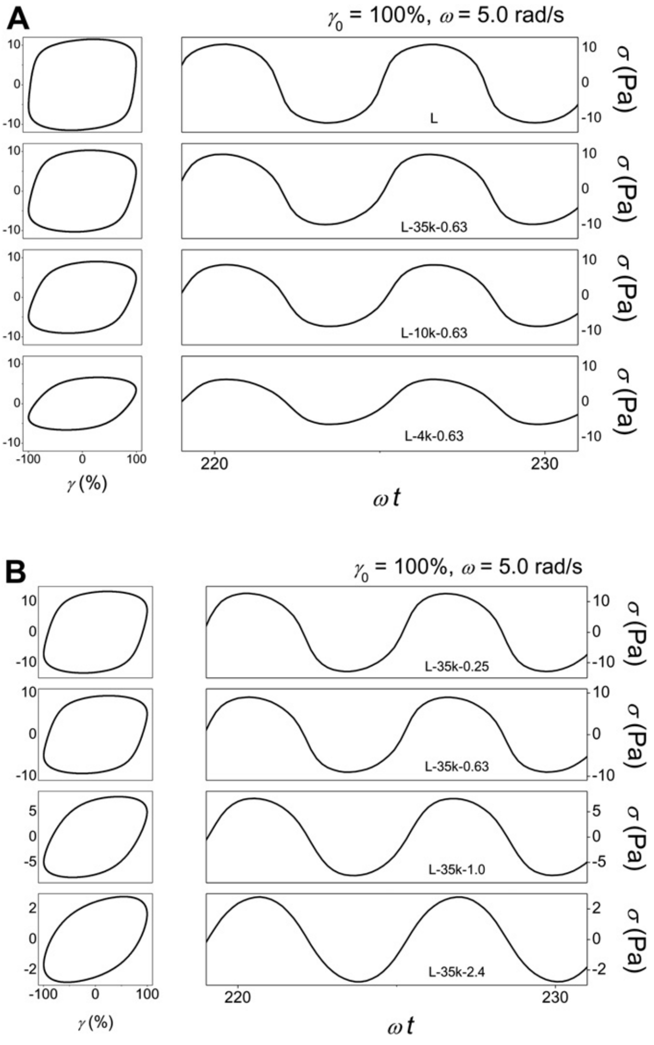

Fig. 2. Responsive stress in LAOS experiments: (A) effect of PEG M_w; (B) effect of PEG concentration.

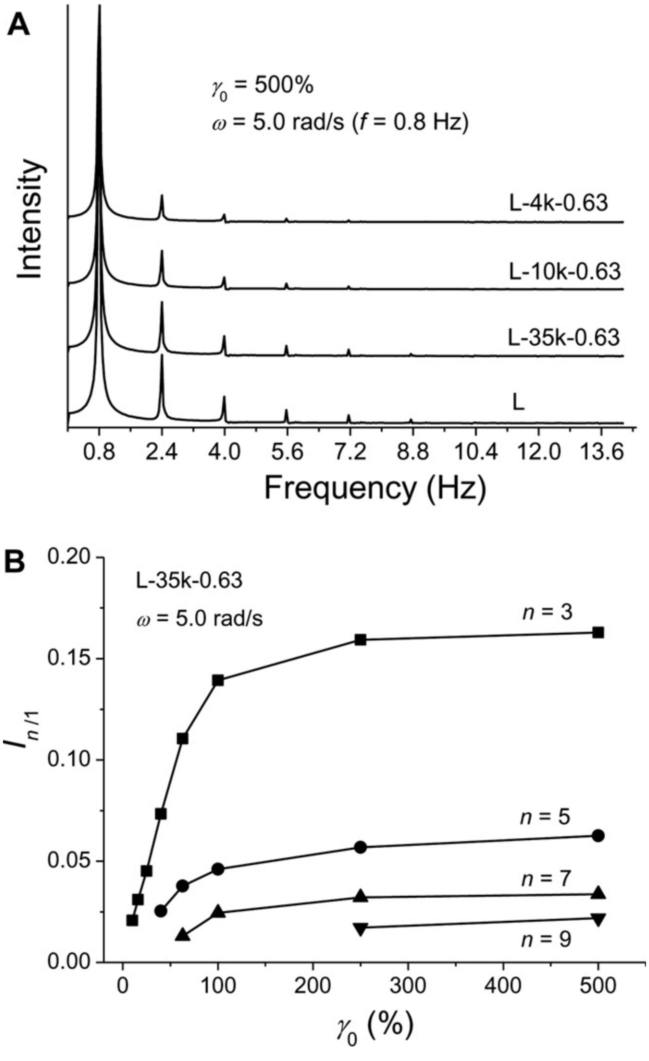

Fig. 3. (A) Fourier-transform spectra of samples L, L-35 k-0.63, L-10 k-0.63 and L-4 k-0.63 with the primary frequency of $\omega/2\pi = 0.8$ Hz and $\gamma_0 = 500\%$, the curves were vertically shifted to avoid overlapping; (B) γ_0 dependence of the relative intensity $I_{n/1}$ for the nth harmonics for the sample L-35 k-0.63.

the stress waveform responsive to a sinusoidal strain γ at the amplitude γ_0 of 100%. The Lissajous curves were shown in the left column and the corresponding stress waveforms were shown in the right column. Nonlinear viscoelasticity was clearly indicated by nonsinusodal stress response and non-ellipse shape of Lissajous curves. As shown in Fig. 2, addition of PEG weakens the nonlinear behavior of the suspension compared with that of the neat Laponite suspension L. Increasing PEG M_w or decreasing PEG concentration was found to enhance the nonlinearity.

The viscoelastic nonlinearity can be interpreted with by Fourier-transform of the responsive stress, which results in a series of odd high harmonics. Fig. 3A demonstrates the Fourier-transform of the stress in the frequency domain at the amplitude γ_0 of 500% for the samples at a constant PEG concentration. The number and intensity of the resolved high harmonic peaks decrease the following sample sequence of L, L-35 k-0.63, L-10 k-0.63, and L-4 k-0.63, suggesting the decrease in viscoelastic nonlinearity with decreasing PEG M_w.

The intensity of the nth harmonics related to the primary one $I_{n/1}$ is plotted as a function of oscillatory strain amptitude γ_0 in Fig. 3B for the suspenstion L-35 k-0.63 as an example. With increasing γ_0, the intensity of high harmonics becomes more evident as $\gamma_0 < 200\%$, and then levels off at higher γ_0. At the same time, the intensity of higher n harmonics becomes undistinguishable.

Therefore, the relative intensity of the amplitude of the 3rd harmony to the primary one, $I_{3/1}$ is widely used to characterize the nonlinear viscoelasticity. In Fig. 4, $I_{3/1}$ is plotted against γ_0. For all samples, $I_{3/1}$ increases dramatically with γ_0 at small γ_0 (30–100%), while is almost a constant at large γ_0 (>100%). The $I_{3/1}$ plateau level here is higher than those reported in literature [24–28], manifesting that the present system has more evident viscoelastic nonlinearity as an ideal object for using LAOS. The increase of $I_{3/1}$ with γ_0 becomes steeper with higher plateau value for the sample with higher M_w or lower c_p of PEG. The range of γ_0 (30–100%) where $I_{3/1}$ increases steeply in Fig. 4 coincides with the γ_0 range where G' begins to decrease and G'' displays a peak in Fig. 1. Therefore, this increase in $I_{3/1}$ would be related to the yielding in the samples. The yielding transition is the sharpest for the neat Laponite suspension L because the interparticle interaction has no any segregation due to absent of PEG.

The above results indicate that the Laponite/PEG suspensions are complex yield stress fluids (YSFs) whose yielded flow state shows nonlinear viscoelasticity rather than simple plasticity [42,43], The value of $I_{3/1}$ depends on PEG M_w and concentration, similar to the G' dependence on M_w and c_p in the linear regime, so that the viscoelastic nonlinearity in the yielding flow may be linked

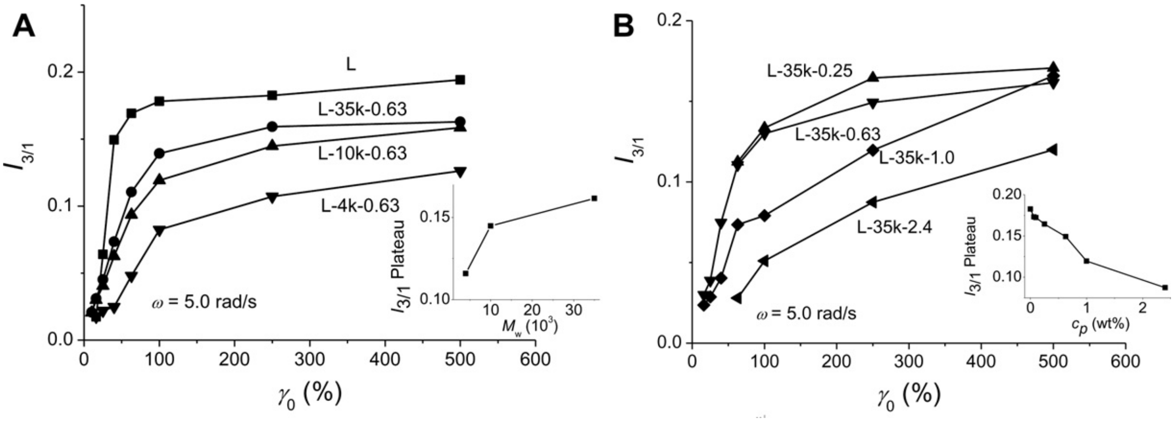

Fig. 4. Relative intensity $I_{3/1}$ of the 3rd harmonic to the primary one varying with amptitude γ_0: (A) suspensions with indicated PEG M_w at 0.63 wt% and the inset presents the M_w dependence of the $I_{3/1}$ plateau value; (B) suspensions with indicated PEG concentration c_p and the inset is the c_p dependence of the $I_{3/1}$ plateau value.

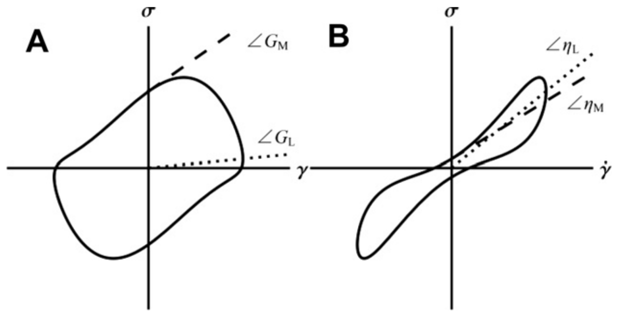

Fig. 5. Schematic representation for the definition of (A) minimum- and large-strain modulus G_M and G_L, as well as (B) minimum- and large-strain rate viscosity η_M and η_L.

to the elasticity before yielding, i.e., in the linear regime. Lower PEG M_w and higher c_p lead to a restricted gelation by PEG adsorption on the platelets and separation of the particle aggregation. Therefore, if G' is lower in the linear regime, the corresponding viscoelastic nonlinearity is also lower in the yielded flow under the LAOS.

3.3. Descriptive parameters G_M, G_L, η_M, and η_L

The $I_{3/1}$ parameter cannot represent the overall viscoelastic nonlinearity of the present Laponite suspensions containing PEG and NaCl because the harmonic higher than the 3rd is ignored. Alternatively, the Lissajous curve allows us to examine the overall nonlinear stress response by comparing the curve shape. Fig. 2 illustrates some nonlinear stress responses with the Lissajous curve. Ewoldt et al. [22] proposed a series of parameters describing the deviation of Lissajous curve from ellipse in order to characterize nonlinear viscoelasticity. The minimum-strain modulus G_M and large-strain modulus G_L were defined as:

$$G_M \equiv \frac{d\sigma}{d\gamma}\bigg|_{\gamma=0}, \quad G_L \equiv \frac{\sigma}{\gamma}\bigg|_{\gamma=\pm\gamma_0} \tag{1}$$

Similarly, the minimum- and large-strain rate viscosity η_M and η_L were defined as:

$$\eta_M \equiv \frac{d\sigma}{d\dot{\gamma}}\bigg|_{\dot{\gamma}=0}, \quad \eta_L \equiv \frac{\sigma}{\dot{\gamma}}\bigg|_{\dot{\gamma}=\pm\dot{\gamma}_0} \tag{2}$$

where the oscillatory strain rate $\dot{\gamma}(t) = \gamma_0\omega\cos\omega t = \dot{\gamma}\cos\omega t$, where $\dot{\gamma}_0$ was the amplitude of strain rate. The geometrical representation of these parameters is illustrated in Fig. 5. G_M and G_L represent the elastic (in-phase) response to the LAOS strain, while η_M and η_L the viscous (out-of-phase) response. In the case of linear viscoelasticity, the Lissajous curve is an ellipse, hence $G_M = G_L$ and $\eta_M = \eta_L$. These parameters were evaluated by the MITLaos program [33] using the Fourier-transform relations derived by Ewoldt et al. [22], in which the strain and stress waveforms were input.

Fig. 6 displays G_M, G_L, η_M, and η_L for the Laponite suspensions with 0.63 wt% PEG of different M_w as a function of strain amplitude γ_0. For all the samples, G_M and G_L curves are similar to those in Fig. 1A, exhibiting a plateau in the linear regime ($\gamma_0 \leq 30\%$) and a decrease with γ_0 in the nonlinear regime, except for the sample L-4 k-0.63 which is a liquid. These features come from their nature of the elastic component of viscoelasticity and the plateau value of G_M

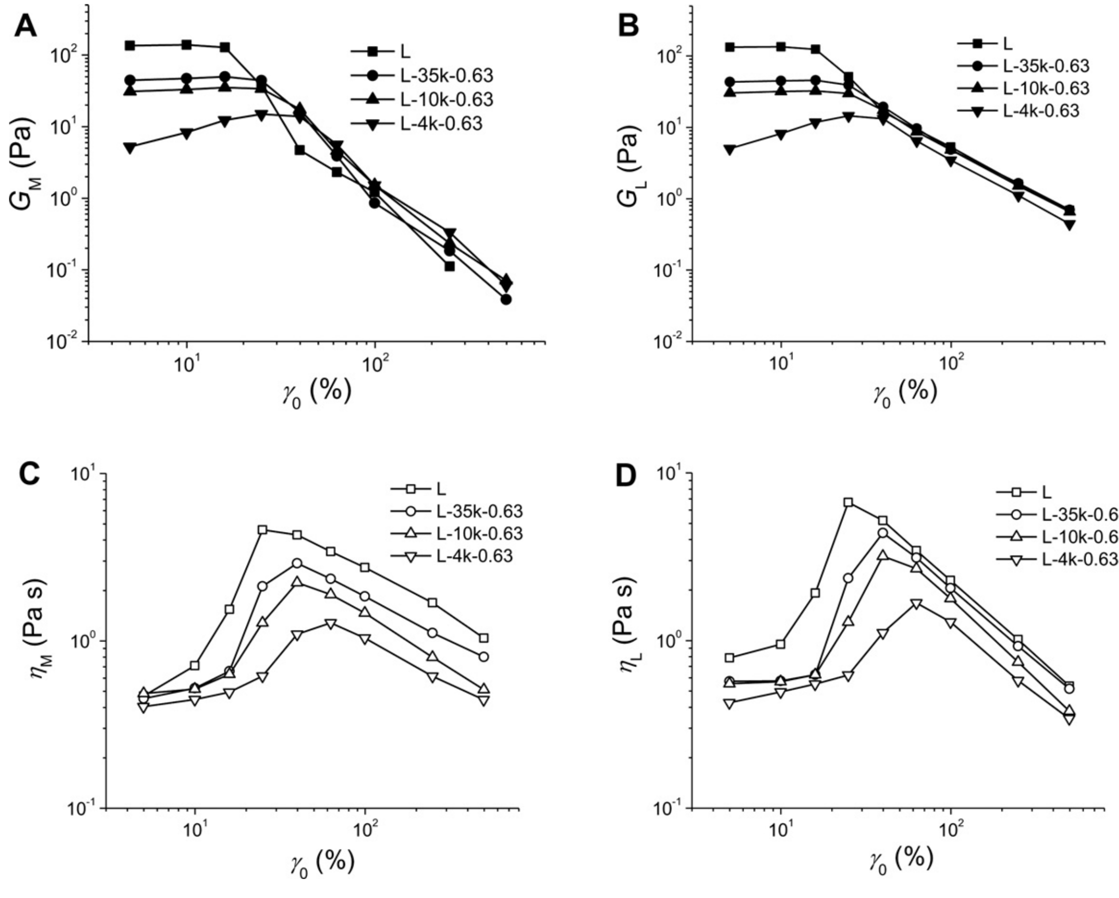

Fig. 6. Minimum-strain modulus G_M (A), large-strain modulus G_L (B), minimum-strain rate viscosity η_M (C), and large-strain rate viscosity η_L (D) as a function of strain amplitude γ_0 at $\omega = 5.0$ rad/s.

and G_L decreases as L > L-35 k-0.63 > L-10 k-0.63 > L-4 k-0.63, the same sequence as G' in Fig. 1A. On the other hand, the appearance of nonlinearity can be clearly recognized from the deflection of each curve. However, G_M and G_L become indistinguishable for different samples in the nonlinear regime ($\gamma_0 > 30\%$).

There is a peak at each curve of η_M and η_L against γ_0 for the four samples, similar to that in Fig. 1B due to the structural rearrangement. But the difference in different samples is more obvious in Fig. 6C and D. The peak position and peak value vary with the samples. The peak of η_M and η_L appears at lower γ_0 with higher value following the sample sequence as L-4 k-0.63, L-10 k-0.63, L-35 k-0.63, and L, which is similar to that of G'' in Fig. 1B. But the appearance of nonlinearity becomes easier to be identified from these η_M and η_L against γ_0 curves. The η_M and η_L from the Lissajous curve appear to be more sensitive to the slight structure change for the Laponite suspension in the nonlinear regime. The γ_0 dependence curve of G_M, G_L, η_M, and η_L for the Laponite suspensions containing PEG-35 k at several concentrations is similar to the corresponding one in Fig. 6 and not shown here for succinctness.

3.4. Parameters for overall nonlinear viscoelasticity

From the schematic illustration in Fig. 5, one may expect that the detail shape of the Lissajous curve, especially distortion from the ellipse (linear response), can be deduced quantitatively by relating the parameters G_M and G_L for elastic response and η_M and η_L for viscous response. Because the difference between G_M and G_L and between η_M and η_L characterizes the deviation of Lissajous curve from the ellipse and hence the viscoelastic nonlinearity. Thus, we suggest two parameters N_E and N_V to express the overall nonlinearity in viscoelasticity as:

$$N_E = \frac{G_L - G_M}{G'_1}, \quad N_V = \frac{\eta_L - \eta_M}{G''_1/\omega} \tag{3}$$

where (see Appendix)

$$\begin{aligned} G_L - G_M &= \sum_{n=3,\text{odd}}^{\infty} G'_n \cdot \left[n - (-1)^{\frac{n-1}{2}}\right] \\ \eta_L - \eta_M &= \sum_{n=3,odd}^{\infty} \frac{G''_n}{\omega} \cdot \left[n(-1)^{\frac{n+1}{2}} - (-1)^n\right] \end{aligned} \tag{4}$$

Therefore, N_E and N_V is the sum of all the higher harmonic storage moduli and dynamic viscosities ($n \geq 3$) relative to the first ones ($n = 1$), respectively, characterizing the *overall* nonlinearity in viscoelasticity. In the linear viscoelastic regime, $N_E = N_V = 0$. For nonlinear viscoelastic response, N_E and N_V can be positive, negative, or zero, depending on the shape of the Lissajous curve. The value of N_E and N_V can be higher than unity because there is a multiplier in the square bracket which may be large than unit. In Fig. 7, N_E and N_V calculated from equation (3) were plotted against γ_0. For all samples, N_E, the elastic part of nonlinear response, increases from 0 at low γ_0 with increasing γ_0. In contrast, N_V decreases with increasing γ_0 even to negative values. We can observe the different nonlinear responses for our samples at high γ_0 more clearly than from other figures. The sample L shows the strongest nonlinearity. Addition of PEG with lower M_w or higher concentration weakens the nonlinearity of the suspension at high γ_0. Although the physical meaning of N_E and N_V is still unknown, like the case of parameters G_M, G_L, η_M, and η_L, it is more effective to reveal and compare the nonlinear viscoelastic response of the Laponite suspensions containing PEG and NaCl with these parameters.

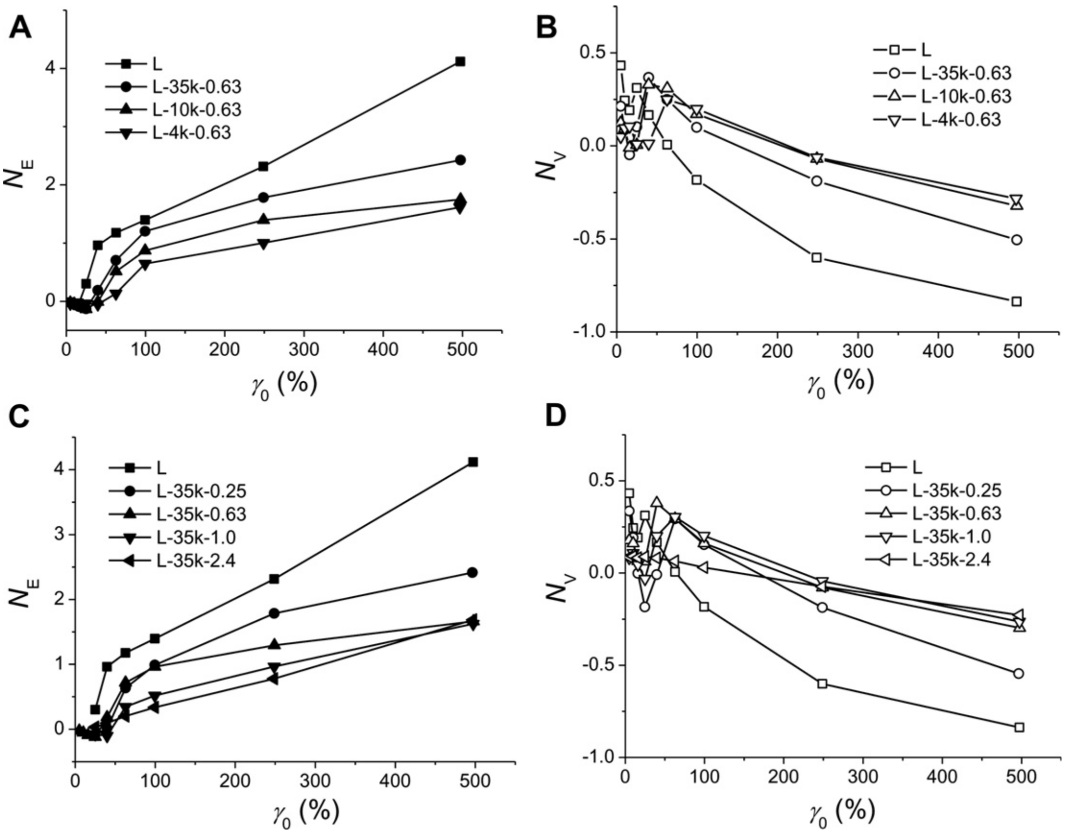

Fig. 7. Overall nonlinear viscoelasticity parameters N_E (A and C) and N_V (B and D) plotted against γ_0 at $\omega = 5.0$ rad/s.

4. Conclusions

Laponite suspension is a yielding fluid with aggregated structure of the "house-of-cards". PEG chains in the Laponite suspension are adsorbed on the platelets to change the interparticle interaction and to hinder the formation of platelet networks. This is the first experimental observation of the LAOS rheology on the nonlinear viscoelastic behavior of the Laponite suspension containing PEG and NaCl. Increase in PEG M_{w} or decrease in PEG concentration enhanced the nonlinear viscoelasticity of the clay suspension, showing macromolecule effect. The relative intensity $I_{3/1}$ of the 3rd harmonic reflected the delicate difference in the nonlinear viscoelasticity induced by added PEG with different M_{w} and concentrations, which was hardly distinguished by conventional dynamic strain sweep. We proposed two parameters N_{E} and N_{V} for describing the Lissajous curve modified from the geometric parameters G_{M} and G_{L}. N_{E} and N_{V} can reveal the difference in the overall nonlinear viscoelasticity more clearly and more effectively. Consequently, the LAOS rheology provided the information about the microstructure change in the clay-polymer suspension and the appropriate interpretation was desired to explore this unclear information.

Acknowledgments

The financial support from the NSF of China (50773024 and 21074040), the National High Technology Research and Development Program of China (2009AA03Z102), and the Fundamental Research Funds for the Central Universities, SCUT is gratefully acknowledged.

Appendix. Derivation of N_{E} and N_{V}

The Lissajous curve is obtained by plotting $\sigma(t)$ against $\gamma(t)$. For an incompressible fluid under uniform shear flow, the equation of the Lissajous curve can be expressed by the following functions:

$$\begin{cases} \gamma(t) = \gamma_0 \sin(t') \\ \sigma(t) = \sum\limits_{n=1,\mathrm{odd}}^{\infty} \sigma_n \sin(nt' + \delta_n) \end{cases}$$

where $t' = \omega t$, $t' > 0$. From the definitions of G_{M} and G_{L},

$$\begin{aligned} G_M &\equiv \left(\frac{\mathrm{d}\sigma}{\mathrm{d}\gamma}\right)\Big|_{\gamma=0} \\ &= \frac{(\mathrm{d}\sigma/\mathrm{d}t')}{(\mathrm{d}\gamma/\mathrm{d}t')}\Big|_{t'=k\pi} \\ &= \sum_{n=1,\mathrm{odd}}^{\infty} \frac{n\sigma_n \cos(nk\pi + \delta_n)}{\gamma_0 \cos k\pi}, (k = 0,1,2,\ldots) \end{aligned}$$

$$\begin{aligned} G_L &\equiv \frac{\sigma}{\gamma}\Big|_{\gamma=\pm\gamma_0} \\ &= \frac{\sigma}{\gamma}\Big|_{t'=k\pi+\frac{\pi}{2}} \\ &= \sum_{n=1,\mathrm{odd}}^{\infty} \frac{\sigma_n \sin\left[n\left(k\pi + \frac{\pi}{2}\right) + \delta_n\right]}{\gamma_0 \sin\left(k\pi + \frac{\pi}{2}\right)} \\ &= \sum_{n=1,\mathrm{odd}}^{\infty} \frac{\sigma_n \sin\left[n\left(k\pi+\frac{\pi}{2}\right)+\delta_n\right]}{\gamma_0 \cos k\pi}, (k = 0,1,2,\ldots) \end{aligned}$$

$$\therefore G_L - G_M = \sum_{n=1,\mathrm{odd}}^{\infty} \frac{\sigma_n}{\gamma_0} \cdot a_n$$

Here,

$$a_n = \frac{n\cos(nk\pi + \delta_n) - \sin\left[n\left(k\pi + \frac{\pi}{2}\right) + \delta_n\right]}{\cos k\pi}, (k = 0,1,2,\ldots,n = 1,3,5,\ldots)$$

Note that

$$\begin{aligned} a_1 &= 0 \\ a_3 &= 4\cos\delta_3 \\ a_5 &= 4\cos\delta_5 \\ &\vdots \\ a_n &= \left[n - (-1)^{\frac{n-1}{2}}\right]\cos\delta_n, (n = 1,3,5,\ldots) \\ \therefore G_L - G_M &= \sum_{n=3,\mathrm{odd}}^{\infty} G'_n \cdot \left[n - (-1)^{\frac{n-1}{2}}\right] \end{aligned}$$

where

$$G'_n = \frac{\sigma_n}{\gamma_0}\cos\delta_n$$

Similarly, we can obtain that

$$\eta_L - \eta_M = \sum_{n=3,\mathrm{odd}}^{\infty} \frac{G''_n}{\omega} \cdot \left[n(-1)^{\frac{n+1}{2}} - (-1)^n\right]$$

where

$$G''_n = \frac{\sigma_n}{\gamma_0}\sin\delta_n$$

References

[1] Ramsay JDF. J Colloid Interface Sci 1986;109:441–7.
[2] Avery RG, Ramsay JDF. J Colloid Interface Sci 1986;109:448–54.
[3] Tanaka H, Meunier J, Bonn D. Phys Rev E 2004;69:031404.
[4] Abou B, Bonn D, Meunier J. Phys Rev E 2001;64:021510.
[5] Cocard S, Tassin JF, Nicolai T. J Rheol 2000;44:585–94.
[6] Tanaka H, Jabbari-Farouji S, Meunier J, Bonn D. Phys Rev E 2005;71:021402.
[7] Di Leonardo R, Ianni F, Ruocco G. Phys Rev E 2005;71:011505.
[8] Nelson A, Cosgrove T. Langmuir 2004;20:2298–304.
[9] Nelson A, Cosgrove T. Langmuir 2004;20:10382–8.
[10] Hu X, Wang T, Xiong L, Wang C, Liu X, Tong Z. Langmuir 2009;26:4233–8.
[11] Mongondry P, Nicolai T, Tassin J-F. J Colloid Interface Sci 2004;275:191–6.
[12] Baghdadi H, Jensen E, Easwar N, Bhatia S. Rheol Acta 2008;47:121–7.
[13] Loizou E, Butler P, Porcar L, Kesselman E, Talmon Y, Dundigalla A, et al. Macromolecules 2005;38:2047–9.
[14] Crowl VT, Malati MA. Discuss Faraday Soc 1966;42:301–12.
[15] Napper DH. Polymeric stabilization of colloidal dispersions. Academic Press; 1983.
[16] Sato T, Ruch R. Stabilization of colloidal dispersions by polymer adsorption. Marcel Dekker; 1980.
[17] Frith WJ, Strivens TA, Mewis J. J Colloid Interface Sci 1990;139:55–62.
[18] Grover GS, Bike SG. Langmuir 1995;11:1807–12.
[19] de LCostello BA, Luckham PF, Tadros TF. J Colloid Interface Sci 1992;152: 237–46.
[20] Elliott SL, Russel WB. J Rheol 1998;42:361–78.
[21] Cho KS, Hyun K, Ahn KH, Lee SJ. J Rheol 2005;49:747–58.
[22] Ewoldt RH, Hosoi AE, McKinley GH. J Rheol 2008;52:1427–58.
[23] Giacomin AJ, Dealy JM. Using large-amplitude oscillatory shear. In: Collyer AA, Clegg DW, editors. Rheological measurement. Chapman & Hall; 1998. p. 327–56.
[24] Wilhelm M. Macromol Mater Eng 2002;287:83–105.
[25] Hyun K, Baik ES, Ahn KH, Lee SJ, Sugimoto M, Koyama K. J Rheol 2007;51:1319–42.
[26] Hyun K, Wilhelm M. Macromolecules 2009;42:411–22.
[27] Carotenuto C, Grosso M, Maffettone PL. Macromolecules 2008;41:4492–500.
[28] Oelschlaeger C, Gutmann JS, Wolkenhauer M, Spiess H-W, Knoll K, Wilhelm M. Macromol Chem Phys 2007;208:1719–29.
[29] Klein CO, Spiess HW, Calin A, Balan C, Wilhelm M. Macromolecules 2007;40:4250–9.
[30] Klein C, Venema P, Sagis L, van der Linden E. J Non-Newtonian Fluid Mech 2008;151:145–50.
[31] Ewoldt RH, Clasen C, Hosoi AE, McKinley GH. Soft Matter 2007;3:634–43.
[32] Mewis J, Wagner NJ. Adv Colloid Interface Sci 2009;147–148:214–27.

[33] Kang H, Wen Q, Janmey PA, Tang JX, Conti E, MacKintosh FC. J Phys Chem B 2009;113:3799–805.
[34] Baghdadi HA, Sardinha H, Bhatia SR. J Polym Sci B Polym Phys 2005;43:233–40.
[35] Willenbacher N. J Colloid Interface Sci 1996;182:501–10.
[36] Carrier V, Petekidis G. J Rheol 2009;53:245–73.
[37] Mason TG, Weitz DA. Phys Rev Lett 1995;75:2770–3.
[38] Mohan PH, Bandyopadhyay R. Phys Rev E 2008;77:041803.
[39] Rouyer F, Cohen-Addad S, Höhler R, Sollich P, Fielding S. Eur Phys J E 2008;27:309–21.
[40] Marze S, Guillermic RM, Saint-Jalmes A. Soft Matter 2009;5:1937–46.
[41] Mason TG, Bibette J, Weitz DA. Phys Rev Lett 1995;75:2051–4.
[42] Keentok M. Rheol Acta 1982;21:325–32.
[43] Ewoldt R, Winter P, Maxey J, McKinley G. Rheol Acta 2010;49:191–212.

Polymer 52 (2011) 1410–1416

Contents lists available at ScienceDirect

Polymer

journal homepage: www.elsevier.com/locate/polymer

NMR relaxation reveals modifications in rubber phase dynamics during long-term degradation of high-impact polystyrene (HIPS)

Francisco Vilaplana [a,b], Sigbritt Karlsson [a], Amparo Ribes-Greus [b], Christian Schade [c], Nikolaus Nestle [c,*]

[a] Department of Fibre and Polymer Technology, School of Chemical Science and Engineering, KTH – Royal Institute of Technology, Teknikringen 56-58, SE-10044 Stockholm, Sweden
[b] Instituto de Tecnología de Materiales (ITM), Universidad Politécnica de Valencia, Camino de Vera s/n, E-46022 Valencia, Spain
[c] BASF SE, 67056 Ludwigshafen, Germany

ARTICLE INFO

Article history:
Received 27 July 2010
Received in revised form
31 January 2011
Accepted 2 February 2011
Available online 24 February 2011

Keywords:
High-impact polystyrene (HIPS)
Nuclear magnetic resonance relaxation
Polybutadiene rubber

ABSTRACT

The microstructure of rubber-modified polystyrene after thermal ageing at 90 °C and multiple extrusion was analyzed by time-domain nuclear magnetic resonance (TD-NMR) in a non-destructive manner. The transverse magnetization decay behaviour observed in TD-NMR was related to the total rubber fraction and its cross-linking density. The data reveal different mechanisms of long-term rubber degradation in high-impact polystyrene (HIPS) during thermo-oxidation and multiple processing: Multiple processing causes a slight increase in the cross-linking density of the rubber phase, without appreciably altering the total amount of rubber fraction. Thermo-oxidation is accompanied by a significant overall decrease of the rubber fraction, an increase of the cross-linking density, and a pronounced increase of the non-cross-linked fraction (chain ends and fragmented segments). The NMR results correlate well with spectroscopic observations and moderately with macroscopic mechanical properties.

1. Introduction

The high impact resistance of styrenic polymers such as high-impact polystyrene (HIPS) or acrylonitrile-styrene-butadiene copolymer (ABS) is achieved by incorporating a disperse rubber phase (usually polybutadiene or styrene/butadiene rubber) into the styrenic rigid matrix (polystyrene or styrenic copolymers such as styrene/acrylonitrile). In particular, HIPS is generally produced by free radical polymerization of styrene in the presence of variable amounts of polybutadiene (PB) (usually 5–12 weight % PB). The resulting material can be structurally described as a multiphase system in which styrene grafted PB rubber particles are dispersed in a continuous rigid polystyrene (PS) matrix. This multiphase structure confers upon HIPS its improved fracture resistance (impact strength, elongation at break, and fracture toughness) together with reduced transparency, modulus and tensile strength compared with unmodified PS [1,2].

The introduction of a rubbery phase enhances the sensitivity of the material to degradative agents and processes. Previous research has been devoted to the study of the oxidative degradation of ABS [1,3–9] and HIPS [1,10–19]. Early works on the thermal- and photo-oxidation of ABS and HIPS revealed that the PB phase is selectively attacked during the initial stages of degradation, with hydroperoxide formation being the initiation mechanism [4,8,9,11–14]. Further studies employing infrared spectroscopy identified the different steps of the oxidation process [6,16]. The initial degradation of the PB phase leads to the progressive consumption of unsaturated groups and the formation of different products containing oxidized groups [3,6,11,16,20]. With prolonged oxidative exposure, a wide range of cross-linking reactions can take place in the oxidized moieties with the formation of different cross-linked structures, such as unstable peroxide gel, ether gel, and saturated gel structures [3,13]. Finally, chain scission occurs during more severe degradation, leading to fragmentation and scission of the PB-PS graft [3,6,13]. Further oxidation of the PS phase in PB-modified styrenic polymers is promoted by the free radicals formed during degradation of the rubber phase, in contrast to the oxidation process of pure PS [6].

Degradation processes in rubber-modified styrenic copolymers induce a deterioration of the mechanical properties and long-term stability at a macroscopic scale [5,7,10,11,21–24]. The study of such degradation processes to which polymeric materials are subjected during their life cycle is fundamental to assess their further waste management procedures, including their recyclability [25]. A dual experimental approach employing multiple processing and thermo-oxidation has been proposed in our previous work to model the life

---

* Corresponding author. Tel.: +49 621 60 93985; fax: +49 621 60 66 93985.
E-mail address: nikolaus.nestle@basf.com (N. Nestle).

0032-3861/$ – see front matter © 2011 Elsevier Ltd. All rights reserved.
doi:10.1016/j.polymer.2011.02.005

cycle of recycled high-impact polystyrene (HIPS) [24]. Thermo-mechanical degradation induced by multiple processing under high mechanical shear in limited oxygen atmosphere has been shown to cause alterations in the rheological behaviour and the mechanical properties of ABS and HIPS [5,23,24,26–28]; these changes may be due to chain scission in the PS phase and modifications in the physical structure of the rubber phase [23,28]. In addition, thermo-oxidation involves interconnected physical and chemical processes, which affect the structure and the overall properties of both the rigid PS and the rubber PB phases [10]. Large alterations in the tensile, impact, and flow properties have been reported, resulting in an embrittlement of the material [7,10,11,21,29].

Another experimental approach to study the dynamics of rubber components in polymers is nuclear magnetic resonance (NMR) relaxation. The transverse relaxation times in rubbery materials are especially sensitive to cross-linking; rubber components with different degree of cross-linking can therefore be discerned much more easily than by means of other chemical or spectroscopic techniques [30,31]. In this study, relaxation NMR has been applied for the first time to study the mobility of the rubber components in HIPS subjected to long-term degradation. New insights about the degradative effects of multiple processing and thermo-oxidation on the rubber phase in HIPS are revealed, casting some light on the molecular mechanisms that cause deterioration of the macroscopic properties of rubber-modified styrenic polymers. These results are correlated with traditional wet-chemistry measurements, such as swell index and gel content, and with changes in chemical groups and mechanical properties earlier presented [23,24].

2. Experimental

2.1. Materials and sample preparation

Virgin high-impact polystyrene (HIPS), commercial grade Polystyrol 486M (BASF Española S.A., Spain), was employed to simulate the life cycle of recycled HIPS. A dual-pronged experimental approach was used [24]: HIPS processing and recycling was modelled through multiple processing up to nine cycles, employing a double-screw extruder (Collin Kneader 25x30D, Dr. Collin GmbH, Germany) with a maximum extrusion temperature of 200 °C. The degradation processes during service life were simulated by thermo-oxidation at 90 °C in a forced-ventilation oven (Memmert 600, Memmert GmbH, Germany), following the guidelines of the ASTM D 5510-94 standard; the samples were removed for analysis after different exposure times between 1 and 32 days.

2.2. Relaxation NMR

Transverse relaxation time measurements were conducted on a minispec mq 20 NMR analyser (Bruker, Rheinstetten, Germany) equipped with a variable-temperature air-flow probe head. This probe head offers a sample diameter of 10 mm, and the RF field is homogeneous over 10 mm in height. In preparing the samples, it was made sure that the whole sample material was placed inside this homogeneous region. NMR experiments were run at a temperature of 40 °C. The proton NMR frequency used in the experiments was 19.59 MHz, and the typical pulse length was 2.3 μs for the 90°-pulse. The NMR sequence used was a combination of a solid echo with single and double Hahn echoes [32,33]. Using this technique, most of the free induction decay (FID) can be refocused into a solid echo and the additional decay of the FID due to resonance offsets resulting from different chemical shifts and magnetic field inhomogeneity can also be compensated to a great extent. The solid echo decay was sampled using a dwell time of 400 ns, Hahn echoes were acquired from a minimal echo time of 92 μs to about 10 ms or longer. The maximal echo time recorded was chosen automatically by the instrument script on the basis of the residual signal level and the slope of the signal. The solid echoes and the Hahn echoes were acquired in a way that overlapping echo times allowed interpolation and rescaling of the amplitudes. The resulting magnetization decay curves were evaluated both by means of a generalized inverse Laplace transform (ILT) [34] and by fitting the sum of a Gaussian and a single exponential function (*ge* model, Equation (1))

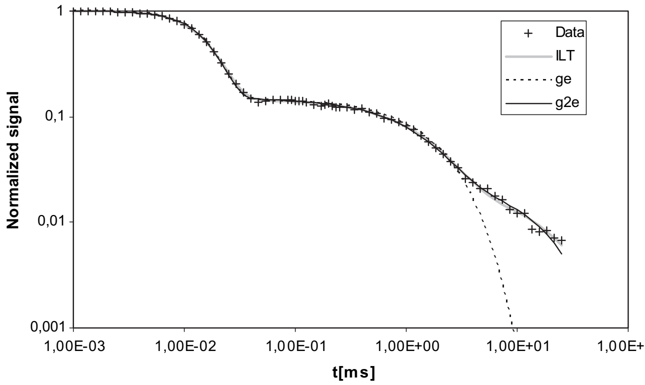

Fig. 1. Magnetization decay curve for the virgin HIPS sample with fits using the inverse Laplace transform (ILT) and the models with one (*ge*) or two (*g2e*) exponential components. While the fit with the *ge* model is obviously suboptimal, the differences in quality between the *g2e* and ILT fits are minimal. All three models show the same signal contribution from PS matrix and rubber (signal level at about $t = 1$ ms).

$$M(t) = p_g \exp\left(\left(-t/T_{2g}\right)^2\right) + p_e \exp(-(t/T_{2e})) \tag{1}$$

or the sum of a Gaussian and two exponentials (*g2e* model, Equation (2))

$$\begin{aligned} M(t) = {} & p_g \exp\left(\left(-t/T_{2g}\right)^2\right) + p_{e1} \exp(-(t/T_{2e1})) \\ & + p_{e2} \exp(-(t/T_{2e2})) \end{aligned} \tag{2}$$

to the data. $M(t)$ denotes the transverse proton magnetization signal as a function of time, p_g the normalized amplitude of the Gaussian component, T_{2g} the corresponding relaxation time, p_e and T_{2e} and p_{ei} and T_{2ei} the amplitudes and relaxation times of the exponential components. In Fig. 1, a comparison of the fit quality achieved with the different evaluations is given for the virgin HIPS sample. The components p_{e1} and p_{e2} can be interpreted as the signal contributions from cross-linked butadiene rubber (p_{e1}) and from non cross-linked material such as loose chain ends and mineral oil (p_{e2}).

2.3. Gel content, swell index, molecular weight distributions, and rubber particle size measurements

For gel content and swell index determination, 2.6 g of HIPS sample were suspended in 43 g of toluene, centrifuged, and the supernatant solution discarded. The swollen gel was isolated and dried. The swell index is given by the amount of solvent, which the dry gel had absorbed prior to drying. The gel content is the fraction of the dry gel versus the initial material loading. Molecular weight distributions were determined using size exclusion chromatography (SEC) in THF solution against relative calibration with polystyrene standards. The SEC was equipped with an Agilent 1100 pump system (Agilent, Santa Clara, USA), 5 PLGel mixed-B columns (Varian, Germany) and an Agilent 1100 refractive index detector (Agilent, Santa Clara, USA). The separation was performed on 100 μl injections of 2 g/l samples with a THF flow rate of 1.2 ml/min at 35 °C. Rubber particle size determinations were done in cyclohexane suspension by Mie-Fraunhofer scattering.

2.4. Spectroscopic and mechanical properties

The chemical changes induced by multiple processing and thermo-oxidation on HIPS structure were studied by infrared and Raman spectroscopy. The unsaturated indexes from PB (trans-1,4, cis-1,4, and vinyl-1,2 indexes) were calculated from Raman spectroscopy following a deconvolution methodology previously presented [23]. FTIR was employed to monitor the formation of oxidized moieties in HIPS (carbonyl and hydroxyl indexes) and the variation in vinyl-1,2 and trans-1,4 PB unsaturated groups [24].

Tensile tests were conducted on reprocessed and thermo-oxidated HIPS samples, following the procedure reported elsewhere [24]; the elastic modulus, stress at break and strain at break were thus obtained and here correlated with the results from TD-NMR. The viscoelastic relaxations, including the glass transitions of the PB and PS phases in degraded HIPS were investigated using dynamical-mechanical-thermal analysis (DMTA) [23]. The storage (E′) and the loss modulus (E″) were recorded at a range of frequencies and temperatures, and the free volume parameter from the Vogel-Fulcher-Tammann-Hesse theory (VFTH) was thus calculated [23].

3. Results and discussion

3.1. NMR relaxation studies of degraded HIPS

The raw magnetization decay curves obtained for all the repetitive extrusion series and the thermal ageing series exhibit the typical structure for rubber-modified styrenics (See supplementary data): A fast decay corresponding to the polystyrene matrix and a slower decaying component that can be attributed to the butadiene rubber. In order to separate the signal contributions from the polystyrene and rubber phases, fitting the *ge* model with a Gaussian and a single component is sufficient (Eq. (1)). While the overall rubber quantity (amplitude p_e of the single exponential *ge* model) can be determined adequately with this model, the relaxation properties of the rubber phase are poorly described by only a single exponential component.

Multiple processing does not significantly alter the rubber fraction up to nine extrusion cycles, evidencing the stability of the rubber phase during repetitive mechanical recycling. However, the effect of thermo-oxidation on the rubber phase is different. The resulting rubber fractions for the thermal oxidation series are plotted in Fig. 2. The time evolution of the rubber fraction component *pe* through thermo-oxidation clearly shows an induction period at short exposure times, which may be related to the initial protective effect of the incorporated stabilizer system; for longer exposure times, a progressive decrease in the rubber fraction is clearly observed, confirming the degradative effects of thermo-oxidation on the rubber phase.

The relaxation time distribution resulting from the inverse Laplace transform (ILT) model suggests two exponential components in the rubber signal, related to rubber phase segments with different mobility (see supplementary data for selected results). The double exponential model *g2e* is therefore preferred to analyze the effects of long-term degradation on the different components of the rubber phase. Figs. 3 and 4 display the signal fractions and relaxation times obtained in the fit of model *g2e* for the reprocessing series and for the thermal oxidation series, respectively. Along with the individual components' relaxation times, also the average relaxation time $1/\langle 1/T_2\rangle$ is given (Eq. (3)).

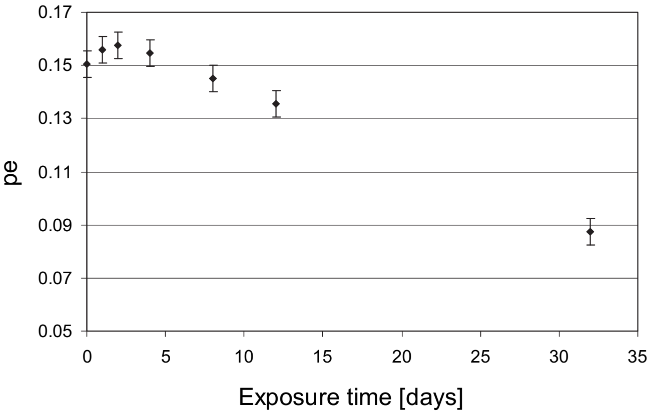

Fig. 2. Rubber signal fraction *pe* obtained by evaluation of the magnetization decay data with the *ge* model for the thermal oxidation and the reprocessing series.

$$\frac{1}{\langle 1/T_2\rangle} = \frac{p_{e1}+p_{e2}}{p_{e1}/T_{2e1}+p_{e2}/T_{2e2}} \tag{3}$$

A small decrease in all relaxation times can be observed for the repetitive extrusion series (Fig. 3), this decrease being only statistically significant for the fast-relaxing, cross-linked component T_{2e1}. As it was pointed out earlier, the reduction of rubber fraction is almost negligible through reprocessing cycles, but the slight reduction in relaxation times and thus mobility in the rubber phase

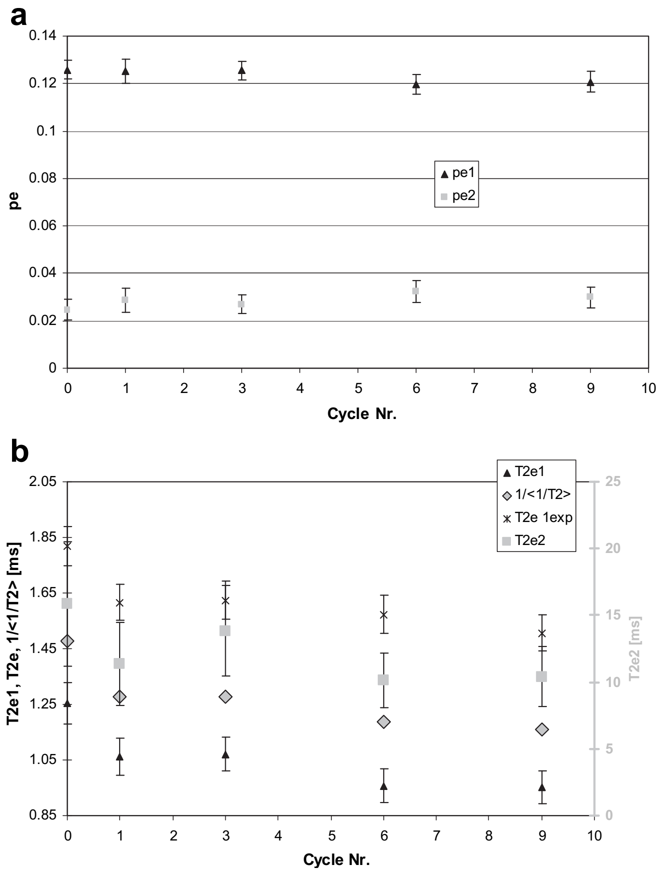

Fig. 3. Components (a) and relaxation times (b) of the rubber signal fraction in the repetitive extrusion series.

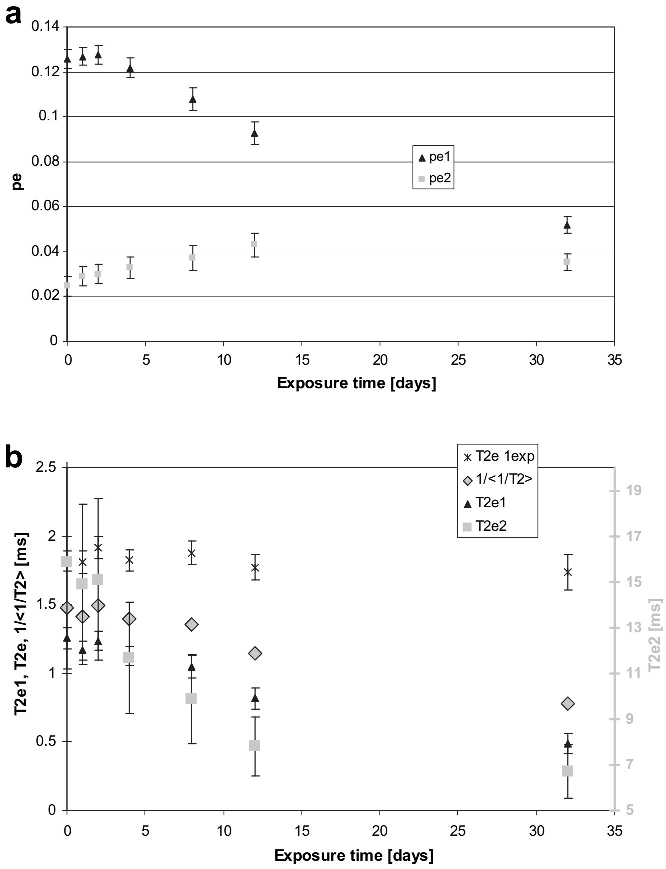

Fig. 4. Components (a) and relaxation times (b) of the rubber signal fraction in the thermal oxidation series. Note the increase of the slow-relaxing signal component pe2 and the decrease of the relaxation times.

may be linked to the occurrence of additional cross-linking reactions caused by the elevated temperature and mechanical shear in the extruder. A clearer trend for the relaxation time values is visible in the thermal oxidation series for both components T_{2e1} and T_{2e2}, and the average relaxation time $1/\langle 1/T_2\rangle$ (Fig. 4). Again, an initial induction period can be observed, followed by a marked reduction for longer exposure times. Decreasing relaxation times are hardly a surprise as oxidation is expected to lead to additional cross-linking in the rubber phase [3,13]. However, the increase of the fraction p_{e2} of slow-relaxing material with oxidation times seems to be in contradiction with this simple picture. This result may reveal the occurrence of an additional chain scission mechanism of the original rubber populations, leading to the formation of shorter chain fragments with higher mobility due to a larger fraction of chain ends. These irreversible chemical phenomena (cross-linking and chain scission) may occur simultaneously and competitively during the prolonged thermo-oxidation of HIPS, leading to the catastrophic deterioration of the structure and properties of the material. This correlation between the mobility parameters from NMR relaxation during long-term degradation of HIPS and the subsequent macroscopic properties will be analyzed in the following sections.

3.2. Macroscopic analysis: swell index, gel content, rubber particle size measurements, and average molar mass determination

Traditional chemical analyses of the macroscopic properties of degraded HIPS were performed, to measure the swell index, gel content, rubber particle size and average molecular weight of the PS matrix; the full results are presented in Tables 1 and 2 for the multiple processed and thermo-oxidized series, respectively. Multiple extrusion of HIPS leads to a systematic decrease in the matrix average molar mass, swell index and gel content (Fig. 5), with matrix and swell index being only moderately affected. The slight decrease of the swell index corresponds to minor additional cross-linking of the rubber phase, in line with the minimal reduction of the rubber relaxation times observed (see Supplementary data for suitable correlations). The gel content comprises the total rubber phase, i. e. insoluble rubber and included matrix in the rubber particles; its decrease partly corresponds to a decrease of the rubber signal p_{e1}. A decrease in gel content might also arise from cutting the rubber particles and releasing included polystyrene material to the matrix; however, the rubber particle size (median value d_{50}) seems not to be affected. The progressive reduction in the average molar mass of the PS matrix is related to

Table 1
Macroscopic properties for the multiple processing series: QI (swell index); gel content (Gel), weight-average molecular weight from DRI (Mw_{RI}); rubber particle size (D); rubber particle size median value (D_{50}).

Extrusion Cycles	QI [%]	Gel [%]	Mw$_{RI}$ [Da]	D	D(v,0,5) [μm]
0	11.1	30.7	203210	2.66	2.28
1	11.1	30.0	202310	2.78	
2	11.0	29.4			
3	10.6	28.4	199420	2.65	
4	10.6	28.2			
5	10.3	27.3			
6	10.2	26.7	194590	2.53	
7	9.9	26.1			
8	10.0	26.0			
9	9.7	25.5	188370	2.68	2.28

Table 2
Macroscopic properties for the thermo-oxidized series: weight-average molecular weight from DRI (Mw_{RI}); rubber particle size (D); rubber particle size median value (D_{50}).

Thermal Storage [days]	Mw$_{RI}$ [Da]	D	D(v,0,5) [μm]
0	203210	2.66	2.28
1	202760	2.63	
2	201880	2.70	
4	202500	2.76	
8	199720	2.80	
12	201870	2.79	
36	199480	2.74	2.18

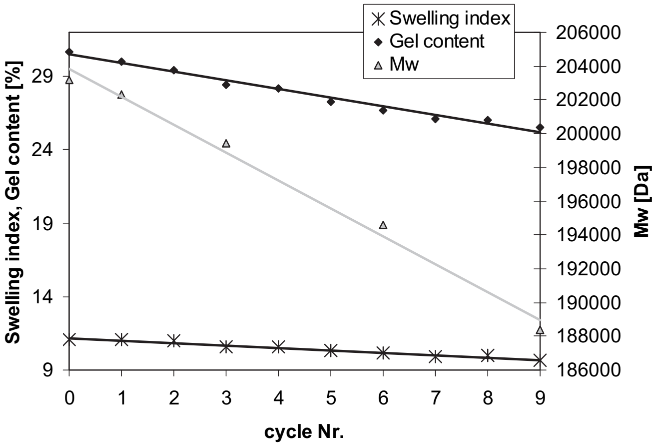

Fig. 5. Swell index, gel content, and matrix molar mass M_w in the repetitive extrusion series.

chain scission reactions induced during thermo-mechanical extrusion of HIPS, in agreement with previous observations [23,24,26]. It is worth mentioning, though, that the reduction of the average molar mass is only 10% after 9 repetitive extrusion cycles, confirming again the recyclability of the material.

Swell indices and gel content could not be determined for the thermal oxidation series due to lack of material. Neither matrix molar mass nor rubber particle size were significantly affected by thermo-oxidation; this is a surprising result taking into account the observed changes in the rubber phase dynamics using NMR relaxation and the dramatic disruption of the structure and mechanical properties reported in previous studies for this material [23,24]. This indicates that the chemical reactions involved in thermo-oxidation affect principally the PB component. The rubber particles are composed of included PS (roughly 75%) and PB (roughly 25%); as long as the rubber maintains some integrity due to its cross-linked structure, the rubber particle size will not change significantly.

3.3. *Correlation of relaxation NMR results with mechanical and spectroscopic properties*

The NMR relaxation time data presented in section 3.1 provide important clues into the microstructural changes in HIPS during repeated extrusion and thermo-oxidative degradation. In this passage, the relationship between the NMR results and those from mechanical and spectroscopic analysis reported in previous studies [23,24] will be explored.

In the multiple extrusion series, stress at break and strain at break correlate nicely with the relaxation time T_{2e1} of the rubber component (Fig. 6a); the correlation coefficient is similar to that found for the correlation between elongation at break and strain at break ($R^2 = 0.804$, results not presented here). The correlations between the mechanical properties and the macroscopical chemical tests are even better (Fig. 6b). These correlations indicate that the mechanical changes induced by repeated extrusion are well described by the reported alterations in rubber phase cross-linking and the reduction on the PS average molar mass using NMR relaxation and SEC, respectively. The correlation between the relaxation time of the cross-linked rubber population T_{2e1} and the trans-1,4 index obtained after deconvolution of the Raman spectrograms to the PB microstructures [23] is presented in Fig. 7a for the reprocessed series. Despite quite large error bars in the Raman index results, the correlation with the relaxation times of the cross-linked PB rubber is quite good for the trans-1,4 microstructure ($R^2 = 0.9058$); the correlations for the other microstructures are not as evident (see supplementary data for such correlations), especially for the vinyl-1,2 microstructure. This is indeed expected and indicates the chemical nature of the increase of cross-linked structures during multiple processing through the reactions of the trans-1,4 unsaturated bonds in the PB phase. Similar correlation trends can be observed for the maximum of the loss modulus for the PB phase ($E''_{\mathrm{max,PB}}$) obtained from dynamical-mechanical analysis (DMA) and the relaxation time T_{2e1} (Fig. 7b); indeed, if the

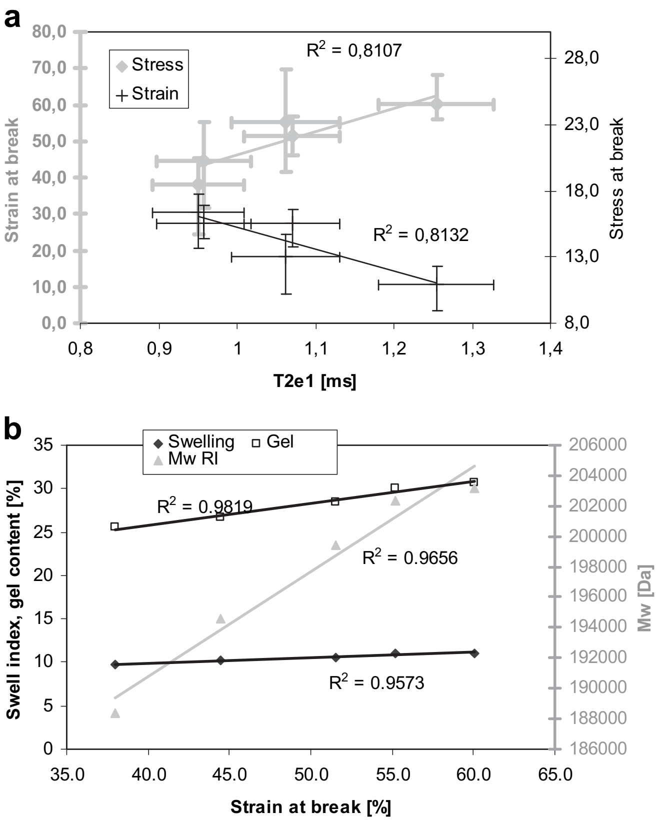

Fig. 6. Correlations for the mechanical properties [24] in the reprocessing series: (a) T_{2e1} and strain at break and stress at break; (b) classical chemical parameters and strain at break.

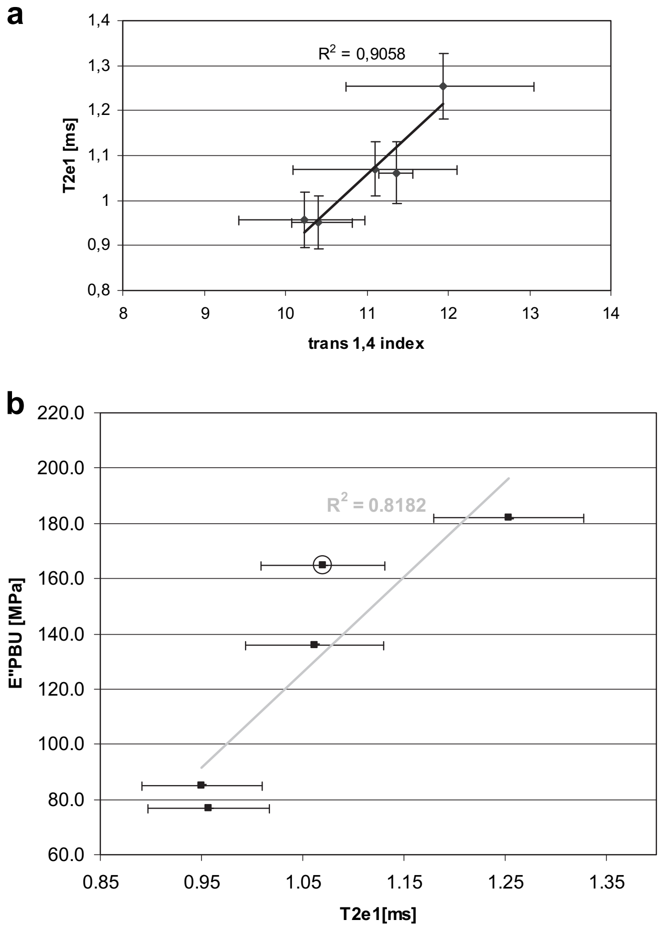

Fig. 7. Correlation for the relaxation time with chemical and dynamical properties of the rubber phase for the repetitive extrusion series: (a) correlation between T_{2e1} and the Raman trans-1,4 index; (b) correlation between T_{2e1} and $E''_{\mathrm{max,PB}}$. The Raman trans-1,4 index and the $E''_{\mathrm{max,PB}}$ from DMTA analysis were obtained as reported elsewhere [23]. The circled value corresponds with an outlier of the fitting.

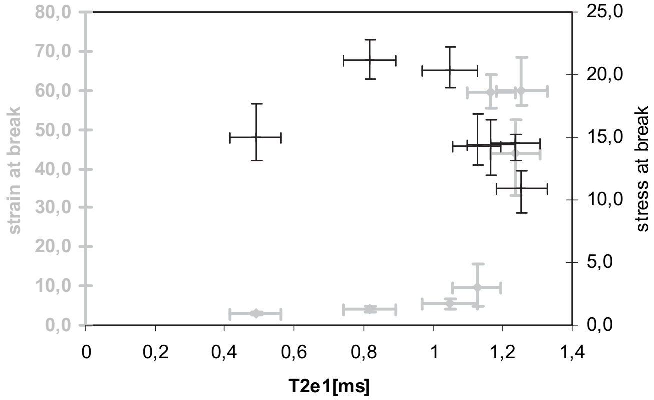

Fig. 8. Correlation between the mechanical properties [24] and the relaxation time T2e1 during thermo-oxidation.

outlier value for cycle 4 is omitted, the correlation coefficient increases to $R^2 = 0{,}95$. This effect is again explained by the occurrence of cross-linking during multiple processing, which hinders the mobility of the PB chains and therefore reduces the overall loss modulus values.

Thermo-oxidation of rubber-modified styrenic polymers has been described as a complex process with simultaneous physical and chemical phenomena. As Fig. 8 shows, there is no apparent correlation between the NMR results and the mechanical properties for the thermal oxidation series. The relaxation time T_{2e1} is mainly sensitive to additional cross-linking in the PB phase, while the evolution of the mechanical properties reflects the overall changes in the microstructure of the material. For shorter exposure times, the relaxation time T_{2e1} shows an induction period related to the protective effect of stabilizers against oxidative reactions in the PB phase, whereas the mechanical properties are drastically affected by physical ageing [10,24]. For longer exposure times, the mechanical performance of the system may be more affected by competing chain fragmentation reactions rather than additional cross-linking. On the other hand, spectroscopic and NMR data are expected to exhibit parallel trends, since both NMR and spectroscopic information are essentially determined by changes on the molecular length scale. This is in agreement with the good correlation observed between the relaxation time T_{2e1} and the trans-1,4 index from FTIR measurements (Fig. 9); similar correlations are observed for the Raman PB microstructural indexes (see Supplementary data). A cluster of data points can be observed related to the induction period for shorter exposure times where no appreciable changes are observed for the relaxation times and the PB indexes; for longer exposure times, thermo-oxidation induces irreversible chemical effects in the PB phase, which now can be linked to the occurrence of additional cross-linking reactions that cause a general reduction of the PB unsaturated groups and a decrease of the relaxation time T_{2e1}. Important information about the nature of the cross-linking reactions occurring during thermo-oxidation can be inferred from such correlations; cis-1,4 and especially trans-1,4 microstructures seem to be more susceptible to cross-linking than vinyl-1,2, in agreement with previous studies for several rubber-modified styrenic polymers [3,23,35]. The complex correlations between NMR relaxation results and viscoelastic behaviour from DMA analyses evidence again the complex nature of the effects induced by thermo-oxidation (Fig. 10). On one hand, the correlations between the relaxation time T_{2e1} and both the loss modulus $E''_{\max,PB}$ and the free volume parameter from the Vogel-Fulcher-Tammann-Hesse theory (VFTH) are discernable, while a much better correlation is found for the VFTH free volume and the sum of the rubber signal components. The correlation between free volume and the relaxation time T_{2e1} is obvious, since a decreasing free volume will result in a reduced mobility of the PB polymer chains, while the other correlations are less obvious and may be influenced by other simultaneous physical and chemical effects caused by thermo-oxidation.

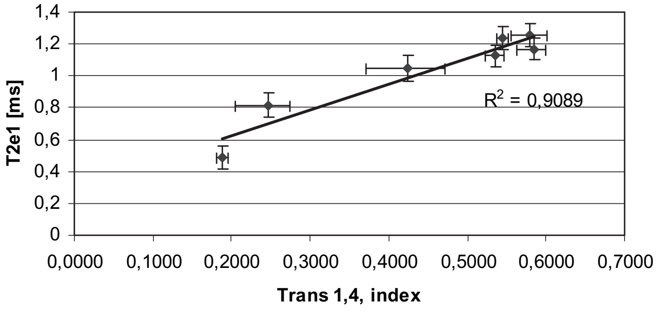

Fig. 9. FTIR Trans-1,4 index [24] and relaxation time T_{2e1} in the thermal oxidation series.

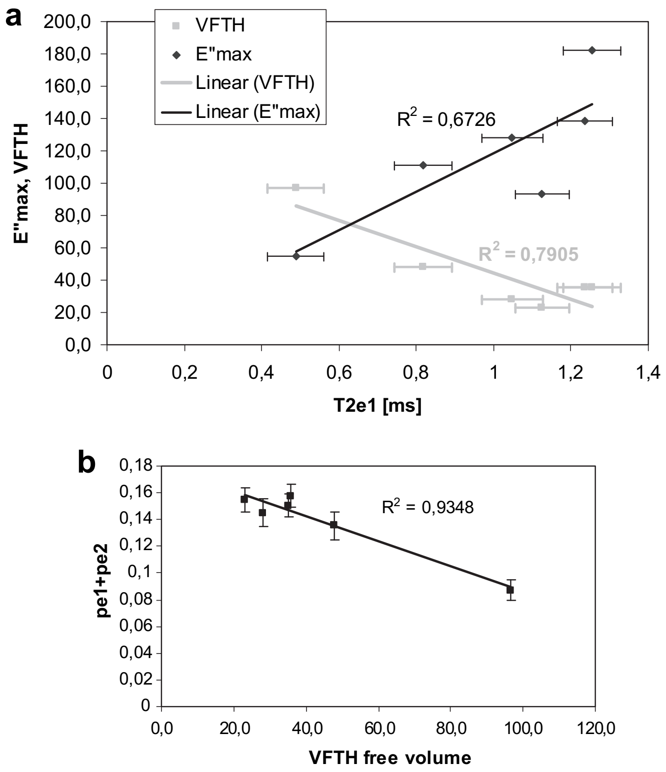

Fig. 10. Correlations between NMR relaxation and viscoelastic behaviour from [23] for the thermal oxidation series: (a) correlation between T_{2e1} and $E''_{\max,PB}$ and VFTH free volume parameter for the PB phase; (b) correlation between VFTH free volume for the PB component and the rubber signal amplitude.

4. Conclusions

Relaxation NMR offers new insights into the degradation mechanisms affecting the rubber phase during multiple extrusion and thermo-oxidation of HIPS samples. NMR studies allow to detect the fraction of the rubber network responsible for elastic properties and also to describe its cross-linking density. The results from NMR relaxation correlate sensibly with other microscopic and macroscopic properties, including mechanical properties, spectroscopic chemical changes, and viscoelastic behaviour, offering a more complete picture of the complex effects caused by long-term degradation.

In the multiple extrusion series, small reductions in the rubber network fraction and a moderate increase in its cross-linking density lead to a reduction of the swell index of the rubber, which manifests in a progressive deterioration of the mechanical properties. The same process also equilibrates the trans-1,4 index of the rubber, as shown by infrared spectroscopy. Thermo-oxidative degradation causes, on the other hand, more severe rubber structural changes. The rubber network fraction rapidly decreases and becomes further cross-linked, whereas the fraction of non-crosslinked material (chain ends, oxidative bond scission and fragmentation) significantly increases. This phenomenon may evidence the occurrence of competing and simultaneous cross-linking and chain scission reactions in the PB phase, which are responsible for the changes in chemical structure, morphology, and macroscopic properties of the material. The good correlation between the NMR and the spectroscopic results indicate that the changes on the molecular scale proceed continuously over the whole observation period.

NMR relaxation measurements are non-destructive, require minimal sample preparation and can be conducted in a matter of minutes. NMR relaxation proves therefore to be a valuable analytical tool to analyze the degradative changes in the microstructure of rubber-modified styrenic polymers.

Acknowledgements

The lab support for the NMR studies by Jens Schober and Cornelia Willax is gratefully acknowledged. FV thanks the economical support of the Spanish Ministry of Science and Innovation through the FPU doctoral program.

Appendix. Supplementary material

The supplementary data associated with this article can be found in the on-line version at doi:10.1016/j.polymer.2011.02.005.

References

[1] Gausepohl H, Gellert R. Polystyrol. Kunststoff Handbuch 4. Hanser Verlag, München; 1996.
[2] Maul J, Frushour BG, Kontoff JR, Eichenauer H, Ott K-H, Schade C. Polystyrene and styrene copolymers. Ullmann's encyclopedia of industrial chemistry. 7th ed. New York: John Wiley- VCh; 2007.
[3] Adeniyi JB. Clarification and discussion of chemical transformations involved in thermal and photo-oxidative degradation of ABS. Eur Polym J 1984;20 (3):291–9.
[4] Adeniyi JB, Kolawole EG. Thermal and photo-degradation of unstabilized ABS. Eur Polym J 1984;20(1):43–7.
[5] Boldizar A, Moller K. Degradation of ABS during repeated processing and accelerated ageing. Polym Degrad Stab 2003;81(2):359–66.
[6] Piton M, Rivaton A. Photo-oxidation of ABS at long wavelengths ([lambda] >300 nm). Polym Degrad Stab 1997;55(2):147–57.
[7] Tiganis BE, Burn LS, Davis P, Hill AJ. Thermal degradation of acrylonitrile-butadiene-styrene (ABS) blends. Polym Degrad Stab 2002;76(3):425–34.
[8] Shimada J, Kabuki K. The mechanism of oxidative degradation of ABS resin. Part I. The mechanism of thermooxidative degradation. J Appl Polym Sci 1968;12(4):655–69.
[9] Shimada J, Kabuki K. The mechanism of oxidative degradation of ABS resin. Part II. The mechanism of photooxidative degradation. J Appl Polym Sci 1968;12(4):671–82.
[10] Chen CC, Habibullah M, Sauer JA. Elevated temperature ageing of HIPS. J Appl Polym Sci 1983;28:391–406.
[11] Ghaffar A, Scott A, Scott G. The chemical and physical changes occurring during U.V. degradation of high impact polystyrene. Eur Polym J 1975;11 (3):271–5.
[12] Ghaffar A, Scott A, Scott G. Initiation processes in the photodegradation of high impact polystyrene—I effects of prior thermal oxidation. Eur Polym J 1976;12(9):615–20.
[13] Ghaffar A, Scott A, Scott G. Photo-oxidation of high impact polystyrene—III. The mechanism of the cross-linking reaction. Eur Polym J 1977;13(2):89–93.
[14] Ghaffar A, Scott A, Scott G. Initiation processes in the photodegradation of high impact polystyrene—II. Effects of prior exposure to sensitizing environments. Eur Polym J 1977;13(2):83–8.
[15] Grguric TH, Rek V, Jelcic Z, Hace D, Gomzi Z. Determination of the kinetic parameters of the thermal oxidative degradation of styrene/butadiene copolymers. Polym Eng Sci 1999;39(8):1394–7.
[16] Israeli Y, Lacoste J, Lemaire J, Singh RP, Sivaram S. Photo- and thermoinitiated oxidation of high-impact polystyrene: characterization bt FT-IR spectroscopy. J Polym Sci Part A: Polym Chem 1994;32:485–93.
[17] Kostov GI, Komitov PG, Nikolova ZG. Application of IR-compensation technique for study of the oxidation degree of high impact polystyrene. Eur Polym J 1985;21(6):561–4.
[18] Vishwa-Prasad A, Singh RP. Recent developments in the degradation and stabilization of high-impact polystyrene. J Macromol Sci Part C Rev Macromol Chem Phys 1997;C37(4):581–98.
[19] Saron C, Felisberti MI. Dynamic mechanical spectroscopy applied to study the thermal and photodegradation of poly(2,6-dimethyl-1,4-phenylene oxide)/high impact polystyrene blends. Mater Sci Eng A 2004;370(1–2):293–301.
[20] Piton M, Rivaton A. Photooxidation of polybutadiene at long wavelengths ([lambda] >300 nm). Polym Degrad Stab 1996;53(3):343–59.
[21] Bucknall CB, Soares VLP. Cavitation of rubber particles in high-impact polystyrene: effects of crosslinking by ?-irradiation. J Polym Sci Part B Polym Phys 2004;42(11):2168–80.
[22] Mlinac-Misak M, Jelencic J, Bravar M, Dejanovic R. Thermal and UV degradation of impact-resistant polystyrene (II). Angew Makromol Chem 1990;176 (1):105–12.
[23] Vilaplana F, Karlsson S, Ribes-Greus A. Changes in the microstructure and morphology of high-impact polystyrene subjected to multiple processing and thermo-oxidative degradation. Eur Polym J 2007;43(10):4371–81.
[24] Vilaplana F, Ribes-Greus A, Karlsson S. Degradation of recycled high-impact polystyrene. Simulation by reprocessing and thermo-oxidation. Polym Degrad Stab 2006;91(9):2163–70.
[25] Vilaplana F, Karlsson S. Quality concepts for the improved use of recycled polymeric materials: a review. Macromol Mater Eng 2008;293:274–97.
[26] Santana RC, Manrich S. Studies on thermo-mechanical properties of post-consumer high impact polystyrene in five reprocessing steps. Prog Rubber Plastics Recycl Technol 2002;18(2):99–110.
[27] Santana RC, Manrich S. Studies on morphology and mechanical properties of PP/HIPS blends from postconsumer plastic waste. J Appl Polym Sci 2003;87 (5):747–51.
[28] Soriano F, Morales G, Díaz de León R. Recycling of high impact polystyrene in coextruded sheet: influence of the number of processing cycles on the microstructure and macroscopic properties. Polym Eng Sci 2006;46 (12):1698–705.
[29] Boldizar A, Jansson A, Gevert T, Moller K. Simulated recycling of post-consumer high density polyethylene material. Polym Degrad Stab 2000;68 (3):317–9.
[30] Steenbrink AC, Litvinov VM, Gaymans RJ. Toughening of SAN with acrylic core-shell rubber particles: particle size effect or cross-link density? Polymer 1998;39(20):4817–25.
[31] ten Brinke JW, Litvinov VM, Wijnhoven JEGJ, Noordermeer JWM. Interactions of stober silica with natural rubber under the influence of coupling agents, studied by 1H NMR T2 relaxation analysis. Macromolecules 2002;35 (27):10026–37.
[32] Bergmann K, Schmiedberger H, Unterforsthuber K. Meßverfahren zur Untersuchung der Protonen-Spin-Spin-Relaxation ein und zweiphasiger Polymerer in einem Zeitbereich von fünf Dekaden. Colloid Polym Sci 1984;262 (4):283–93.
[33] Nestle N, Heckmann W, Steininger H, Knoll K. Towards quantification of butadiene content in styrene-butadiene block copolymers and their blends with general purpose polystyrene (GPPS) and the relation between mechanical properties and NMR relaxation times. Anal Chim Acta 2007;604 (1):54–61.
[34] Honerkamp J, Weese J. Tikhonovs regularization method for ill-posed problems. Contin Mech Thermodyn 1990;2(1):17–30.
[35] Wang SM, Chang JR, Tsiang RCC. Infrared studies of thermal oxidative degradation of polystyrene-block polybutadiene-block-polystyrene thermoplastic elastomers. Polym Degrad Stab 1996;52(1):51–7.

Polymer 52 (2011) 1417–1425

Contents lists available at ScienceDirect

Polymer

journal homepage: www.elsevier.com/locate/polymer

Morphology, thermal behavior and mechanical properties of binary blends of compatible biosourced polymers: Polylactide/polyamide11

G. Stoclet*, R. Seguela*, J.-M. Lefebvre

Unité Matériaux Et Transformations, CNRS UMR 8207, Université de Lille1, Cité Scientifique, Batiment C6, 59655 Villeneuve d'Ascq, France

ARTICLE INFO

Article history:
Received 25 November 2010
Received in revised form
31 January 2011
Accepted 1 February 2011
Available online 23 February 2011

Keywords:
Polylactide
Polyamide11
Compatible blends

ABSTRACT

Blends of entirely biosourced polymers, namely polylactide (PLA) and polyamide11 (PA11), have been melt-compounded by twin-screw extrusion without the use of any compatibilizing agent. The crystallization and melting behavior, the morphology and mechanical properties of the melt-compounded binary blends have been investigated over the whole composition range. Albeit immiscibility prevails in all blends, the micronic and sub-micronic dispersion of the minor phase reveals a self-compatibilization behavior of the PLA/PA11 system as directly evidenced via scanning electron microscopy. For PLA compositions below 50%, PLA appears to be dispersed as globules in the PA11 matrix. With increasing PLA content beyond 50%, the blends exhibit co-continuous intertwined phases, then thread-like PA11 phase dispersed in a PLA matrix. For PLA composition greater than 80%, PA11 displays globular dispersion. In the case of PLA-rich blends, the crystallization of PA11 from the melt displayed a contribution of "homogeneous nucleation" corroborating the high degree of dispersion of the minor phase. However, the earlier crystallization of PA11 upon cooling did not promote that of PLA suggesting low interfacial free energy at the boundaries of the phase-separated domains, *i.e.* roughly neutral interactions between the unlike species. The non-symmetric structural behavior of the blends over the whole composition range was found to influence the mechanical properties. If the elastic modulus of the blends roughly obeys an additive mixture law at room temperature (RT), this is not the case above the Tg of both PLA and PA11. More particularly in the PLA-rich range, the thread-like dispersion of the stiff PA11 component plays the role of *in situ* fibrillar reinforcement of the soft PLA matrix. The strain at break and the yield stress also do not obey a simple mixture law, both at RT and above Tg. Perspectives of morphological and mechanical improvements of PLA/PA11 blends are discussed.

1. Introduction

Polymers issued from renewable resources, more particularly biomass, have received increasing attention in recent years due to their friendly impact on environment. The biodegradability and biocompatibility of this class of polymers have been the most largely investigated properties so far regarding medical issues. However, some of these biosourced materials also display good potentialities for structural applications in substitution to oil-based polymers [1–5]. Poly(lactic-acid) or polylactide (PLA) is a promising aliphatic polyester in this field owing to its relatively high glass transition temperature, $40°C < Tg < 65$ °C [6], and melting point, 120 °C $< T_m < 180$ °C [7], depending on the D/L stereoisomer ratio. However, PLA cannot challenge usual commodity plastics regarding thermomechanical properties such as stiffness, strength and toughness. Several physical approaches have been tempted in order to overwhelm this drawback. Improvement of PLA crystallization capabilities has been a matter of extensive studies, via thermal or thermomechanical treatments, plasticizers or nucleating agents [8–17]. Many endeavours have also been focused at enhancing PLA mechanical properties via compounding with more or less miscible polymers [18–34] or with nanofillers [35–41]. In this domain, blending of PLA with biosourced polymers such as starch, chitosan, poly(hydroxybutyrate), poly(butylene-succinate) [42–53] are the target of increasing attention, as well as nanocomposites with polysaccharide nanocrystals [54–57] that have been shown to provide mechanical reinforcement for a large variety of synthetic and natural polymers [58,59]

Poly(amino11-undecanoic acid), otherwise polyamide11 (PA11), is also a biomass-stemmed polymer known since the early 50's, its monomer being issued from castor oil. PA11 looks similar to PLA regarding the glass transition temperature $Tg \approx 45$ °C in the dry state and the melting point $T_m \approx 190$ °C, yet it displays superior

---

* Corresponding authors. MATEIS, INSA de Lyon, Bat. Blaise Pascal, 69621 Villeurbanne, France. Tel.: +33 3 20 43 47 80; fax: +33 3 20 43 65 91.

E-mail addresses: gregory.stoclet@univ-lille1.fr (G. Stoclet), roland.seguela@insa-lyon.fr (R. Seguela).

0032-3861/$ – see front matter © 2011 Elsevier Ltd. All rights reserved.
doi:10.1016/j.polymer.2011.02.002

mechanical performances mainly due to intermolecular hydrogen (H) bonding both in the crystalline and amorphous state. Furthermore, if the optimum crystallinity index is very close for the two polymers, *i.e.* about 40%, the crystallization of PA11 is much faster.

Regarding PLA/PA11 blends, immiscibility is expected though the respective low and high polarities of the two polymers make them *a priori* compatible without the use of a surfactant additive. Indeed, PLA blends with low polarity polymers such as poly(methyl-acrylate) or poly(methyl-methacrylate) [18,21], poly(hydroxybutyrate) [42,43], poly(ethylene-terephthalate) [32], poly(caprolactone) [23,26,29,30,34] and poly(ethylene-glycol) [24,25,31] have been shown to display a significant degree of miscibility in the melt that may be partly destroyed upon crystallization of the PLA. In the present study, the possibility of H-bonding between the amino (NH) groups of PA11 and the carbonyl (CO) groups of PLA supports the assumption of potential miscibility or at least good compatibility. Scarce experimental evidences of H-bonding via spectroscopic measurements have been reported regarding binary blends PLA with higher polarity polymers containing OH or NH groups [19,28,31]. In contrast, no specific interactions have been reported to occur in some PLA blends with OH- or NH-containing polymers, though these blends displayed quite good compatibility as judged from the high degree of dispersion [27,33,44,48]

The present work deals with the structural and mechanical study of PLA/PA11 blends, an *a priori* compatible binary system involving entirely biosourced polymers. Although both polymers are produced at industrial scale, not any academic work has been reported so far regarding this quite attractive system. It is also worth noticing that studies are very scarce about PLA blends with any kind of polyamides or related polymers [16,28,33] so that little is known about their physical properties and potential mechanical performances.

2. Experimental

2.1. Material and preparation

The polylactide (PLA) of the study is a commercial material purchased from *Natureworks* (USA) as grade 4042D. It contains 4.3 mol % of D-isomer units and its number- and weight-average molecular weights are $M_n = 116$ kDa and $M_w = 188$ kDa, respectively. The polyamide11 (PA11) having $M_n = 12$ kDa and $M_w = 25$ kDa is manufactured by *Arkema* (France) under the trade name *Rilsan*. Both polymers contained only antioxidant as additives. Nine PLA/PA11 binary blends covering the whole composition range were compounded without compatibilizer, using a co-rotating twin-screw *micro-compounder* from *DSM-Xplore* (Geleen, The Netherlands), under nitrogen. The extrusion parameters were: barrel temperature = 200 °C, screw speed = 100 rpm, residence time = 10 min. The two pure polymers were also processed using the same extrusion conditions for the sake of comparison with the blends at equivalent thermomechanical history. The polymers and blends were further compression-moulded into 0.2 mm and 2 mm thick sheets, between *Milar*-covered steel plates in a hot press for 5 min at 200 °C, then cooled down to room temperature (RT) at about 40 °C/min. Finally, in order to erase physical ageing due to storage for various durations at RT, all compression-moulded sheets were rejuvenated for 5 min at 70 °C prior to any physical characterization, *i.e.* about $Tg +$ 10 °C for PLA and $Tg + 20$ °C for PA11. All materials were stored under dry atmosphere, prior and after processing.

2.2. Dynamic melt rheology

Melt rheology was investigated on an ARES equipment from *TA Instruments* in the plane–plane configuration, using 2 mm thick sample discs of diameter 25 mm. Experiments were carried out at 200 °C, *i.e.* the same temperature as that used for blend processing, in the frequency range 10^{-1} Hz $< \omega <$ 10^{+2} Hz, applying a shear strain of 1%.

2.3. Wide-angle X-ray Scattering (WAXS)

WAXS experiments were performed using the Ni-filtered radiation of a INEL 2000 generator equipped with a 2 kW copper target sealed tube. 2D-WAXS patterns were recorded on a CCD camera from *Photonic Science Ltd*. Intensity profiles were obtained by 180°-azimuthal integration of the patterns using FIT2D® software.

2.4. Differential scanning Calorimetry (DSC)

DSC was performed on a Pyris Diamond apparatus from *Perkin Elmer*. The 10 mg samples were scanned at a heating rate of 10 °C/min under nitrogen gas flow. The temperature and heat flow scale were calibrated using a high purity indium and zinc samples according to standard procedures. The crystalline weight fraction was computed from the enthalpy of the melting exotherm using the specific enthalpy of fusion of the perfect crystal, $\Delta H_f \approx 94$ J/g [60,61] for PLA and $\Delta H_f^\circ \approx 200$ J/g [62,63] for PA11.

2.5. Scanning electron microscopy (SEM)

The blend morphology was investigated using a *Hitachi* S4700 microscope operated under accelerating voltage of 2–6 kV. The SEM observations were carried out on the rupture surfaces of cryo-fractured samples. The specimens were immersed in liquid nitrogen for 2 min before breaking. The fracture surface was chromium-coated prior to observation. Two different specimens of every sample were analyzed for confirmation.

2.6. Dynamic mechanical thermal Analysis (DMTA)

A RSA3 apparatus from *TA Instrument* was used for the DMTA. Experiments were performed in the temperature range 25–80 °C at a frequency of 10 Hz. The dynamic strain amplitude, $\varepsilon_o = 0.4 \times 10^{-3}$, was determined after preliminary measurement of the strain domain for which the material obeys linear viscoelasticity.

2.7. Tensile drawing behavior

Uniaxial tensile tests were carried out using an *Instron* machine Model 4466 equipped with an environmental chamber. The dumbbell specimens having 22 mm and 5 mm in gauge length and width were cut out from the 0.2 mm thick sheets and strained at a constant crosshead speed of 50 mm/min, *i.e.* an initial strain rate $\dot{\varepsilon} = 4 \times 10^{-2}$ s^{-1}. Five specimens were tested for every blend and experimental condition. The yield stress, σ_y, is defined at the stress overshoot prior to necking for RT, or at the stress plateau at the onset of plastic flow for $T = 80$ °C. The strain at break, ε_{break}, is defined as the ratio of the sample length at break to the initial gauge length of the sample.

3. Results and discussion

3.1. Rheological behavior

Fig. 1 shows the complex viscosity versus frequency for the two neat polymers at 200 °C, *i.e.* the temperature of compounding and compression-molding of the blends. Although PA11 has a significantly lower molar weight than PLA, its complex viscosity is between 6 and 4 times higher than that of PLA at low and high

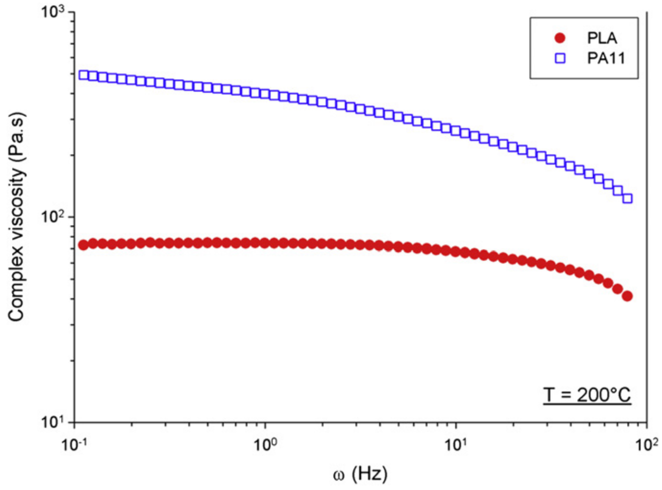

Fig. 1. Complex viscosity of PLA and PA11 as a function of frequency at 200 °C.

shear rates, respectively. This may be assigned to two combining effects: 1) the “dynamic” hydrogen (H) bonding between the amides groups of the PA11 chains that exist in the melt [64], and 2) the molecular weight between entanglements that is much lower in PA11 ($M_e \approx 2$ kDa) [65] than in PLA ($M_e \approx 10$ kDa) [66]. This phenomenon is of prime importance for the process-controlled morphogenesis of the blends.

3.2. WAXS analysis

The WAXS intensity profiles of Fig. 2 show that pure PLA is thoroughly amorphous under the processing conditions of the present study whereas pure PA11 displays its stable α triclinic crystal form [67,68]. This is consistent with the very slow crystallization of PLA [13]. All blends only exhibit crystalline reflections from PA11, indicating that PLA is also amorphous in the blends. This suggests that the blends were phase-separated in the melt leading to crystalline PA11 and amorphous PLA upon cooling.

3.3. Blend morphology

SEM images of the cryo-fractured blends are reported in Fig. 3. For blends with predominant PA11 content, *i.e.* 20/80 and 40/60 blends, the morphology consists of PLA globules dispersed in the PA11 matrix. It is noteworthy that the size of the PLA globules ranges from micronic to sub-micronic. This is an indication of the rather good compatibility of the unlike species due to low interfacial free energy. Indeed, in case of high interfacial free energy between PLA and PA11, the high specific surface of sub-micronic domains would involve a highly unstable situation. It is also worth noticing that, in the case of the 40/60 blend, a plastic deformation of the PA11 matrix appears at the bottom of several extracted PLA globules. This is a hint that some physical adhesion exists at the PA11–PLA boundary.

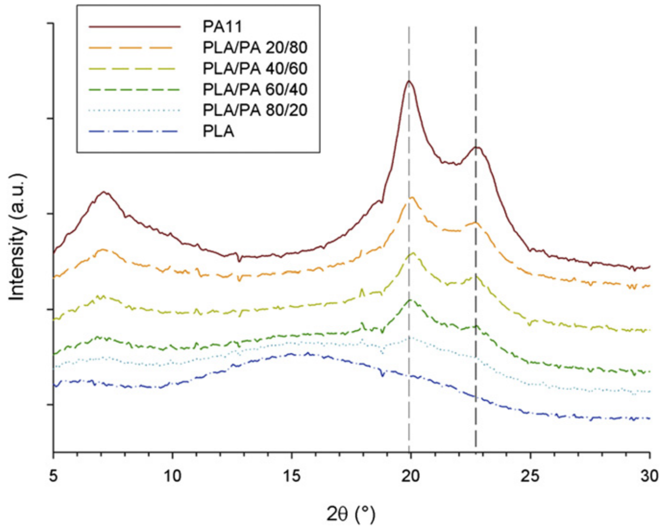

Fig. 2. WAXS intensity profiles of the PLA/PA11 blends and the neat components.

With increasing PLA composition in the range 50–60%, the blends display a rather rough fracture surface without any evidence of the footprint of phase-separated domains. Apparently the topographic contrast that is generally induced by the extraction of the dispersed domains from the matrix at the fracture surface of the SEM samples is missing for the blends in the mid-composition range. This suggests the presence of co-continuous intertwined phases that break concomitantly in a brittle manner below Tg.

For the PLA compositions in the range 60–80%, PA11 displays a thread-like morphology with some globules dispersed in the PLA matrix. The width of the threads is yet much larger than the average globule diameter.

For PLA compositions greater than 80%, PA11 appears as a globular dispersion in a PLA matrix. It is again to be noticed that the size of the PA11 globules ranges from micronic to sub-micronic. This is a confirmation of the good compatibility of the unlike species.

Fig. 4 shows a schematic of the blend morphology evolution with composition as assessed from the SEM images of Fig. 3. This sketch is similar to the one proposed for PLA/PCL blends [30], particularly regarding the co-continuous morphology in the intermediate composition domain.

Composition is well-known to be the major factor to govern the dispersion morphology of immiscible blends, particularly on the extremes of the composition range. However, viscosity ratio together with interfacial surface free energy may strongly influence morphology [69–76]. In the intermediate composition range, thread-like morphology is generally stable when $\eta_{dispersion}/\eta_{matrix} < 1$ [71,74–76]. In the present work, the observation of a thread-like morphology for the blends 65/35–75/25 (Fig. 3) is rather surprising in consideration of the viscosity ratio $\eta_{PA11}/\eta_{PLA} > 1$. Meng and Tjong [71] reported similar finding for a chemically analogous binary system consisting of a liquid crystalline polyester (LCP) dispersed in polyamide 6 (PA6) matrix with $\eta_{LCP}/\eta_{PA6} > 1$. These authors ascribed the *a priori* unexpected behavior to the elastic properties of the components. Indeed, the elasticity ratio of binary blend components, with or without compatibilizer, has been shown to modify the morphological habits of the phase dispersion, in a similar manner as the viscosity ratio [30,70]. However, all the key parameters are far from being identified considering the observation of inconsistent experiments with models, as pointed out by Steinmann et al. [76]

3.4. Melting and crystallization

Fig. 5 shows the DSC heating traces of the blends and pure polymers, in the temperature domain of the glass transition. PLA displays a heat capacity jump over a rather narrow temperature range, accompanied with a post-Tg endothermic peak. In contrast, PA11 exhibits a broad glass transition without post-Tg endotherm. In spite of the close Tg of the two polymers, this significant difference in their DSC shapes over the whole glass transition range allows concluding that the DSC traces of the blends obey a simple additive mixing rule of the pure polymers. Besides, one should notice that the PLA post-Tg endotherm occurs at the same

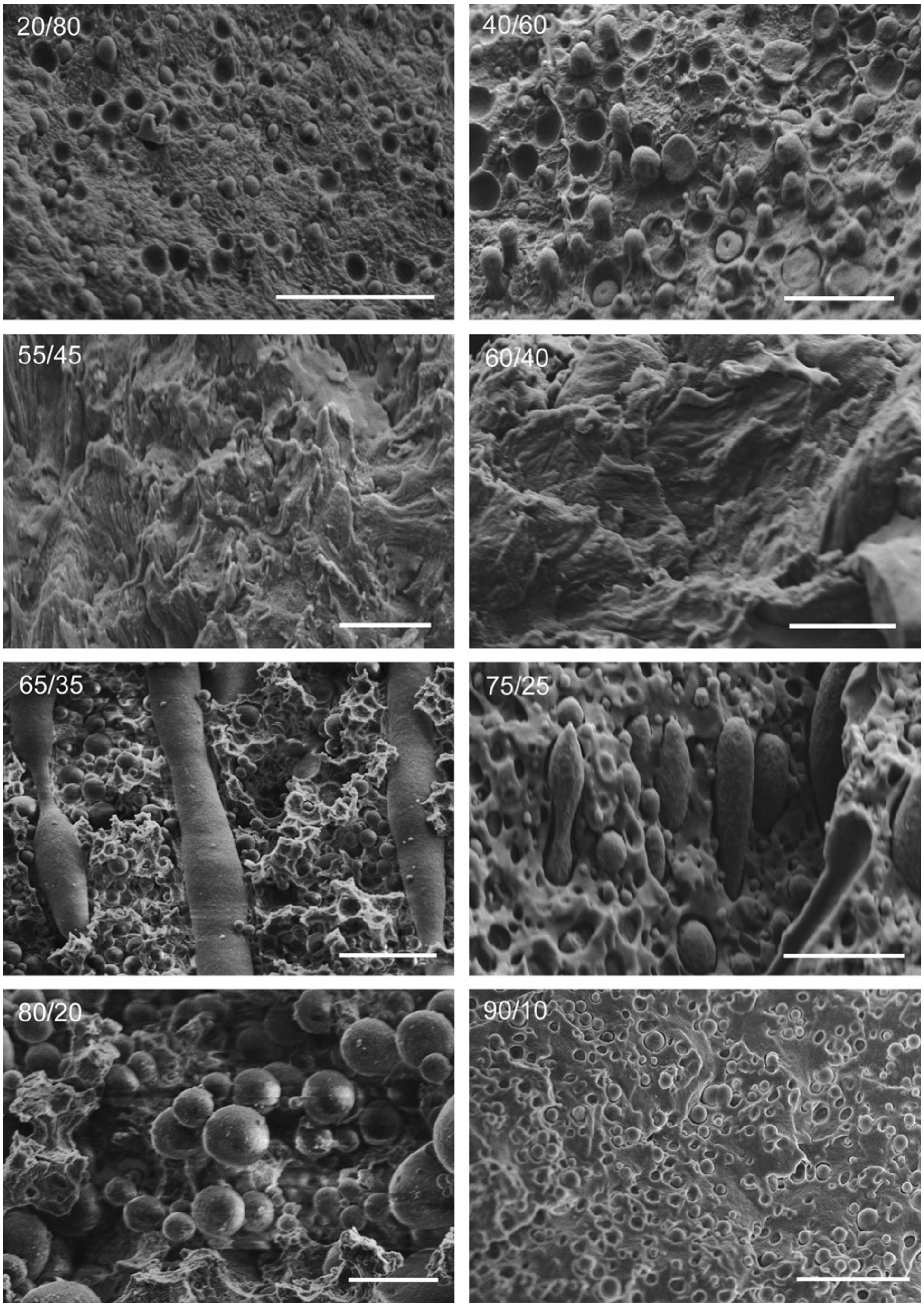

Fig. 3. SEM images of the PLA/PA11 blends (scale bar = 5 μm).

temperature irrespective of the blend composition, within the experimental reproducibility. These observations are strong hints that blends are phase-separated in the amorphous regions.

Fig. 6 reports the DSC heating traces of the blends and pure polymers, in the temperature range beyond the glass transition. The exotherm in the range 100–135 °C results from the cold-crystallization of PLA during the heating scan. The endotherm in the range 135–155 °C results from the melting of the crystalline PLA whereas the melting of PA11 gives rise to the endotherm in the range 170–190 °C.

Regarding the PLA cold-crystallization, the gradual shift to low temperature with increasing PA11 content in the blends suggests a nucleating effect from PA11 at the interface of the unlike domains. In parallel to this nucleating effect, significant change can be observed in the shape of the melting endotherms of PLA, *i.e.* the amplitude ratio of the high temperature (HT) to low temperature (LT) components is increasing with increasing PA11 content. The double melting endotherm of PLA is usually assigned to a melting-recrystallization phenomenon during the heating scan, due to unstable defective crystals [7,77,78]. Therefore, the above observation is an indication of an increasing proportion of defective PLA crystals that is subjected to the melting-recrystallization process. This can be understood by the fact that the slightly PA11-promoted crystallization of PLA is likely to result in more and more defective

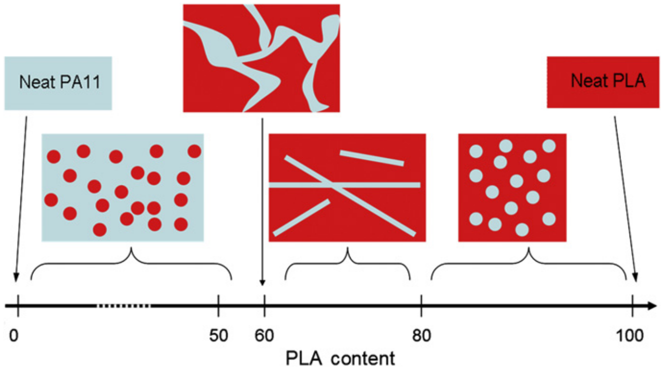

Fig. 4. Schematic of the morphology evolution of the PLA/PA11 blends as a function of composition.

crystals due to the downward temperature shift of the cold-crystallization. The melting enthalpy of PLA reported in Fig. 7 as a function of blend composition yet does not indicate significant deviation from the additive mixture law, the average value of the crystallinity index being $X_{PLA} \approx 32\%$. This contrasts with the improved crystallization capabilities of PLA in binary blend with PCL [34]

The melting endotherm of PA11 also displays a bimodal shape. This phenomenon occasionally reported in literature [79] can again be ascribed to a melting-recrystallization phenomenon of defective crystallites, due to processing conditions. Notwithstanding, these crystallites display the stable triclinic form of PA11, according to the WAXS data.

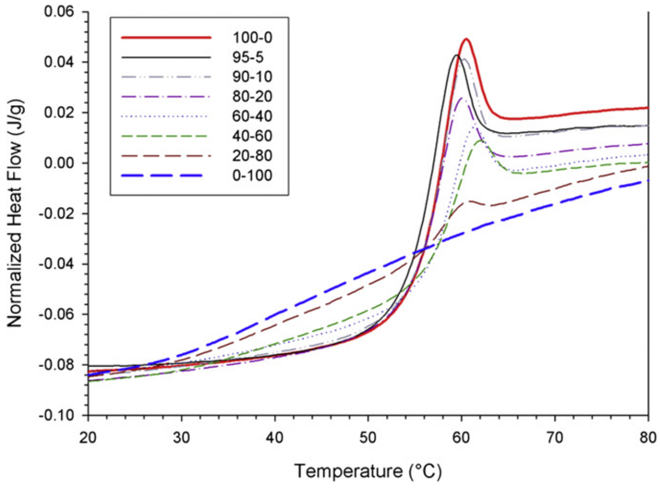

Fig. 5. DSC heating traces of the PLA/PA11 blends and the neat components in the temperature range of the glass transition.

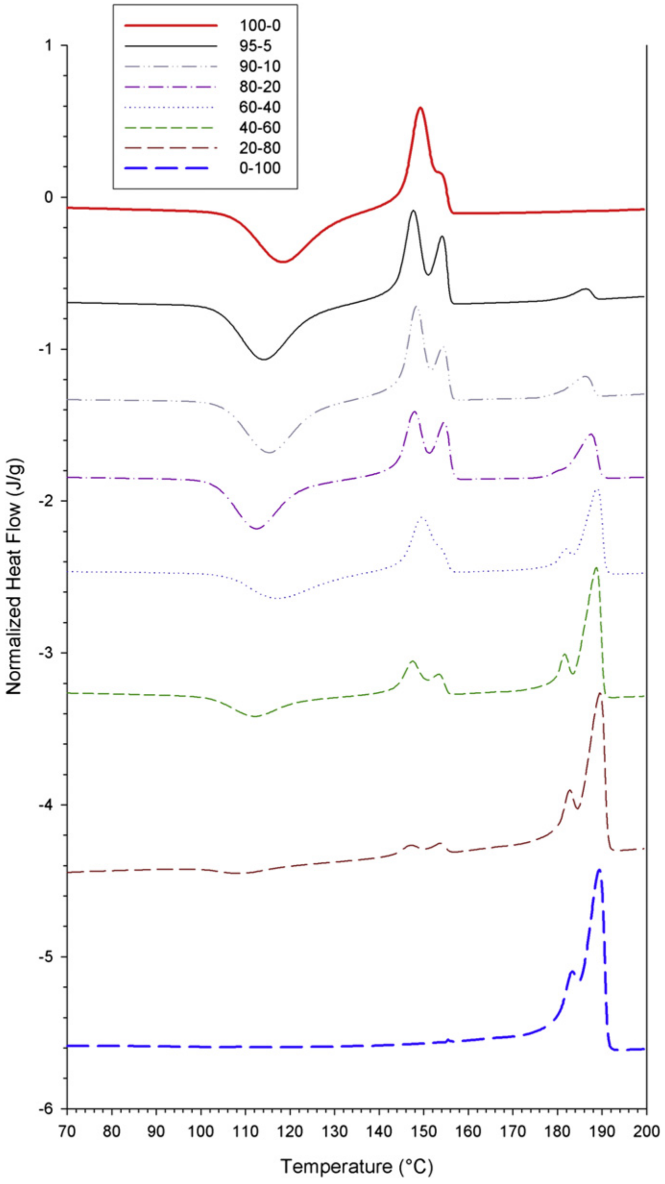

Fig. 6. DSC heating traces of the PLA/PA11 blends and the neat components in the temperature range above the glass transition.

The DSC cooling traces of Fig. 8 show that there is little if any incidence of blending on the crystallization kinetics of PA11, the exotherm peak temperature being $T_c \approx 165$ °C irrespective of blend composition (Fig. 8a). This is a hint that PLA chains are not miscible in the PA11 phase. This is also an indication of low interfacial free energy at the boundaries of the phase-separated domains, *i.e.* neither favorable nor unfavorable interactions between the unlike species. The very faint exotherm that can be discerned at $T \approx 98$ °C might be ascribed to minute crystallization of PLA upon cooling. Indeed, if PA11 has a weak nucleating effect on PLA upon heating, it could also work the same upon cooling, considering that PA11 is already crystallized at $T = 98$ °C. However, as can be seen on the close-up view of Fig. 8b, the missing of this thermal event for PLA/PA11 compositions 20/80 and 40/60 does not support this assumption. An alternative explanation is a homogeneous nucleation of PA11 within the smallest droplets at low PA11 content. This phenomenon has been largely investigated as the so-called “droplet crystallization” [80–91]. When crystallizable polymers are highly dispersed into micronic and sub-micronic droplets within a non-nucleating liquid medium, heterogeneous nucleating impurities are sequestrated within some of the droplets so that most of the polymer must crystallize via homogeneous nucleation within the impurity-free droplets. This process occurs at much lower temperature than that of the common heterogeneous nucleation. Crystallization temperature depression of 70–80 °C has been reported for various polymers including nanostructured block copolymers. This is roughly the depression presently observed for PA11, *i.e.* $T_c \approx 98$ °C for the LT crystallization versus $T_c \approx 165$ °C for the HT crystallization (Fig. 8a). Besides, the fact that the phenomenon only occurs for PA11 contents ≤40%, *i.e.* when PA11 is dispersed as droplets in the blends (Fig. 8b), thoroughly supports

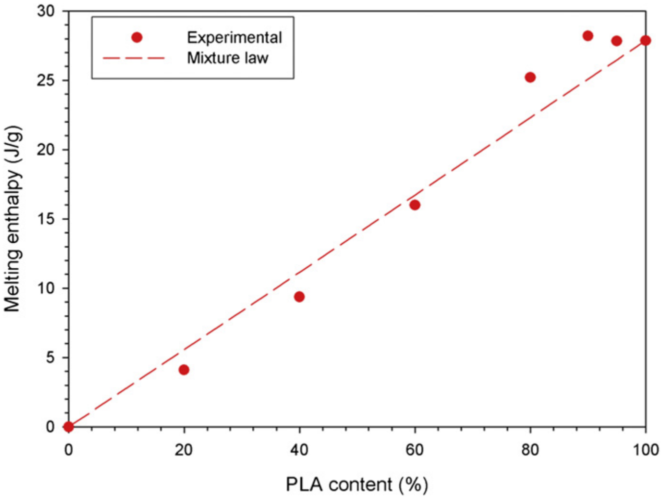

Fig. 7. Melting enthalpy of the PLA component in the blends as a function of composition.

the hypothesis of partial homogeneous nucleation of PA11. As an additional supporting hint, worth noticing is that the 90/10 blend containing only 10% of PA11 displays a greater LT crystallization peak compared with the HT one: this means that the lower the PA11 content in the blend, the higher the PA11 propensity to heterogeneous nucleation. This phenomenon is indirectly a confirmation of 1) the very fine dispersion of PA11 in the PLA matrix of PLA-rich blends and 2) the self-compatibility of the unlike species.

3.5. DMTA behavior

The evolution with temperature of the storage modulus, E', is plotted in Fig. 9 for the PLA/PA11 blends and the neat components. At room temperature, *i.e.* below Tg for both polymers, the PA11 stiffness is somewhat lower than that of PLA. The RT moduli of the blends roughly obey a linear mixing rule with composition as shown in Fig. 10. Due to the closeness of the two polymer moduli, the morphological changes with blend composition have very weak effect of the modulus of the blends.

When increasing the temperature up to 80 °C, *i.e.* above the Tg value of both polymers, the PA11 stiffness decreases by only 2/3-decade (Fig. 9) owing to the crystalline phase that preserves a reinforcing effect in spite of the fact that the predominant amorphous phase in PA11 is rubbery. In contrast, the PLA stiffness exhibits a 3-decade drop for the same temperature increase. Moreover, the data of Fig. 9 reveal that the modulus of the blends at 80 °C does not follow a monotonic decrease with increasing PLA content. A drastic drop appears in the PLA composition range 60–80%.

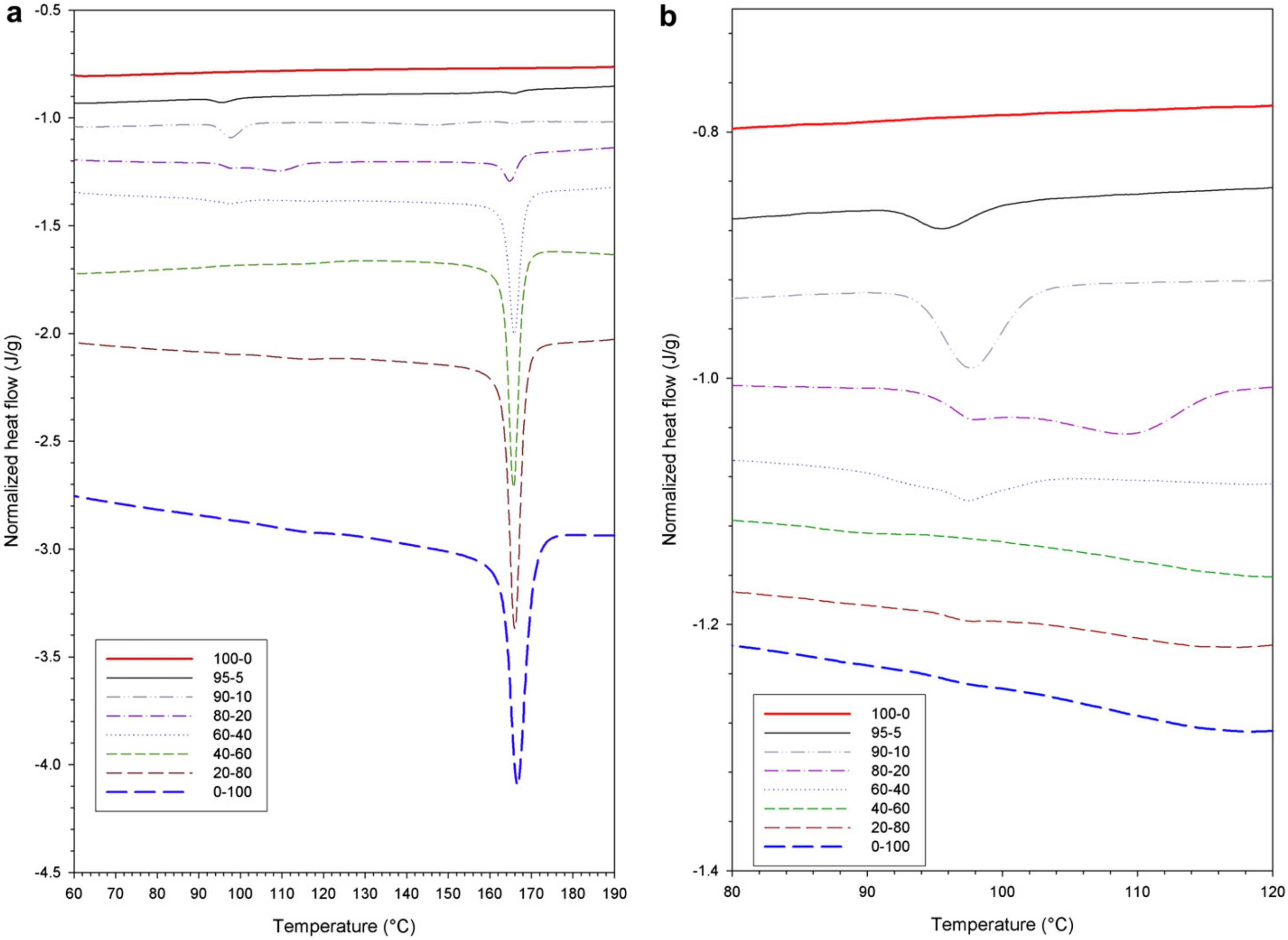

Fig. 8. DSC cooling traces of the PLA/PA11 blends and the neat components: a) DSC recordings over the temperature range 190–60 °C; b) close-up view of the temperature domain 120–80 °C.

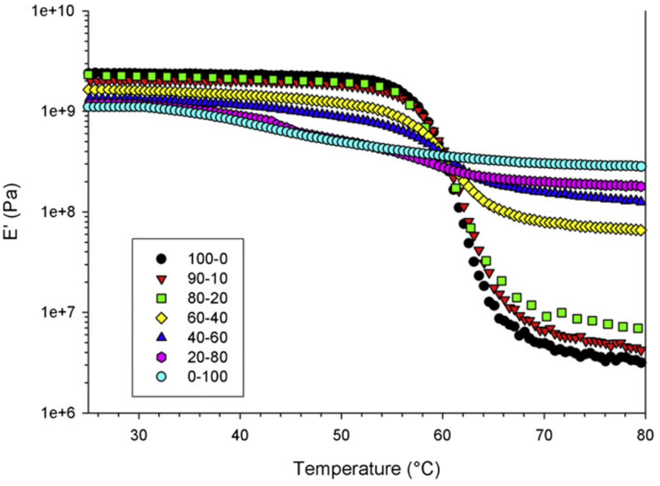

Fig. 9. Storage modulus as a function of temperature for the PLA/PA11 blends and the neat components.

Fig. 11 reports the E'(80 °C) evolution as a function of blend composition together with the computed Voigt and Reuss boundaries, *i.e.* the *parallel* and *series* mechanical coupling models of the two components. The experimental variation curve is typically sigmoidal in log scale. In the PLA-rich composition range, the proximity of the data to the lower limit of the *series* model is consistent with PA11 being dispersed as droplets in the PLA matrix. Indeed, the *series* mechanical coupling gives predominance to the softer phase, namely PLA that is rubbery in the present experimental conditions. Conversely, in the PA11-rich range, the proximity of the experimental data to the upper limit of the *parallel* model is consistent with PA11 being the continuous phase since the *parallel* mechanical coupling gives predominance to the stiffer PA11 phase. In the intermediate composition range, the stiffness of the 60/40 PLA/PA11 blend, and the 65/35 blend as well, are closer to the *parallel* model in spite of the minor PA11 content. This can be assigned to the thread-like morphology of the stiff PA11 phase imbedded in the rubbery PLA matrix which plays the role of a fibrillar reinforcing filler: this is a kind of self-reinforcement of the blends.

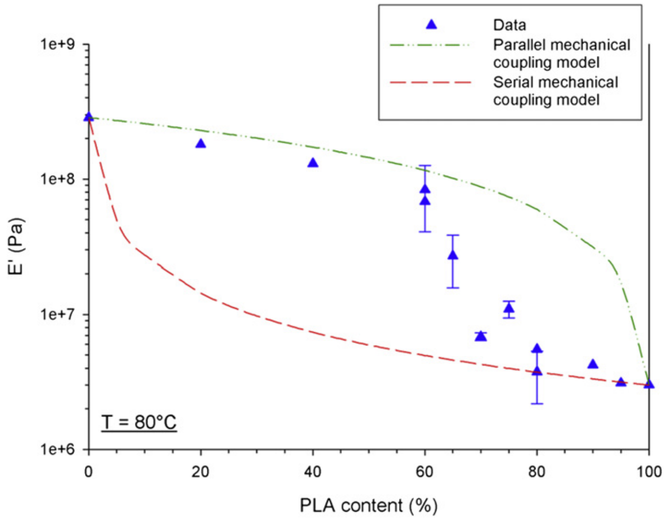

Fig. 11. Storage modulus of the PLA/PA11 blends as a function of composition at $T = 80$ °C.

Fig. 12 shows the tanδ variations for the blends and neat components in the temperature range of the main mechanical relaxation of the amorphous phase of both components. These data confirm the non-monotonic evolution of mechanical behavior of the blends as a function of composition, more particularly in the mid-composition range. Indeed the tanδ peak amplitude of the 80/20 blend is only 1/2 that of neat PLA in spite of the largely predominant PLA content. For the blend 60/40, the tanδ value at peak drops to 1/4 that of neat PLA in spite of the 60% PLA composition in the blend. This is clear indication that, in spite of higher PLA content, the tanδ of the above mentioned blends is more sensitive to the weak damping behavior of PA11 than to the strong one of PLA in the temperature range of the main relaxation of the amorphous phase of the two components. It means that PLA is less load-bearing than one could expect according to its weight fraction. This is a consequence of the morphology-governed mechanical coupling of the unlike phases that promotes the contribution of the stiff PA11 component, noticeably in the case of the PA11 thread-like morphology for 30–40% PA11 contents.

3.6. Tensile drawing

From the study of the uniaxial tensile drawing, the evolution with composition of the yield stress and the strain at break of the

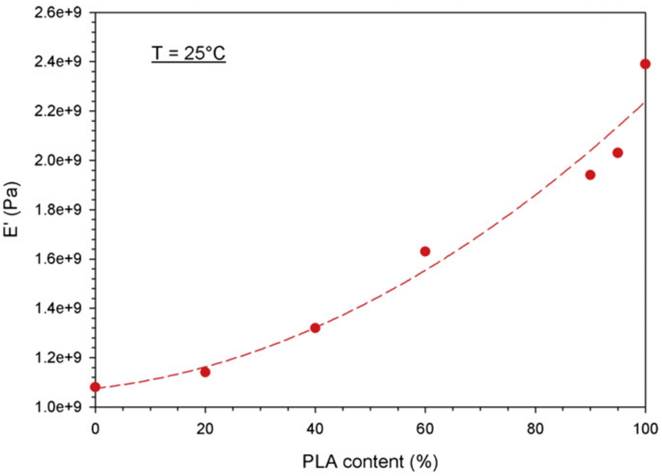

Fig. 10. Storage modulus of the PLA/PA11 blends as a function of composition at room temperature.

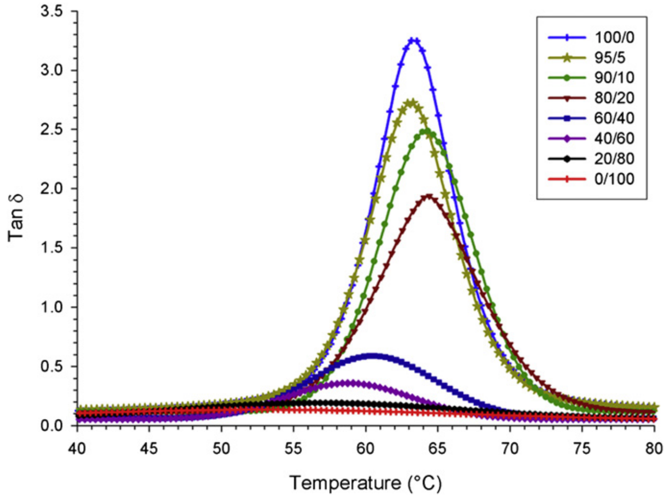

Fig. 12. Loss tangent in the temperature range of the glass transition for the PLA/PA11 blends and the neat components.

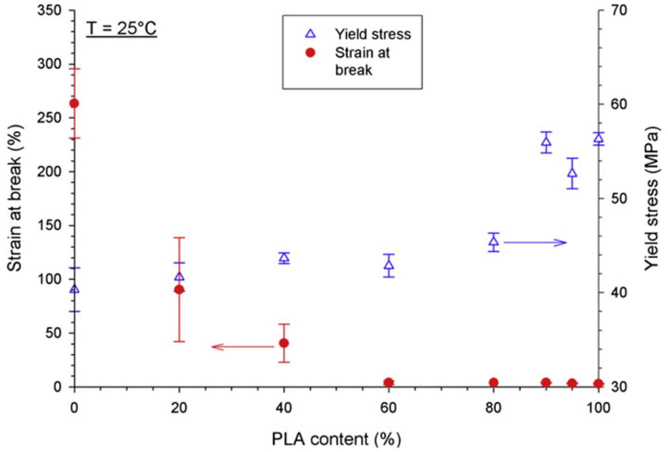

Fig. 13. Yield stress and strain at break as a function of composition for the PLA/PA11 blends at room temperature.

blends at RT have been reported in Fig. 13. The yield stress roughly follows a linear mixture law between the limiting values $\sigma_y^{PA11} \approx 42$ MPa and $\sigma_y^{PLA} \approx 55$ MPa, in a similar manner as the RT storage modulus (Fig. 10). On the one hand, the similarity is quite logical considering that plastic flow requests overwhelming the energy barriers between chains, *i.e.* the molecular interactions, to which the storage modulus is also directly dependent. On the other hand, the linearity is not surprising since the limiting values of the yield stress of the components are only slightly different, and the limiting values of the modulus as well. The strain at break decreases smoothly from 260% for neat PA11 down to a few percents for the composition 60/40. The brittle behavior of PLA seems to govern the overall behavior of the blends when PLA is predominant. It seems however that blends with PA11 content >50% display positive combination of yield stress and strain at break resulting in advantageous impact strength at RT.

In contrast, the yield stress data from Fig. 14 at $T = 80$ °C exhibit a non-uniform drop with increasing PLA content in the blends from the upper bound of the plastic PA11 component, $\sigma_y^{PA11} \approx 23$ MPa, to the lower bound of the rubbery PLA, $\sigma_y^{PLA} \approx 1$ MPa. In parallel, the strain at break increases from $\varepsilon_{break} \approx 330\%$ for the plastic PA11 up to $\varepsilon_{break} \approx 1000\%$ for the rubbery PLA. The combination of the two properties suggests an optimum impact strength of the blends for PLA compositions in the range 60–65%, at $T = 80$ °C.

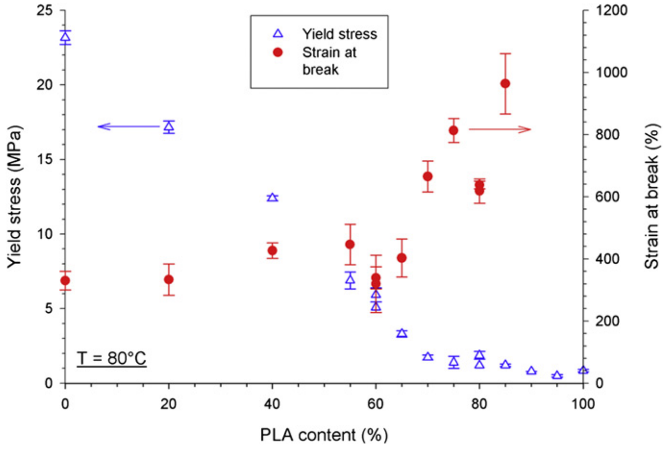

Fig. 14. Yield stress and strain at break as a function of composition for the PLA/PA11 blends at $T = 80$ °C.

3.7. Concluding remarks

The present study has revealed good self-compatibility of PLA/PA11 immiscible binary blends without using a compatibilizing agent, as judged from the micronic to sub-micronic dispersion of the minor component in the matrix of the major component, on both sides of the composition range. Recent studies regarding melt-compounded PLA blends with polyurethane [27] or polyamide [33] elastomers reported excellent compatibility of the two compounds without the use a surfactant. Although the authors of these reports did not argue on the origin of successful dispersion of the binary blends, one may suspect the relative polarity of the two components to be a prime role factor. Indeed, sub-micronic dispersion of immiscible blends entails a high specific interfacial area that can be thermodynamically stable only if the interfacial free energy is very low, *i.e.* if the interactions between unlike chain species are not much different from the ones between chains of the same kind. In contrast to the case of PLA blends with hyper-branched polyester-amide [28], there was no evidence of H-bonding between unlike chains in the present PLA/PA11 binary system, as assessed from infrared spectroscopy in the region of the PLA carbonyl groups. It seems that when most of the H-bonds are formed between chains of the PA11 phase in the molten state [64], the unlike chains interact friendly at the boundary of the phase-separated domains, so that a low surface free energy results.

The above argumentation is supported by the almost unchanged crystallization behavior of both PA11 and PLA in the blends since either attractive or repulsive interactions would be capable of promoting crystal nucleation. On the one hand, attractive interactions reduce the molecular mobility at the vicinity of the interface, which is a favorable factor for nucleation. On the other hand, in the case of repulsive interactions, thermodynamics would promote early crystallization owing to the decrease of interfacial free energy between the separated phases. The experimental findings for PLA/PA11 blends vouch in favour of neutral interactions between the unlike chains. Besides, the observation that crystallized PA11 does not operate a nucleating effect on PLA, both upon cooling and heating, gives evidence of no capability of PLA for epitaxial crystallization onto the PA11 crystal surface.

At room temperature, the mechanical properties of the blends do not exhibit a significant morphology-sensitivity, probably due to the fact that both polymers are stiff. Only blends with PA11 content >50% seem to benefit from the plastic behavior of the PA11 component. However, at 80 °C, the thread-like morphology of the stiff PA11 component in the blends of PLA composition 60–65% provides a reinforcing effect to the rubbery PLA matrix. This kind of self-reinforcement phenomenon can be compared with the *in situ* reinforcement of PA6 by oriented PET microfibrils reported by Fakirov et al. [92] as a result of melt-processing and heat treatment of PET/PA6 blends. Similar property enhancement has also been reported for polyamide66 (PA66) or PA6 blends with liquid crystalline polyester (LCP), the latter component being in the form of process-oriented microfibrils [74,93]. The main difference in the present case is that the PA11 thread-like morphology is isotropically distributed, so that the reinforcement is also isotropic and therefore much less remarkable than for unidirectional fibril orientation. Besides, reinforcement is only observed when PLA is rubbery. Therefore, orientation via processing appears to be an attractive issue for the mechanical property improvement of PLA/PA11 blends. One may also expect reaching better self-reinforcement effect of these blends by appropriate adjustment of the viscosity ratio of the two components in order to promote the thread-like PA11 morphology in the PLA matrix, at rather low PA11 contents. This expected morphological modification should also benefit the RT behavior.

The mechanical behavior of these blends after crystallization of the PLA matrix is another attractive perspective of investigation. In addition to the stiffness enhancement via both blend morphology and PLA crystallinity, one may expect an impact strength improvement of the blends with respect to the neat crystalline PLA which is typically brittle at RT, benefiting from the PA11 toughness.

Acknowledgements

The authors are indebted to *Arkema* (France) for the generous supply of the polyamide11 and its molecular characteristics. Dr. A. Addad (UMET – Univ. Lille1) is also acknowledged for technical assistance in the Scanning Electron Microscopy.

References

[1] Sinclair RG. J Macromol Sci – Pure Appl Chem 1996;33:585–97.
[2] Garlotta D. J Polym Environ 2002;9:63–84.
[3] Auras RA, Harte B, Selke S. Macromol Biosci 2004;4:835–64.
[4] Gupta AP, Kumar V. Eur Polym J 2007;43:4053–74.
[5] Averous L. Polylactic acid: synthesis, properties and applications. In: Belgacem MN, Gandini A, editors. Monomers, Polymers and composites from renewable resources. Oxford, UK: Elsevier Ltd.; 2008. p. 433–50.
[6] Urayama H, Kanamori T, Kimura Y. Macromol Mater Eng 2001;286: 705–13.
[7] Sarasua J-R, Prud'homme RE, Wisniewski M, Le Borgne A, Spassky N. Macromolecules 1998;31:3895–905.
[8] Vasanthakumari R, Pennings AJ. Polymer 1983;24:175–8.
[9] Tsuji H, Ikada Y. Macromol Chem Phys 1996;197:3483–99.
[10] Abe H, Kikkawa Y, Inoue Y, Doi Y. Biomacromolecules 2001;2:1007–14.
[11] Pluta M, Galeski A. J Appl Polym Sci 2002;86:1386–95.
[12] Masirek R, Piorkowska E, Galeski A, Mucha M. J Appl Polym Sci 2007;105:282–90.
[13] Stoclet G, Seguela R, Lefebvre J-M, Elkoun S, Vanmansart C. Macromolecules 2010;43:1488–98.
[14] Martin O, Averous L. Polymer 2001;42:6209–19.
[15] Tsuji H, Takai H, Saha SK. Polymer 2006;47:3826–37.
[16] Nam JY, Okamoto M, Okamoto H, Nakano M, Usuki A, Matsuda M. Polymer 2006;47:1340–7.
[17] Li H, Huneault MA. Polymer 2007;48:6855–66.
[18] Eguiburu JL, Iruin JJ, Fernandez-Berridi MJ, San Roman J. Polymer 1998;39:6891–7.
[19] Shuai X, He Y, Asakawa N, Inoue Y. J Appl Polym Sci 2001;81:762–72.
[20] Zhang G, Zhang J, Zhou X, Shen D. J Appl Polym Sci 2003;88:973–9.
[21] Zhang G, Zhang J, Wang S, Shen D. J Polym Sci. Polym Phys 2003;41:23–30.
[22] Cao X, Mohamed A, Gordon SH, Willett JL, Sessa DJ. Thermochimica Acta 2003;406:115–27.
[23] Broz ME, VanderHart DL, Washburn NR. Biomaterials 2003;24:4181–90.
[24] Hu Y, Hu YS, Topolkaraev V, Hiltner A, Baer E. Polymer 2003;44:5681–9.
[25] Hu Y, Rogunova M, Topolkaraev V, Hiltner A, Baer E. Polymer 2003;44:5701–10.
[26] Lopez-Rodriguez N, Lopez-Arraiza A, Meaurio E, Sarasua JR. Polym Eng Sci 2006;49:1299–308.
[27] Li Y, Shimizu H. Macromol Biosci 2007;7:921–8.
[28] Lin Y, Zhang K-Y, Dong Z-M, Dong L-S, Li Y-S. Macromolecules 2007;40:6257–67.
[29] Sarazin P, Li G, Orts WJ, Favis BD. Polymer 2008;49:599–609.
[30] Wu D, Zhang Y, Zhang M, Zhou W. Eur Polym J 2008;44:2171–83.
[31] Lai W-C, Liau W-B, Yang L-Y. J Appl Polym Sci 2008;110:3616–23.
[32] Chen H, Pyda M, Cebe P. Thermochimica Acta 2009;492:61–6.
[33] Zhang W, Chen L, Zhang Y. Polymer 2009;50:1311–5.
[34] Simoes CL, Viana JC, Cunha AM. J Appl Polym Sci 2009;112:345–52.
[35] Ray S, Maiti P, Okamoto M, Yamada K, Ueda K. Macromolecules 2002;35:3104–10.
[36] Maiti P, Yamada K, Okamoto M, Ueda K, Okamoto K. Chem Mater 2002;14:4654–61.
[37] Chang J-H, An YU, Cho D, Giannelis EP. Polymer 2003;44:3715–20.
[38] Nam PH, Kaneko M, Ninomiya N, Fujimori A, Masuko T. Polym Intern 2006;55:916–22.
[39] Fujimori A, Ninomiya N, Masuko T. Polym Eng Sci 2008;48:1103–11.
[40] Wu D, Wu L, Wu L, Xu B, Zhang Y, Zhang M. J Nanosci Nanotechnol 2008;8:1658–68.
[41] Bordes P, Pollet E, Averous L. Prog Polym Sci 2009;34:125–55.
[42] Zhang L, Xiong C, Deng X. Polymer 1996;37:235–41.
[43] Ohkoshi I, Abe H, Doi Y. Polymer 2000;41:5985–92.
[44] Park JW, Im SS, Kim SH, Kim YH. Polym Eng Sci 2000;40:2539–50.
[45] Park JW, Im SS. J Polym Sci. Polym Phys 2002;40:1931–9.
[46] Park JW, Im SS. J Appl Polym Sci 2002;86:647–55.
[47] Averous L. J Macromol Sci. Polym Rev 2004;44:231–74.
[48] Peesan M, Supaphol P, Rujiravanit R. Carbohydr Polym 2005;60:343–50.
[49] Bhatia A, Gupta RK, Bhattacharya S, Choi HJ. Korea–Australia Rheol J 2007;19: 125–31.
[50] Schwach E, Six J-L, Averous L. J Polym Environ 2008;16:286–97.
[51] Yokohara T, Yamaguchi M. Eur Polym J 2008;44:677–85.
[52] Huneault MA, Li H. Polymer 2007;48:270–80.
[53] Correlo VM, Boesel LF, Bhattacharya M, Mano JF, Neves NM, Reis RL. Mater Sci Eng A 2005;403:57–68.
[54] Mathew AP, Oksman K, Sain M. J Appl Polym Sci 2005;97:2014–25.
[55] Kvien L, Tanem BS, Oksman K. Biomacromolecules 2005;6:3160–5.
[56] Yu J, Ai F, Dufresne A, Gao S, Huang J, Chang PR. Macromol Mater Eng 2008;293:763–70.
[57] Lin N, Chen G, Huang J, Dufresne A, Chang PR. J Appl Polym Sci 2009;113: 3417–25.
[58] Azizi Samir MAS, Alloin F, Dufresne A. Biomacromolecules 2005;6:612–26.
[59] Dufresne A. J Nanosci Nanotechnol 2006;6:322–30.
[60] Fischer EW, Sterzel HJ, Wegner G. Kolloid Z Z Polym 1973;21:980–90.
[61] Huang J, Lisowski MS, Runt J, Hall ES, Kean RT, Buehler N, et al. Macromolecules 1998;31:2593–9.
[62] Inoue M. J Polym Sci 1963;1:2697–709.
[63] Zhang Q, Mo Z, Liu S, Zhang H. Macromolecules 2000;33:5999–6005.
[64] Skrovanek DJ, Painter PC, Coleman MM. Macromolecules 1986;19:699–705.
[65] Dorgan JR, Williams JS, Lewis DN. J Rheol 1999;43:1141–55.
[66] (a) Aharoni SM. Macromolecules 1983;16:1722–8;
(b) Wu S. Polym Eng Sci 1992;32:823–30.
[67] Slichter WP. J Polym Sci 1959;36:259–66.
[68] Kim KG, Newman BA, Scheinbeim JI. J Polym Sci. Polym Phys 1985;23: 2477–82.
[69] Wu S. Polym Eng Sci 1987;27:335–43.
[70] Berger W, Kammer HW, Kummerloewe C. Makromol Chem. Suppl 1984;8: 101–8.
[71] Meng YZ, Tjong SC. Polymer 1998;39:99–107.
[72] Lee JK, Han CD. Polymer 1999;40:6277–96.
[73] Everaert V, Aerts L, Groeninckx G. Polymer 1999;40:6627–44.
[74] Wang H, Lee KW, Chung T-S, Jaffe M. Polym Compos 2000;21:114–23.
[75] Jana SC, Sau M. Polymer 2004;45:1665–78.
[76] Steinmann S, Gronski W, Friedrich C. Polymer 2001;42:6619–29.
[77] Yasuniwa M, Tsubakihara S, Sugimoto Y, Nakafuku C. J Polym Sci. Polym Phys 2004;42:25–32.
[78] Kulinski Z, Piorkowska E. Polymer 2005;46:10290–300.
[79] Roguet E, Tence-Girault S, Castagnet S, Grandidier JC, Hochstetter G. J Polym Sci. Polym Phys 2007;45:3046–59.
[80] Cormia RL, Price FP, Turnbull D. J Chem Phys 1962;37:1333–40.
[81] Koutsky JA, Walton AG, Baer E. J Appl Phys 1967;38:1832–9.
[82] O'Malley JJ, Pacansky TJ, Stauffer WJ. Macromolecules 1977;10:1197–9.
[83] Robitaille C, Prud'homme J. Macromolecules 1983;16:665–71.
[84] Schaaf P, Lotz B, Wittman J-C. Polymer 1987;28:193–200.
[85] Loo Y-L, Register RA, Ryan AJ. Phys Rev Lett 2000;84:4120–3.
[86] Massa MV, Carvalho JL, Dalnoki-Veressa K. Eur Phys J E 2003;12:111–7.
[87] Tol RT, Mathot VBF, Groeninckx G. Polymer 2005;46:2955–65.
[88] Müller AJ, Balsamo V, Arnal ML. Adv Polym Sci 2005;190:1–63.
[89] Sanchez MS, Mathot V, van den Poel G, Groeninckx G, Bruls W. J Polym Sci. Polym Phys 2006;44:815–25.
[90] Sun Y-S, Chung T-M, Li Y-J, Ho R-M, Ko B-T, Jeng U-S, et al. Macromolecules 2006;39:5782–8.
[91] Jin Y, Hiltner A, Baer E. J Polym Sci. Polym Phys 2007;45:1138–51.
[92] Fakirov S, Evstatiev M, Schultz JM. Polymer 1993;43:4669–79.
[93] Tjong SC, Meng YZ. Polymer 1997;38:4609–15.

Polymer 52 (2011) 1426–1435

Contents lists available at ScienceDirect

Polymer

journal homepage: www.elsevier.com/locate/polymer

Structural characterization of the δ-clathrate forms of syndiotactic polystyrene with *n*-alkanes

Oreste Tarallo*, Maria Maddalena Schiavone, Vittorio Petraccone

Dipartimento di Chimica "Paolo Corradini", Università degli Studi di Napoli Federico II, Complesso di Monte S. Angelo, via Cintia, 80126 Napoli, Italy

ARTICLE INFO

Article history:
Received 25 November 2010
Received in revised form
19 January 2011
Accepted 19 January 2011
Available online 27 January 2011

Keywords:
Syndiotactic polystyrene
n-Alkanes
Co-crystals

ABSTRACT

The δ-clathrate forms of syndiotactic polystyrene (s-PS) containing a homologous series of guests characterized by an increasing molecular volume (*n*-alkanes ranging from *n*-pentane to *n*-dodecane) have been investigated. The present analysis allows concluding that the volume of the guest plays a crucial role in the choice of the type of δ-clathrate that can be obtained. As a matter of fact, longer *n*-alkanes, such as *n*-octane, *n*-nonane or *n*-decane, turned out to give rise triclinic δ-clathrates presenting a guest/monomeric-unit ratio of 1/8, while δ-clathrates containing shorter alkanes, like *n*-hexane or *n*-heptane, instead, present a monoclinic or a triclinic structure with a guest/monomeric-unit ratio of 1/4. These results confirm the validity of a simple criterion to predict the type of s-PS δ-clathrate with a certain guest on the basis of the experimental d_{010}, as described in *Macromolecules* 2010, *43*, 8549–8558. Moreover, our analysis confirms previous solid state ^{13}C NMR and Raman spectroscopy data, indicating that shorter *n*-alkanes molecules, like *n*-hexane, are hosted in the cavities with an all-*trans* conformation while longer alkanes, like *n*-nonane, present bent conformations. The effect of *n*-alkanes molecules on the crystallization of s-PS amorphous samples has been investigated too.

1. Introduction

Syndiotactic polystyrene (s-PS) presents a very complex polymorphic behavior, including pure crystalline phases and different types of cocrystalline forms with a large number of low-molecular-mass guest molecules [1–35]. Moreover, by using suitable guest removal techniques, two different nanoporous crystalline forms (δ and ϵ), exhibiting a density ($\rho = 0.98$ g/cm^3) definitely lower than that of the amorphous s-PS ($\rho = 1.05$ g/cm^3), can be obtained [8,21]. In particular, in these forms the empty space is organized as isolated cavities and channels, for δ and ϵ crystalline phases, respectively (Fig. 1) [8,21].

These polymorphs can be considered as the first examples of polymeric molecular sieves, as they display high sorption selectivity similar to zeolites [3,4]. s-PS is the first case of semi-crystalline polymer whose sorption ability is higher for the crystalline phase than for the amorphous phase. The sorption of suitable guest molecules into these nanoporous phases leads to the formation of co-crystalline phases, which may display interesting properties depending on the guest molecule: for example, films presenting s-PS/active-guest co-crystals have been proposed as advanced fluorescent, non-linear optical, photo-reactive and magnetic materials [24–35].

It is worth pointing out that the formation of co-crystals with suitable polymer hosts constitutes an innovative approach in the area of functional polymeric materials, which are generally characterized by a disordered distribution of active groups into amorphous phases, since co-crystals reduce diffusivity of active molecules in the solid state and they prevent their self-aggregation [36–39]. Moreover, a particularly relevant feature of s-PS co-crystalline phases is the possibility to achieve three different kinds of uniplanar orientation, which allow controlling the orientation of the guest molecules not only in the crystalline phase but also in macroscopic films [40–43].

Most s-PS co-crystals present a monoclinic unit cell (with $P2_1/a$ symmetry) in which isolated molecules are imprisoned as guests into centrosymmetric cavities formed between *ac* layers of close packed alternated enantiomorphous **s**(2/1)2 polymer helices, typical of the nanoporous δ phase (Fig. 1A) [6–11]. These s-PS co-crystals have been defined as δ-clathrates and are generally characterized by a maximum guest/monomer-unit molar ratio of 1/4. In these clathrates, guests exhibit orientation of their main molecular plane nearly perpendicular to the axis of the polymer helices while, as the bulkiness of the guest

---

* Corresponding author. Tel.: +39 081 674443; fax: +39 081 674090.
E-mail addresses: oreste.tarallo@unina.it (O. Tarallo), mariamaddalena.schiavone@unina.it (M.M. Schiavone), vittorio.petraccone@unina.it (V. Petraccone).

0032-3861/$ – see front matter © 2011 Elsevier Ltd. All rights reserved.
doi:10.1016/j.polymer.2011.01.041

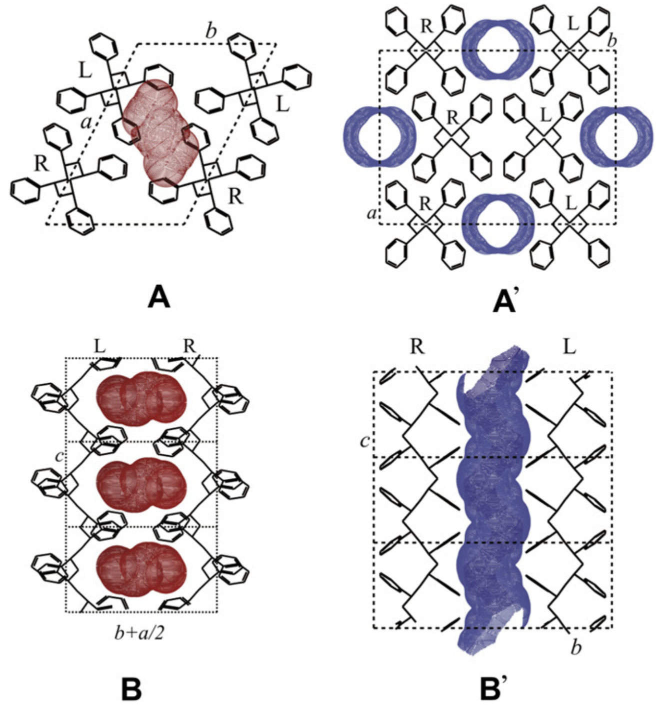

Fig. 1. Schematic representation of the nanoporous δ (A, B) and ϵ (A′, B′) crystalline phases of s-PS: (A, A′) projections along the *c* axis; (B, B′) projections perpendicular to the *c* axis. The shapes of the cavities and of the channels (determined by the Connolly methods with a probe radius of 0.17 nm) are reported in red and blue respectively. In B and B′ only one couple of polymer chains delimiting the cavities are reported. R = right-handed, L = left-handed helical chains. (For interpretation of the references to color in this figure legend, the reader is referred to the web version of this article).

increases, there is an increase of the spacing ($d_{010} = b\sin\gamma$) between the *ac* layers (in the range 1.06–1.2 nm) [11,19].

Very recently, it has been shown that, within δ-clathrates, beside the monoclinic ones, also triclinic crystalline structures can be obtained [14,16] in which guest molecular planes are inclined in respect to the polymer chain axes. Moreover, within the triclinic δ clathrates two definitely different organizations have been described [14,16]. A first type has been described up to now only in the case of the cocrystalline phase containing 4-nitroaniline (NA), in which the maximum guest/monomeric-unit ratio of ¼ and the very efficient close packing of enantiomorphous helices in the *ac* plane (typical of the nanoporous δ phase) are still present, but these planes are shifted along the *c* axis direction of the unit cell in respect to the monoclinic forms [14]. In the second type, described for bulky molecules such as dibenzofuran (DBF) [16], the maximum guest/monomeric-unit ratio is halved since, in order to make room for these very cumbersome guests, couples of close packed chains are alternated to couples of polymer helices delimiting the cavities in which guest are hosted. Consequently the close packing within the *ac* layers of polymer helices is partly lost [16].

In the s-PS co-crystals obtained from the ϵ form, defined as ϵ-clathrates, guest molecules are imprisoned into the channels formed between enantiomorphous **s**(2/1)2 polymer helices, typical of the nanoporous ϵ phase (Fig. 1A'–B') [21–23]. As a consequence, also very long guest molecules can be hosted by placing their main molecular axis nearly parallel to the axis of the polymer helices [20–23]. In these cases, the continuous nature of the channels could allow stacking of a variable number of guest molecules per monomer unit, whose maximum value depends only on the specific guest molecule.

In the present paper we investigate the crystalline structures of the δ clathrates of s-PS with *n*-alkanes ranging from *n*-pentane to *n*-dodecane by means of X-ray diffraction, FT-IR spectroscopy, thermogravimetric analysis and molecular mechanics calculations. They represent a class of flexible guest molecules that have been only marginally studied from the structural point of view [3,44–47]. Moreover, the systematic study of a homologous series of guest molecules characterized by an increasing molecular volume can be useful to a deeper understanding of the factors governing the choice of a particular type of clathrate structure between those previously described.

Up to now, different authors have already investigated the s-PS δ clathrates with these guests by several techniques [3,44–47]. In particular, Kaneko et al. [45,47] has pointed out the unusual behavior of these co-crystals in respect to the d_{010} lattice spacing changes with respect to the chain length of guest *n*-alkane. As a matter of fact, differently to what shown in literature up to that time, they noticed that, ongoing from smaller to bulkier molecules (i.e. from *n*-hexane to *n*-decane), the d_{010} value seems first to expand in the case of *n*-hexane and *n*-heptane, then to markedly decrease at *n*-octane and then to increase slightly again up to *n*-decane [47]. A similar behavior for rigid molecules has been very recently discussed by us and clarified in terms of variations of structural symmetry (from monoclinic to triclinic) and of molecular encumbrance [16]. Kaneko et al. did not examine in detail the crystalline structure but, by ^{13}C NMR and Raman spectroscopy data, attributed this unusual behavior to conformational changes of the guest molecules in the co-crystalline phase [47]. In particular, according to their data, *n*-hexane and *n*-heptane molecules took extended chains conformations while longer *n*-alkanes took bent chain structures [47]. Since we would expect that, in the crystalline state, guest molecules should assume the absolute minimum energy conformation, that for the *n*-alkanes is the all-*trans* one [48–51], these literature data moved us further on to examine the crystalline structures of these co-crystalline forms in detail.

Finally, it is worth pointing out that, very recently, some of use investigated the crystalline structure of s-PS ϵ-clathrates containing *n*-alkane guest molecules (from *n*-hexane to *n*-dodecane) showing that, independently from the length of the *n*-alkane, the examined structures are all very similar and present guests arranged in an all-*trans* conformation with their main molecular axis almost parallel to the axis of the channels [23].

In this paper, for the first time, the effect of *n*-alkanes molecules on the crystallization of s-PS amorphous samples has been investigated too.

2. Experimental section

2.1. Materials

The s-PS used in this study was manufactured by Dow Chemical Company under the trademark Questra 101. The ^{13}C nuclear magnetic resonance characterization showed that the content of syndiotactic triads was over 98%. The weight-average molar mass obtained by gel permeation chromatography in trichlorobenzene at 135 °C was found to be $M_w = 3.2 \times 10^5$ with the dispersity index $M_w/M_n = 3.9$.

Chloroform, *n*-alkanes and the other solvents used for the preparation of the samples were purchased from Aldrich and used without any further purification.

Oriented s-PS/*n*-alkane δ-clathrate samples were obtained by immersion in the pure liquid *n*-alkane at room temperature (up to 1 month) of oriented s-PS/CHCl$_3$ δ-clathrate samples, keeping the ends of the specimen fixed. Oriented s-PS/CHCl$_3$ δ-clathrate samples were obtained by exposure of oriented samples in the α form to liquid CHCl$_3$ at room temperature, for 36–48 h, keeping fixed the ends of the specimen. Fibers of the α form were obtained

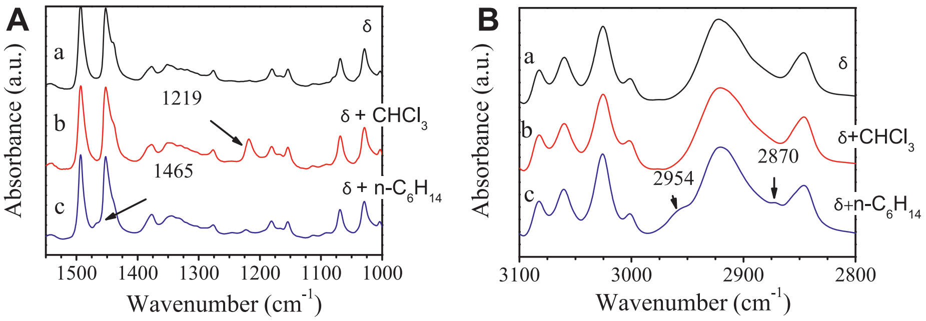

Fig. 2. FT-IR spectral changes during the exchange process of *n*-hexane (curve c) into an unoriented s-PS/CHCl$_3$ δ cocrystalline sample (curve b). (A) 1550–1000 cm^{-1} region. (B) 3100–2800 cm^{-1} region. As the substitution of CHCl$_3$ guest molecules goes ahead, the band at 1219 cm^{-1} (due to C–H deformation of chloroform) decreases in intensity while the shoulders at 1465 cm^{-1} (due to CH$_2$ symmetrical bending), at 2870 cm^{-1} (due to *n*-hexane CH$_3$ symmetric stretching) and at 2954 cm^{-1}(due to the CH$_3$ asymmetric stretching) increase in intensity [55–58]. The same spectral regions have been reported for comparison also for the nanoporous δ form (curve a).

by drawing unoriented α form samples with a miniature mechanical tester apparatus (Reometric Scientific Minimat) at a drawing rate of 10 mm/min at a temperature in the range 105–110 °C. Unoriented α form specimens were prepared in a hot press by melting as supplied samples at 270 °C and successive rapid cooling.

Unoriented samples of s-PS δ clathrates with *n*-alkanes were obtained by immersion of s-PS/CHCl$_3$ δ-clathrate powders in the pure liquid at room temperature up to 1 month depending on the length of the *n*-alkane molecule. Unoriented s-PS/CHCl$_3$ δ-clathrate samples were obtained by immersion in chloroform of powders in the crystalline δ form for 24–36 h at room temperature. Unoriented s-PS δ form samples were in turn obtained by removing (by acetone treatment) the guest from s-PS/toluene δ-clathrate samples prepared by casting of a solution of the as supplied polymer in toluene for 4 h.

Amorphous s-PS samples were prepared in a hot press by melting as supplied samples at 300 °C and successive rapid quenching in liquid nitrogen.

2.2. TGA measurements

Thermogravimetric analysis was carried out for each s-PS/*n*-alkane δ-clathrate sample using an SDT 2960 Simultaneous DSC-TGA (TA Instruments) in the range 20–300 °C, with a scanning rate of 10 °C/min.

2.3. FT-IR measurements

Infrared spectra were obtained at a resolution of 2.0 cm^{-1} with a Jasco FT/IR-430 spectrometer. The scanned wavenumber range was 3500–500 cm^{-1}. 64 scans were signal averaged to reduce the noise. The thickness of films used was always between 20 and 40 μm, in order to keep peaks of interest in the range of absorbance-concentration linearity. Measurements on powders were performed in the form of KBr pellets. All spectra are reported in absorbance units and are normalized when necessary with respect to the band at 1601 cm^{-1}.

2.4. X-ray diffraction

The X-ray fiber diffraction patterns of oriented samples were obtained on a BAS-MS imaging plate (FUJIFILM) with a cylindrical camera (radius 57.3 mm, Ni-filtered Cu-Kα radiation monochromatized with a graphite crystal) and processed with a digital scanner (FUJI-BAS 1800). Calculated intensities were obtained as $I_c = F_c \cdot M_i \cdot B \cdot Lp$ where F_c is the calculated structure factor, M_i is the multiplicity, B is a thermal factor ($B = 8$ Å^2) and Lp is the Lorentz-polarization factor for X-ray fiber diffraction:

$$\mathrm{L_p} = \frac{\left(\frac{0.5\left(\cos^2 2\theta + \cos^2 2\theta_M\right)}{1+\cos^2 2\theta_M} + \frac{0.5\left(1+\cos 2\theta_M + \cos^2 2\theta\right)}{1+\cos 2\theta_M}\right)}{\left(\sin^2 2\theta - \varsigma^2\right)^{1/2}} \tag{1}$$

with $2\theta_M = 26.6°$ the inclination angle of the monochromator and $\zeta = \lambda(l/c)$, l and c being the order of the layer line and the chain axis periodicity, respectively, and λ the wavelength of the used radiation (1.5418 Å). Calculated structure factors were obtained as $F_c = (\sum |F_i|^2 M_i)^{1/2}$, where the summation is taken over all reflections included in the 2θ range of the corresponding spot observed in the X-ray fiber diffraction pattern. Atomic scattering factors from Ref. [[52]] were used. The observed intensities I_{obsd} were evaluated integrating the crystalline peaks observed in the X-ray diffraction

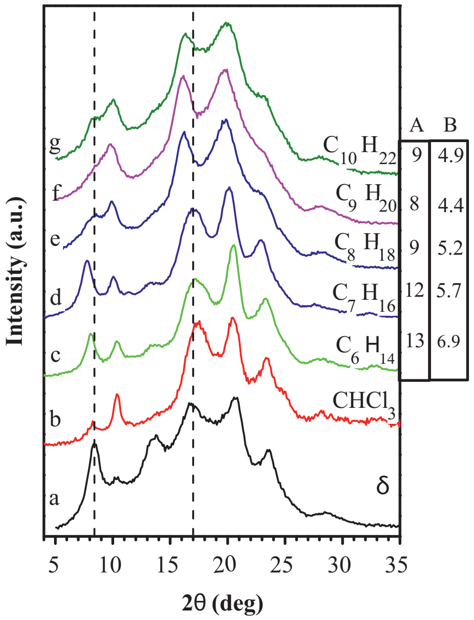

Fig. 3. X-ray powder diffraction patterns of the s-PS/*n*-alkane δ clathrate forms including: (c) *n*-hexane, (d) *n*-heptane, (e) *n*-octane, (f) *n*-nonane and (g) *n*-decane. For each one, the weight fractions (%) of *n*-alkane determined by thermogravimetric analysis are indicated (column A: samples dried in air for two days; column B: samples dried in air for three months). In (a) and (b) the X-ray powder diffraction patterns of the nanoporous s-PS δ form and of the s-PS/CHCl$_3$ δ clathrate from which the cocrystalline samples with *n*-alkane were obtained are reported for comparison, respectively.

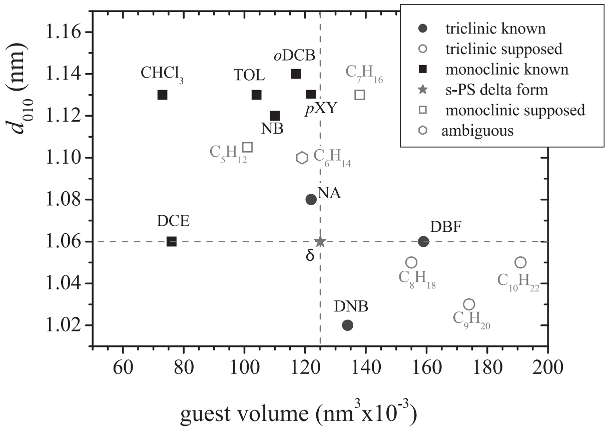

Fig. 4. d_{010} distances for the s-PS/*n*-alkane δ-clathrates studied in this paper and for some δ-clathrates whose structure is described in literature [6,9,10,14–16] *versus* the guest molecular volume. Supposed or known monoclinic clathrates are indicated with empty or filled squares respectively, while supposed or known triclinic ones are indicated with empty or filled circles respectively. The red star (whose position is highlighted by the two red dashed lines) indicates the d_{010} and volume of the cavities of the s-PS δ form [15,61]. TOL = toluene; NB = nitrobenzene; *p*XY = *p*-xylene; *o*DCB = *o*-dichlorobenzene; NA = 4-nitroaniline; DCE = 1,2-dichloroethane; DBF = dibenzofuran; DNB = 1,4-dinitrobenzene. As far as the s-PS/*n*-pentane δ-clathrate, see paragraph 3.5. (For interpretation of the references to color in this figure legend, the reader is referred to the web version of this article).

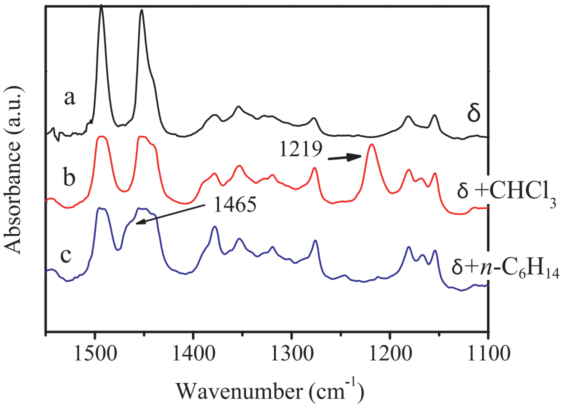

Fig. 5. FT-IR spectral changes during the exchange process of *n*-hexane into an oriented s-PS/$CHCl_3$ δ co-crystalline sample. The substitution of $CHCl_3$ with the alkane guest molecules causes the disappear of the band at 1219 cm^{-1} (due to C—H deformation of chloroform) and the appearance of a shoulder at 1465 cm^{-1} (due to CH_2 symmetrical bending of *n*-hexane) [55,56]. The same spectral region has been reported for comparison also for the nanoporous δ form (curve a).

profiles, read along different layer lines, after the subtraction of the background and amorphous contributions. Owing to the different shapes of the reflections on the equator and on the first and second layer lines, due to the different dimensions of the lamellar crystals in the direction perpendicular and parallel to the chain axis, different factors were used to scale the observed and calculated structure factors on the diverse layer lines. The discrepancy factor R has been evaluated as $R = \Sigma\,|F_{obsd}-F_{calcd}|/\Sigma F_{obsd}$ taking into account only the observed reflections.

Wide-angle X-ray diffraction patterns of unoriented samples were obtained with nickel-filtered Cu Kα radiation with an automatic Philips powder diffractometer operating in the θ/2θ Bragg–Brentano geometry using 2 mm thick specimen holders.

Calculated X-ray powder diffraction pattern were obtained with the *Diffraction-Crystal* module of the software package *Cerius*^{2} (version 4.2 by *Accelrys Inc.*) using an isotropic thermal factor ($B = 8$ Å^2). A Gaussian profile function having a half-height width regulated by the average crystallite size along a, b, and c axes (L_a, L_b and L_c, respectively) was used. A good agreement with the half-height width of the peaks in the experimental profile has been obtained for $L_a = L_b = 10$ nm and $L_c = 8$ nm.

2.5. Energy and volumes calculation methods

Energy calculations were carried out by using the Compass force field [53] within the *Open Force Field* module of *Cerius*^{2} by the smart minimizer method with standard convergence. The starting conformation of the s-PS polymer chains was that found by molecular mechanics calculations reported in the literature [54].

Volumes of the guest molecules have been determined with the *Connolly Surface* module of *Cerius*^{2} using a probe radius of 0.11 nm and a density dot of 0.1 nm^{-2}.

3. Result and discussion

3.1. Effect of chain length of n-alkanes on s-PS δ co-crystalline phases

Unoriented samples of δ co-crystals of s-PS with several *n*-alkanes (ranging from *n*-hexane to *n*-decane) have been prepared

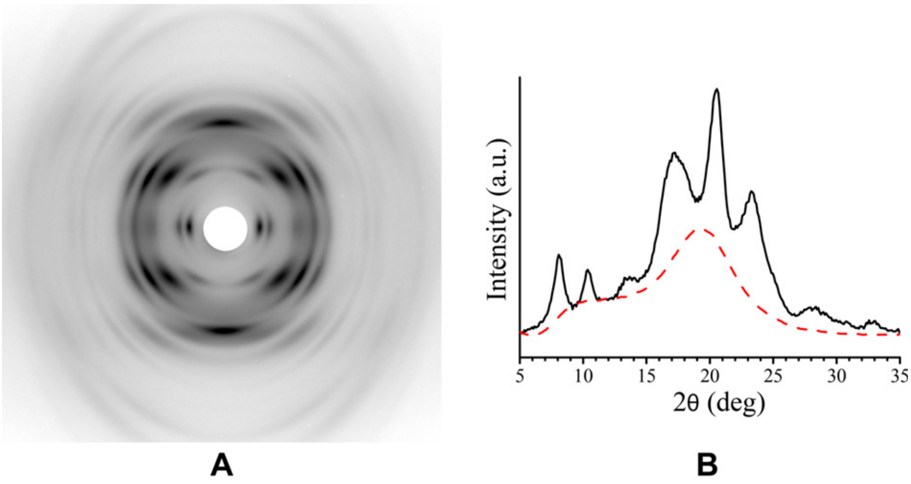

Fig. 6. X-ray diffraction patterns of (A) a uniaxially stretched film and (B) of an unoriented sample presenting the s-PS/*n*-hexane δ cocrystalline form. In (A) fiber axis is vertical. In (B) the amorphous and background contribution is indicated with a dashed line.

Table 1
Diffraction angles ($2\theta_{obsd}$), Bragg distances (d_{obsd}) and intensities (I_{obsd}) of the reflections observed on the layer lines (l) in the X-ray fiber diffraction pattern of Fig. 6A after subtraction of the contributions of amorphous and background.

l	$2\theta_{obsd}$ (deg)	d_{obsd} (nm)	I_{obsd} (a.u.)
0	8.0	1.11	4265
0	10.25	0.86	1556
0	16.9	0.52	2256
0	20.4	0.44	1180
0	23.3	0.38	741
1	13.3	0.67	1047
1	16.7	0.53	4735
1	20.35	0.44	2887
1	23.3	0.38	1331
2	24.3	0.37	436
2	28.1	0.32	362
2	32.8	0.27	58

by guest exchange starting from s-PS/$CHCl_3$ δ co-crystals. The guest exchange process was monitored thorough FT-IR spectroscopy. As already reported in the literature [45], we noticed that the sorption process proceeded much slower with the increase of the chain length of the n-alkane. For example, it was complete in 6 days in the case of n-hexane while it took almost 1 month in the case of n-decane. Fig. 2 shows the FT-IR spectral changes of the clathrate form containing chloroform as a guest on exposure to n-hexane. The replacement of the chloroform molecules in the sample with n-hexane causes the band at 1219 cm^{-1} (due to C–H deformation of chloroform) [55] to decrease in intensity while that at 1465 cm^{-1} (due to the CH_2 symmetrical bending) to increase in intensity (see Fig. 2) [56]. The substitution of $CHCl_3$ with n-hexane is revealed also by the appearance of the bands at 2954 cm^{-1} and at 2870 cm^{-1} due to the CH_3 asymmetric and symmetric stretching of n-hexane, respectively [56–58]. On the other hand, it is worth pointing out that absorption peaks characteristic of the s(2/1)2 helical polymer chain conformation (i.e. polymer chains included in the crystalline δ phase of s-PS), such as the C–H deformation mode at 1276 cm^{-1}, remain almost unchanged [59].

Analogous results have been obtained for all the other studied cocrystalline samples with n-alkanes.

Once we were sure no residual chloroform was present in the s-PS/n-alkane δ cocrystalline samples, we characterized them by thermogravimetric analysis and by X-ray diffraction. Thermogravimetric analyses have been carried out at different times in order to follow the removal of the guest from the amorphous phase of the samples. Fig. 3 shows the X-ray powder diffraction patterns of the samples. For each one the weight fractions (%) of n-alkane for the samples dried in air for two days and after three months are reported too. During this time, any remarkable change has been noted in the X-ray powder diffraction patterns of the samples.

The X-ray diffraction data reported in Fig. 3 are in very good agreement with those reported in literature by Gowd et al. [3] (even if in their samples containing longer n-alkanes a minor amount of ϵ form was present, probably due to the experimental procedure used to obtain the samples [60]). Moreover, on the basis of the position of the lowest angle reflections, corresponding to the (010) plane, it can be noted that, similarly to what already pointed out by Kaneko et al. [47], the d_{010} increases on going from n-hexane to n-heptane, but markedly decreases at n-octane and then remains practically constant (within the experimental error) with further increasing the chain length of the n-alkane guest molecule, assuming values slightly lower than that of the empty δ form (see Fig. 4).

It worth recalling that in a very recent paper by some of us [16] we found that, for several very bulky guest molecules, despite their greater volume in respect to that of the cavity of the nanoporous δ form, the d_{010} spacing was similar or even reduced with respect to that of the empty δ phase [8,16]. This has been rationalized in terms of the formation of a new type of triclinic clathrate structures describable by a sequence of layers of chains nearly parallel to the $\bar{2}10$ planes in which couples of close packed chains alternate to couples of chains delimiting regions in which guest molecules are hosted [16]. In that paper we suggested also a sort of predictive criterion in order to determine “a priori” the monoclinic or triclinic nature of a δ-clathrate. As a matter of fact, by reporting the d_{010} value *versus* the guest molecular volume it can be seen that monoclinic δ-clathrates are obtained with guests whose molecular volume is significantly lower than that of the cavity of the δ nanoporous crystalline phase (≈ 0.125 nm^3) [15,61]. On the other hand, triclinic δ-clathrates are obtained with guests whose molecular volume is significantly higher than that one of the cavity of the δ nanoporous crystalline phase. Guest molecules having a volume similar to the cavity volume of the δ phase, instead, present a more complex behavior and, in order to establish to which one of the two classes the clathrate belongs, it is important to perform further structural analyses. In particular, for d_{010} spacing decidedly higher that of the nanoporous δ form, the structures are expected to be monoclinic while for d_{010} spacing similar or lower than that of the

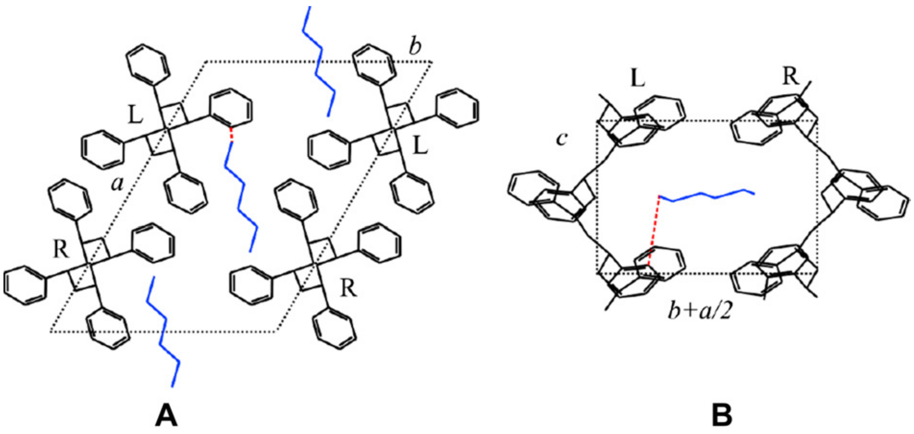

Fig. 7. Packing model proposed for the crystal structure of s-PS/n-hexane δ cocrystalline form according the $P2_1/a$ space group. (A) Projection along c. (B) Projection in the $c(b+a/2)$ plane. In (B) only one couple of enantiomorphous polymer chains are shown. R = right-handed, L = left-handed helices. The shortest distances (0.36 nm) between non-bonded atoms are indicated with dashed red lines. (For interpretation of the references to color in this figure legend, the reader is referred to the web version of this article).

Table 2
Diffraction angles ($2\theta_{\mathrm{obsd}}$) and Bragg distances (d_{obsd}) of the reflections identified on the layer lines (l) of the X-ray fiber diffraction pattern of the s-PS/n-nonane δ-clathrate sample of Fig. 11.

l	$2\theta_{\mathrm{obsd(deg)}}$	$d_{\mathrm{obsd(nm)}}$
0	8.55	1.03
0	9.85	0.90
0	16.15[a]	0.55
0	19.3[a]	0.46
1	14.0	0.63
1	16.1	0.55
1	19.8	0.45
1	23.15	0.38
2	24.5	0.36
2	28.1	0.32

[a] broad.

δ form, triclinic clathrate structure are expected in which the maximum guest/monomeric-unit ratio may be 1/4 (like in the case of the co-crystalline phase containing NA, [14]) or 1/8 (like in the case of the co-crystalline phase containing DNB, [16]).

Fig. 4 reports the plot of d_{010} distance *versus* the guest molecular volume for some s-PS δ-clathrates whose crystalline structure has been already determined together with that for the clathrate forms with n-alkanes whose diffraction patterns are reported in Fig. 3. From the positioning of these experimental points we have inferred that in the cases of the clathrate forms containing n-octane, n-nonane and n-decane a triclinic structure of the new type (with a maximum guest/monomer-unit ratio of 1/8) should be present while in the case of n-heptane the crystalline structure should be monoclinic. A reliable expectation concerning the clathrate form with n-hexane could not be drawn since the experimental data is placed in an ambiguous region between the "classical" monoclinic [6,7,9–11] and the triclinic case similar to that found in the case of the clathrate form containing NA [14].

In order to validate these hypotheses, confirming at the same time also the predictive capabilities of the proposed method, we have examined in detail the crystalline structures of the s-PS δ-clathrate forms containing n-hexane and n-nonane.

3.2. Crystalline structure of the s-PS δ-co-crystals with n-hexane

Oriented samples of the δ-clathrate form of s-PS with n-hexane have been prepared as described in the Experimental Part. The removal of $CHCl_3$ guest and its substitution with n-hexane was confirmed by FT-IR spectroscopy (see Fig. 5). The X-ray fiber diffraction pattern of an oriented sample in the clathrate δ form of s-PS with n-hexane is reported in Fig. 6A while Fig. 6B shows the X-ray diffraction pattern of an unoriented sample (already presented in Fig. 3c). All the reflections observed in the fiber pattern of Fig. 6A are listed in Table 1.

Similarly to the other δ-clathrate forms of this polymer whose structure has been already reported in literature [6,7,9–11], also in this case it would be possible indexing the experimental data in terms of a monoclinic unit cell (with constants $a = 1.78$ nm, $b = 1.29$ nm, $c = 0.77$ nm, $\gamma = 120°$) and to propose the space group $P2_1/a$, in agreement with the systematic absence of *hk0* reflections with h=2n + 1 and *00l* reflections with l=2n + 1.

Following the hypothesis of a structure isomorphous to those already found for other δ-clathrates of this polymer, we performed packing energy calculations assuming a $P2_1/a$ symmetry, keeping constant the unit cell parameters and optimizing the position of the guest molecule in the cavities. The best result was found for the situation represented in Fig. 7.

Despite the convincing packing of the proposed monoclinic model shown in Fig. 7 (whose fractional coordinates are reported in Table 1 of the Supplementary Material), and the promising discrepancy factor R (equal to 0.15) between experimental and calculated structure factors (the complete list is reported in Table 2 of the Supplementary Material), if we analyze in detail the comparison between the experimental and calculated diffraction patterns (shown in Fig. 8 as far as the first layer line is concerned) some problems can be pointed out. In particular, the proposed model gives a poor agreement on the first layer line, mainly as for the position of the $1\bar{2}1$ reflection (see Fig. 8A).

As already reported in literature by some of us in the case of the clathrate form containing NA [14], the position of this reflection can be adjusted by varying the α angle of the unit cell. This variation corresponds to a shift of the *ac* layers of close packed helices along the c direction of the unit cell, transforming the proposed monoclinic unit cell in a triclinic one [14]. This shift has a valuable effect on the position of the $1\bar{2}1$ reflection already for small variation of the α angle, while keeps almost unchanged all the positions and intensities of the equatorial reflections [14]. With this in mind, in order to have a good positioning of the $1\bar{2}1$ reflection, we have varied the α angle of the unit cell in a very small angular range centered around 90° refining each model by molecular mechanics and assuming a $P\bar{1}$ symmetry. A better agreement with the experimental data is obtained for $\alpha = 94°$ (see Fig. 8B). For such a small distortion from the monoclinic case, no change of the other

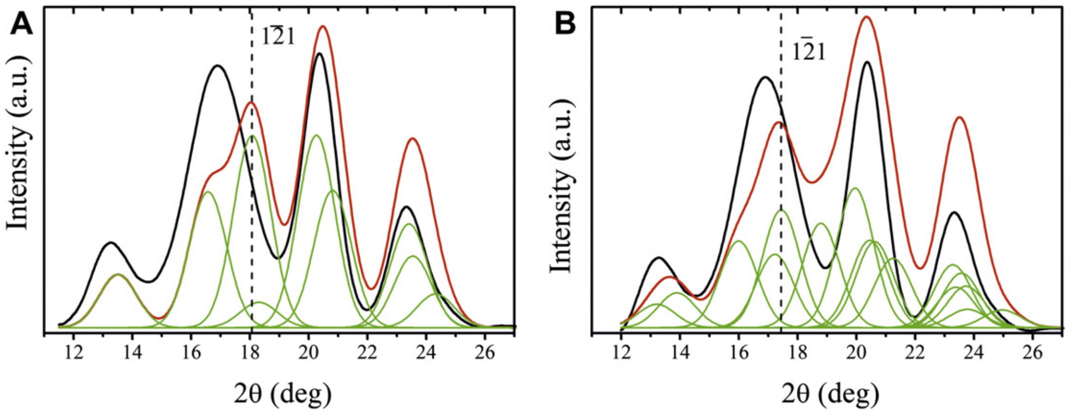

Fig. 8. First layer line intensity profiles for the s-PS/n-hexane δ clathrate: experimental (black line) and calculated (red line) according the (A) $P2_1/a$ model of Fig. 7 and (B) $P\bar{1}$ model of Fig. 9. Green thin lines report, as Gaussians, the contributions to the calculated profile of each single significant reflection. The calculated position for the $1\bar{2}1$ reflection is also indicated. (For interpretation of the references to color in this figure legend, the reader is referred to the web version of this article).

unit cell parameters was necessary in order to keep on successfully indexing all the observed reflections. The final model is reported in Fig. 9, being characterized by energy only slightly higher than the minimum value that corresponds to the monoclinic model reported in Fig. 7 ($\approx$1 kcal/mol-unit-cell). In this model the *n*-hexane guest molecule assumes an all-*trans* conformation (as in the monoclinic model reported in Fig. 7) and, as found in the case of the other triclinic δ-clathrates of s-PS [14,16], its molecular axis is not perfectly perpendicular to the polymer chain axis but slightly inclined.

For this model the packing is still very good and the discrepancy factor R is 0.14 (Table 4 of Supplementary Material). Fractional coordinates of the carbon atoms of the asymmetric unit for the model of Fig. 9 are reported in Table 3 of Supplementary Material.

A further confirmation of the correctness of the model is given in Fig. 10, where the calculated X-ray powder diffraction profile is compared to the experimental X-ray powder diffraction pattern (reported in Fig. 6B), after subtraction of the background and amorphous contribution. A fairly good agreement is apparent.

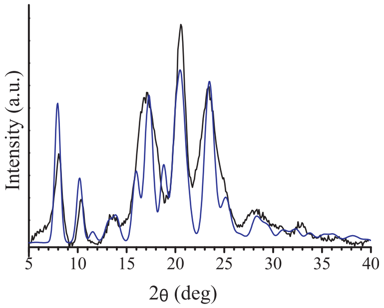

Fig. 10. Comparison between the experimental X-ray powder diffraction pattern (black solid line) of the s-PS/*n*-hexane δ-clathrate after subtraction of the background and amorphous halo (see Fig. 6B) and the calculated one (blue solid line) according to the triclinic structural model proposed in Fig. 9. (For interpretation of the references to color in this figure legend, the reader is referred to the web version of this article).

3.3. *Crystalline structure of δ-co-crystals of syndiotactic polystyrene with n-nonane*

Also in this case, oriented samples of δ co-crystals of s-PS/*n*-nonane have been prepared by guest exchange starting from s-PS/$CHCl_3$ δ co-crystals and the exchange process was monitored thorough FT-IR spectroscopy (see Fig. 1 of Supplementary Material).

The X-ray fiber diffraction pattern of an oriented sample is reported in Fig. 11A while Fig. 11B reports the X-ray diffraction pattern of an unoriented sample (already shown in Fig. 3f). Table 2 lists the position of all the reflections identified in the fiber diffraction pattern.

Following a procedure analogous to that described in Ref. [16], the reflections listed in Table 2 have been indexed in terms of the following triclinic unit cell: $a = 1.83$ nm, $b = 1.42$ nm, $c = 0.77$ nm, $\alpha = 101°$, $\beta = 90°$ and $\gamma = 130°$. Using this unit cell, we have then obtained a minimum energy packing model imposing one guest per unit cell as proposed in the case of the δ-clathrate forms of s-PS with dibenzofuran and dinitrobenzene (i.e. guest/monomer-unit molar ratio of 1/8) [16], under the $P1$ symmetry. The minimum energy packing model obtained is given in Fig. 12.

A confirmation of the correctness of the model is given in Fig. 13, where the calculated X-ray powder diffraction profile is compared to the experimental X-ray powder diffraction pattern (reported in Fig. 3B), after subtraction of the background and amorphous contribution. A fairly good agreement is apparent.

As already suggested in ref. [16], it is worth adding that the agreement between calculated and observed structure factors can be improved by introducing in the triclinic model of Fig. 12 some structural disorder. In fact, the largest disagreement that occurs for the equatorial layer line reflection centered at $2\theta = 6.4°$ (indexed as (100), see Table 6 of the Supporting Information) can be dramatically reduced by hypothesizing the likely presence of a disorder in the alternation of full and empty zones along the $(\bar{2}10)$ plane. The presence of disorder in similar triclinic clathrates has been already discussed in ref. [16]. No further refinement was performed since, as supposed in the previous paragraph, this structure turned out to be analogous to others already described in literature [16].

Fractional coordinates for the model of Fig. 12 and the complete list of calculated relative intensities are reported in Tables 5 and 6 of Supplementary Material, respectively.

It is worth pointing out that in the model of Fig. 12 the *n*-nonane guest molecule is inclined in respect to the polymer chain axis, and, according to what already suggested by Kaneko et al. [47], it presents a bent conformation (the sequence of torsion angle is $G^{+}(\sim)\,G^{+}(\sim)\,T\,G^{-}(\sim)\,G^{-}(\sim)\,G^{-}(\sim)$). This conformation presents a conformational energy of $\approx$ 2 kcal/mol higher than that of the all-trans one [48].

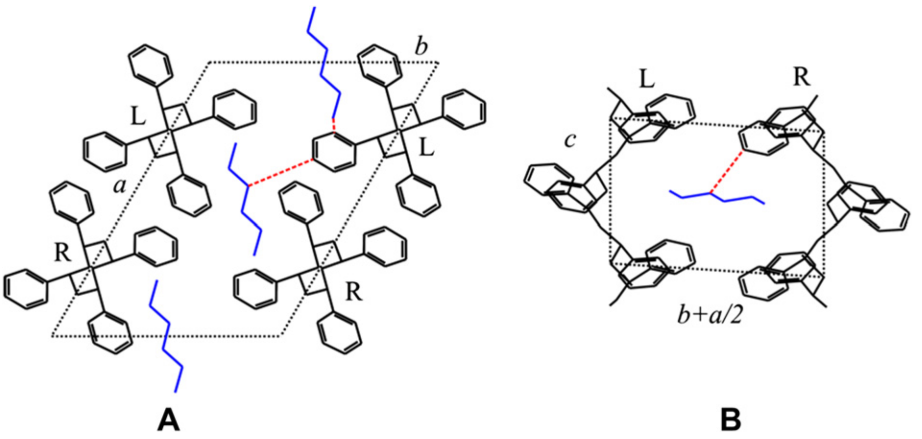

Fig. 9. Packing model proposed for the crystal structure of s-PS δ co-crystalline form containing *n*-hexane according the triclinic unit cell with constants $a = 1.78$ nm, $b = 1.29$ nm, $c = 0.77$ nm, $\alpha = 94°$, $\beta = 90°$ and $\gamma = 120°$ and the $P\bar{1}$ space group. In the $c(b{+}a/2)$ projection only one couple of enantiomorphous polymer chains is shown. The shortest distances (0.36 nm) between non-bonded atoms are indicated with dashed red lines. R = right-handed, L = left-handed helices. (For interpretation of the references to color in this figure legend, the reader is referred to the web version of this article).

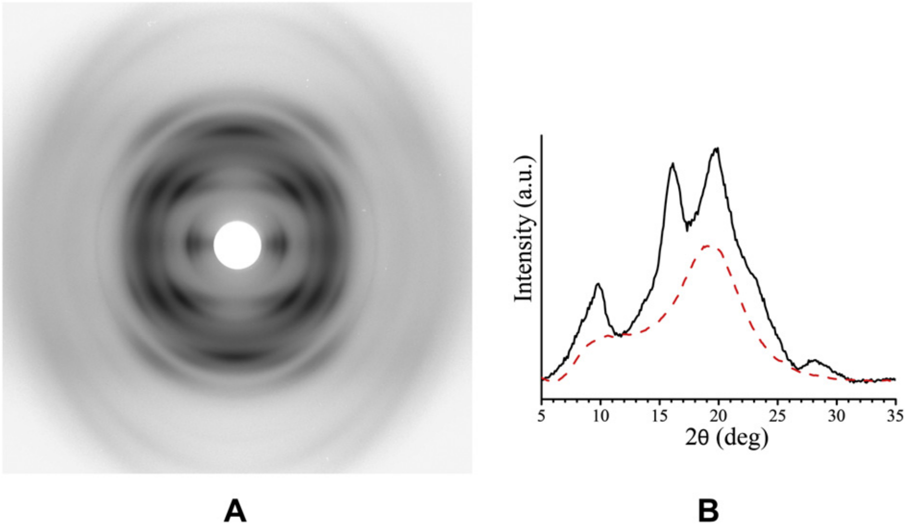

Fig. 11. (A) X-ray diffraction patterns of (A) a uniaxially stretched film and (B) an unoriented powder sample presenting the s-PS/*n*-nonane δ co-crystalline form. In (A) fiber axis is vertical. In (B) amorphous and background contributions are indicated with a dashed line.

In order to determine if guest with an all-*trans* conformation could be arranged in the cavities of this clathrate form, a systematic molecular mechanics analysis has been carried out too. Despite several attempts, our analysis concluded that no satisfactory packing model for these cases could be possible without introducing a tremendous increase in the packing energy (up to 40 kcal/mol-unit-cell). This increase can be easily explained if we consider that the length of the *n*-nonane molecule that in the bent conformation proposed in the model of Fig. 12 is of ≈ 1.1 nm increases up to ≈ 1.5 nm when the molecule assumes an all-*trans* conformation, a dimension decidedly too big to be hosted in the cavity formed by the polymer chains of the proposed model (several 0.31 and 0.32 nm distances between non-bonded carbon atoms belonging to guest and polymer helices appear). These data induced us to exclude the possibility of arranging such kind of flexible guests with an all-*trans* conformation in this type of s-PS δ-clathrate form.

On this point, it is worth pointing out that in a recent paper by some of us [23] in which we have presented the crystalline structures of the s-PS ϵ-clathrates with different *n*-alkanes (ranging from *n*-hexane to *n*-dodecane) we have demonstrated that, on the contrary, the *n*-alkanes guest molecules, independently from their length, are arranged in the channels in fully *trans*-planar conformation and the possibility of having in the channels *n*-alkane guest with a bent conformation has been ruled out [23].

3.4. Thermogravimetric data

The crystallographic analyses presented before for the s-PS δ-clathrates with *n*-hexane and *n*-nonane have allowed us to conclude that the structural hypotheses we have done discussing Fig. 4 are correct. In order to have a further support for these two (solved) cases and for the structural models we supposed for the other s-PS δ-clathrate with *n*-alkanes reported in Fig. 4, we have performed also a thermogravimetric analysis.

Table 3 reports the thermogravimetric data obtained on the powder samples of the s-PS/*n*-alkanes δ-clathrates studied in this paper after three months of air exposure. These data have been already shown in column B of Fig. 3. It is apparent that these data support the structural models we have suggested for the δ-clathrates containing *n*-hexane and *n*-nonane as well as the suppositions we have done for those containing *n*-heptane, *n*-octane and *n*-decane.

As a matter of fact, the very long exposure to air of the samples (three months) accompanied to the invariance of the X-ray diffraction patterns during this time, allow hypothesizing that the guest is mainly contained in the crystalline phase of the samples. In this hypothesis, and considering a likely degree of crystallinity of the samples equal to 40%, the guest contents determined by TGA are in very good agreement with a guest/monomer-unit molar ratio

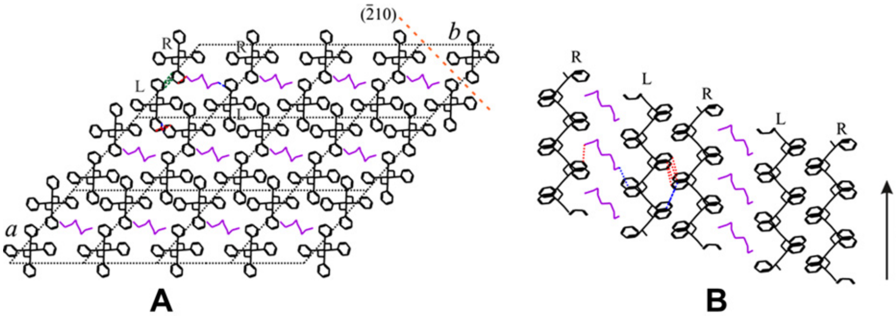

Fig. 12. Packing model proposed for the crystal structure of s-PS/*n*-nonane δ co-crystalline form according the space group $P1$ in the unit cell $a = 1.83$ nm, $b = 1.42$ nm, $c = 0.77$ nm, $\alpha = 101°$, $\beta = 90°$ and $\gamma = 130°$. (A) View along the *c* axis. (B) View of a layer of enantiomorphous chains and of guest molecules along a direction perpendicular to the $(\bar{2}10)$ plane (whose trace is reported by a dashed orange line in A). R = right-handed, L = left-handed helices. The shortest non-bonded distances between atoms are indicated (green for 0.33 nm, red for 0.34 and blue for 0.35 nm). (For interpretation of the references to color in this figure legend, the reader is referred to the web version of this article).

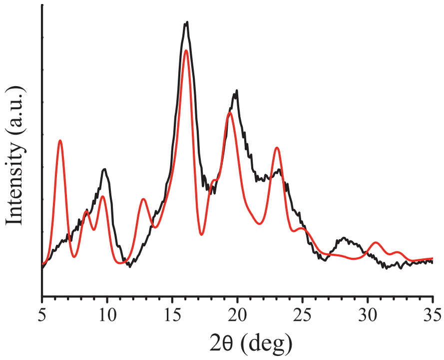

Fig. 13. Comparison between the experimental X-ray powder diffraction pattern (black solid line) of the s-PS/*n*-nonane δ clathrate after subtraction of the background and amorphous halo (see Fig. 11B) and the calculated one (red solid line) according to the triclinic structural model proposed in Fig. 12. (For interpretation of the references to color in this figure legend, the reader is referred to the web version of this article).

of 1/4 (corresponding to δ-clathrate structures monoclinic or triclinic similar to that containing NA) in the cases of the clathrate containing *n*-hexane and *n*-heptane, while the guest content for the samples containing *n*-octane, *n*-nonane and *n*-decane is in better agreement with a guest/monomer-unit molar ratio of 1/8 (corresponding to the recently described new triclinic δ-clathrate structures).

3.5. *Effect of n-alkanes on the crystallization of s-PS amorphous samples*

s-PS δ cocrystalline structures can be obtained by several procedures. Most δ co-crystals can be prepared by solution crystallization or by sorption of suitable compounds (e.g. toluene or chloroform) in amorphous s-PS samples as well as in samples in the α form or γ form [1–4].

δ-clathrates can be easily and rapidly obtained also by guest sorption into s-PS samples in the δ phase or by guest exchange in already formed co-crystals with other guest molecules. In particular, this last method has been proposed in order to incorporate in the guest locations of the δ form very large molecules that otherwise wouldn't produce clathrate forms, greatly enlarging the range of possible guest molecules also to functional molecules [3,4]. In this respect it is worth pointing out that the crystallization of amorphous s-PS films when induced by bulky solvents, whose molecules are too big to be enclosed as guest of s-PS δ-clathrate phases, generally leads to the formation of the γ phase [62]. In the present paragraph we report some results on the crystallization of s-PS amorphous samples with *n*-alkanes that can be useful for the understanding of the behavior of this class of homologous guests.

Table 3
Experimental and calculated weight fractions of the *n*-alkane molecules in the s-PS/*n*-alkanes δ-clathrates samples studied. Bold characters have been used to facilitate the comparison.

Guest	A[a] (%)	B[b] (%)	C[c] (%)	D[d] (%)
n-hexane	6.9	**17.3**	**17.1**	9.4
n-heptane	5.7	**14.3**	**19.4**	10.7
n-octane	5.2	**13.0**	21.5	**12.0**
n-nonane	4.4	**11.0**	23.5	**13.3**
n-decane	4.9	**12.3**	25.5	**14.6**

[a] Experimental (after being dried in air for three months) weight fraction of the guest determined by thermogravimetric analysis.

[b] Calculated weight fraction of the guest in the assumptions that *n*-alkane molecules are hosted only in the clathrate phase of the samples and that the degree of crystallinity is equal to 40%.

[c] Theoretical weight fraction of the guest in the hypotheses of a molar ratio *n*-alkane/monomeric-unit of 1/4.

[d] Theoretical weight fraction of the guest in the hypotheses of a molar ratio *n*-alkane/monomeric-unit of 1/8.

s-PS amorphous films (100–150 μm) samples were soaked in liquid *n*-alkanes (ranging from *n*-hexane to *n*-dodecane) at room temperature up to 50 days and monitored through X-ray powder diffraction at different times (see Fig. 14).

These data clearly indicate that this class of guest molecules can induce the crystallization of s-PS amorphous samples in the dense γ form, irrespectively of the bulkiness of the *n*-alkanes used in the dipping process. This allows inferring that the δ-clathrates with this class of guest molecules are less stable than the γ form. Moreover, it must be noted that, as far as the *n*-hexane guest, a minor amount of δ-clathrate is likely to be present for short exposure time (see curve c of Fig. 14A) as revealed by the presence of a broad peak at $2\theta = 8°$ in the powder diffraction pattern. However, this δ-clathrate is not stable for longer dipping time (see curves c in Fig. 14B and C) since it is transformed into γ form.

Moved by the peculiar behavior of the *n*-hexane guest molecule, we have then exposed amorphous samples also to *n*-pentane. Differently from the other *n*-alkanes examined, in this case we obtained a stable δ-clathrate form (see curve b of Fig. 14A–C). For this clathrate, according to the placement of the experimental point in the graph reported in Fig. 4, we can expect a monoclinic structure.

Finally, the samples dipped in *n*-undecane and *n*-dodecane do not show any appreciable crystallization even for soaking time up to 50 days (see curves h and i of Fig. 14C).

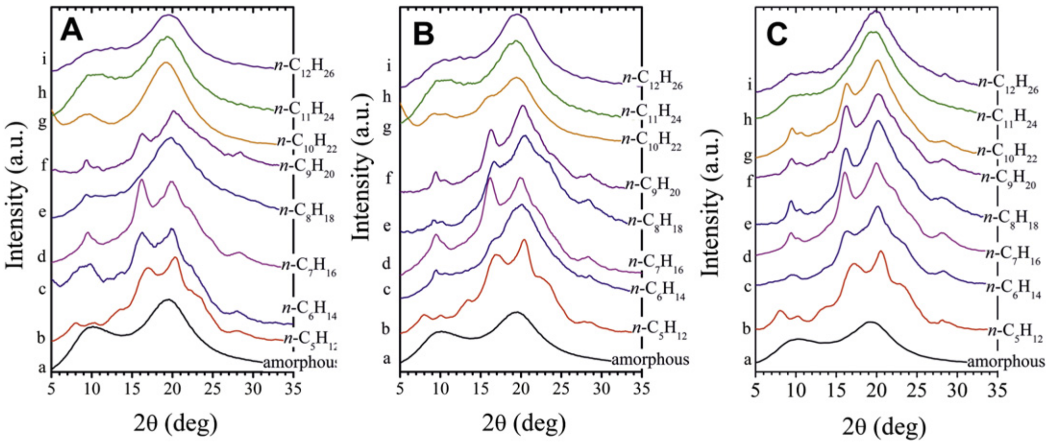

Fig. 14. X-ray powder diffraction patterns of s-PS amorphous samples dipped in the indicated *n*-alkane for: (A) 3 days, (B) 7 days, (C) 50 days. The X-ray diffraction pattern of the starting amorphous s-PS samples is reported too.

4. Conclusions

The structural characterization of δ clathrate forms of syndiotactic polystyrene containing a homologous series of guest molecules characterized by an increasing molecular volume (*n*-alkanes ranging from *n*-pentane to *n*-dodecane) have been investigated.

From the present analysis it can be concluded that the volume of the guest plays a crucial role in the choice of the type of δ-clathrate that can be obtained. As a matter of fact, longer *n*-alkanes, such as *n*-octane, *n*-nonane or *n*-decane, turned out to give rise triclinic δ-clathrates presenting a guest/monomeric-unit ratio of 1/8, similarly to what already found in literature for analogous structure with guest presenting a volume decidedly higher than that of the cavity of the nanoporous δ form [16]. δ-clathrates containing shorter alkanes, like *n*-hexane or *n*-heptane, instead, present a monoclinic or a triclinic structure with two guests per cell (guest/monomeric-unit ratio $= 1/4$).

These results confirm the validity of a simple criterion to predict the type of s-PS δ-clathrate with a certain guest on the basis of the experimental d_{010}, as described in ref. [16].

Moreover, in agreement to what reported in literature on the basis of solid state NMR and Raman spectroscopy data [47], our analysis establishes that *n*-hexane molecule is hosted in the cavities with a *trans*-planar conformation while longer alkanes, like *n*-nonane, present a bent conformation.

In is worth pointing out that this behavior is completely different to that highlighted by some of us when the same guest molecules are hosted in the channels of the nanoporous ϵ form [23]. In fact, in those cases, independently from the length of the *n*-alkane, the cocrystalline structures are all very similar and present *n*-alkane guests arranged in an all-*trans* conformation with their main molecular axis almost parallel to the axis of the channels [23].

The data reported in the present paper and those of ref. [23] allow concluding that the conformational freedom of the *n*-alkane guest give to this class of flexible molecules the possibility to “adapt” their shape to the shape of the cavity in the process of s-PS co-crystal formation.

Finally, through the investigation of the effect of *n*-alkanes molecules on the crystallization of s-PS amorphous samples we can infer that the δ-clathrate forms containing this class of guest molecules, with the exception of *n*-pentane, are unstable in respect to the dense γ form.

Acknowledgements

Financial support of the Ministero dell’Istruzione, dell’Università e della Ricerca" (PRIN2007), and of the Consortium INSTM (PRISMA01/2007 project) is gratefully acknowledged. Dr. Rocco Di Girolamo is acknowledged for useful discussion.

Appendix. Supplementary material

Supplementary data related to this article can be found online at doi:10.1016/j.polymer.2011.01.041.

References

[1] Guerra G, Vitagliano V, De Rosa C, Petraccone V, Corradini P. Macromolecules 1990;23:1539–44.

[2] Chatani Y, Shimane Y, Inoue Y, Inagaki T, Ishioka T, Iijtsu T, et al. Polymer 1992;33:488–92.

[3] Gowd EB, Tashiro K, Ramesh C. Prog Polym Sci 2009;34:280–315.

[4] Milano G, Guerra G. Progr Mater Sci 2009;54:68–88.

[5] Immirzi A, de Candia F, Iannelli P, Zambelli A, Vittoria V. Makromol Chem Rapid Commun 1988;9:761–4.

[6] Chatani Y, Shimane Y, Inagaki T, Iijtsu T, Yukimori T, Shikuma H. Polymer 1993;34:1620–4.

[7] Chatani Y, Inagaki T, Shimane Y, Shikuma H. Polymer 1993;34:4841–5.

[8] De Rosa C, Guerra G, Petraccone V, Pirozzi B. Macromolecules 1997;30:4147–52.

[9] De Rosa C, Rizzo P, Ruiz de Ballesteros O, Petraccone V, Guerra G. Polymer 1999;40:2103–10.

[10] Tarallo O, Petraccone V. Macromol Chem Phys 2004;205:1351–60.

[11] Tarallo O, Petraccone V. Macromol Chem Phys 2005;206:672–9.

[12] Malik S, Rochas C, Guenet JM. Macromolecules 2005;38:4888–93.

[13] Dawn A, Rochas C, Guenet JM. Macromolecules 2009;42:6633–9.

[14] Tarallo O, Petraccone V, Daniel C, Guerra G. CrystEngComm 2009;11:2381–90.

[15] Tarallo O, Schiavone MM, Petraccone V. Eur Polym J 2010;46:456–64.

[16] Tarallo O, Petraccone V, Albunia AR, Daniel C, Guerra G. Macromolecules 2010;43:8549–58.

[17] Daniel C, Deluca MD, Guenet JM, Brulet A, Menelle A. Polymer 1996;37:1273–80.

[18] Petraccone V, Tarallo O, Venditto V, Guerra G. Macromolecules 2005;38:6965–71.

[19] Tarallo O, Petraccone V, Venditto V, Guerra G. Polymer 2006;47:2402–10.

[20] Rizzo P, Daniel C, De Girolamo Del Mauro A, Guerra G. Chem Mater 2007;19:3864–6.

[21] Petraccone V, Ruiz de Ballesteros O, Tarallo O, Rizzo P, Guerra G. Chem Mater 2008;20:3663–8.

[22] Tarallo O, Schiavone MM, Petraccone V, Daniel C, Rizzo P, Guerra G. Macromolecules 2010;43:1455–66.

[23] Tarallo O, Schiavone MM. Soft Materials 2011;9: doi: 10.1080/1539445X.2011.552349.

[24] Stegmaier P, De Girolamo Del Mauro A, Venditto V, Guerra G. Adv Mater 2005;17:1166–8.

[25] Uda Y, Kaneko F, Tanigaki N, Kawaguchi T. Adv Mater 2005;17:1846–50.

[26] Venditto V, Milano G, De Girolamo Del Mauro A, Guerra G, Mochizuki J, Itagaki H. Macromolecules 2005;38:3696–702.

[27] Kaneko F, Kajiwara A, Uda Y, Tanigaki N. Macromol Rapid Commun 2006;27:1643–7.

[28] D’Aniello C, Musto P, Venditto V, Guerra G. J Mater Chem 2007;17:531–5.

[29] Daniel C, Galdi N, Montefusco T, Guerra G. Chem Mater 2007;19:3302–8.

[30] De Girolamo Del Mauro A, Carotenuto M, Venditto V, Petraccone V, Scoponi M, Guerra G. Chem Mater 2007;19:6041.

[31] Itagaki H, Sago T, Uematsu M, Yoshioka G, Correa A, Venditto V, et al. Macromolecules 2008;41:9156–64.

[32] Daniel C, Alfano D, Venditto V, Cardea S, Reverchon E, Larobina D, et al. Adv Mater 2005;17:1515–8.

[33] Albunia AR, D’Aniello C, Guerra G, Gatteschi D, Mannini M, Sorace L. Chem Mater 2009;21:4750–2.

[34] Rizzo P, Daniel C, Guerra G. Macromolecules 2010;43:1882–7.

[35] Albunia AR, D’Aniello C, Guerra G. CrystEngComm 2010;12:3942–9.

[36] Yokoyama M, Ishihara H, Iwamoto R, Tadokoro H. Macromolecules 1969;2:184–92.

[37] Point JJ, Coutelier C. J Polym Sci Polym Phys Ed 1985;23:231–9.

[38] Matsumoto A, Odani T, Sada K, Miyata M, Tashiro K. Nature 2000;405:328–30.

[39] Tarallo O, Esposito G, Passarelli U, Petraccone V. Macromolecules 2007;40:5471–8.

[40] Rizzo P, Lamberti M, Albunia AR, Ruiz de Ballesteros O, Guerra G. Macromolecules 2002;35:5854–9.

[41] Rizzo P, Spatola A, De Girolamo Del Mauro A, Guerra G. Macromolecules 2005;38:10089–93.

[42] Albunia AR, Rizzo P, Tarallo O, Petraccone V, Guerra G. Macromolecules 2008;41:8632–42.

[43] Albunia AR, Rizzo P, Guerra G. Chem Mater 2009;21:3370–5.

[44] Uda Y, Kaneko F, Kawaguchi T. Macromol Rapid Commun 2004;25:1900–4.

[45] Uda Y, Kaneko F, Kawaguchi T. Macromolecules 2005;38:3320–6.

[46] Guerra G, Milano G, Venditto V, Loffredo F, Ruiz de Ballesteros O, Cavallo L, et al. Macromol Symp 1999;138:131–7.

[47] Kaneko F, Uda Y, Kawaguchi T, Koichi U, Yamamuro O. Macromol Symp 2006;242:113–9.

[48] Balabin RM. J Phys Chem A 2009;113:1012–9.

[49] Klauda JB, Pastor RW, Brooks BR. J Phys Chem B 2005;109:15684–6.

[50] Balabin RM. J Chem Phys 2008;129:164101–5.

[51] Balabin RM. Chem Phys 2008;352:267–75.

[52] Ibers JA, Hamilton WC. International tables for X-ray crystallography, Vol. 4. Birmingham, England: The Kynoch Press; 1974.

[53] Sun HJ. Phys Chem B 1998;102:7338–64.

[54] Corradini P, Napolitano R, Pirozzi B. Eur Polym J 1990;26:157–61.

[55] Gibian TJ, McKinney DS. J Am Chem Soc 1951;73:1431–4.

[56] Silverstein RM. Spectrometric identification of organic compounds. 7th ed. New York: John Wiley & Sons; 2005.

[57] Schachtschneider JH, Snyder RG. Spectrochim Acta 1963;19:117–68.

[58] Snyder RG. J Chem Phys 1967;47:1316–60.

[59] Torres FJ, Civalleri B, Meyer A, Musto P, Albunia AR, Rizzo P, et al. Chem Phys B 2009;113:5059–71.

[60] Daniel C, Montefusco T, Rizzo P, Musto P, Guerra G. Polymer 2010;51:4599–605.

[61] Milano G, Venditto V, Guerra G, Cavallo L, Ciambelli P, Sannino D. Chem Mater 2001;13:1506–11.

[62] Rizzo P, Albunia AR, Guerra G. Polymer 2005;46:9549–54.

Polymer 52 (2011) 1436–1446

Contents lists available at ScienceDirect

Polymer

journal homepage: www.elsevier.com/locate/polymer

A novel method for improving the surface quality of microcellular injection molded parts

Jungjoo Lee [a], Lih-Sheng Turng [a,*], Eugene Dougherty [b], Patrick Gorton [b]

[a] Polymer Engineering Center, Department of Mechanical Engineering, University of Wisconsin-Madison, Madison, WI 53706, United States
[b] Energizer Personal Care Products, Dover, DE 19904, United States

ARTICLE INFO

Article history:
Received 25 October 2010
Received in revised form
12 January 2011
Accepted 14 January 2011
Available online 21 January 2011

Keywords:
Microcellular injection molding
Plastic foaming
Swirl-free surface

ABSTRACT

Microcellular injection molding is the manufacturing method used for producing foamed plastic parts. Microcellular injection molding has many advantages including material, energy, and cost savings as well as enhanced dimensional stability. In spite of these advantages, this technique has been limited by its propensity to create parts with surface defects such as a rough surface or gas flow marks. Methods for improving the surface quality of microcellular plastic parts have been investigated by several researchers. This paper describes a novel method for achieving swirl-free foamed plastic parts using the microcellular injection molding process. By controlling the cell nucleation rate of the polymer/gas solution through material formulation and gas concentration, microcellular injection molded parts free of surface defects were achieved. This paper presents the theoretical background of this approach as well as the experimental results in terms of surface roughness and profile, microstructures, mechanical properties, and dimensional stability.

1. Introduction

The commercially available microcellular injection molding process (a.k.a. the MuCell Process) consists of four distinctive steps, namely, gas dissolution, nucleation, cell growth, and shaping [1]. In the gas dissolution stage, polymer in the injection barrel is mixed with supercritical fluid (SCF) nitrogen, carbon dioxide, or another type of gas using a special screw which is designed to maximize the mixing and dissolving of the gas in the polymer melt. During injection, a large number of nucleation sites (orders of magnitude higher than conventional foaming processes) are formed by a rapid and substantial pressure drop as the polymer/gas solution is injected into the mold cavity, thus causing the formation of cells (bubbles). During the rest of the injection molding cycle, cells continue to grow to fill and pack out the mold and subsequently compensate for the polymer shrinkage as the material cools inside the mold. The cell growth is driven by the amount and spatial distribution of the dissolved gas. The cell growth is also controlled by processing conditions such as melt pressure and temperature as well as material properties such as melt strength and gas solubility. Finally, the shaping of the part takes place inside the mold until the mold opens allowing the part to be ejected.

Since the microcellular injection molding process was invented, there have been numerous studies on process, material, and technical developments aimed at materializing the full process potential. According to previous studies [1–5], microcellular injection molding offers a number of advantages such as cost savings, weight reduction, ease in processing due to low viscosity, and outstanding dimensional accuracy. Due to these advantages, the microcellular injection molding process has been used in many industries such as automotive, electrical goods, and home appliances using a broad range of thermoplastics.

Despite these advantages, however, the surface imperfections associated with microcellular injection molded parts—such as unique gas flow marks, referred to as swirl marks throughout this paper, and a lack of smoothness—still remain one of the main drawbacks surrounding microcellular injection molding. In order to eliminate or reduce these surface imperfections there have been several studies attempted, as reported in Refs. [6–14]. Some researchers have focused on temperature modification of the mold surface to improve the surface quality of microcellular injection molded parts [6–8]. With polymeric foam, it was found that bubbles forming at the advancing melt front are first stretched by the fountain flow behavior toward the mold surface and subsequently dragged against the mold wall causing swirl marks [9]. During the filling stage of polymer melts, keeping the mold wall temperature high enough for bubbles at the mold surface to be eliminated improves the surface quality of microcellular injection

---

* Corresponding author. Tel.: +1 608 262 0586; fax: +1 608 265 2316.
E-mail address: turng@engr.wisc.edu (L.-S. Turng).

0032-3861/$ – see front matter © 2011 Elsevier Ltd. All rights reserved.
doi:10.1016/j.polymer.2011.01.026

molded parts. By controlling the mold temperature rapidly and precisely using mold temperature control units or other kinds of thermal or surface heating devices, microcellular foamed plastics with glossy and swirl-free surfaces can be produced.

There have also been efforts to eliminate the swirl marks on microcellular injection molded parts without any mold temperature controller. In particular, it was proposed that inserting an insulator onto the mold wall might help keeping the interface temperature between the mold and the polymer melt high. This technique basically yields the same result as temperature modification of the mold [10]. Thermal analysis and experimental results prove that the addition of an insulator layer on the mold can improve the surface quality of microcellular injection parts [11].

Another method of producing parts with an improved surface quality leads to a microcellular co-injection molding process [12]. In this technique, a proper amount of solid skin material is injected prior to the injection of a foaming core material. This can yield a sandwiched (solid skin–foamed core–solid skin) structure with a surface finish similar to a conventionally molded component while partially maintaining the advantages of microcellular injection molding.

Another approach for improving the surface quality of microcellular injection molded parts is the gas counter pressure process [13,14]. In this process, a high-pressure gas is injected into the mold prior to the polymer/gas solution to suppress cell nucleation and bubble growth while the polymer/gas solution is being injected into the mold cavity. Toward the end of injection, counter gas pressure is released and bubbles begin to form within the cavity. Since a majority of the part surface is already solidified, gas flow marks are eliminated.

In spite of these efforts to improve the surface quality, there have been difficulties in applying the microcellular injection molding process in industries requiring parts with high surface qualities because these techniques entail additional equipment which results in high costs or maintenance. There have been no reported studies on improving the surface quality of microcellular injection molded parts without any additional equipment or modification to existing equipment.

This paper proposes a novel approach to improve the surface quality of microcellular injection molded parts by controlling the cell nucleation rate. In this study, the cell nucleation rate was dramatically lowered or delayed by controlling the degree of supersaturation so that cell nucleation was delayed during the filling stage. After the polymer/gas solution volumetrically filled the mold cavity, intentionally delayed nucleation occurred and bubbles formed in the polymer matrix, except on the surface where the material had already solidified upon touching the mold surface. Theoretical background and experimental results are described in this paper. Microstructure, surface profile, surface roughness, mechanical properties, and dimensional stability are also investigated in this study.

2. Theoretical

2.1. Nucleation theory for polymeric foams

In polymeric foams, nucleation refers to the initial stage of the formation of gas bubbles in the polymer–gas solution. For nucleation, gas bubbles must overcome the free energy barrier before they can survive and grow to macroscopic size [15]. According to classical nucleation theories [16–18], the nucleation rate is controlled by the macroscopic properties and states of the polymer and gas such as solubility, diffusivity, surface tension, gas concentration, temperature, and the degree of supersaturation.

One representative equation for the nucleation rate of polymeric foams was reported by Colton and Suh [19,20]. In addition to the mathematical representation, they also verified their nucleation theory experimentally for a batch foaming process using a high pressure vessel. The nucleation equation for microcellular foams dominated by the classical nucleation theory [16–18] can be expressed as

$$N = fC\exp\left(-\Delta G^{**}/kT\right) \tag{1}$$

where N is the nucleation rate, f is the frequency of atomic molecular lattice vibration, C is the concentration of gas molecules, k is the Boltzmann's constant, T is the absolute temperature, and ΔG^{**} is the activation energy barrier for nucleation.

According to previous studies [19,20], the nucleation rate of polymeric foams is composed of two components: a homogeneous term and a heterogeneous term. The activation energy for homogeneous nucleation is given by

$$\Delta G^{**}_{\text{hom}} \cong \frac{16\pi\gamma^3}{3\Delta P^2} \tag{2}$$

where γ is the surface energy of the bubble interface and ΔP is assumed to be the gas saturation pressure. More precisely, $\Delta P = |P'_r - P_r|$ where P'_r is the pressure that is exerted in a high pressure vessel and P_r is the pressure of the supersaturated vapor in the sample [16]. That is, ΔP is the pressure difference between the pressure that is applied to the sample and the pressure of the supersaturated vapor in the sample. When the pressure that saturates the gas in a high pressure vessel is suddenly released to trigger the so-called thermodynamic instability by rendering the sample into the supersaturated state, P'_r becomes 1 bar—so low compared to P_r that ΔP can be approximated as P_r.

On the other hand, the activation energy for heterogeneous nucleation is affected by a geometric factor that depends on the contact (wetting) angle between the polymer and the particle and can be expressed as

$$\Delta G^{**}_{\text{het}} = \Delta G^{**}_{\text{hom}} \times f(\theta) \tag{3a}$$

$$f(\theta) = \frac{1}{2} - \frac{3}{4}\cos\theta + \frac{1}{4}\cos^3\theta \tag{3b}$$

where $f(\theta)$ is a geometric factor that is dependent upon the contact angle, θ, of the interface between the polymer and a second phase, and has values of less than or equal to 1. For a typical wetting angle of around 20° on the interface between a solid particle and the polymer melt, the geometric factor is 2.7×10^{-3}, suggesting that the energy barrier for heterogeneous nucleation can be reduced by three orders of magnitude with the presence of an interface [20,21].

2.2. Nucleation theory for microcellular injection molding

In the batch foaming process, the theory of Colton and Suh was verified by their experiments. Due to the large difference between the pressure exerted in a high pressure vessel and the pressure of the supersaturated vapor in the sample, the gas pressure dissolved in the polymer, the ΔP in the Gibbs free energy equation, can be approximately assumed to be the saturation gas pressure. The assumption that ΔP is the gas saturation pressure is fairly reasonable in a batch foaming process although the ΔP can still have an error of about 30–40% due to overestimation as reported in a previous study [15].

The nucleation theory by Colton and Suh is a simplified form derived and modified from classic nucleation theories [16–18] and is generally adequate for the batch foaming process. However, there is a need for this theory to be modified in cases of microcellular injection molding and extrusion systems because ΔP cannot be directly controlled and measured. To predict nucleation in microcellular injection molding and extrusion processes more precisely, this paper proposes a cell nucleation theory of a different form, which includes a term for the degree of supersaturation because it is a directly controllable factor.

To avoid misestimating ΔP, and to consider the degree of supersaturation, a more proper activation energy equation for nucleation can be derived from the following equation [16,17]

$$\Delta P = \left|P_r' - P_r\right| = \frac{2\gamma}{r_c} \tag{4}$$

where r_c is the radius of a characteristic droplet, and the W. Thomson equation

$$RT\ln\frac{P_r}{P_\infty} = \frac{2\gamma \cdot M}{r \cdot \rho} \tag{5}$$

where P_∞ is the pressure of the saturated vapor (i.e., the equilibrium pressure), R is the universal gas constant, M is the molar mass, and ρ is the density. These equations yield

$$\Delta P = \frac{RT\rho\ln\frac{P_r}{P_\infty}}{M} \tag{6}$$

which can be alternatively expressed as

$$\Delta P = kT\rho_l \ln S \tag{7}$$

where ρ_l is the molecular density of the bulk liquid, and $S(= P_r/P_\infty)$ is defined as the degree of supersaturation.

Thus, the activation energy equation (cf. Equation (2)) for nucleation in the microcellular injection molding process can be given by

$$\Delta G^{**} = \frac{16\pi\gamma^3}{3(kT\rho_l \ln S)^2} \tag{8}$$

Hence it can be stated that the activation energy for nucleation is inversely proportional to the square of the natural logarithm of the supersaturation degree.

In the microcellular injection molding process, the polymer/gas solution becomes a metastable supersaturation solution when it is injected into the mold cavity. This is because the amount of gas able to be dissolved in the polymer in the presence of a rapid pressure drop is less than the gas amount originally dissolved in polymer melts. In particular, assuming the air in the cavity is properly vented, the pressure at the advancing melt front is at the atmospheric pressure. The solubility of a gas in a polymer at atmospheric pressure and processing temperature can be obtained by an Arrhenius-type expression with regard to temperature [22]

$$S_{@1\ \text{atm, melt temperature}} = S_{@\text{STP}} \exp\left(-\frac{\Delta\overline{H}_s}{R}\left(\frac{1}{T_{\text{melt}}} - \frac{1}{298}\right)\right) \tag{9}$$

where $S_{@\text{STP}}$ is the solubility of the gas in the polymer at standard temperature and pressure conditions (298 K and 1 atm). The parameter $\Delta\overline{H}_s$ is the molar heat of sorption, and T_{melt} is the polymer melt temperature.

Thus, the degree of supersaturation is given by

$$S = \frac{m_g}{S_{@\ \text{STP}}} \exp\left(\frac{\Delta\overline{H}_s}{R}\left(\frac{1}{T_{\text{melt}}} - \frac{1}{298}\right)\right) \tag{10}$$

where m_g is the gas dosage which can be controlled by the supercritical fluid (SCF) supply system.

The heat of sorption, $\Delta\overline{H}_s/R_g$, of various polymer/gas systems at standard temperature has been studied and summarized in many previously published studies. In order to obtain the degree of supersaturation for a polymer/gas solution in the microcellular injection molding process, one has to either measure the solubility of the gas in the polymer at standard temperature and pressure or consult published data on the solubility of the gas in the polymer. Then, the activation energy barrier for nucleation in Equation (8), ΔG^{**}, can be obtained based on the calculated degree of

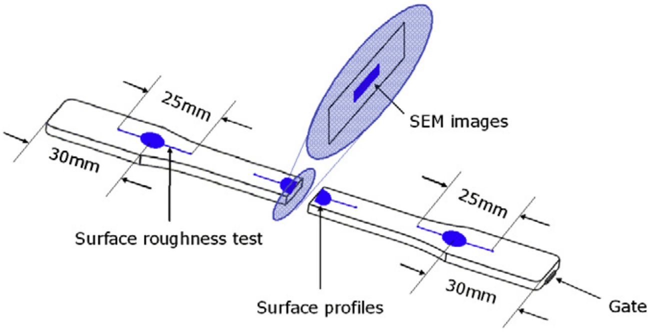

Fig. 1. Schematic of ASTM tensile test bar and the testing locations.

Table 1
Gas dosages (concentrations) employed in the microcellular injection molding process.

Simplified Characters	Polymer	Gas Type	Gas Injection Flow Rate (kg/hr)	Gas Dosage Time (s)	Approximate Gas Dosage (wt%)
MC1-L	LDPE	Nitrogen	0.05	0.7	0.102
MC2-L	LDPE	Nitrogen	0.06	0.75	0.135
MC3-L	LDPE	Nitrogen	0.07	0.8	0.173
MC4-L	LDPE	Nitrogen	0.08	1.0	0.255
MC5-L	LDPE	Nitrogen	0.08	1.5	0.418
MC6-L	LDPE	Nitrogen	0.11	1.5	0.575
MC1-P	PP	Nitrogen	0.05	0.7	0.102
MC2-P	PP	Nitrogen	0.07	0.8	0.173
MC3-P	PP	Nitrogen	0.08	1.0	0.255
MC4-P	PP	Nitrogen	0.11	1.5	0.575

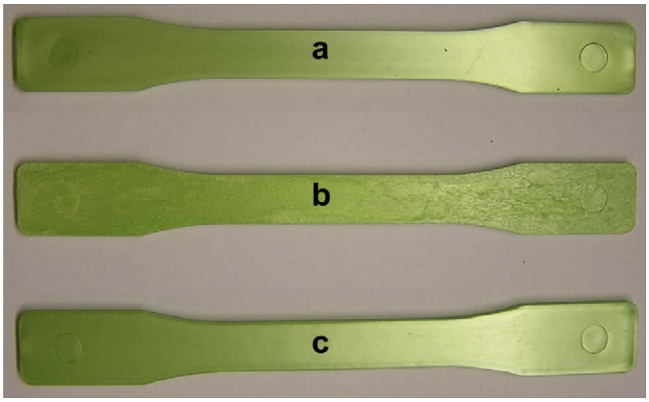

Fig. 2. Representative injection molded LDPE parts: (a) conventional solid injection molded part, (b) microcellular injection molded part with high gas concentration (>0.173wt%, and (c) microcellular injection molded part with low gas concentration (≤0.173wt%). To better reveal the surface quality, 5 wt% colorant was added to the material. In all other molding experiments reported herein, the materials were used as received without the colorant.

supersaturation and the surface energy of the bubble interface, γ. Given the activation energy barrier and the frequency factor, f, the nucleation rate (expressed in Equation (1)) can then be calculated. The estimate of the surface energy of the bubble interface and the frequency factor is discussed below.

In microcellular injection molding, the polymer/gas solution can be treated as a liquid mixture. Thus, the surface energy of the bubble interface, γ, can be expressed as [23,24]

$$\gamma_{\mathrm{mix}} = \gamma_{\mathrm{polymer}} \left(\frac{\rho_{\mathrm{mix}}}{\rho_{\mathrm{polymer}}} \right)^4 (1 - w_{\mathrm{gas}}) \tag{11}$$

where $\gamma_{\mathrm{polymer}}$ is the surface energy of the polymer, ρ's are the densities, and w_{gas} is the weight fraction of gas.

In addition, a frequency factor for a gas molecule, f, in Eq. (1) can be expressed as [24–26]

$$f = Z\beta \left(4\pi r_c^2 \right) \tag{12}$$

where z is the Zeldovich factor, which accounts for the many clusters that have reached the critical size, r_c, but are still unable to grow to sustainable bubbles. The parameter β is the impingement rate at which gas molecules collide with the wall of a cluster. The parameter $z\beta$ can be used as a correction factor and is determined experimentally.

Once the nucleation rate as a function of the degree of supersaturation is obtained, one can control the gas (SCF) content in the polymer melt to control or delay the onset of cell nucleation so that no bubble will form at the advancing melt front during the injection filling stage, thus, allowing microcellular parts with solid, swirl-free surface to be injection molded.

3. Experimental

3.1. Materials

The material used in this study was an injection molding grade low density polyethylene, LDPE (Chevron Phillips Chemical

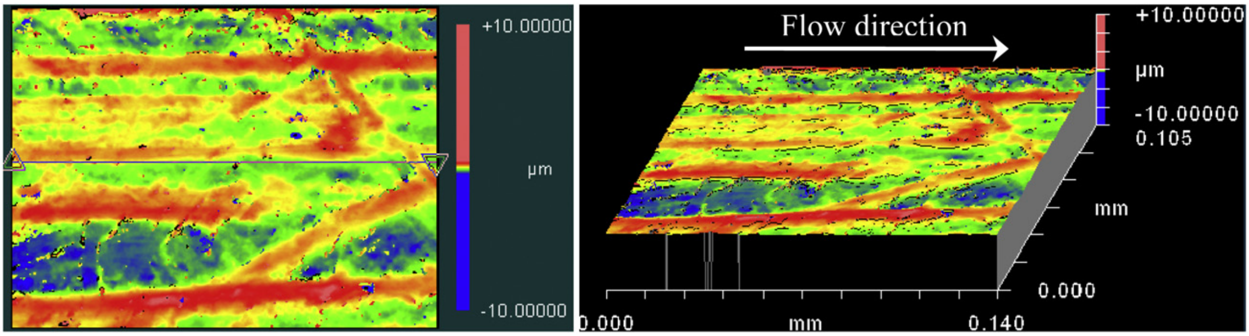

a Conventional injection molded parts

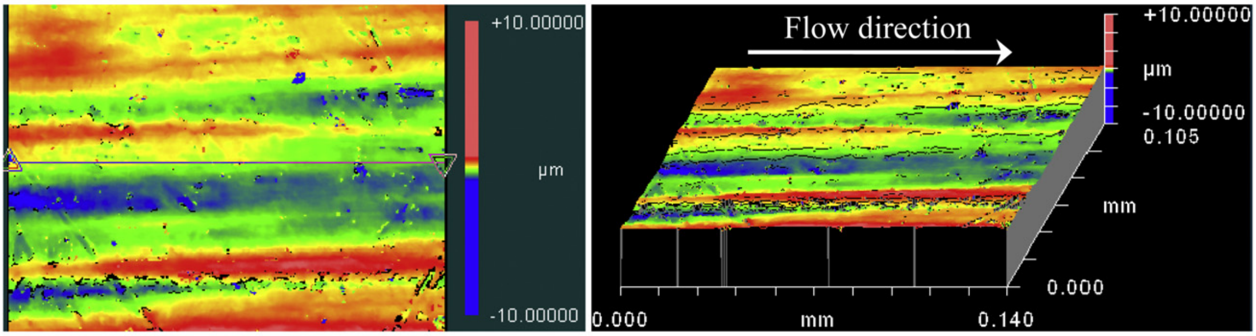

b Microcellular injection molded parts with low gas concentration (≤ 0.173wt%)

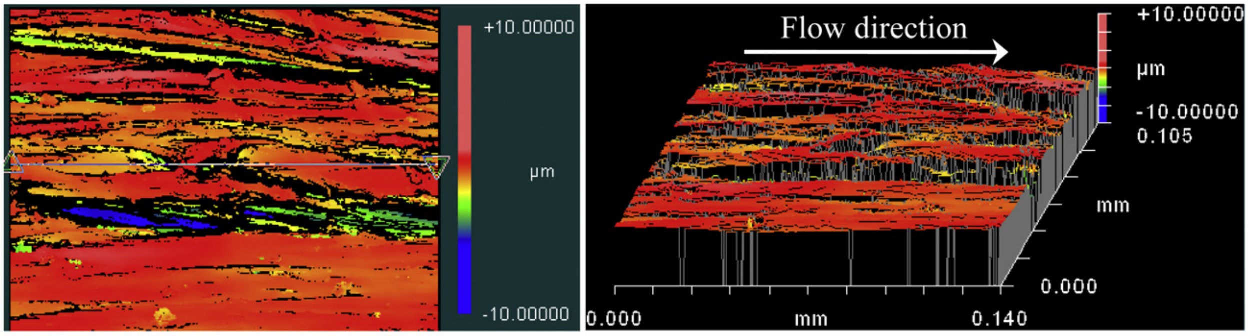

c Microcellular injection molded parts with moderate and high gas concentration (> 0.173wt%)

Fig. 3. Representative surface profiles of LDPE injection molded parts.

Table 2
Theoretical nucleation rate of microcellular injection molded parts.

Formulation	C (number/cm^3)	γ (dyne/cm)	S (g/g)	ΔP (Pa)	ΔG^{**} (J)	N (cm^{-3}sec^{-1})
MC1–L	1.92E19	20.9	3.28	1.65E7	5.59E-19	3.93E-22
MC2–L	2.55E19	20.9	4.35	2.05E7	3.65E-19	7.74E-10
MC3-L	3.27E19	20.8	5.58	2.40E7	2.63E-19	2.37E-3
MC4-L	4.83E19	20.8	8.24	2.94E7	1.75E-19	9.36E2
MC5-L	7.91E19	20.6	13.5	3.63E7	1.11E-19	1.03E7
MC6-L	1.09E20	20.5	18.5	4.07E7	8.72E-20	3.91E8
MC1-P	1.90E19	17.9	2.43	1.24E7	6.29E-19	1.77E-26
MC2-P	3.24E19	17.9	4.13	1.98E7	2.46E-19	3.07E-2
MC3-P	4.78E19	17.8	6.10	2.52E7	1.49E-19	4.08E4
MC4-P	1.08E20	17.5	13.7	3.65E7	6.74E-20	6.38E9

Company, Texas, USA). It has a melt index of 25 g/10 min and a density of 0.925 g/cm^3.

To confirm the theory for improving surface quality by controlling the degree of supersaturation, a random copolymer polypropylene (PP) was also used in this study. The PP used in this study was Titanpro SM668 (Titan Chemicals Corp., Malaysia), with a melt flow index of 20 g/10 min and a density of 0.9 g/cm^3. Both materials were used as received without any colorant, fillers, or additives.

Commercial grade nitrogen was used as a physical blowing agent for the microcellular injection molding trials.

3.2. Microcellular injection molding

In this study, an Arburg 320S injection molding machine (Arburg, Germany) was used for both the solid conventional and microcellular injection molding experiments. The supercritical fluid (SCF) supply system used in this study was the S11-TR3 model (Trexel, Woburn, MA, USA). The total gas dosage was controlled by adjusting the gas injection time, t, and the gas injection flow rate, $\dot{m}_g$. A tensile test mold, which produces tensile test specimens that meet the ASTM D638 Type I standards, was used for this experiment.

For injection molding of both LDPE and PP tensile test specimens, nozzle and mold temperatures were set at 221 °C and 25 °C, respectively. The cycle time was 40 s. An injection speed of 80 cm^3/s was employed. In this study, six different gas dosages (concentrations) were used for injection molding of LDPE as shown in Table 1. Also, four different gas dosages were employed for microcellular injection molding of PP. The supercritical fluid was injected into the injection barrel at 140 bar pressure to be mixed with the polymer melts in this experiment. The weight reduction of foamed versus solid plastic parts was targeted at 8 ± 0.5% for each specimen. For the conventional injection molding experiment, the shot size of 20.2 cm^3 and a packing pressure of 800 bars were employed for 6 s. For the microcellular injection molding experiments, the shot size of the polymer melt was 19.2 cm^3 and the packing stage was eliminated.

3.3. Analysis methods

To analyze the surface roughness of the molded tensile bar specimens, a Federal Surfanalyzer 4000 (Federal Product Corporation, RI, USA) was used. The surface roughnesses of conventional and microcellular injection molded parts were evaluated at three locations shown in Fig. 1 and the averaged surface roughness based on measurements done at all three locations was recorded and reported. The cutoff, drive speed, and drive length for the test were 0.75 mm, 2.5 mm/s, and 25 mm, respectively. For each process condition, ten specimens and three points on each specimen were tested.

In addition to the surface roughness, swirl marks commonly observed in microcellular injection molded samples can also be clearly revealed by a 3-D surface profiler. Zygo NewView (Zygo Corporation, CT, USA), a non-contact 3-D surface profiler, was employed to examine the surface profile of injection molded parts in this study using a scan distance of ±10 μm.

A JEOL JSM-6100 scanning electron microscope with an accelerating voltage of 15 kV was employed for observing the microstructures of the foamed parts. To observe the cross section of the microcellular injection molded parts, test specimens were frozen by liquid nitrogen and subsequently fractured. Representative images of each process condition were selected and cell sizes and densities were analyzed. A UTHSCSA Image Tool was employed as the image analysis software to evaluate cell densities and sizes.

A MTS Sintech 10GL screw driven machine was used to test the mechanical properties of the molded specimens, including the yield stress, strain at break, modulus, and ultimate stress. Ten specimens for each condition were tested. The tensile test speed was 50.8 mm/min. The schematic of the ASTM tensile bar and locations of the various analyses are shown in Fig. 1.

To test the dimensional stability of the injection molded specimens, a dial caliper made by Mitutoyo was used. Dimensions of the mold cavity were first measured and then the injection molded parts were measured and compared with the actual dimensions of the mold cavity.

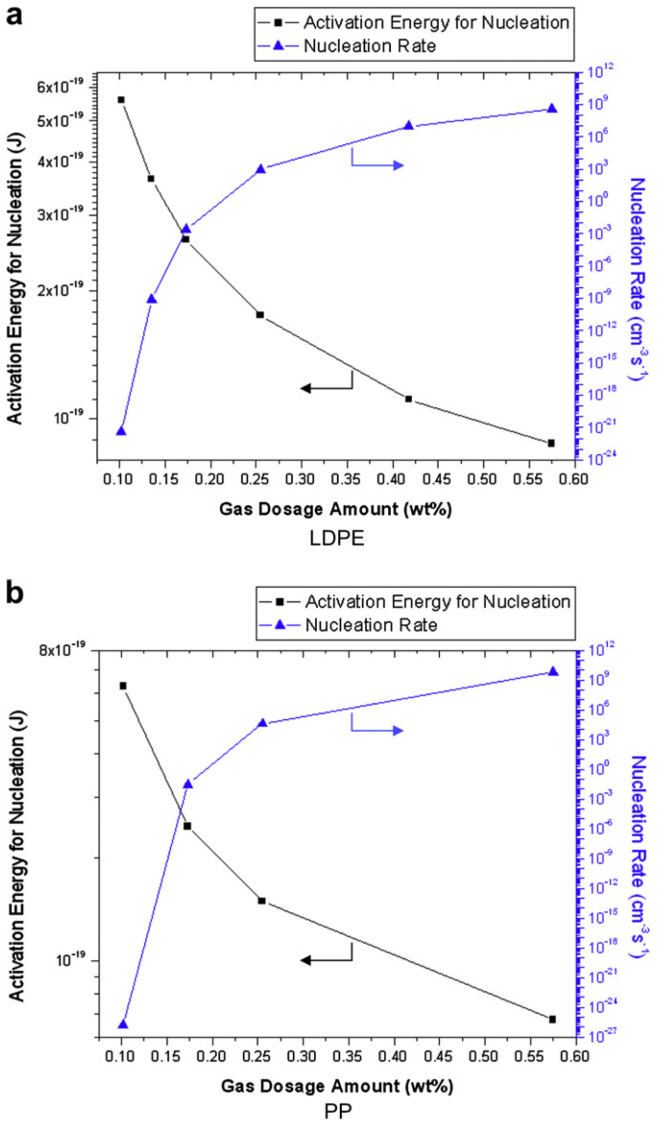

Fig. 4. Activation energy for nucleation and nucleation rate versus gas dosage for (a) LDPE and (b) PP.

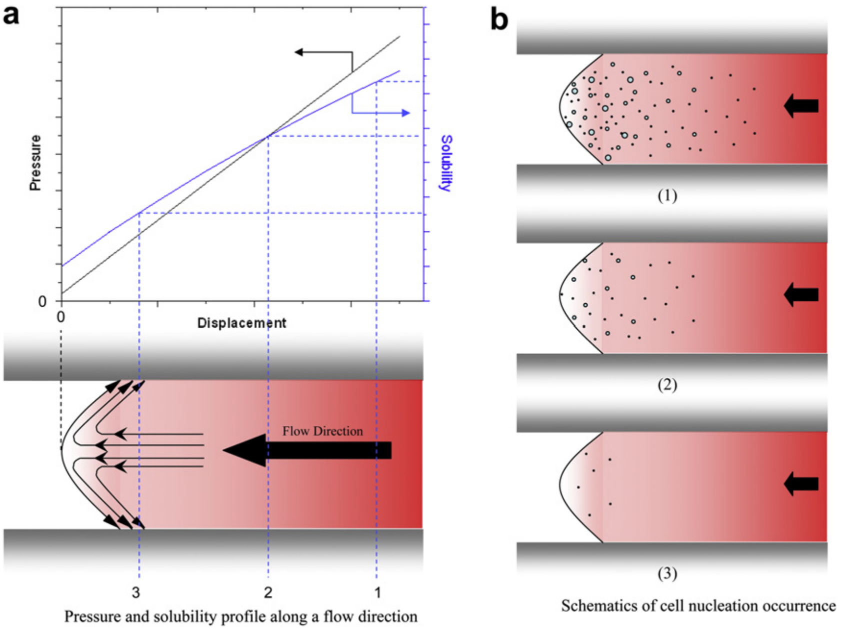

Pressure and solubility profile along a flow direction

Schematics of cell nucleation occurrence

Fig. 5. Starting point of cell nucleation for (1) high gas concentration, (2) moderate gas concentration, and (3) low gas concentration during the filling stage.

4. Results and discussion

4.1. Surface profile and roughness measurement

As a visual illustration, Fig. 2 shows the representative injection molded low density polyethylene (LDPE) parts. To better reveal the surface quality in the photo, 5wt% colorant was added to the material although the same surface quality was obtained without colorant. As anticipated, the conventional solid injection molded part (Fig. 2(a)) has a glossy and flawless surface. On the other hand, the typical microcellular injection molded part (Fig. 2(b)) produced with a moderate or high gas concentration has a lusterless surface due to swirl marks. A microcellular plastic part (Fig. 2(c)) molded with a carefully controlled gas concentration of 0.173 wt% or less has a high quality surface finish comparable to the conventional solid injection molded part. No swirl marks or defects are observed on the surface. For polypropylene (PP), it was observed that microcellular injection molded parts produced with a gas amount of 0.173 wt% or less also exhibited swirl-free and shiny surfaces.

Fig. 3 shows the representative surface profiles of injection molded parts made from LDPE. For this material, microcellular plastic parts molded with a gas amount of 0.173 wt% or less—i.e., MC1-L, MC2-L and MC3-L (cf. Table 1)—have a surface quality equivalent to that of conventional injection molded parts. For those parts, any swirl marks on the surface were invisible to the naked eye (cf. Fig. 2). Also, the lack of smoothness and brightness typically found in microcellular injection molded parts were imperceptible to touch or to the human eye. Microcellular injection molded PP specimens show similar results to LDPE and thus are not shown. MC1-P and MC2-P have swirl-free surfaces without any noticeable surface defects. On the other hand, MC3-P and MC4-P, which have a higher gas amount, show swirl marks on their surfaces and have a rough surface like one might associate with typical microcellular injection molded parts.

As shown in Fig. 3(a), the surface of the conventional LDPE injection molded part has streaks on it due to either machining marks or normal wear induced by the repeated flow of polymer melt over its surface. Except for these streaks, it has a smooth and even surface profile. Fig. 3(b) shows the representative surface profile of the microcellular LDPE injection molded with a gas concentration of 0.173 wt% or less. It has a smooth and even surface profile, comparable to that of conventional injection molded parts.

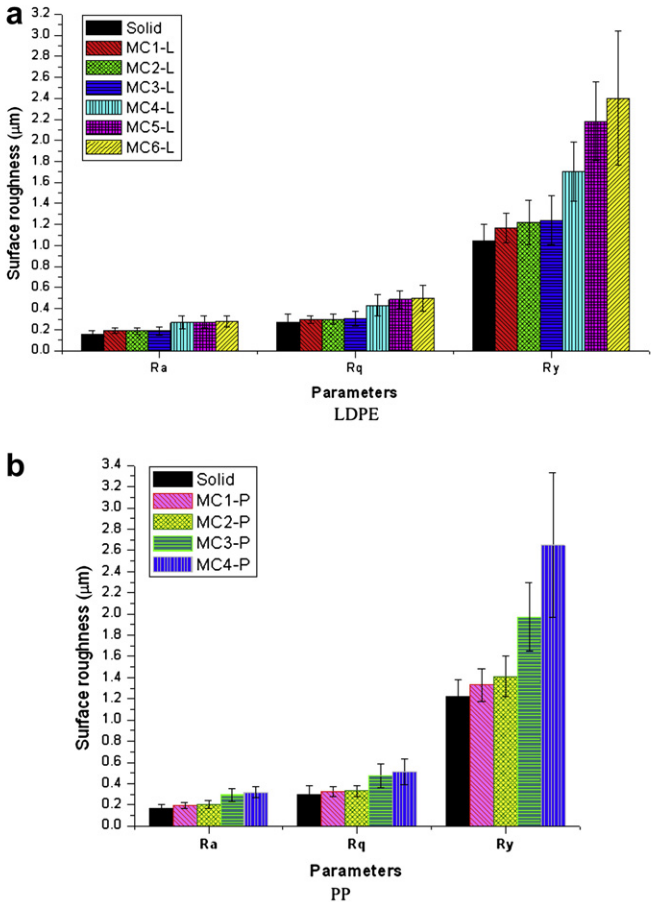

Fig. 6. Surface roughness of conventional and microcellular injection molded parts. (a) LDPE. (b) PP.

Table 3
Cell sizes and cell densities of microcellular injection molded parts.

Formulation	Cell Sizes (μm)	Cell Densities (# of cells/cm^3)
MC1-L	677 ± 228	8.26E + 2
MC2-L	572 ± 143	1.07E + 3
MC3-L	595 ± 158	8.91E + 2
MC4-L	496 ± 159	1.80E + 3
MC5-L	353 ± 111	6.44E + 3
MC6-L	296 ± 118	7.26E + 3
MC1-P	254 ± 146	8.05E + 3
MC2-P	149 ± 40	2.67E + 4
MC3-P	34.6 ± 15.2	5.77E + 6
MC4-P	20.0 ± 12.4	1.62E + 7

On the other hand, swirl marks and a rough surface are evident on the surface of microcellular LDPE plastics molded with nitrogen over 0.173 wt% as shown in 2-D and 3-D surface maps of Fig. 3(c). The area shown as black in Fig. 3(c) is the domain in which the surface profiler could not measure the height difference due to an uneven surface that exceeds the pre-set measurement limits (i.e., ±10 μm). The surface profiles of conventional and microcellular PP injection molded parts are very similar to their LDPE counterparts.

As mentioned previously, surface imperfections of the microcellular injection molded parts, such as swirl marks and a lack of smoothness, are caused by bubbles forming at the advancing melt front during the mold filling stage. These bubbles are transported toward the mold surface by fountain flow behavior and are subsequently stretched and dragged against the mold wall by the incoming polymer melt [6,9]. The use of a small amount of gas in the microcellular injection molding process results in a reduction of supersaturation that leads to a great increase in the activation energy needed for nucleation. An elevated activation energy causes a large drop in the nucleation rate, which retards the nucleation and subsequent growth of bubbles so that the probability of bubbles being formed at the advancing melt front, and subsequently being dragged and stretched against the mold wall, dramatically decreases.

Table 2 shows the theoretical nucleation rate of microcellular injection molded parts based on the nucleation theory containing the degree of supersaturation presented previously. For the materials and experiments under consideration, constant $z\beta$ is assumed to be 1.0×10^{11} [s^{-1} m^{-2}]. The solubility of nitrogen in LDPE was obtained from reference [27]. The solubility of nitrogen in PP is known to be around 35% more than that of LDPE according to previous studies conducted by Park and his colleagues [[28–30], and unpublished research results]. Thus, given the same amount of gas, the degree of supersaturation for PP/N_2 becomes about 25% lower than that for $LDPE/N_2$.To take into account the effect of temperature on the surface tension, the Guggenheim equation reported in reference [31] was used for the calculation of surface tension with regard to temperature. The density of nitrogen was obtained by Engineering Equation Solver (EES) using the property data of real gases [32].

As shown in Table 2, theoretical nucleation rates of MC1-L, MC2-L, MC3-L, MC1-P, and MC2-P—i.e., microcellular injection molded parts not having swirl marks on the surface—are significantly small. On the other hand, as the degree of supersaturation increases with a gas dosage beyond 0.173 wt%, the activation energy for nucleation decreases while the nucleation rate increases sharply. Dramatic changes in the nucleation rate and activation energy as a function of gas dosage are plotted in Fig. 4. As the amount of gas increases incrementally, the nucleation rate increases significantly and, at a certain point, numerous cell nuclei form enough bubbles to cause swirl marks on the surface of the microcellular injection molded parts. In Table 2, it is believed that the difference in the nucleation rate and cell size between LDPE and PP is primarily due to differences in the surface tension of polymer melts and solubility of nitrogen in polymers.

Fig. 5 illustrates the mechanism of cell nucleation when the polymer/gas solution is injected into the mold cavity. As the polymer/gas solution is injected into the mold, the pressure drops along the flow direction toward the advancing melt. At this point, the pressure is at atmospheric pressure. As the pressure decreases, the solubility of nitrogen in the polymer decreases and the degree of supersaturation increases so that nucleation starts to occur. Theoretically, the starting point for cell nucleation to occur is at the point where the degree of supersaturation becomes greater than unity. However, the cell nucleation rate remains too small and thus is negligible at this moment. To become an issue for the surface quality, a significantly high cell nucleation rate—which can cause swirl marks on the surface of foamed plastics—should be approximately around 10^{-1} to 10^{1} cm^{-3} s^{-1}. This cell nucleation rate range corresponds to a degree of supersaturation between 6.1 and 7.0 for

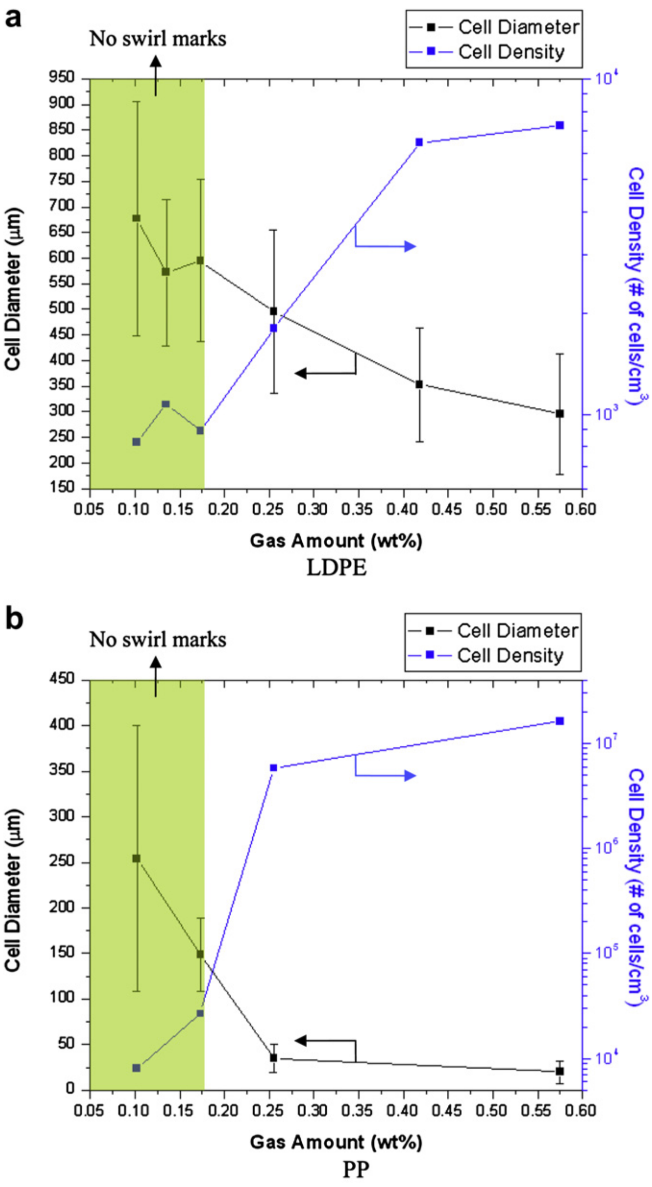

Fig. 7. Cell diameters and cell densities of microcellular injection molded parts versus gas amount. (a) LDPE. (b) PP.

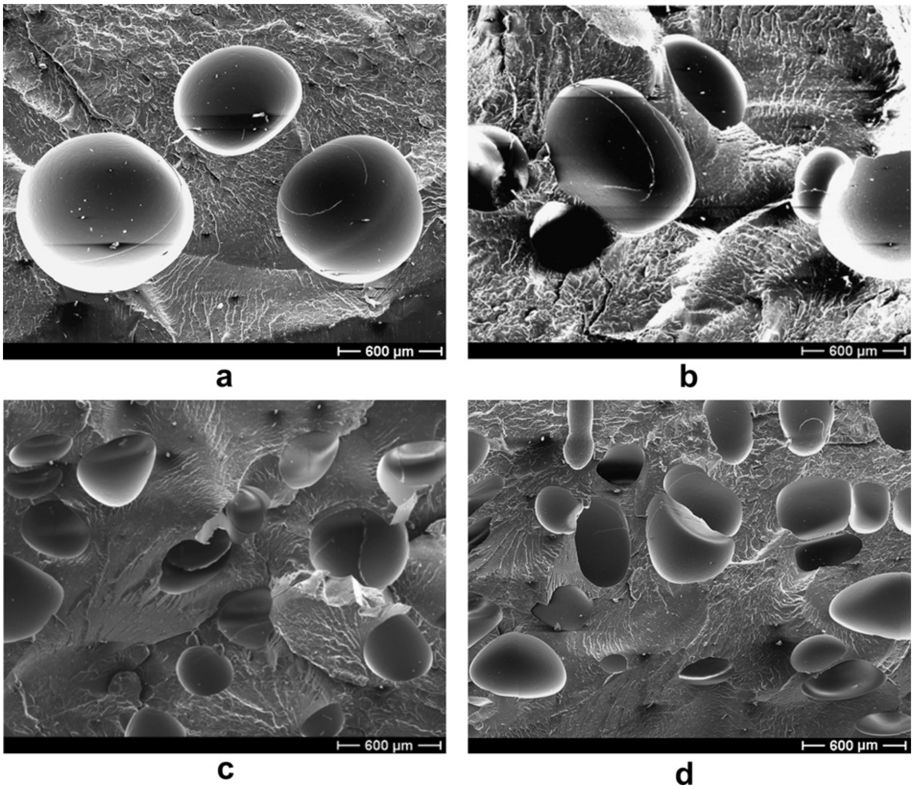

Fig. 8. SEM images of microcellular injection molded LDPE parts. (a) MC1-L, (b) MC2-L, (c) MC5-L, and (d) MC6-L.

LDPE and between 4.2 and 4.7 for PP. As shown in Fig. 5(a), as the gas amount decreases, the starting point for cells to nucleate is delayed. It is conceivable that, below a certain degree of supersaturation, cell nucleation does not occur before the melt front of the polymer/gas solution touches the mold wall. Once a solid skin layer solidifies, a swirl-free surface is formed. After that, cells start to nucleate and grow in the hot polymer core until the material solidifies within the chilled mold.

By controlling the degree of supersaturation, and thus the cell nucleation rate, bubble formation on the surface of the foamed part can be delayed or suppressed. This is the reason why microcellular injection molded LDPE parts with a nitrogen content of 0.173 wt% or less have much smoother surfaces than those with a higher gas dosage (cf. Fig. 6). In Fig. 6, R_a, R_q and R_y are the average, root-mean-square, and maximum peak-to-valley height roughnesses, respectively. MC4-L, MC5-L, and MC6-L have 75–101% rougher surfaces, on average, than conventional injection molded parts. In addition, these microcellular injection molded parts show a wide deviation of roughness which demonstrates the difficulty of controlling surface roughness. On the other hand, samples injection molded with a nitrogen of 0.173 wt% or less have much smoother surfaces than those with moderate or high gas concentrations, although they are still 11–20% rougher than conventional injection molded parts. When the standard deviation of the surface roughness is considered, swirl-free microcellular injection molded parts have fairly comparable surfaces to those of conventional molded parts. Test results for PP show similar patterns to those of LDPE, as shown in Fig. 6(b).

4.2. Microstructures

Table 3 and Fig. 7 show the cell diameters and densities of microcellular injection molded parts versus gas amount. The cell diameters and densities were analyzed and calculated based on the SEM images of cell structures shown in Fig. 8 and using imaging analysis software (UTHSCSA Image Tool). As gas amount increases, average cell diameter decreases and cell density increases. It is believed that cells nucleate more and earlier during the filling stage due to the increase in cell nucleation rate with a higher degree of supersaturation. For microcellular injection molded LDPE parts with no swirl marks on their surfaces, the average cell diameter is over 550 μm. On the other hand, microcellular injection molded LDPE parts having swirl marks can have average cell diameters of less than 300 μm and cell densities about 8 times more than their swirl-free counterparts.

For PP, microcellular injection molded parts with bubbles of diameters 149 μm and cell densities of 27,000 per cubic centimeter on average were achieved without swirl marks on their surfaces. MC1-P had bigger and sparser bubbles than MC2-P and had a huge cell size distribution. On the other hand, MC3-P and MC4-P had small and denser bubbles inside. Also, bubble sizes of MC3-P and MC4-P were much more regular than the MC1-P specimen. MC2-P had smaller, more even, and denser bubbles than MC1-P although it had relatively bigger and sparser bubbles than the MC3-P or MC4-P specimen.

From these microstructure analyses, it can be concluded that typical microcellular plastics molded with moderate or high gas concentrations have smaller and denser bubbles than those molded with lower gas contents. For swirl-free microcellular injection molded parts, there is a trade-off for finer and denser cell morphology since cell nucleation occurs more slowly and later during the filling stage than typical microcellular injection molding. With lesser number of nuclei, the molded parts tend to have larger and sparser bubbles. While the cells were large (due to a slower nucleation rate) compared to those in typical microcellular injection molded parts, those cells are still in the sub-mm range. Nonetheless, it should be pointed out that typical microcellular injection molded parts normally have a cell size of 100 μm or less and a cell density around 10^6 cells/cm^3. In addition, the cell

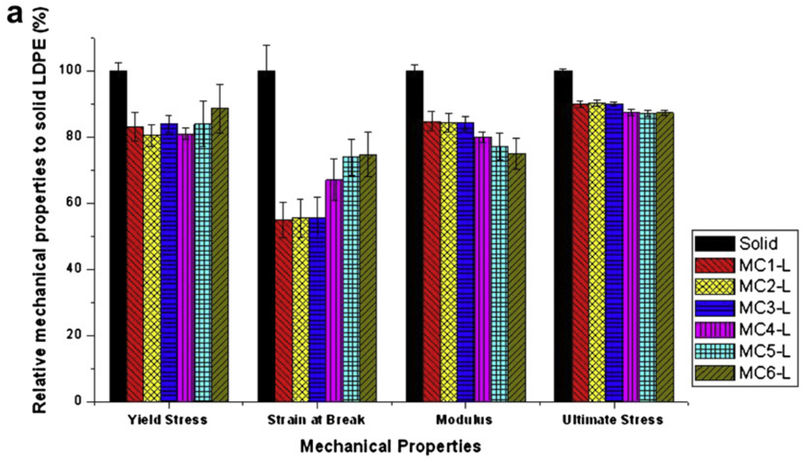

LDPE

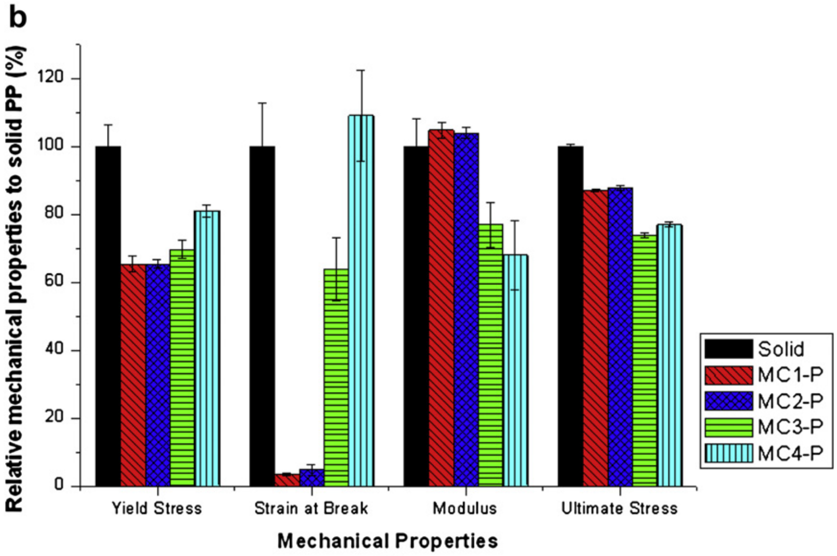

PP

Fig. 9. Relative mechanical properties of microcellular injection molded parts as compared to conventional injection molded parts. (a) LDPE. (b) PP.

morphology can affect both the mechanical properties and the dimensional stability. Further research on both will be introduced in the following sections. The effect of gas foaming on crystallization and crystal morphology as well as mathematical modeling and numerical prediction in microcellular injection molding (cf. [33–35]) require further studies.

4.3. Mechanical properties

Fig. 9 shows the relative mechanical properties of microcellular injection molded parts as compared to conventional injection molded parts. For LDPE, the strain at break of swirl-free microcellular injection molded parts was noticeably lower than the rest of microcellular parts that have smaller, denser, and more uniform bubbles associated with higher gas concentrations and thus a more uniform and longer elongation before fracture. For yield stress, no noticeable change with regard to different gas amount was found.Interestingly, swirl-free microcellular injection molded parts have better moduli and ultimate stresses than typical microcellular injection molded parts. This is because decreasing the blowing agent increases the thickness of the skin layer which is not foamed such that some of the mechanical properties of the microcellular injection molded parts are increased [36–38].

The PP specimens behaved similarly to the LDPE specimens for the mechanical properties shown. The moduli of MC1-P and MC2-P were significantly greater than those of MC3-P and MC4-P. Also, injection molded parts with low gas contents had higher ultimate stresses than their counterparts. Strains at break of swirl-free microcellular injection molded parts were much less than those of typical microcellular injection molded specimens. It is evident that the cell morphologies of microcellular plastics strongly affect their mechanical properties. It is also likely that the strain at break is strongly affected by the cell morphology. A microcellular injection molded part with more tiny bubbles and a uniform bubble distribution tends to exhibit greater strain at break than the ones with fewer but larger bubbles.

4.4. Dimensional stability

The dimensional stability of injection molded parts versus gas concentrations are shown in Fig. 10. As gas content increases, the shrinkage of microcellular injection molded parts distinctly decreases. Changes in the thickness direction are greater than the flow and transverse directions for both LDPE and PP specimens. If cell nucleation is too low, the benefit of improvement in dimensional stability may not be fully realized. The shrinkage of

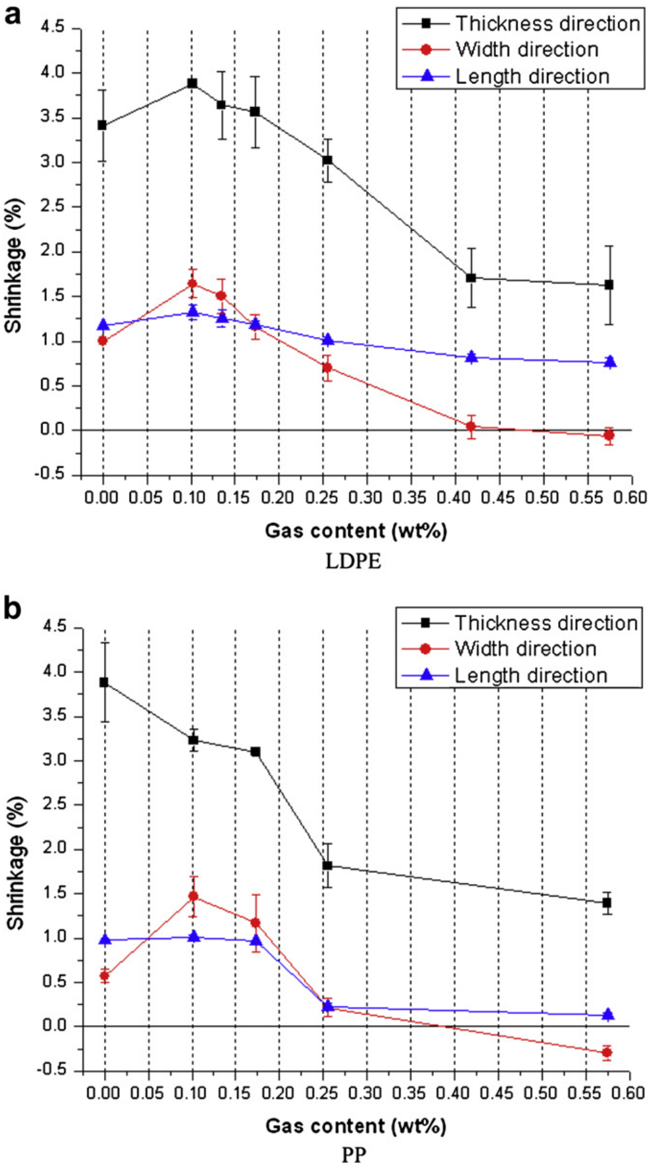

Fig. 10. Shrinkage of injection molded parts versus gas dosage. (a) LDPE. (b) PP.

a microcellular LDPE part molded with 0.173 wt% of nitrogen was closest to a conventional injection molded part among the six different batches of specimens studied. For PP, similar patterns on shrinkage were observed. Due to the smaller and denser bubbles of PP as compared with LDPE specimens, shrinkage in every direction was lower than that of the microcellular injection molded LDPE.

5. Conclusions

By reducing the degree of supersaturation, the activation energy for cell nucleation will increase, thereby greatly reducing the cell nucleation rate. This retards cell nucleation during the mold filling stage, thus preventing bubble formation on the melt front of the polymer/gas solution, resulting in swirl-free microcellular injection molded parts. This research demonstrates the feasibility of this approach both theoretically and experimentally.

The swirl-free microcellular injection molded parts produced in this study had comparable surface qualities to conventional injection molded parts with the added bonus of an 8 percent reduction in weight. Surface imperfections such as lack of brightness, gas flow marks, and rough surfaces—which have long been considered unavoidable shortcomings of the microcellular injection molded process—were eliminated without any additional equipment or equipment modification, as required by other methods.

The microstructure of typical microcellular injection molded parts show smaller and denser bubbles than swirl-free microcellular injection molded parts. It can be seen that, as gas amount increases gradually, injection molded parts possess a reduced bubble size and an increased bubble density while maintaining surface quality, until a certain degree of supersaturation or gas dosage is reached. When this threshold is reached, however, the cell nucleation rate is high enough that swirl marks begin to appear on the surface. How precisely to maintain the desirable cell morphology—that is, smaller and denser bubbles—for a swirl-free surface for microcellular injection molded parts requires further investigation.

The strain at break of a swirl-free microcellular injection molded part is noticeably lower than that of a typical microcellular injection molded part. On the other hand, a swirl-free microcellular injection molded part exhibits a higher modulus and ultimate stress than a typical microcellular injection molded part. For dimensional stability, the shrinkage of microcellular injection molded parts is reduced with increasing gas dosage. A swirl-free microcellular LDPE specimen molded with 0.173 wt% nitrogen shows acceptable shrinkage properties which are comparable to, or better in some cases than, a conventional injection molded part.

In this study, a constant mold filling rate was used. However, different mold filling rates will affect the pressure history in the cavity, thereby affecting the cell nucleating rate. This mold filling rate effect and the effect of gas foaming on crystallization and crystal morphology as well as mathematical modeling and numerical prediction in microcellular injection molding require further studies.

Acknowledgments

The authors are grateful to Energizer Personal Care Products for their financial and technical support. Also, the authors sincerely thank Microcellular Plastics Manufacturing Laboratory at the University of Toronto for providing some of the technical data used in this research.

References

[1] Trexel, Inc. Web site, http://www.trexel.com.
[2] Knights M. Plastics Technology 1999;45:41.
[3] Kramschuster A, Cavitt R, Turng LS, Chen ZB, Ermer D. Plastics, Rubber and Composites 2007;35:198.
[4] Yoon JD, Cha SW, Chong TH, Ha YW. Polymer-Plastics Technology and Engineering 2007;46:815.
[5] Shen C, Kramschuster A, Ermer D, Turng LS. International Polymer Processing 2006;21:393.
[6] Cha SW, Yoon JD. Polymer-Plastics Technology and Engineering 2005;44:795.
[7] Smith C. Plastics and Rubber Weekly 2004;4:22.
[8] Chen SC, Chang JA, Jong WR, Lin YW. Proceedings of the Polymer Processing Society 24th Annual Meeting; 2008;44:p. 795.
[9] Pierick DE, Anderson JR, Cha SW, Chen L, Stevenson JF, Laing DE. U.S. Patent 6,884,823; 2005.
[10] Yoon JD, Hong SK, Kim JH, Cha SW. Cellular Polymers 2004;23:39.
[11] Lee JJ, Turng LS. Polymer Engineering and Science 2010;50:1281.
[12] Turng LS, Kharbas H. International Polymer Processing 2004;19:77.
[13] Bledzki AK, Kirschling H, Steinbichler G, Egger P. Journal of Cellular Plastics 2004;40:489.
[14] Andrezej KB, Omar F, Hendrik K, Joanna K, Adam J. Polimery 2006;10:697.
[15] Tomasko DL, Burley A, Feng L, Yeh SK, Miyazono K. Journal of Supercritical Fluids 2009;47:493.
[16] Volmer M, Weber A. Zeitschrift fur Physikalische Chemie; 1926, March:277.
[17] Ari L, Vicente T, David WO. Annual Review of Physical Chemistry 1995;46:489.
[18] Emo C, Roberto S. Biodegradable polymers and plastics. Springer; 2002. 275.
[19] Colton JS. Plastics Engineering; 1988, August:53.
[20] Colton JS, Suh NP. Polymer Engineering and Science 1987;27(7):485.
[21] Colton JS, Suh NP. Polymer Engineering and Science 1987;27(7):493.

[22] Donald GB, Dimitris IC. Polymer processing – principles and design. John Wiley & Sons, Inc; 1998. 72–82.
[23] Reid RC, Prausnitz JM, Poling BE. The properties of gases and liquids. McGraw-Hill Book; 1986. 644.
[24] Goel SK, Beckman EJ. Polymer Engineering and Science 1994;34:1137.
[25] Tsivintzelis I, Angelopoulou AG, Panayiotou C. Polymer 2007;48:5928.
[26] Gabbard RG, Ph.D. Thesis at New Jersey Institute of Technology; May 2002, 17.
[27] Lee JG, Flumerfelt RW. Journal of Applied Polymer Science 1995;58:2213.
[28] Li G, Gunkel F, Wang J, Park CB, Altstadt V. Journal of Applied Polymer Science 2007;103:2945.
[29] Li G, Wang J, Park CB, Simha R. Journal of Polymer Science Part B-Polymer Physics 2007;45:2497.
[30] Li G, Wang J, Park CB, Moulinie P, Simha R, SPE, ANTEC, Technical Papers, 2004, Paper #421.
[31] Wu S. Polymer interface and adhesion. CRC Press; 1982. 67–95.
[32] http://sel.me.wisc.edu/ees/new_ees.html.
[33] Osorio A, Turng LS. Polymer Engineering and Science 2004;44:2274.
[34] Moon Y, Lee KS, Cha SW. Journal of Mechanical Science and Technology 2009;23:3349.
[35] Goel SK, Beckman EJ. American Institute of Chemical Engineers (AIChE Journal) 2004;41:357.
[36] Barzegari MR, Rodrigue D. Polymer Engineering and Science 2009;49:949.
[37] Lee JJ, Cha SW. Cellular Polymers 2005;24:279.
[38] Lee JJ, Cha SW. Polymer-Plastics Technology and Engineering 2006;45:871.

Polymer 52 (2011) 1447–1457

Contents lists available at ScienceDirect

Polymer

journal homepage: www.elsevier.com/locate/polymer

Verification of numerical simulation of the self-assembly of polymer-polymer-solvent ternary blends on a heterogeneously functionalized substrate

Yingrui Shang*, Liang Fang, Ming Wei, Carol Barry, Joey Mead, David Kazmer*

Department of Plastics Engineering, University of Massachusetts at Lowell, Lowell, MA, USA

A R T I C L E I N F O

Article history:
Received 9 November 2010
Received in revised form
15 January 2011
Accepted 18 January 2011
Available online 26 January 2011

Keywords:
Numerical simulation
Phase separation
Polymer blends

A B S T R A C T

The directed self-assembly of polymer-polymer-solvent ternary blends on heterogeneously functionalized substrate is investigated with a three dimensional numerical model. The numerical simulation results are quantitatively verified by the experimental results. The phase separation of PS-PMMA-DMF blends are spin coated on a substrate functionalized by ODT/NH_2 on Au surface. While many simulation parameters are set to the experimental conditions, other unmeasurable material constitutive model parameters are estimated from the real experiment observations. The effects of the spin speed, pattern periodicity, PS/PAA composition ratio, and the PAA molecular weight are investigated in both the experiments and numerical simulation. The simulation results are verified by comparison to the experimental results. During the verification process, numerical optimization methods are employed to determine the unmeasurable physical parameters. Quantitative methods are introduced for assessment of the results.

1. Introduction

The polymer self-assembly directed by a heterogeneously functionalized substrate has attracted significant interests in recent years for its promising applications such as lithographic processes, biosensors, and semiconductor devices [1]. When the immiscible blends with solvent are quenched into a spinodal region, the phase separation can be initiated by very small fluctuations in composition. The functionalization on the pattern can be used to direct the morphology evolution during the phase separation. The phase separation and self-assembly of polymer blends on heterogeneously functionalized substrates are studied extensively by experimentalists [2–14]. It has been observed in the experiments that the domain size of the morphology evolves in a power law relation with time. The speed of evolution is determined by the diffusivity and the polymer concentration. A composition wave is also observed, which propagates inward from the functionalized substrate. The processing parameters such as pattern size in the substrate, the gradient energy coefficient, the degree of polymerization, and the solution concentration will affect the refinement of the morphology.

The mechanisms of spinodal decomposition in an isotropic system of nonuniform composition can be described by the Cahn–Hilliard equation [15,16]. Using this governing equation, numerical simulation methods were employed to investigate the mechanisms of the spinodal decomposition. Scott and Robert [17] numerically studied the thermodynamics of a polymer-polymer-solvent ternary system with Flory–Huggins type of local free energy and the conclusions of numerical simulation were verified by experimental results. Hsu and Prausnitz [18] used an approach similar to Scott and Robert's work to calculate the phase diagram of a ternary system. Chen [19] numerically simulated the phase separation of a generalized ternary blends, in which three components were immiscible with each other. Huang et al. established a numerical model for a polymer-polymer-solvent ternary system based on the Flory–Huggins free energy and non-linear diffusion equations [20]. An interface segregation was observed in the symmetric ternary polymer blends without the effects of mechanical flow. More complex system with other effects were also researched with numerical methods. Altena and Smolders [21] calculated the binodal line of a polymer-non-solvent-solvent system. Zhou and Powell [22] numerically studied the morphology evolution of a similar system with hydrodynamical effects included. Tong et al. [23] numerically studied the phase domain growth with chemical reaction involved. He and Nauman [24] investigated the influence of polymer chain length on the phase separation. In their simulation it is observed that the long chains of polymers will destabilize the blends and increase the quench depth. The directed assembly of polymer blends on functionalized patterns was also numerically investigated in terms of evolution mechanisms and the

---

* Corresponding authors.
E-mail addresses: yingrui.shang@gmail.com (Y. Shang), david_kazmer@uml.edu (D. Kazmer).

0032-3861/$ – see front matter © 2011 Elsevier Ltd. All rights reserved.
doi:10.1016/j.polymer.2011.01.038

optimization of production parameters. Muthukumar et al. [25] studied the effects of the alternative patterns on the kinetics of phase separation of a thin polymer film. Checkerboard-like composition fluctuations were found in a wide range of patterns. This structural phenomenon is related to interaction strength, thermal noise, and film thickness. Karim et al. [9] also numerically investigated the checkerboard structure in the bulk of a thick film during phase separation on a patterned substrate, with the combined effects of the bulk phase separation and the interaction force on the functionalized pattern.

Though the mechanisms of the spinodal decomposition and the influences of homogeneous and heterogeneous patterns were discussed in previous works, few of them implemented the actual experimental and environmental parameters into the numerical simulation. Thus to the experimentalists, the results from the computer modeling are merely qualitative other than quantitative. In this paper, phase separation of a polymer-polymer-solvent ternary blend on heterogeneously patterned substrates are studied in numerical simulation in three dimensions [26,27]. The Cahn–Hilliard equation are used to calculate the free energy of the mixture and the Flory–Huggins model are employed to account for the bulk free energy. The real processing parameters and material properties are modeled in the numerical simulation. Since the values of some of the materials constitutive parameters in ternary phase separation are difficult to measure, necessary assumptions and numerical determination methods are employed to estimate the values of some constitutive model parameters used in the numerical simulation. Also, new commensurability measures are introduced to assess the quality of the pattern from self-assembly. To the authors' knowledge, this is the first attempt to quantitatively validate the numerical simulation results with real experimental results. The effects of the processing parameters such as the composition of the polymer blends, the attracting factors of the patterned substrate, and the rate of the evaporation are investigated both in simulation and experiments. The computed morphology is quantitatively compared with the images from experiment results. It can be seen that the numerical model can predict the main effects of various factors as verified by the experiments.

2. Experiment

To compare the simulated results with a real experimental system, we directed the morphologies of polystyrene (PS)/polyacrylic acid (PAA) blends using chemically heterogeneous patterns. More specifically, alkanethiols with different chemical functionalities were patterned by electron beam lithography, which were then used to direct the assembly of PS/PAA blends during the spin coating from their mutual solvent [28].

2.1. Materials

PS with M_w of 18.1 kDa, PAA with M_w of 2 kDa, and the solvent including anhydrous ethanol, acetone, and N,N-dimethylformamide (DMF) were purchased from Aldrich. 11-amino-1-undecanethiol hydrochloride (MUAM) with 99% purity was purchased from Asemblon, Inc. And 1-octadecanethiol (ODT) with 98% purity was also purchased from Aldrich.

2.2. Fabrication of chemically patterned substrate

The poly(methyl methacrylate) (PMMA) trench templates (the width and spacing ratio was 3/7) with different sizes were first produced. With 5 nm thick Cr as the adhesion layer, Au layer with 120 nm thickness was evaporated onto a Si (100) wafer. The PMMA resist with 150 nm thickness was then spin coated onto the Au substrate. Electron beam lithography was then utilized to write patterns of lines on the PMMA films. The exposed PMMA regions were developed using Methyl isobutyl ketone (MIBK). And the remaining PMMA resist at the bottom of the PMMA trench was removed by the treatment of oxygen plasma for 5 s. Then, the PMMA trench templates were immersed into MUAM solution (1 mM in ethanol) for 24 h to form well-developed hydrophilic SAMs at the PMMA trench area. Afterward, the templates with assembly MUAM SAMs were rinsed by ethanol for several times to remove the multiple MUAM layers on the top of the SAMs at the trench area. Then, PMMA resist was removed by extraction of acetone with a Soxhlet extractor for 24 h. Finally, the templates were immersed in ODT solution (1 mM in ethanol) for 24 h to produce well-ordered hydrophobic SAMs on the remaining gold area and then rinsed several times using ethanol.

2.3. Spin coating

The chemically patterned templates were immediately put on the rotating plate of a spin coating machine after a secondary treatment of alkanethiol. High purity nitrogen gas was prefilled into the coating chamber to control the humidity. A droplet of polymer solution, 1 wt.% PS/PAA with 7/3 composition ratio in DMF, was placed on the patterned area of the template. After 6–7 min, the polymer solution was spin coated on the template surface with varying rotation speeds for 30 s.

2.4. Characterization

A JOEL 7401F field-emission scanning electron microscopy (FESEM) was used to provide the FESEM images. Atomic force images and topographic images were examined using a scanned probe microscopy (Veeco NanoScope IIa, PSIA XE-150) in noncontact mode. Fourier transform analysis was performed by using commercial AFM image analysis software XEI (PSIA corp. version 1.5)

3. Numerical simulation

In this paper, the asymmetric polymer-polymer-solvent ternary blend is considered isothermal and diffusion controlled. No predominant dynamic flow is present in the domain [29].

The total free energy of a ternary system, F, can be derived from the thermodynamic principles presented by Cahn and Hilliard [30,31],

$$F(C_1, C_2, C_3) = \int_V \left\{ f(C_1, C_2, C_3) + \sum_{i=1,2,3} \left[\kappa_i (\nabla C_i)^2 \right] \right\} dV \tag{1}$$

where f is the local free energy density of homogeneous material, C_i is the lattice volume fraction of component i, and κ_i is the gradient energy coefficient for the component i. The Flory–Huggins type of free energy is used as the bulk free energy density [32],

$$\begin{aligned} f(C_1, C_2, C_3) &= \frac{RT}{v_{site}} \left(\frac{C_1}{m_1} \ln C_1 + \frac{C_2}{m_2} \ln C_2 + C_3 \ln C_3 + \chi_{12} C_1 C_2 \right. \\ &\quad \left. + \chi_{13} C_1 C_3 + \chi_{23} C_2 C_3 \right) \end{aligned} \tag{2}$$

where m_i is the degree of polymerization of component i, T is the temperature in K, R is the ideal gas constant, χ_{ij} is the Flory–Huggins interaction parameters between two components, which is dependent on temperature, and v_{site} is the molar volume of the reference site in the Flory–Huggins lattice model.

A non-linear diffusion model is employed [33].

$$J_{i,net} = J_i - C_i \sum_{j=1,2,3} J_j \tag{3}$$

the equation to calculate the evolution rate of C_1 and C_2, the compositions of two polymers can be derived from Equations (1–3).

The time evolution of the composition of component i can be represented as [20],

$$\begin{aligned}\frac{\partial C_i}{\partial t} = {} & M_{ii}\nabla^2\left[\frac{\partial f}{\partial C_i} - \frac{\partial f}{\partial C_3} - 2\kappa_{ii}\nabla^2 C_i - 2\kappa_{ij}\nabla^2 C_j\right] \\ & + M_{ij}\nabla^2\left[\frac{\partial f}{\partial C_j} - \frac{\partial f}{\partial C_3} - 2\kappa_{ji}\nabla^2 C_i - 2\kappa_{jj}\nabla^2 C_j\right]\end{aligned} \tag{4}$$

where the subscripts i and j represent components 1 and 2, and

$$\begin{aligned} M_{ii} &= (1-\overline{C}_i)^2 M_i + \overline{C}_i^2 \sum_{j\neq i} M_j \quad i = 1,2; j = 1,2,3 \\ M_{ij} &= -\sum_{i\neq j}\left[(1-\overline{C}_i)\overline{C}_j\right] M_i + \overline{C}_i\overline{C}_j M_3 \quad i = 1,2; j = 1,2 \end{aligned} \tag{5}$$

where $\overline{C}_i$ is the average composition of component i. To simplify Equation (4), $\kappa_{ii} = \kappa_i + \kappa_3$, and $\kappa_{12} = \kappa_{21} = \kappa_3$, where κ_i is the gradient energy coefficient for component i, as shown in Equation (1).

Equation (4) is a fourth order non-linear parabolic partial differential equation. The cosine transform spectral method is applied to solve the evolution equation. The 3 dimensional numerical modeling of ternary phase separation is discussed in a previous article [27].

4. Constitutive modeling

The values of parameters implemented in the simulation are listed in Table 1. Many parameters are readily available while others were derived as follows.

4.1. Lattice volume fraction

The lattice volume fraction is the nonuniform property used in calculation of the Flory–Huggins free energy, which is related to the composition. The relation of the composition C_i and the mole fraction $C_{m,i}$, of component i is,

$$\begin{aligned} C_i &= \frac{m_i C_{m,i}}{\sum_{j=1,2} m_j C_{m,j} + C_{m,3}} \quad i = 1,2 \\ C_i &= \frac{C_{m,i}}{\sum_{j=1,2} m_j C_{m,j} + C_{m,3}} \quad i = 3 \end{aligned} \tag{6}$$

In the spin coating process, the compositions change due to the evaporation of the solvent.

4.2. Flory–Huggins interaction parameter

The Flory–Huggins interaction parameter, χ, denotes the immiscibility of different components in the blends. To induce the phase separation, the χ values of the two polymers have to be selected so that there is a free energy barrier between the immiscible polymer pairs. Since the two polymers are immiscible, the free energy increases while the solvent concentration is decreasing. In a ternary phase separation the critical value of the interaction parameter for spinodal decomposition to occur between two polymers can be estimated as,

$$\chi_{12,c} = \frac{1}{2}\left(\frac{1}{\sqrt{m_1}} + \frac{1}{\sqrt{m_2}}\right)^2 \tag{7}$$

Table 1
Parameter values in the simulation.

Parameter	Value	Unit	Comments
$M_{w,1}$	18100	g/mol	molecular weight of PS.
$M_{w,2}$	2000, 50000, 450000	g/mol	molecular weight of PAA, $M_{w,PAA}$ and $M_{w,PS}$ can alter the shape of the mixing free energy curve.
DP_1	27.78	1	Degree of polymerization of PS
DP_2	174.04	1	Degree of polymerization of PAA
δ_1	19.09	$MPa^{-\frac{1}{2}}$	Solubility parameter of PS [34]
δ_2	24.6[a]	$MPa^{-\frac{1}{2}}$	Solubility parameter of PAA [35]
$\chi_{12,critical}$	0.0360	1	Critical Flory–Huggins interaction parameter between PS and PAA
χ_{12}	0.221	1	Flory–Huggins interaction parameter between PS and PAA
χ_{13}	0	1	Flory–Huggins interaction parameter between PS and DMF
χ_{23}	0	1	Flory–Huggins interaction parameter between PAA and DMF. The Flory–Huggins interaction parameter determine the compatibility of the species.
$w_{polymer}$	3	%	Weight percentage of homopolymers in the solution
$w_1 : w_2$	30:70, 50:50, 70:30	%	Weight ratios of PS and PAA polymers
$W_1 : W_2$	467:200, 700:300, 933:400	nm	Width of functionalized strips. W_{PS} and W_{PAA} represent the strips attractive to PS and PAA, respectively.
t_e	30	s	Time of evaporation
D_3	5×10^{-13}	m^2/s	Diffusivity of PAA and PS monomers, and DMF
$\lvert s_1\rvert$	4.82×10^3	$J/(m^2)$	Magnitude of the functionalized substrate surface energy for PS, the sign is alternating along the direction normal to the substrate pattern strips.
$\lvert s_2\rvert$	4.82×10^3	$J/(m^2)$	Magnitude of the functionalized substrate surface energy for PAA, the sign of s_2 is opposite to s_1.
$M_1, M_2, and M_3$	3.63×10^{-21}	$m^5/(J\cdot s)$	Mobility of PS and PAA monomers, and DMF
v_{site}	1.80×10^{-5}	m^2	Lattice volume
a	6.3×10^{-8}	m	Monomer size [36]
$\kappa_1, \kappa_2, and \kappa_3$	1.821×10^{-7}	J/m	Gradient energy coefficients of PS and PAA monomers, and DMF
$L_x \times L_y \times L_z$	$4 \times 2 \times L_Z$	μm	Real modeling dimensions, where L_z changes during evaporation.

[a] The value of solubility parameter for PAA is considered to be close to that of acrylic acid [37].

The Flory–Huggins interaction parameter for a real polymer blend is difficult to measure. In the phase separation of a polymer-polymer-solvent ternary system, the solubility of the polymers in the solvent are much higher than the solubility of the polymers to each other [35]. Therefore, the interaction parameters between the solvent and two polymers are set to be 0. The interaction parameter between two polymers is estimated by the following equation [32],

$$\chi_{12} = \frac{v_{site}(\delta_1 - \delta_2)^2}{RT} \tag{8}$$

where δ_1 and δ_2 are the solubility parameters of PS and PAA. Their values are listed in Table 1. The interaction parameter, χ_{12}, can be calculated as 0.22, which satisfies the requirement, $\chi_{12} > \chi_c$.

4.3. Solvent evaporation constant

The effects of solvent evaporation were studied. In the experiments, the thickness of the concerning domain is very thin compared to the width and length. Since the solvent is equally absolutely miscible to the two polymer components, the solvent concentration is considered to be uniform through the depth of the film. The decrease of the average solvent composition in the three dimensional area was shown to obey the relation as follows [38],

$$C_{m,3,t} = C_{m,3,0}e^{-\alpha t} \tag{9}$$

where $C_{m,3,t}$ is the mole fraction of the solvent in time t, $C_{m,3,0}$ is the initial solvent amount, α is a constant, and t is time. The thickness decrease due to the evaporation of the solvent is also captured in the numerical simulation.

The evaporation constant, α, is determined by measuring the thickness change during the spin coating. The thickness of the film before the spin coating is measured at 3 s to exclude the spin off effect at the beginning of the spin. The thickness is determined by dividing the weight of the sample at 3 s by the template area. The weight of the sample is obtained by subtracting the empty template weight from the template weight with sample loaded. The final thickness was measured by contact mode atomic force microscopy immediately after the completed spin coating stage (30 s). The solvent evaporation constant, α, can then be calculated by substituting the start and final film thicknesses into Equation (9). The measurements and the calculated κ values for different spin coating speeds are listed in Table 2. It can be seen that the evaporation rate increases with the spin speed as expected due to increased convection.

4.4. Gradient energy coefficient

The gradient energy coefficient, κ, denotes the magnitude of the influence of composition on the total free energy. The higher the value of κ, the greater the composition gradient will affect the total free energy, and as a result the thicker the interface between phase domains, and *vise versa*. The gradient energy coefficient can be estimated using the random phase approximation [39].

$$\kappa_i = \left(\frac{RTa^2}{3v_{site}}\right) i = 1,2,3 \tag{10}$$

where a is the monomer size. The contribution of short range van der Waals force to κ_i is neglected in this study, since in polymers the short range intermolecular force is $\frac{1}{N}$ smaller than the inner-molecular effects [16]. The gradient energy coefficient κ_{11} and κ_{22} are assumed to be equal in this simulation [40]. The diffusivity, D, is estimated as $1\times10^{-13} m^2/s$, and $1\times10^{-10} m^2/s$ for polymers and small molecule solvent, respectively. These are typical values for diffusivities [22,41–44].

4.5. Mobility

The mobility, M, is a measurement on the speed of transport of the mass during phase separation. The mobility of the system can be evaluated with the relation [45],

$$M_i = \frac{Dv_{site}}{RT} \tag{11}$$

Table 2
Estimation of the evaporation constant.

Rotation Speed	$L_{z,t=3s}$	$L_{z,t=30s}$	Initial thickness, $L_{z,t=0s}$	Evaporation constant, α
1000 rpm	1.819×10^{-5} m	1.572×10^{-7} m	1.949×10^{-5} m	0.821
3000 rpm	7.561×10^{-7} m	1.346×10^{-7} m	1.6863×10^{-5} m	1.098
7000 rpm	5.337×10^{-7} m	1.029×10^{-7} m	1.2893×10^{-5} m	1.130

4.6. Substrate functionalization

The substrate functionalization in the experiments is summarized in Table 3. The PS/PAA polymer pair is dissolved in DMF and spin coated on the substrate chemically patterned with NH_2 and ODT. One type of functionalized surface will attract one type of polymer and meanwhile repel the other type of polymer. In numerical simulation, the additional term representing the surface energy on the blend–substrate interface is treated as a linear function with the concentrations of C_1 and C_2 [46,47].

$$f_s(C_1, C_2, \mathbf{r}) = s_1(\mathbf{r})\left(C_1 - C_{1,ref}\right) + s_2(\mathbf{r})\left(C_2 - C_{2,ref}\right) + s_0(\mathbf{r}) \tag{12}$$

where $s_0(\mathbf{r})$, $s_1(\mathbf{r})$, and $s_2(\mathbf{r})$ are functions of the coordinate vector on the substrate. $C_{i,ref}$ are arbitrary reference compositions. For simplicity $C_{i,ref}$ are selected as 0, and $s_0(\mathbf{r})\equiv 0$. $s_1(\mathbf{r})$, and $s_2(\mathbf{r})$ are tuned so that there are alternating attraction forces to the different type of polymers on the strips of the functionalized substrate. To qualitatively depict the functionalization of the substrate, the values of s_1 and s_2 are set with opposite signs to alternate around zero across the x direction. Therefore $s_1 = -s_2$ and the absolute values are referred to as $|f_s|$ in this paper. As such, s_1 and s_2 represent the experimental condition that one type of functionalization on the surface will attract one polymer and repel the other.

The values for gradient energy coefficient, mobility and the spacial surface energy coefficients, $|f_s|$, are not accurately determined theoretically. More sophisticated methods such as molecular dynamic simulation have to be applied to achieve the accurate values of these parameters. The details of the parameter estimation process will be discussed in a following section.

5. Result assessment methods

Numerical methods are introduced to validate the numerical and experimental result morphology.

5.1. Characteristic length, R

The characteristic length, R, represents the average domain size of the morphology. To measure the R value of the simulation result, the pair-correlation function g_i is calculated with Equation 13

$$g_i = \frac{1}{N_j}\sum_{k_j=1}^{N_j} g_{i,k_j}(d,t) \tag{13}$$

where $g_{i,k_j}(d,t)$ is defined as,

$$g_{i,k_j}(d,t) = \langle \psi(\mathbf{k} = (k_i,k_j),t)\psi(\mathbf{k} = (k_i,k_j+d),t)\rangle \tag{14}$$

and $\psi(\mathbf{k},t)$ is the order parameter which equals to the composition difference of the two polymers on the $\mathbf{k}$ th grid node, and d is a positive variable that varies from 1 to $k_{i.}$ The angle brackets denote the average value of the expression inside the brackets over all the lattice nodes. The characteristic length in the i th dimension, $R_i(t)$ is the value of d when g_i first time changes the sign from positive to negative.

Table 3
Substrate functionalization.

Polymer	Attracting/Repelling forces	Funcionalization groups	
		NH_2	ODT
PS	Hydrophobic	4.82 kJ/m^2	−4.82 kJ/m^2
PAA	Negative static electrical force	−4.82 kJ/m^2	4.82 kJ/m^2

The characteristic domain length of the experiment result patterns is measured from AFM topography images by Fourier transfer analysis. The 5μm AFM images and Fourier transform diagrams of different spin coating rotation speeds are shown in Fig. 1. The radius of the intensified ring in the FFT image represents the inverse of the characteristic length of the original image. Therefore in the FFT image, the larger the radius of the intensified ring, the smaller the characteristic length in the original image.

The R values are measured from the experiment pattens on different spin coating speed, as shown in Fig. 1.

5.2. Commensurability index, C_s

Usually the phase separated morphology is not perfectly compatible with the desired shape. To investigate the quality of the phase separation according to the substrate patterns, a commensurability index, $C_{s,}$ is introduced to quantitatively measure the compatibility of the morphology to the substrate patterns. C_s is defined as:

$$C_s = \frac{1}{2}\langle|\psi(\mathbf{k}) - S_k|\rangle \tag{15}$$

and,

$$S_k = \begin{cases} \frac{s_1(\mathbf{k})}{|s_1(\mathbf{k})|}, & s_1(\mathbf{k}) \neq 0 \\ 0, & s_1(\mathbf{k}) = 0 \end{cases} \tag{16}$$

where $s_1(\mathbf{k})$ is the parameter in the surface energy expression for polymer one, which denotes the strength of the surface attraction. S_k is the quantitative representation of the substrate attraction. Obviously,

$$C_s \in [0, 1] \tag{17}$$

A greater value of C_s implies the phase separated morphology is more compatible to the substrate pattern. When C_s equals 1, it shows that the result pattern replicates the substrate pattern exactly. Meanwhile C_s equal to 0.5 represents random phase separation, and C_s equal to 0 denotes a totally opposite phase pattern as designed by the substrate pattern.

6. Determination of κ, *M*, and $|f_s|$

An optimization process is employed to determine the remaining undefined parameters. First the gradient energy coefficient, κ, and mobility, *M*, are varied to match the characteristic length, *R*, to the *R* value of AFM image of experiment results on spin speed 3000 rpm. The AFM image can be seen in Fig. 1. To solve the problem, optimization method is used. To tune the two parameters concurrently, a least square optimization of κ and *M* values are illustrated in Fig. 2 and Fig. 3. The *M* and κ are determined to be $3.633\times10^{-21}\mathrm{m}^5/(\mathrm{J}\cdot\mathrm{s})$ and $1.821\times10^{-7}\mathrm{J/m}$, respectively.

It can be seen that when other parameters are unchanged, the characteristic length of the domain increases with the increasing gradient energy coefficient. This result is in accord with Equation (1), from which it can be seen that the gradient energy coefficient, κ, denotes the influence of the gradient to the free energy. Since the system intrinsically minimizes the free energy, the larger the value of κ, the smaller the composition gradient and the smaller the interface area the system is able to resist in a stable state. Therefore the domain size tends to be larger with smaller composition gradient and thicker interface. Meanwhile, the higher the mobility, *M*, the faster the small molecules and the monomers can

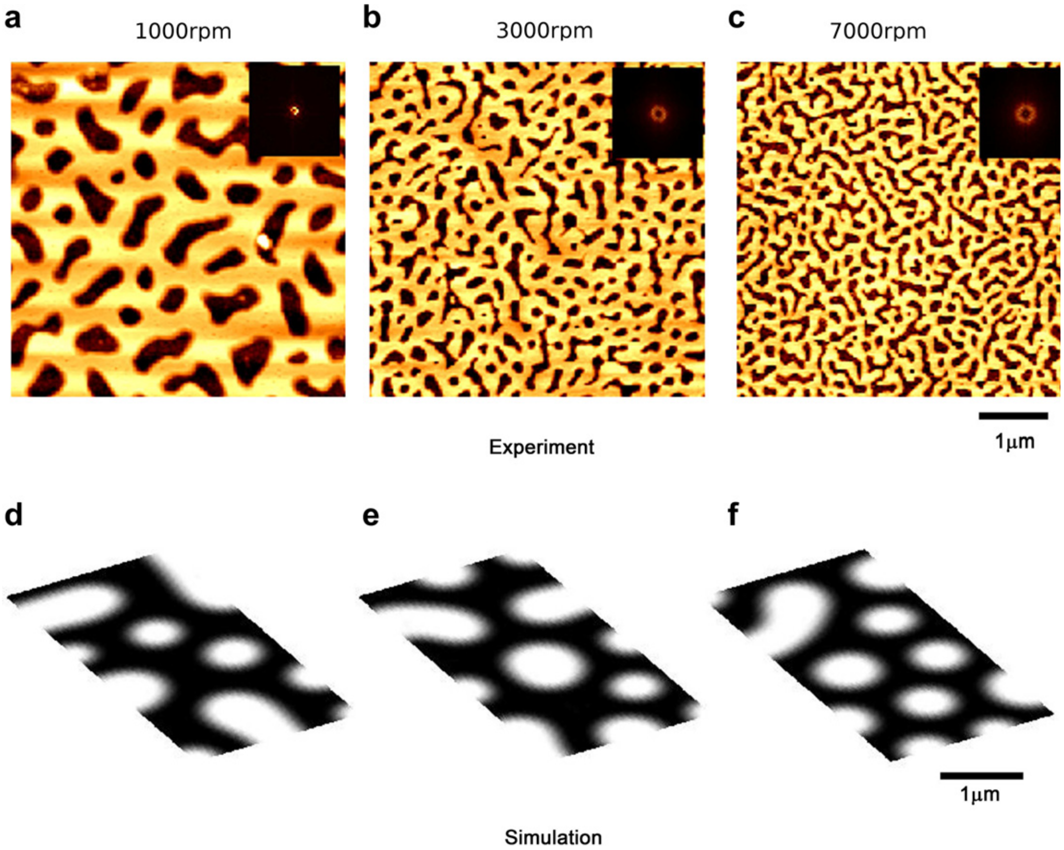

Fig. 1. AFM images of experimental patterns and the Fourier transform diagrams of different rotation speed.

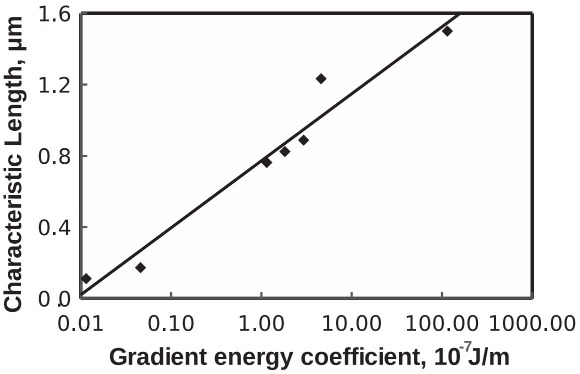

Fig. 2. The change of the characteristic length with the gradient energy coefficient, κ_{12}, in 3000 rpm spin coating rotation speed and mobility is $3.633\times10^{-21}\mathrm{m}^5/(\mathrm{J}\cdot\mathrm{s})$.

diffuse to the desired position, and the faster the domain pattern grows. Thus the higher mobility of the system results in a higher domain size.

After the numerical model is benchmarked in this system, the magnitude of the surface functionalization, f_s, in numerical simulation can be determined. Different $|f_s|$ values are implemented in a series of numerical tests. The C_s value from the numerical simulation with different f_s values are plotted in Fig. 4. The composition ratio PS:PAA = 70:30 and pattern strip width ratio is ODT: NH_2 = 700 nm:300 nm. The x axis value in the plot is the absolute value of f_s, as show in Fig. 4.

It can be seen that the compatibility of the morphology increases with the value of $|f_s|$ exponentially. By comparing to the experimental results with different conditions, the value of $|f_s|$ is estimated to be $4.82\times10^3\mathrm{J/m}^2$. The values with signs of the surface energy are listed in Table 3.

7. Non-dimensionalization

The parameters in the equation are non-dimensionalized. The original values are divided by characteristic values to vanish the units. The characteristic length and time are chosen as follows,

$$\begin{aligned} L_c^2 &= \frac{\kappa\nu_{site}}{RT} \\ t_c &= \frac{L_c^2\nu_{site}}{M_cRT} \end{aligned} \tag{18}$$

where M_c is the characteristic mobility for non-dimensionalization. Other characteristic parameters can be derived from Equation (4) and Equation 18, as listed in Table 4.

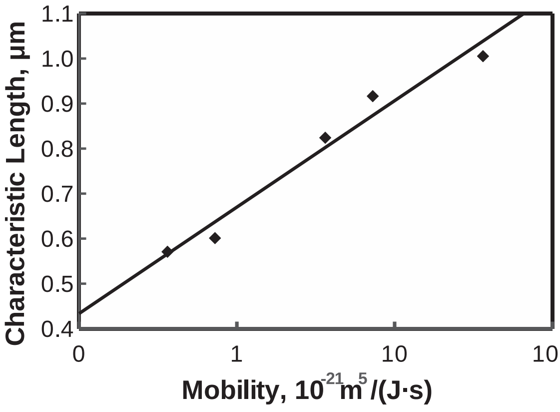

Fig. 3. The change of the characteristic length with the mobility, M_{12}, in 3000 rpm spin coating rotation speed and gradient energy coefficient is $1.821\times10^{-7}\mathrm{J/m}$.

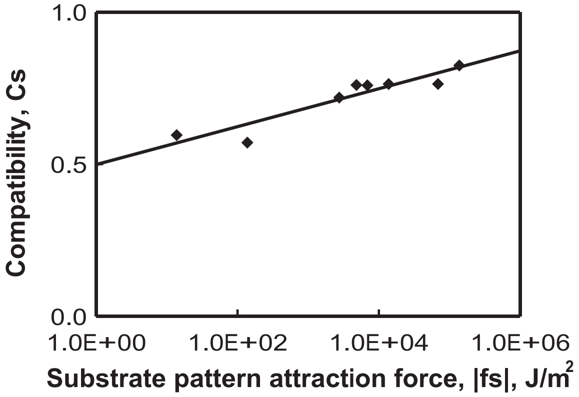

Fig. 4. Attraction force effects on the compatibility, C_s.

Table 4
Non-dimensionalization of parameters.

Characteristic variable	Expression
L_c^2	$\frac{\kappa\nu_{site}}{RT}$
t_c	$\frac{L_c^2\nu_{site}}{M_cRT}$
f_c	$\frac{RT}{\nu_{site}}$
κ_c	$\frac{RTL_c^2}{\nu_{site}}$
M_c	M_{11}

8. The MATLAB GUI software

A program with a graphical user interface (GUI) is developed in MATLAB for numerical simulation of self-assembly of polymer blends phase separation [49]. The program provided an efficient simulation engine to investigate the morphology evolution, which allows this computationally intensive task to be completed on a PC. In addition, the user can easily change the functionalized surface, material, and environment parameters from the user interface components, and analyze the results. This software has been made available through the Matlab Central file exchange [48].

9. Results and validation

A 128 × 64 × 16 finite element model in three dimensions is established to investigate the composition profile. The physical dimension of the slab before non-dimensionalization is also listed

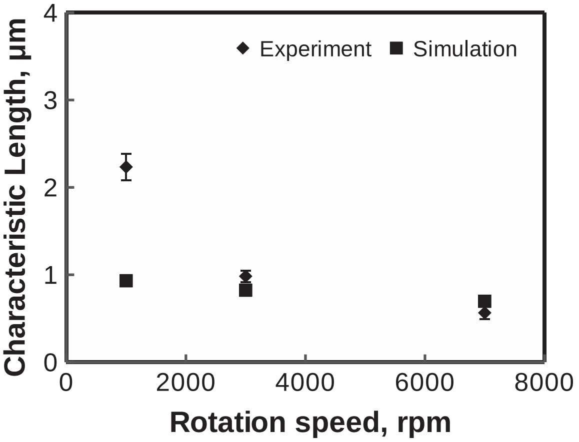

Fig. 5. Comparison of the characteristic length of simulation and experimental patterns in different rotation speeds.

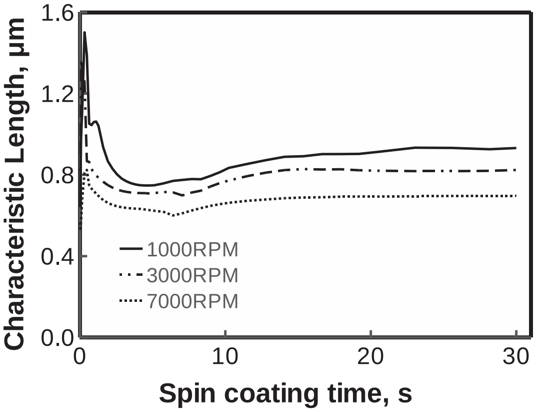

Fig. 6. Evolution of the characteristic length with time in different rotation speed.

in Table 1. After all the parameters are determined based on the experimental conditions, the effects of different processing conditions are investigated in the established numerical model. The numerical results are compared with the experimental results.

9.1. Spin speed

After the parameters are determined, the phase separation with the effects of solvent evaporation at different spin coating rotation speeds are investigated. Fig. 1 a–c shows NCM-AFM topography images of PS/PAA phase separated morphologies at different spin speeds on a neutral substrate. The bright/dark areas in the images corresponded to the PS/PAA regions. Smaller coarsening behaviors of polymer blends during spin coating were time-dependent. With increasing spin speed, less time was allowed for PS/PAA macromolecules to move during phase separation due to faster solvent evaporation. Therefore, more refined morphology was produced in higher spin speed. Fast Fourier Transform (FFT) was used to calculate the characteristic length of the domain from AFM images. The FFT images are shown at the upper-left corner of the original AFM images. The larger radius of the most intense ring in the FFT images denotes a smaller average domain size from the AFM images. It can be seen in Fig. 5 that the characteristic length of the domain, *R*, decreases when the rotation speed increases. Fig. 1 d–f shows the behavior of the simulation results with increasing rotation speed. The solvent evaporation constant, α, in different spin speeds are implemented in the numerical simulation. Similar to the experiment results, the higher spin speed also produces a smaller *R*. The characteristic length of the simulation results are also shown in Fig. 5. It can be seen that though in both of experiment and simulation results the *R* value decrease with increasing spin speed, the *R* value decreases faster with increasing spin speed in experimental results. The slight differences between the simulation and experiment results may due to the homogeneity assumption of the evaporation model. The inaccuracy of measurements on the film thickness may also introduce inaccuracy to the estimation of α values. The effects of spin speed can be better simulated by implementing a more sophisticated evaporation model and improve the measurements of the film thickness.

In numerical simulation the evolution of the morphology during the solvent evaporation can be investigated, as can be seen in Fig. 6. The spin coating rotation speed affects the rate of evaporation. A higher rotation speed in spin coating results in a faster evaporation of the solvent and thus a thinner film. It can be observed that the characteristic length stables after the surge in early stage. In the later stage, the morphology evolutes slowly and the characteristic length increases moderately. This process during solvent evolution was also investigated in our previous work [26]. It can also be seen that the aggregated domains grow slower in condensed solutions than in diluted solutions.

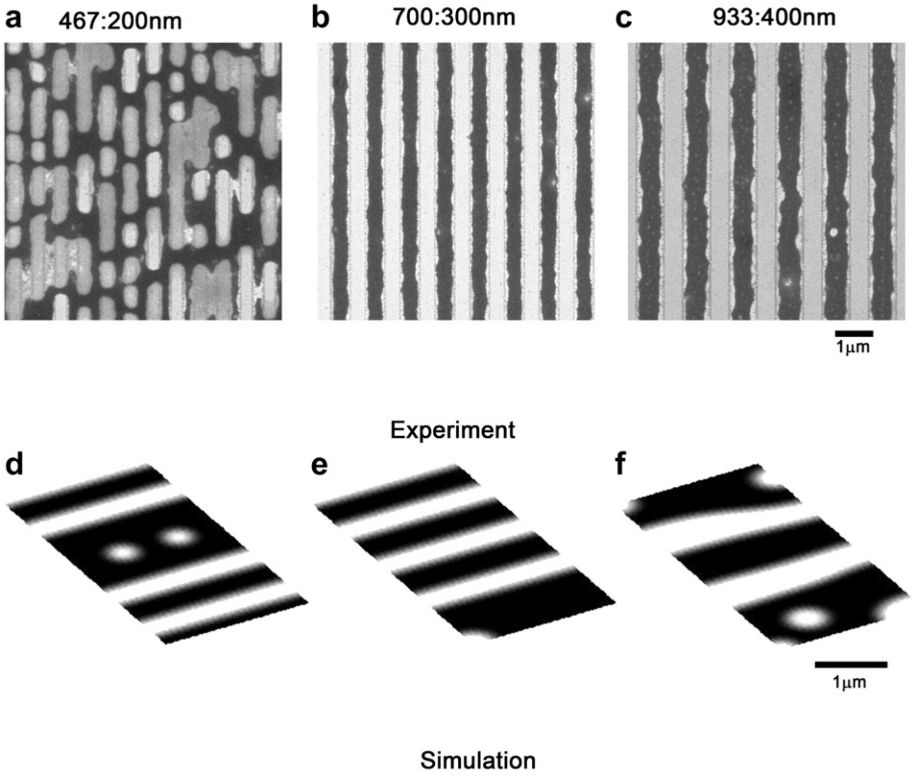

Fig. 7. Phase separation on different pattern strip width. ODT:MUAM. a,b,c – FESEM images from the experimental results; d,e,f – images from the simulation results.

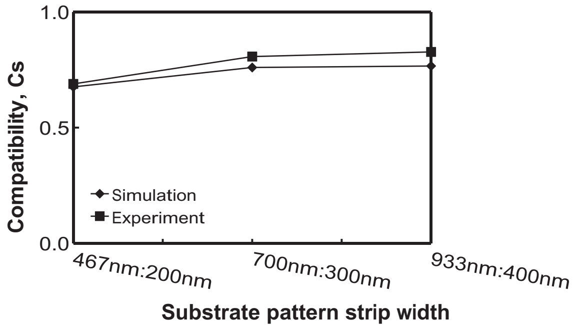

Fig. 8. C_S change with the pattern strip width.

9.2. Pattern periodicity

Experimental and simulation results both show that when intrinsic characteristic length is commensurate with the strip pattern periodicity, a well-order pattern replication is formed. To investigate the influence of the pattern strip width on the results, the PS/PAA/solvent blend is spin coated in 3000 rpm on substrate with patterns of different pattern strip width.

Three pattern sizes are investigated in experiments and simulation—ODT:MUAM = 467 nm:200 nm, 700 nm:300 nm, 933 nm: 400 nm. Fig. 7 shows the FESEM images of PS/PAA self-assembly on chemically patterned substrate with various pattern periodicity. During the morphology evolution, PS molecules agglomerate on hydrophobic ODT patterns while PAA molecules assemble on hydrophilic MUAM patterns. The polymer blends have their intrinsic *R* values without the presence of the pattern. Therefore in order to produce a well-ordered result morphology, the pattern periodicity should be compatible with the intrinsic *R* values. As shown previously, the characteristic length, *R*, from spin speed 3000 rpm is 829 nm in experiment, which is between the pattern in the size 467 nm:200 nm and 700 nm:300 nm. When the substrate pattern is smaller than the intrinsic characteristic length of the blend, the agglomerates of the polymers can not be confined within the attractive pattern strips. The strip-like structures in the morphology of the polymer blends will be interrupted by the intrinsic interaction forces within the polymer, which can be seen in Fig. 7 a and d, for experiment and simulation results, respectively. Though the 700 nm:300 nm and 433 nm:900 nm patterns have a greater alternative pattern width than the intrinsic *R* of the polymer blends, the polymer can still be aligned and spread over the corresponding pattern strip. The striped pattern of the phase separation morphology remains continuous though not perfectly aligned with the underlying substrate pattern, which can be seen in Fig. 7 b, c for experiment results and e, f for simulation results. Therefore on the 700 nm:300 nm and 933 nm:400 nm patterns the compatibility coefficients, $C_{S,}$ is higher than that on the 467 nm:200 nm pattern. In both the experiment and simulation results, the polymer blend morphology on 933 nm:400 nm pattern has a slightly higher C_S value than that on 700 nm:400 nm pattern, though the difference is subtle, which is shown in Fig. 8. Besides the characteristic length, other factors such as the ratio of each polymer types in the blend, the functionalization on the substrate, and the immiscibility of the polymer blends may also affect the

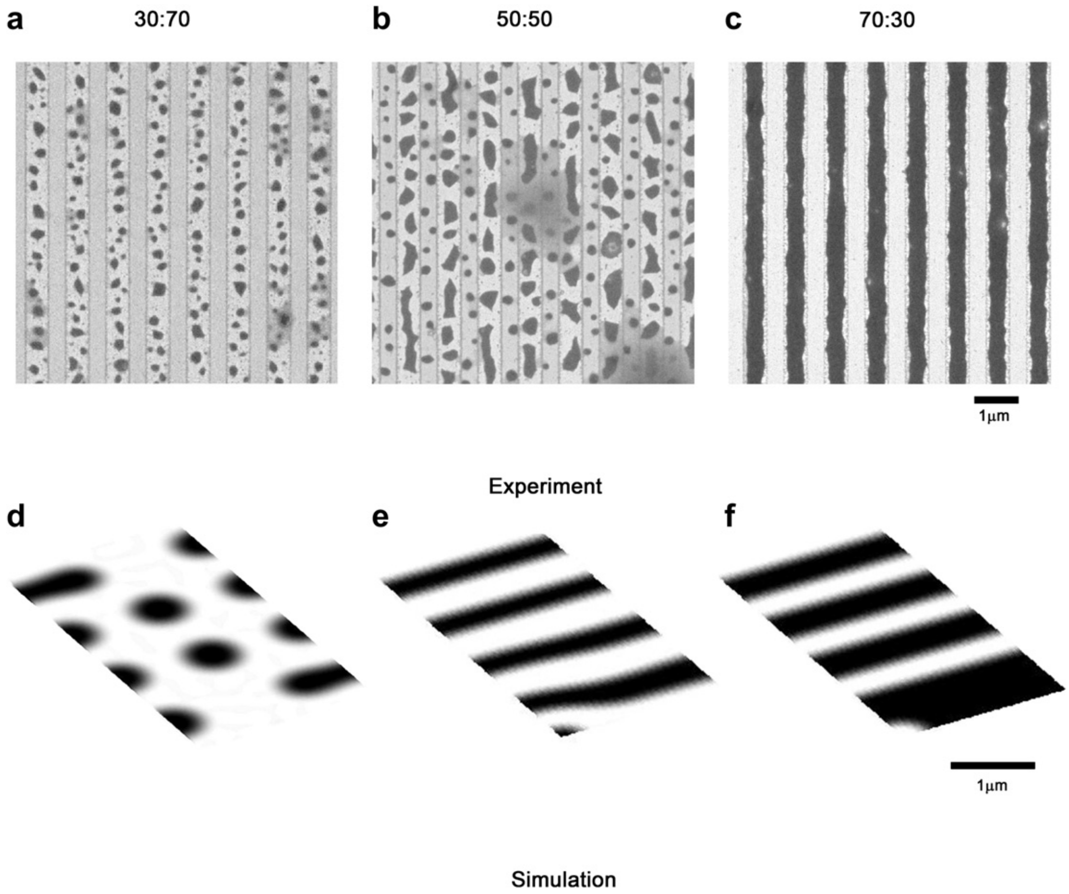

Fig. 9. Phase separation morphology in different polymer weight ratios, PS:PAA. a,b,c – FESEM images from the experimental results; d,e,f – images from the simulation results.

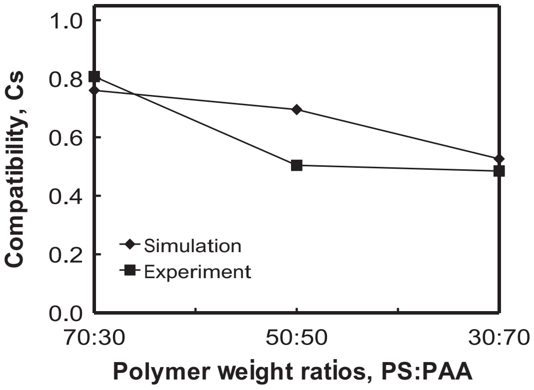

Fig. 10. C_S change with the polymer weight ratio.

self-assembly. These factors can be further investigated in simulation to determine the preferred pattern periodicity for specific self-assembly processes.

9.3. PS:PAA weight ratio

The SEM images of the phase separated patterns with different PS:PAA weight ratios are shown in Fig. 9 a–c. It can be seen that in the simulation, the solution with a weight ratio PS:PAA = 70:30 has the highest C_s value, as shown in Fig. 9c. The numerical simulation results with various PS:PAA weight ratio produce similar results to experiment, as shown in Fig. 9d–f. The strip width is ODT:MUAM equals to 700 nm:300 nm.

To generate a designed morphology according to the pattern, the PS:PAA ratio has to be compatible with the ODT:MUAM area ratio, so that the polymers can cover the respective areas of the pattern having the correct attractive force. It can be seen from the FESEM images that when the PS:PAA ratio is small, the PS polymer can not form a continuous structure. The PS agglomerates in dots among continuous PAA domains and the PS dots are aligned along the strips, which can be seen in Fig. 9 a and d. When the PS weight ratio increases, the PS agglomerates grow and turns more continuous. Due to a smaller concerning domain, the numerical result shown in Fig. 9 e only shows the continuous part. The polymer blend with PS:PAA ratio of 70:30 produces the highest C_s value. In Fig. 9c and f, it can be seen that after phase separation PS and PAA covered areas are both continuous. The polymer weight ratio is commensurate with the ratio of different functionalization pattern areas. The C_s values increase when the PS:PAA weight ratio increases from 30:70 to 70:30, as can be seen in Fig. 10. The simulation results represent the increase of C_s value when PS:PAA ratio increases, though there is a noticeable difference between experimental and simulated C_s value when PS:PAA equals 50:50. This may due to the confined model domain in simulation which is not large enough to represent the experimental morphology statistically.

9.4. PAA molecular weight

The effect of the molecular weight of PAA is studied. The molecular weight affects the thermodynamics and kinetics of the phase separation. The Flory–Huggins type of local free energy can be affected by the molecular weights of the polymers. The free energy barrier of two pure polymer phases is higher with higher molecular weight. Therefore the polymers with higher molecular weights are less compatible with each other, which will result in a sharper interface between different polymer domains. The M_w of PAA 2 kDa, 50 kDa, and 450 kDa are implemented in both

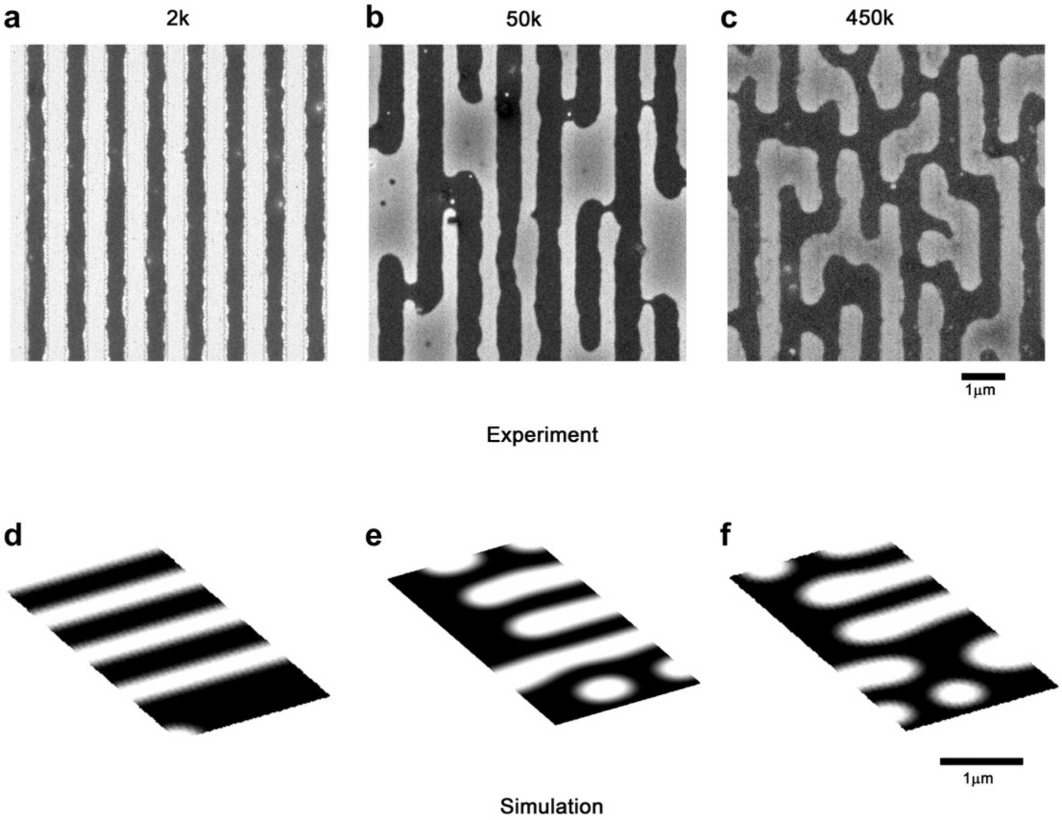

Fig. 11. Phase separation morphology with different PAA molecular weight. a,b,c – FESEM images from the experimental results; d,e,f – images from the simulation results.

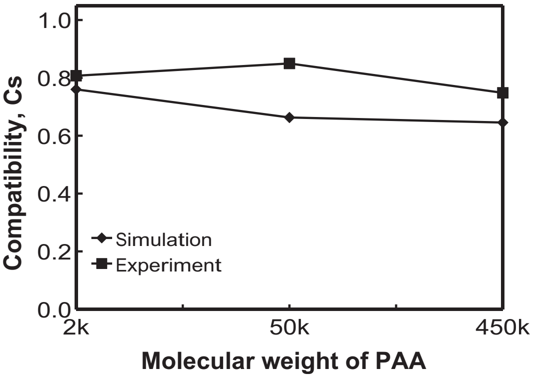

Fig. 12. C_s change with different PAA molecular weight.

experiments and simulation. Domain coarsening of PS/PAA is facilitated by increasing mixing energy of PS and PAA, therefore when the PAA M_w increases from 2 kDa to 50 kDa the characteristic length will increase. When the PAA M_w increases from 50 kDa to 450 kDa, the system viscosity increases with polymer chain length, so that the characteristic length will not change significantly.

Fig. 11a–c show the FESEM images of substrate pattern directed phase separation of PS/PAA blends with different PAA M_w values whereas the pattern periodicity keeps constant at ODT:MUAM = 700 nm:300 nm. The well formed morphology can be seen in Fig. 11 a when PAA M_w equals 2 kDa. Although the PS polymer domain is aligned with the underlying attractive pattern, the width of the polymer strip is smaller than the underlying strip, which make the C_s value smaller. When the PAA M_w increases to 50 kDa, it is observed that the average domain size increases. The polymer strip patterns is interrupted, while the width of the PS polymer strip is as wide as the underlying substrate pattern strip. Further increase in the PAA M_w to 450 kDa can not change the characteristic length significantly, but the increase in viscosity will confine the movement of the molecules to the thermodynamically favorable area, thus the C_s value decreases slightly with PAA $M_w = 450$ kDa.

Fig. 11d–f show that the simulation results generally replicate the PAA M_w influence on experiment results. As shown in Fig. 11e, a less ordered self-assembly is found when the M_w of PAA is increased to 50 kDa. More discontinuous patterns are found when M_w of PAA is further increased to 450 kDa, which matches the experimental results. The C_s value changes with PAA M_w can be seen in Fig. 12. In the simulation results the C_s value decreases with increasing PAA $M_{w.}$ Whereas in the experiment results, the C_s value with PAA $M_w = 50$ kDa is higher than that with PAA $M_w = 2$ kDa. Though the pattern is disordered due to increased characteristic length, the width of the self-assembled polymer patten strip is compatible with the underlying substrate pattern strip, which compensates the effects of the disordered morphology.

10. Conclusions

A 3 dimensional numerical model of self-assembly with a polymer-polymer-solvent system is established. The Cahn–Hilliard equation is implemented in the numerical simulation and the Flory–Huggins free energy equation is employed as the local free energy. The simulation parameters are obtained from the experiments of self-assembly by spin coating PS-PAA-DMF solvent phase separation on a heterogeneously functionalized patterns. Parameters which are difficult to characterize, such as the gradient energy coefficient, mobility, and the surface energy are obtained by matching the simulation and experimental results using an optimization method. The simulation can then quantitatively simulate the main effects of various process conditions and material properties as validated by experimental observations.

The characteristic length of the pattern is calculated and a compatibility parameter is introduced to evaluate the result morphology. The effects of evaporation are also included in the numerical simulation. The effects of processing parameters such as the pattern strip width ratio, the polymer weight ratio, and the PAA molecular weight are investigated both numerically and experimentally. From both the experiment and simulation results, the characteristic length, R, of the morphology will increase when the spin speed is increased. To obtain a well-ordered morphology according to the functionalized substrate pattern, the characteristic length should be compatible with the pattern periodicity. The weight ratio of PS:PAA in the polymer blend should also be compatible with the corresponding area ratio of ODT:MUAM to produce a favorable morphology pattern. The molecular weight of the polymer will affect the intrinsic characteristic length, such that a higher polymer molecular weight will increase the viscosity of the blends to thereby decrease the C_s value.

Acknowledgment

The authors appreciate the financial support from the National Science Foundation to this research (grant number NSF-0425826), and all the people and agencies that contribute to this work.

References

[1] Fink Y, Winn JN, Fan S, Chen C, Michel J, Joanopoulos JD, et al. Science 1998;282:1679–82.
[2] Jones RAL, Norton LJ, Kramer EJ. Phys Rev Lett 1991;66:1326–9.
[3] Jones RAL, Kramer EJ, Rafailovich MH, Sokolov J. Phys Rev Lett 1989;62:280–3.
[4] Puri S, Frisch HL. J Phys. Condens Mat 1997;9:2109–33.
[5] Brown G, Chakrabarti A. Phys Rev 1992;A 46:4829–35.
[6] Seok C, Freed KF. J Chem Phys 2000;112:6443.
[7] Winesett DA, Ade H, Sokolov J, Rafailovich M, Zhu S. Polym Int 2000;49: 458–62.
[8] Venugopalt G, Krause S. Macromolecules 1992;25:4626–34.
[9] Karim A, Douglas JF, Lee BP, Glotzer SC, Rogers JA, Jackman RJ, et al. Phys Rev E 1998;57:6273–6.
[10] Wang H, Composto RJ. Macromolecules 2002;35:2799–809.
[11] Cyganik P, Bernasik A, Nudkowski A, Bergues B, Kowalski K, Rysz J, et al. Surf Eng Surf Inst Vac Tech 2001;63:307–13.
[12] Cui L, Zhang Z, Li X, Han Y. Polym Bull 2005;55:131–40.
[13] Boltau M, Walheim S, Mlynek J, Krausch G, Steiner U. Nature 1998;391:877–9.
[14] Walheim S, Boltau M, Mlynek J, Krausck G, Steiner U. Macromolecules 1997; 30:4995–5003.
[15] Cahn JW. J Chem Phys 1959;30:1121–4.
[16] Cahn JW, Hilliard JE. J Chem Phys 1958;28:258–67.
[17] Scott RL. J Chem Phys 1949;17:279–84.
[18] Hsu CC, Prausnitz JM. Macromolecules 1973;7:320–4.
[19] Chen L-q. Acta Matall Mater 1994;42:3503–13.
[20] Huang C, Cruz M O d l, Swift BW. Macromolecules 1995;28:7996–8005.
[21] Altena FW, Smolders CA. Macromolecules 1982;15:1491–7.
[22] Zhou B, Powell A. J Membr Sci 2006;268:150–64.
[23] Tong C, Zhang H, Yang Y. J Phys Chem B 2002;106:7869–77.
[24] He DQ, Nauman EB. J Polym Sci Pol Phys 1997;35:897–907.
[25] Muthukumar M, Ober CK, Thomas EL. Science 1997;277:1225–32.
[26] Shang Y, Kazmer D, Wei M, Mead J, Carol B. J Chem Phys 2008;128.
[27] Shang Y, Kazmer D, Wei M, Mead J, Barry C. Poly Eng Sci 2010;50:2329–39.
[28] Wei M, Fang L, Lee J, Somu S, Xiong X, Barry C, et al. Adv Mater 2009;21: 794–8.
[29] Krausch G. Mater Sci Eng 1995;14:1–94.
[30] Cahn JW. Adv Funct Mater 1961;9:795–801.
[31] Cahn JW. J Chem Phys 1965;42:93–9.
[32] Flory PJ. Principles of polymer chemistry. Ithaca, NY: Cornell University Press; 1953.
[33] Kramer EJ, Green P, Palmstrom C. Polymer 1984;25:473–80.
[34] Shvarts AG. Kolliodn, Zh 1956;18:755.
[35] Brandrup J, Immergut EH, Grulke EA, Abe A, Bloch DR, editors. Polymer handbook. 4th ed. John Wiley & Sons; 2003.
[36] Wise S.M. Diffuse interface model for microstructural evolution of stressed, binary thin films on patterned substrates. Ph.D. thesis: University of Virginia; 2003.
[37] Yu Y, Zhang L, Eisenberg A. Macromolecules 1998;31:1144–54.
[38] Bornside DE, Macosko CW, Scriven LE. J Appl Phys 1989;66:5185.
[39] Gennes P G d. J Chem Phys 1980;72:4756–63.

[40] Saxena R, Caneba GT. Poly Eng Sci 2002;42:1019.
[41] Bartels CR, Crist B, Graessley WW. Macromolecules 1984;17:2702–8.
[42] Tsay CS, McHugh AJ. J Polym Sci Pol Phys 1990;20:1327–65.
[43] Chen L-P, Lin D-J, Shih C-H, Dwan A-H, Gryte CG. J Polym Sci Pol Phys 1999;37:2079–92.
[44] Kim YD, Kim JY, Lee HK, Kim SC. J Membr Sci 2001;190:69–77.
[45] Wheeler AA, Boettinger WJ, McFadden GB. Phys Rev E 1993;47:1893–909.
[46] Jones RAL. Phys Rev E 1993;47:1437–40.
[47] Johnson WC, Wise SM. Appl Phys Lett 2002;81:919–21.
[48] Simlation software for self-assembly of polymer blends, http://www.mathworks.com/matlabcentral/fileexchange/28170-simlation-software-for-self-assembly-of-polymer-blends; 2010.
[49] Y. Shang, D. O. Kazmer, Int J Comput Aided Eng Tech, accepted for publication.

Polymer 52 (2011) 1458–1468

Contents lists available at ScienceDirect

Polymer

journal homepage: www.elsevier.com/locate/polymer

Structure of polymer–acid complexes in solution and crystal-solvate phases of rigid-rod heterocyclic polymer - poly(p-phenylene benzobisoxasole)

N.V. Lukasheva*

Institute of Macromolecular Compounds, Russian Academy of Sciences, Bol'shoi pr. 31, St. Petersburg 199004, Russia

A R T I C L E I N F O

Article history:
Received 1 November 2010
Received in revised form
8 January 2011
Accepted 10 January 2011
Available online 31 January 2011

Keywords:
Polyelectrolites
Polymer–acid complexes
Rigid-rod polymers

A B S T R A C T

Investigations of the structures of the complexes formed by di-protonated oligomer molecules of poly (p-phenylene benzobisoxasole) (PBO) with charged and neutral molecules of orthophosphoric acid (OPA) by quantum-chemical and molecular mechanics methods are described. The complexes with partially compensated, fully compensated, and overcompensated PBO molecular charges as models of the polymer–acid complexes in solution and in crystal-solvate phases (Phase I and Phase II) are considered. It is shown that the structures with one anion associated with two heterocycles are most energetically favorable for the complexes with a partially compensated polycation charge. The polymer molecule bending resulting from this association can contribute to an enhanced PBO chain flexibility in solution. The PBO chains in Phase I are protonated due to the presence of neutral acid molecules. The protonated state of the PBO molecules in Phase II can be explained by the presence of excess anions.

1. Introduction

Rigid-rod polymers attract considerable attention because of their high tensile modulus and strength, high thermal/oxidative stability and environmental resistance, and their third order nonlinear optical properties [1]. Rigidity and the regularity of the molecular structure along the chain render these polymers processable only from solutions in strong protonating acids. Protons from the acids can be bound to definite atoms of the polymer molecules. Protonation is a precondition to dissolution. Polymers are solubilized by repulsive Coulombic interactions caused by polymer chain protonation. The resulting polyelectrolyte solution consists of positively charged polymer molecules (polycations), anions (counterions), and neutral acid molecules. Such polymers demonstrate similar structure transitions [2–7] and transform into a condensed state when a certain polymer concentration (≤20%) is reached or the nematic phase is exposed to a very small amount of moisture. Such electrostatic self-assembly is of great importance for charged polymeric systems widely used in different industrial, biotechnological, and medical applications.

Poly (p-phenylene benzobisoxazole) (PBO) is a representative of the high performance aromatic heterocyclic rigid-rod polymers. The structure of its monomer unit is (Fig. 1).

The solvent often used to dissolve PBO is poly (phosphoric acid) (PPA) [3]. Dissolution is accompanied by the protonation of heterocycles. As shown in [8], the protonation of nitrogen atoms is energetically more preferable than that of other heteroatoms. This situation typically occurs in strong acids [9].

The polymer precipitates and forms the first crystal phase, i.e., the so-called crystal-solvate phase (Phase I), in dry PPA solutions at room temperature and at a PBO concentration of about 14% [6]. The precipitation is supposed to be in the form of complexes including not only the PBO polycation and PPA anions but also PPA neutral molecules. If some amount of water (to 7% by weight) is added to the first crystal phase, it is transformed into a new crystal-solvate phase (Phase II) [6]. Water deprotonates the neutral acid molecules [4] existing in Phase I, and excess PPA anions appear. It is not clear what happens to these anions. They can be removed from the crystal structure due to electrostatic repulsion or some of them can remain near the PBO polycation. In the latter case the complexes of Phase II can include some amount of excess anions. It is well established that the PBO chains are protonated not only in solution but also in both condensed phases [6].

Thus, the transitions from solution to Phase I and then to Phase II are accompanied by change in the polymer–acid complex composition. Electrostatic interactions play a leading role in the complex formation at every stage. For this reason the changes in the PBO–acid complex composition can be considered in the first approximation as changes in polyion–counterion complexes of a polyelectrolyte system (PE). Under the condensation condition, the electrostatic interactions in PE solution become predominant,

---

* Tel./fax: +8 812 328 85 05.
E-mail address: luk@imc.macro.ru.

0032-3861/$ – see front matter © 2011 Elsevier Ltd. All rights reserved.
doi:10.1016/j.polymer.2011.01.023

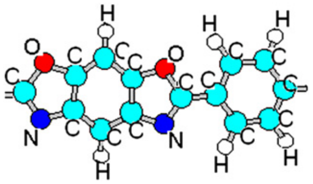

Fig. 1. Poly (p-phenylene benzobisoxazole) monomer unit.

and the complexes consisting of polyions and counterions are formed. For the entropy reasons the counterion number in the complexes is not sufficient to fully compensate the polyion charge. Counterions condense at the PE surface and screen the PE charge, thereby decreasing the repulsion between PE molecules in solution. When the repulsive force is surpassed by the attractive force, aggregation occurs. The polyion charge is totally neutralized at the neutralization point, and the repulsive force drops down to zero. In the presence of the excess counterions the net charge of the complex can change its sign because the charge of the condensed counterions can surpass the bare PE charge. Accumulation of excess counterions in the immediate vicinity of the PE surface is typically referred to as overcharging. These effects - aggregation and overcharging - take place in the systems with strong electrostatic interactions, in particular, in water solutions of DNA and other biological colloids in the presence of multivalent counterions [10–12]. The system under study contains monovalent counterions (singly deprotonated acid molecules [4]). It is important that aggregation in this system occurs at much higher polymer concentrations than in biological polyelectrolytes. As shown in [13], if the dielectric constant is considered to be a function that decreases with increasing polymer concentration, the aggregation in solutions of polyelectrolytes with monovalent counterions can be observed when a certain polymer concentration is reached. Analysis of the phase diagrams [14] constructed by using equations of [13] for the polyelectrolyte system with the characteristics of the PBO solution in PPA shows that the phase transition occurs at the polymer concentration that agrees well with the experimental value. The effect of overcharging in the system under study can be expected because the excess counterions are formed in the aggregated state (crystal-solvate phase) in the system with a low dielectric constant.

The goal of our study was to define the structure of the polymer–acid complexes both in PBO solution and in aggregated states. The following types of the complexes were considered: the complexes with the number of acid anions lower than that required for the polycation charge neutralization (solution); the complexes with the polycationic charge totally neutralized by anions (Phase I), and the complexes including excess anions (Phase II). To determine the structures of the complexes, quantum-chemical (semi-empirical-AM1, ab initio) and molecular mechanics (MM) calculations were carried out. For simplicity, the orthophosphoric acid (OPA) molecules were considered. The main tasks of these calculations were to find out the PBO chain conformations, to reveal preferable positions of charged and neutral acid molecules in the complexes, and to elucidate the role of neutral acid molecules in formation of the structures of the crystal-solvate PBO phases. The paper is organized as follows. Sect. II describes calculation methods and models. Sect. III contains calculation results and their discussion. Conclusions are given in Sect. IV.

2. Computational methods and models

2.1. Methods

The calculations were executed by using the HyperChem-7 molecular modeling package. The semi-empirical molecular orbital (AM1) and molecular mechanics (MM) methods were mainly used. The ab initio RHF 6-31G** method was also applied. The semi-empirical quantum-chemical AM1 method was chosen because it gives a fair description of the intramolecular characteristics of PBO molecules among all other semi-empirical quantum-chemical methods [8,15]. To calculate the energies of the structures of the PBO–acid complexes by the molecular mechanics method, the set of MM + potentials (HyperChem_7 software) was used. This set describes the contributions of various intramolecular and intermolecular interactions to the total system energy. These contributions involve energies of valence bond and angle deformations, torsion energy, and energies of nonvalence and electrostatic interactions. Correct selection of the potential parameters is of essential importance. It was shown [16] that the model molecules with the size larger than that of the repeating polymer unit (consisting of one heterocyclic ring and one phenylene ring) should be used to obtain the appropriate values of the intramolecular potential parameters for the protonated PBO molecule. For this reason, the deformation curves for valence bonds and angles and the internal rotation barrier were calculated by the AM1 method for the model molecule composed of two monomers and one phenyl ring added for symmetry. The magnitudes of the potential parameters describing the deformation of valence bonds and angles and the internal rotation were selected to provide the best fit between the curves calculated by the AM1 and MM + methods. Since the electrostatic interactions play a leading role in the systems under consideration, the results obtained in the MM calculations depend on the atomic charge set used. To this end, the calculations were performed with the atomic charges obtained both by the AM1 and ab initio HF/6-31G** methods (see Appendix). To calculate the van der Waals interactions, the parameters suggested in the software were taken because they are valid for a wide class of organic compounds and polymers. Energy minimization was performed by the conjugated gradients method with a convergence criterion of 10^{-3} kcal/(Ǻ mol).

2.2. Models

The *cis* – stereoisomeric form of the PBO molecules was considered (Fig. 1) since this polymer *was favored from the*

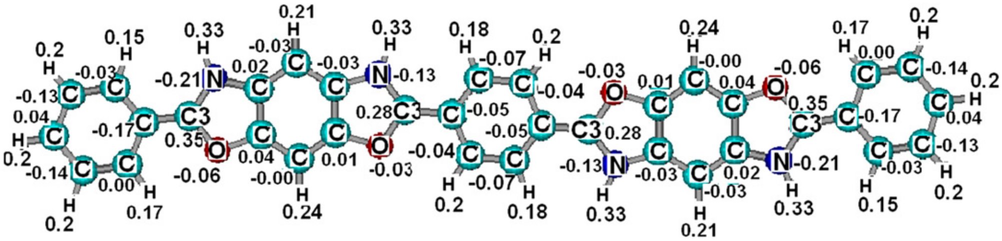

Fig. 2. Protonated PBO molecule with the atomic charges obtained from AM1 calculations.

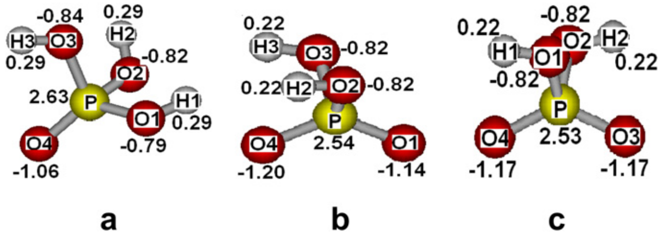

Fig. 3. (a) OPA^0 and (b, c) OPA^- molecules with the atomic charges obtained from AM1 calculations.

standpoint of processability [1]. The term cis here refers to the position of two oxygen (nitrogen) atoms in the heterocycle. In *cis* – stereoisomers both atoms of the same kind are located on one side of the long heterocycle axis. The calculations were performed for the PBO molecules with all diprotonated (at nitrogen atoms) heterocyclic rings. The PBO oligomer molecule composed of two monomer units and one phenyl ring (Fig. 2) was taken as the computational model.

To calculate the minimum energy conformations of the PBO and OPA neutral molecules by the AM1 method, the initial structures were constructed with the use of the standard valence bonds and bond angles. To calculate the optimal PBO (OPA) charged molecule geometry, the protons were added (removed) to (from) neutral molecules in their energetically favorable conformations. The PBO protonated molecule (PBO^+) and the OPA neutral and deprotonated molecules (OPA^0 and OPA^-) in their minimum energy conformations calculated by the AM1 method were used to construct the initial structures of the polymer–acid complexes. The minimum energy structures of the polymer–acid complexes were calculated by the MM and AM1 methods. Since it was important to find out the structure of the complexes formed mainly due to the electrostatic interactions and to define the OPA anion positions near the PBO polycation, the complexes formed by the PBO^+ molecule and the OPA^- molecules alone were considered first of all. The OPA^- molecules in the MM calculations were fixed in their optimal conformations but the intramolecular parameters of the PBO^+ molecule were varied. Finally, the structures of the complexes formed by the PBO^+, OPA^-, and OPA^0 molecules were calculated. The MM minimum energy structures of the complexes were taken as the initial ones in the AM1 calculations. The AM1 energy minimizations were performed with full geometry optimization of all molecules.

3. Results and discussion

3.1. Individual molecules – AM1 minimization

3.1.1. Protonated PBO molecule

To calculate the lowest energy conformation of the PBO^+ molecule, protons (a charge +1 for each) were placed on the nitrogen atoms. As in the case of the *neutral PBO molecule* [15,16], all cyclic moieties are planar *in the* PBO^+ *molecule*. In addition, there are two energy minima, which correspond to two conformations, each having the phenyl and heterocyclic rings arranged in one plane. These conformations have different relative arrangements of the heterocycles along the polymer chain (rotational isomers) when similar heteroatoms are located on different sides (TRANS-isomer) (see Fig. 2) or on one side (CIS-isomer) of the long molecular axis. The energies of these conformations slightly differ, and this difference ($\approx$0.1 kcal/mol) is considerably lower than the thermal energy (kT $\approx$ 0.6 kcal/mol at room temperature). Therefore, both rotational isomers can be considered to be equiprobable, and the PBO^+ molecule can be considered to be inhomogeneous relative to its rotational isomeric composition. The PBO^+ molecule atomic charges are shown in Fig. 2. It can be seen that the charges of the protons (hydrogen atoms) attached to the nitrogen atoms are redistributed in the chain, and, as a result, the hydrogen partial charge is about 1/3 of the proton charge.

3.1.2. Neutral and deprotonated OPA molecules

The minimum energy conformations of the OPA^0 and OPA^- molecules are shown in Fig. 3.

There are two minimum energy structures of the deprotonated OPA molecule (Fig. 3b,c). The OPA molecule deprotonated at the oxygen O1 atom (Fig. 3a) gets the conformation with a parallel OH groups, and partial charges on the O1 and O4 atoms are slightly different (Fig. 3b). But when a proton is deleted from the O2 or O3 atoms, the molecule has the conformation with antiparallel orientation of the OH groups, and the partial charges on the O2 (O3) and O4 atoms become equal (Fig. 3c). The energy difference of these conformations is $\approx$0.6 kcal/mol.

As pointed out above, electrostatic interactions play a leading role in the systems under consideration, and calculation results depend on the applied set of atomic charges. The sets obtained from the AM1 and ab initio HF/6-31G** calculations have different charges on some atoms (Figs. A1 and A2 in Appendix). The essential difference is obtained only for O, N, and C3 atoms of the protonated PBO^+ molecule (Fig. A1 in Appendix) and for P, O1 and O4 (or O3 and O4) atoms of the OPA^- molecule (Fig. A2 in Appendix). The results of the MM minimizations with the charge sets obtained from the AM1 and ab initio calculations are presented in Section 2 and Appendix, respectively. Although the counterion positions in the complexes in these two cases somewhat differ, the main results are the same.

3.2. PBO–OPA complexes

The calculations were divided into two stages. At the first stage the minimum energy structures of the complexes formed by the PBO^+ molecule and OPA^- molecules were calculated by the MM method. At the second stage the OPA^0 molecules were added to the complexes and their structures were calculated by using the MM and AM1 methods.

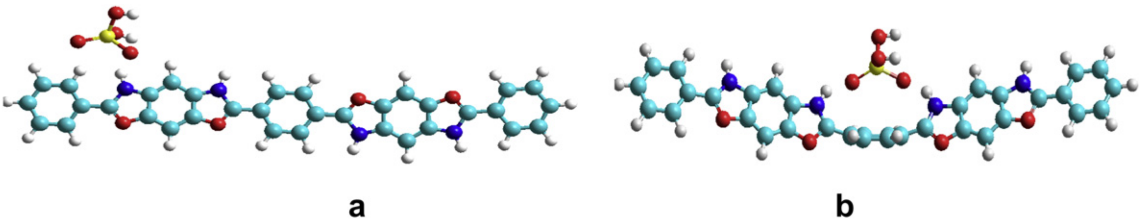

Fig. 4. Complex with one counterion: (a) the initial and (b) minimum energy structures.

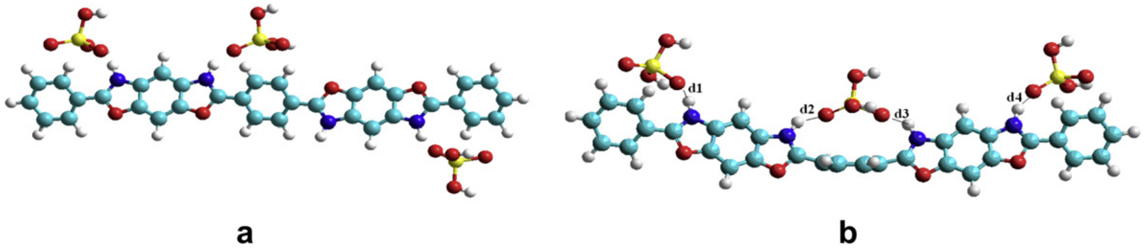

Fig. 5. Two minimum energy structures of the complex with 3 counterions: (a) PBO^+ in TRANS conformation and (b) PBO^+ in CIS conformation.

3.2.1. PBO^+–OPA^- complexes

To model the complexes in solution and in the aggregated phases (Phase I and Phase II), the following types of the PBO^+–OPA^- complexes were considered:

a) undercharged complexes – complexes with a deficient amount of the OPA^- molecules (solution);
b) neutral complexes – complexes with the number of the OPA^- molecules necessary for full compensation of the PBO^+ charge (Phase I);
c) overcharged complexes – complexes with excess OPA^- molecules (Phase II).

The dielectric constant in solution varies with the distance from the polymer backbone. The essential feature is a strong electrostatic interaction between ions at separations of 5–10 Å, which rapidly becomes weaker at longer distances. The local dielectric constant can be taken to be of the order of 2–4 [17] and is about 15–30 times lower than the bulk value ~60 (dielectric constant of phosphoric acid [18]). No information on the dielectric constants of the crystal-solvate phases is available. The PBO dielectric constant ($\acute{\varepsilon} = 3$ [19]) *can be taken to simulate* the complexes of the aggregated phases. Thus, $\acute{\varepsilon} = 3$ was used in the calculations.

3.2.1.1. Undercharged complexes. The model chain of the PBO molecule includes two heterocyclics. At protonation it acquired four protons, which are bound to the nitrogen atoms. The complexes that included one, two, and three OPA^- molecules were considered. In the initial configuration of the complexes, the PBO^+ molecule was taken in the TRANS conformation and the OPA^- molecules were placed at a certain distance from it. The common result for all the complexes was that the structure in which one anion is attracted by two heterocycles (see Fig. 4b and 5b) is preferable in energy. In such a structure the PBO^+ molecule gets the CIS rotational conformation and bent configuration. Only one minimum energy structure was obtained for the complex with one OPA^- molecule (Fig. 4b).

The complex that includes two or three OPA^- molecules has two minimum energy structures. Such structures with TRANS and CIS rotational conformations of the PBO^+ molecule are shown in Fig. 5a,b, respectively, for the case of three OPA^- molecules. In the last structure the PBO^+ chain has the bent configuration, and this structure is more preferable in energy ($\Delta E \approx 3$ kcal/mol).

Therefore, the equal probability of TRANS and CIS rotational isomers, which is inherent in a single PBO^+ chain [16], becomes invalid, and the preferred realization of CIS rotational isomers takes place at the counterion condensation. It has been found [7,20] that the rigid-rod polymers (particularly PBO) in solution have relatively short persistence lengths (~500–650 Å), which are considerably shorter than the actual contour lengths [21] (~1200–1500 Å). The enhanced flexibility of the PBO single chain has been explained by local thermal deformations resulting in the local chain bending [22] because the bending deformation (for bending at C3 and Car atoms) is a soft deformation mode [11,16] for the PBO^+ backbone. The PBO^+ chain bending resulting from its electrostatic interaction with the acid anions can also contribute to the enhanced PBO flexibility in solution. To estimate the effect of the counterion condensation on the persistence length, the PBO chain can be considered as a freely rotating one with a fixed bending angle [23]: $1/a = 1/a + (1 - \cos\theta)/b$, where a and a_t are the experimentally measured persistence length and the contribution of torsional oscillations to this value, respectively, b is the distance between bending points, and θ is the change in the angle between two neighboring monomers. The contour length (~1200–1500 Å) of the supposed rods based on the molecular weight can be used for a_t, a is equal to experimental value ~500 Å, and θ is about 8–10°. This mechanism can describe ~80% of the measured persistence length for our case of b equal to the repeating polymer chain unit. This suggests that both mechanisms of the polymer chain bending (thermal and electrostatic deformations) can contribute to the PBO molecule flexibility in the complex with a partially neutralized PBO^+ chain charge.

To characterize the positions of the counterions they occupy at the PBO^+ chain, the distances between oxygen atom of the OPA^- molecules and hydrogen at the PBO^+ nitrogen atoms (Fig. 4b) were taken. These distances are: d1 = d4 = 1.89 and d2 = d3 = 1.93 Å.

3.2.1.2. Neutral complexes. Two minimum energy structures of the neutral complex are shown in Fig. 6. In these structures the PBO^+

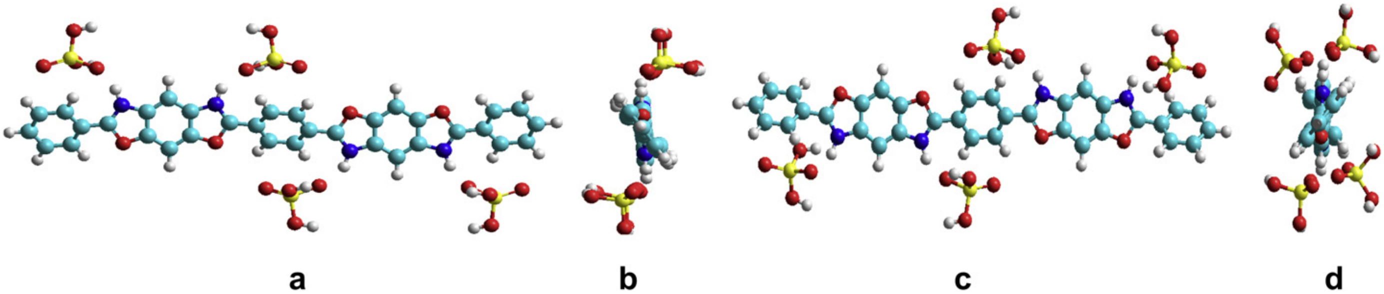

Fig. 6. Two minimum energy structures of the neutral complex: (a, b) phenyl rings are in one plane and (c, d) phenyl rings are in crossed planes. The structures are shown in two projections: (a, c)- parallel and (b, d)- orthogonal to the plane of the heterocycles.

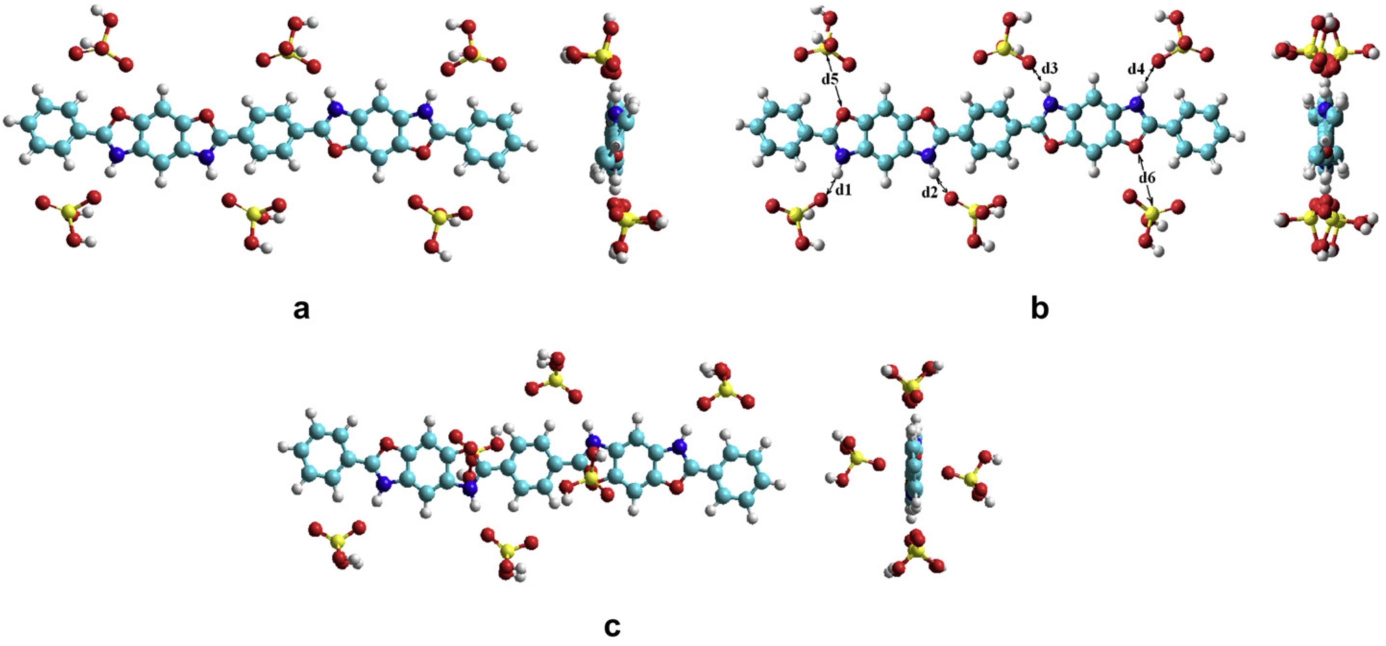

Fig. 7. Overcharged complex: (a) phenyl rings are in one plane, (b) phenyl rings are in crossed planes and (c) all cyclic fragments are in one plane. The structures are shown in the parallel and orthogonal projections to the plane of the heterocycles.

molecule gets the TRANS rotational conformation, and the OPA$^-$ molecules occupy symmetrical positions on opposite sides of the PBO$^+$ molecule. These structures differ by the mutual orientation of the cyclic fragments in the PBO$^+$ chain. In the first structure the phenyl and the heterocyclic rings are arranged in two planes with an angle of ~40 ° between them but in the second structure the phenyl rings are rotated by ±38 ° from the plane of the heterocycles. The energy of the second structure is slightly lower (by ≈0.2 kcal/mol).

Therefore, the PBO$^+$ molecule in the neutral PBO$^+$–OPA$^-$ complex has a homogeneous rotational isomeric composition because the TRANS rotational isomer becomes preferable in energy. The distances between counterions and protons are: $d1 = d4 = 1.76$ and $d2 = d3 = 1.78$ Å.

3.2.1.3. Overcharged complexes. The overcharged complexes were constructed by adding an excess number of the OPA$^-$ molecules into the neutral complex, and the calculations of their minimum energy structures were carried out. It was shown that the minimum number of the excess molecules of the OPA$^-$ is one anion per monomer unit. There are three minimum energy structures of the overcharged complex. The qualitative difference between the first two structures (Fig. 7a,b) is the same as in the case of the similar structure geometries of the neutral complex but the angles between the phenyl and heterocycle planes are 29 ° and ±27 °. The energies of these two structures are very close ($\Delta E \approx 0.3$ kcal/mol), but the energy of the third structure (Fig. 6c) is essentially higher (≈3.5 kcal/mol).

Like in the neutral complex, the PBO$^+$ molecule in the overcharged complex has the TRANS rotational isomeric composition. The distances between counterions and protons in the lowest energy structure (Fig. 7b) are $d1 = d4 = 1.76$ Å and $d2 = d3 = 1.78$ Å, and the distances (P–O) from the PBO$^+$ molecule on which the excess anions are located are $d5 = d6 = 3.78$ Å.

The complex with the excess of the OPA$^-$ molecules is energetically more favorable than the neutral complex. To compare the energy gains due to integration of components (the PBO$^+$ molecule and the OPA anions) into the neutral and overcharged complexes, the self-energies of the individual components were subtracted from the total energy of each complex. The estimate shows that the overcharged complex formation is favorable in energy. The energy gain is higher (by about 11.2 kcal/mol) than for the neutral complex formation. This result agrees with the theoretical findings according to which the energy of the system with overcharging counterions is lower than that of the neutral system [24,25].

Comparison of the structures of the undercharged, neutral, and overcharged complexes obtained by using the ab initio (see Appendix) and the AM1 charge sets revealed differences in the anion positions near the polycation chain. But the main results, such as bending of the PBO$^+$ molecule generated by the electrostatic binding of one anion with two positively charged heterocycles and the energy gain at the formation of the overcharged complex, are the same in both cases.

This Section presented the structural features of the PBO$^+$–OPA$^-$ complexes which are mainly dictated by the

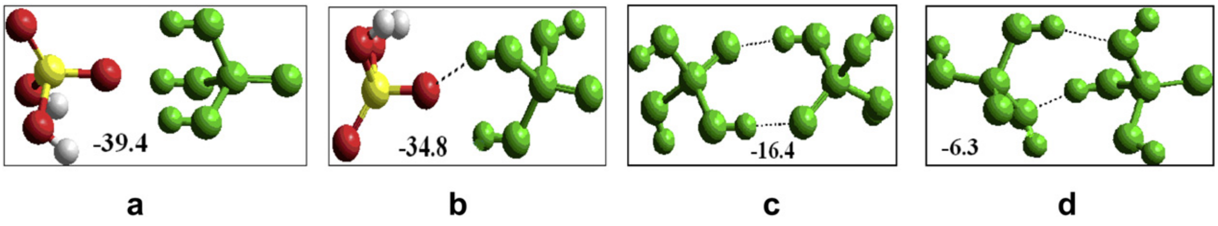

Fig. 8. Minimum energy structures of two interacting molecules: (a, b) - OPA$^-$ with OPA^0 and (c, d) OPA^0 with OPA^0. The intermolecular interaction energies are shown inside the panels (in kcal/mol).

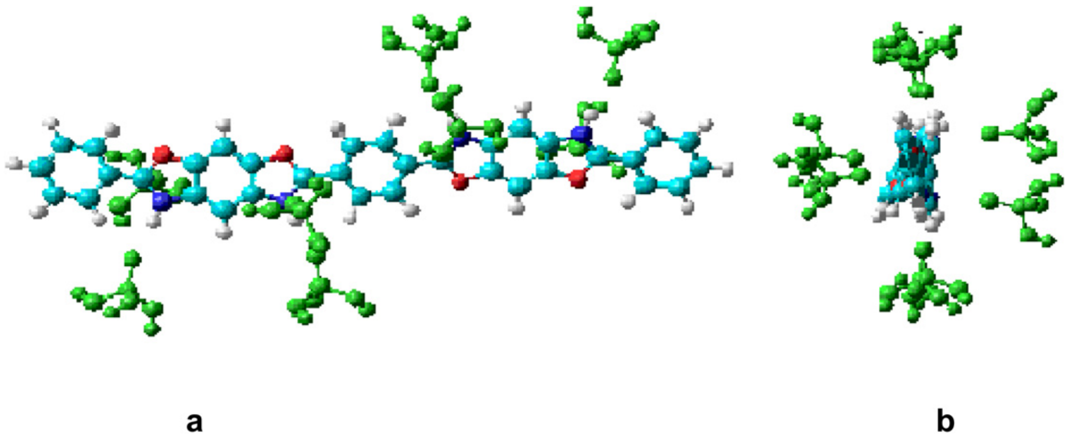

Fig. 9. The minimum energy structure formed by the PBO$^+$ chain and 4 OPA^0 molecules (per PBO monomer) is displayed from the view points which are (a) perpendicular and (b) parallel to the long PBO molecule axis.

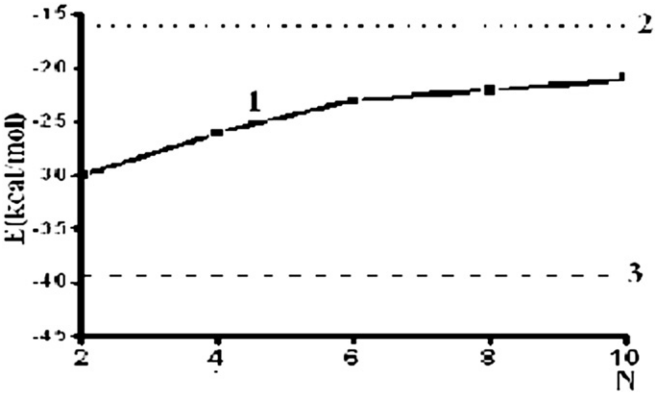

Fig. 10. Energies of the OPA^0–PBO$^+$ (curve 1), OPA^0–OPA^0 (curve 2), and OPA^0–OPA$^-$(curve 3) interactions.

electrostatic interactions obtained by the MM method. The role of the neutral acid molecules in the formation of the structure of the PBO aggregated phases inferred from the AM1 calculations is described below.

3.2.2. Neutral PBO$^+$–OPA$^-$–OPA^0 complexes (Phase I)

The main issues to be addressed revealed by analysis of the experimental data for Phase I are as follows:

a) interactions that hold the neutral acid molecules in the complex;
b) conservation of the protonated state of the PBO chains in Phase I;
c) the number of neutral acid molecules in the complexes of Phase I;

The inclusion of neutral acid molecules into the complexes of Phase I is considered to be due to unique associations between the protonated PBO polycation and neutral acid molecules [5,6]. Namely, it is supposed that the force that holds them in the complex is a strong attractive interaction between the neutral acid molecules and the protonated PBO chain. The precursors of the Phase I complexes are formed in solution where neutral acid molecules surround their own anions and the PBO polycations. To determine the interactions responsible for the inclusion of the neutral acid molecules into the Phase I complexes, the minimum energy structures formed by the OPA^0–OPA$^-$ and OPA^0–OPA^0 molecular pairs and by the PBO$^+$ with various numbers of the OPA^0 molecules were calculated.

The AM1 calculated minimum energy structures formed by the OPA^0–OPA$^-$ and OPA^0–OPA^0 molecular pairs are shown in Fig. 8 (here and below the OPA^0 molecules are shown by a green color). There are two minimum energy structures for each pair (Fig. 8a,b and Fig.8c,d). The energy gains due to the intermolecular interactions (shown in the Figures) were estimated as the differences between the total energies of the minimum energy structures of the molecular pair and the sum of the individual molecule self-energies. The intermolecular interaction in the first pair is much stronger than that in the second molecular pair (minimum difference is ~17.5 kcal/mol).

a) To estimate the interaction energy of the OPA^0 molecule with the PBO$^+$ chain, the minimum energy structures formed by the PBO$^+$ with various numbers of the OPA^0 molecules (N from 2 to 10 per PBO monomer) were calculated. One of the structures with $N = 4$ is presented in Fig. 9. It can be seen that the OPA^0 molecules surround the PBO$^+$ chain and are oriented in a similar fashion relative to it. All P=O bonds are oriented towards the PBO$^+$ chain by the oxygen atom that has a large negative partial charge and interacts with the positively charged hydrogen and C3 atoms (Fig. 2) of the heterocycles.

The energy gain due to the OPA^0–PBO$^+$ intermolecular interaction as a function of N is shown in Fig. 10 (curve 1) together with the lowest energies of the OPA^0–OPA^0 (the dotted line) and the OPA^0–OPA$^-$ (the dashed line) interactions.

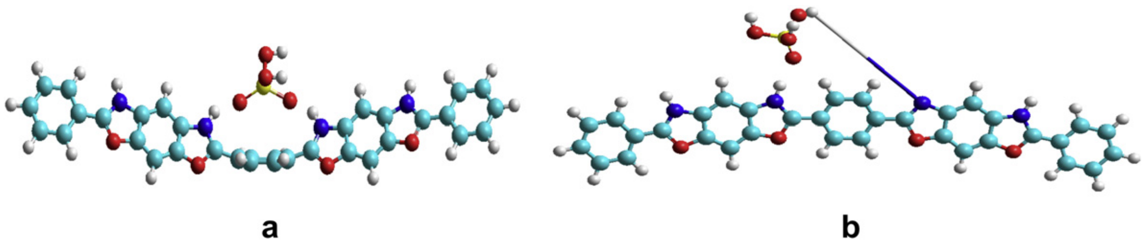

Fig. 11. Undercharged PBO$^+$–OPA$^-$ complex: (a) the initial structure and (b) the structure obtained by AM1 minimization.

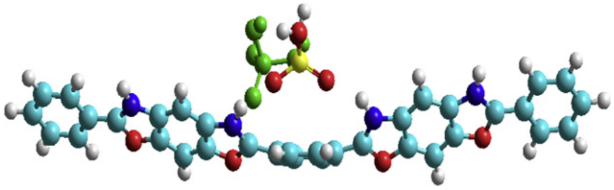

Fig. 12. AM1 minimum energy structure of the undercharged PBO^+–OPA^-–OPA^0 complex.

The protons bound to the nitrogen atoms are the sites of the strongest attraction for the OPA^0 molecules on the PBO^+ chain, so that the OPA^0–PBO^+ interaction energy for the structure with $N = 2$ is about −30 kcal/mol (per OPA^0 molecule). It is comparable to that of the OPA^0–OPA^- interaction. These sites are occupied by the acid anions at the counterion condensation, and the OPA^0 molecules cannot interact with them directly (see the next section).

As N increases, the OPA^0–PBO^+ interaction remains stronger than the interaction between the OPA^0 molecules, but it is appreciably weaker than the OPA^0–OPA^- interaction (see Fig. 10). Thus, the interaction between the neutral and charged acid molecules is the strongest, and, therefore, the acid molecules can be involved in the polymer–acid complex formation together with their own anions already at the stage of the counterion condensation.

b) Remind that according to experimental data the PBO molecules are protonated not only in solution but also in the crystal-solvate phases. Probably, the presence of the neutral acid molecules in Phase I prevents deprotonation of the polymer chain.

Quantum-chemical minimizations of the undercharged and neutral complex structures including only the PBO^+ chain and the OPA^- molecules yield the structures with uncharged molecules. An example of the undercharged complex is shown in Fig. 11.

The same result was obtained for the neutral PBO^+–OPA^- complex. This can be explained by the fact that the polymer molecule protonation as well as the acid molecule deprotonation are energetically unfavorable. The energy losses estimated as the difference between the charged and neutral state energies were ≈159.5 kcal/mol per one proton (for protonation of the PBO nitrogen atom) and ≈20.4 kcal/mol (for a single OPA^0 molecule deprotonation). Obviously the complexes must include additional components (neutral acid molecules in our case) in order to overcompensate these losses by the energy gain due to the realization of new favorable interactions.

On the other hand, the calculations of the complexes, which include also the OPA^0 molecules, give the minimum energy structures with the PBO^+ and the OPA^- molecules remaining charged. Such structures were obtained for the complexes that included as minimum one OPA^0 molecule per one OPA anion. The lowest energy structures of the undercharged and neutral complexes are shown in Figs. 12 and 13, respectively. The OPA anion in the structure in Fig. 12 is associated with two protonated heterocycles. This result is very similar to that obtained in the MM calculation.

Table 1
Atomic charges in the isolated (neutral and protonated) PBO molecule and in the protonated PBO molecules in the neutral and overcharged complexes. H (ph) is the hydrogen of the central phenyl and H (h) is the hydrogen of heterocycle. Other designations are as in Fig. 2.

Atom	Atomic charges in PBO			
	Neutral molecule	Protonated molecule	In neutral complex	In overcharged complex
H (ph)	0.164	0.177	0.204	0.213
H (ph)	0.159	0.199	0.230	0.223
H (ph)	0.159	0.199	0.230	0.223
H (ph)	0.164	0.177	0.204	0.213
C3	0.086	0.281	0.260	0.262
N	−0.116	−0.128	−0.112	−0.130
H (N)	–	0.327	0.398	0.397
O	−0.132	−0.031	−0.050	−0.047
H (b)	0.174	0.212	0.279	0.304
H (b)	0.174	0.235	0.270	0.208
N	−0.125	−0.211	−0.126	−0.174
H (N)	–	0.327	0.381	0.393
C3	0.100	0.345	0.284	0.291
O	−0.134	−0.056	−0.077	−0.023

The atomic charges in a single PBO^+ molecule and in the PBO^+ molecule of the neutral complex are given in Table 1. The atomic charge distributions in both cases are very similar.

As mentioned above, the energy gain due to integration of the protonated polymer molecule with the anions and the neutral acid molecules in a single complex must be higher than the energy losses due to polymer molecule protonation and acid deprotonation. The difference between the energy gain and losses of ≈10 kcal/mol was obtained for the complex that included at least three OPA^0 molecules per one PBO monomer unit.

c) How many OPA^0 molecules can be included in the complexes of Phase I? As shown above, the OPA^0 molecules can be incorporated into the structure of the polyion–counterion complexes due to their strong interaction with their own anions already in solution, at the stage of the counterion condensation. To stay in the complexes that form the aggregated state, the interaction of the OPA^0 molecules with not only their anions but also with the PBO^+ chain must be energetically profitable. The energy gain due to these interactions must be high enough to compensate for the entropy loss caused by the neutral acid molecule localization at the PBO^+ chain. However, estimation of the entropy loss that would allow accurate calculation of the number of the OPA^0 molecules included into the complex cannot be obtained by the methods used in this study.

Analyses of the contributions of all the interactions into the total energies of the PBO^+–OPA^-–OPA^0 complexes with various numbers of the OPA^0 molecules (N from 2 to 10 per one monomer unit of the PBO^+ chain) yielded the estimate of a critical number of

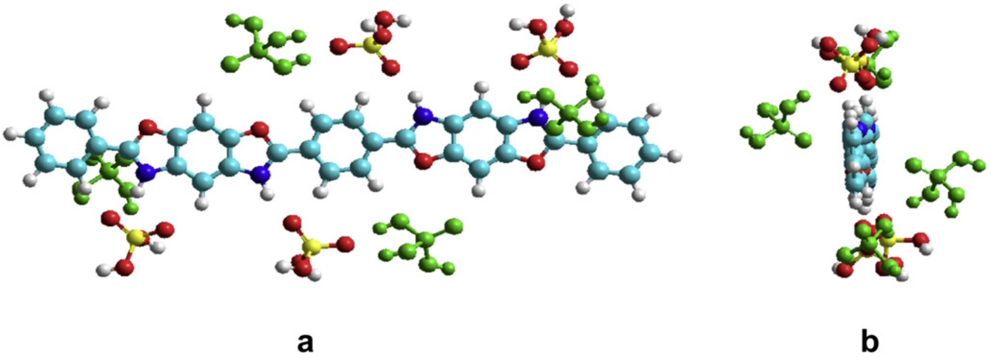

Fig. 13. The minimum energy structure of the neutral complex is shown in the (a) parallel and (b) orthogonal projections to the plane of the heterocycles.

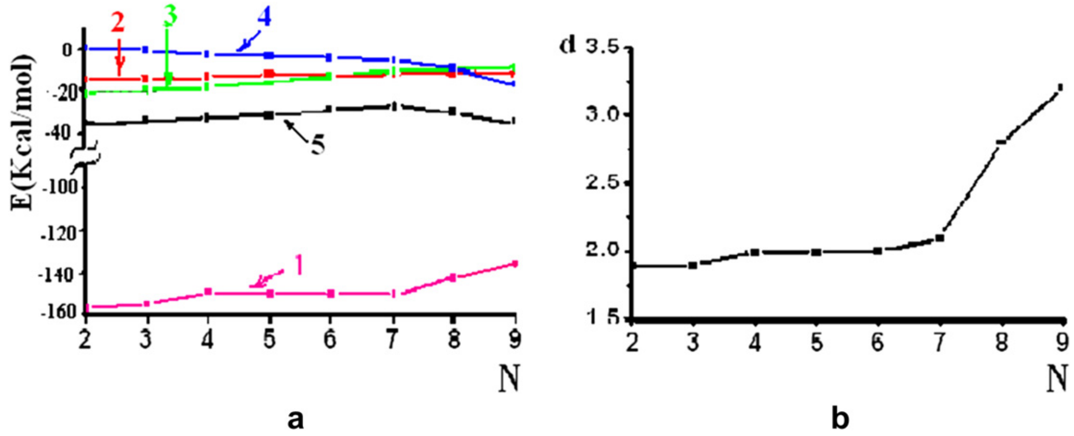

Fig. 14. (a) Different energy contributions as functions of N (the number of the OPA^0 molecules in the complex) into the total energy of the complex: from the $PBO^+–OPA^-$ (curve 1) interaction calculated per one anion, from the $OPA^0–PBO^+$ (curve 2), $OPA^0–OPA^-$ (curve 3), and $OPA^0–OPA^0$ (curve 4) interactions (per one OPA^0 molecule) and their sum (curve 5). (b) Distance d between anions (atom O) and protons on the PBO chain as a function of N.

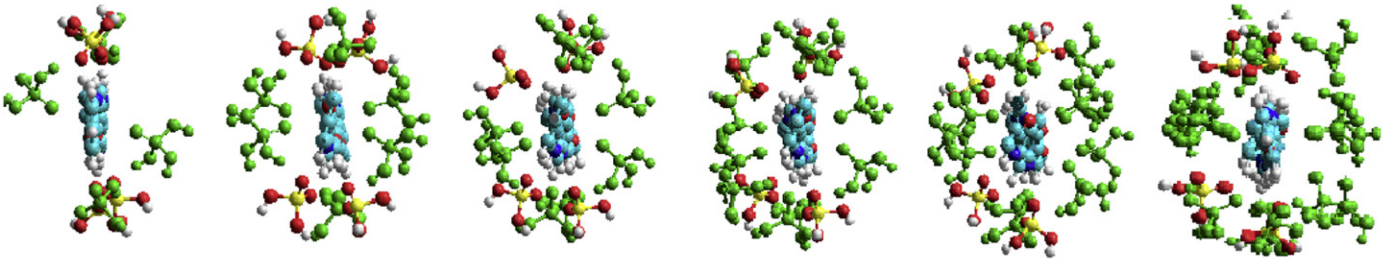

Fig. 15. Minimum energy structures of the neutral complexes with various numbers of OPA^0 molecules (N from 2 to 7) are shown in the projection to the plane orthogonal to the PBO^+ chain axis.

the OPA^0 molecules in the complex. This number was defined as the threshold above which the $PBO^+–OPA^-$ interactions become weaker and, hence, destruction of the basic structure formed by the charged components begins.

The $PBO^+–OPA^-$ interaction energy (calculated per anion (curve 1)) together with the $OPA^0–PBO^+$ (curve 2), $OPA^0–OPA^-$ (curve 3), and $OPA^0–OPA^0$ (curve 4) interaction energies and the sum of curves 2–4 (curve 5) (calculated per OPA^0 molecule) are shown in Fig. 14a versus N. The average distance d between the oxygen atom (deprotonated) of the OPA^- molecule and the hydrogen at the PBO nitrogen atoms is shown as a function of N in Fig. 14b. The $OPA^0–PBO^+$ interaction energy changes only slightly throughout the entire range of N, but the $OPA^0–OPA^-$ interaction becomes much weaker. At the same time, the $OPA^0–OPA^0$ interaction energy increases. The sum (curve 5) increases for N from 2 to 7 (mainly due to the decrease of the contribution of the $OPA^0–OPA^-$ interaction energy) and decreases for $N > 7$ (due to the increase of the $OPA^0–OPA^0$ contribution).

On the other hand, the interaction energies of the charged components of the complexes (curve 1 in Fig. 14a) change only slightly up to $N = 7$, but, as N is further increased, they become significantly weaker due to increasing distances between charged components (Fig.14b). This behavior can be explained by the fact that the number of vacant interaction sites at the PBO^+ chain surface is exhausted. When the amount of the OPA^0 molecules in the complex is small, they occupy the positions at the PBO^+ chain that allows realization of the most favorable interactions with both charged components: the anions and the polycation. The OPA^0 molecules that are added to the complex occupy vacant interaction sites located at larger distances from the anions and realize energetically favorable interactions with the PBO^+ chain and with each other. This manifests itself mainly in the $OPA^0–OPA^-$ interaction energy decrease and the $OPA^0–OPA^0$ interaction energy increase. A considerable weakening in interaction between the charged components of the complex with $N > 7$ means that all the sites of energetically favorable interactions at the PBO^+ chain surface (at

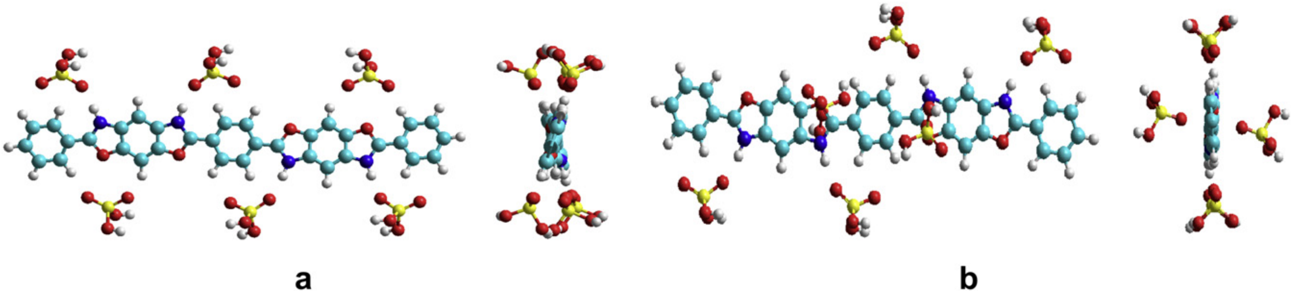

Fig. 16. Overcharged complexes: (a) anions are localized on the opposite sides of the PBO^+ molecule, (b) anions are distributed around the PBO^+ molecule. The structures are shown in the projections parallel and orthogonal to the plane of the heterocycles.

$N = 7$) are already occupied. To form the minimum energy structure, the molecules that are further added ($N > 7$) must realize their own energetically favorable interactions with the PBO^+ and OPA^- molecules by displacing anions from the PBO^+ chain.

Therefore, $N = 7$ can be regarded as a critical number of the OPA^0 molecules, up to which the "electrostatic" complex structure remains nearly unchanged. This means that no more than 9 phosphate groups per PBO monomer unit (including anions) can be in the close vicinity of the PBO^+ chain. The minimum energy structures of the complexes with N from 2 to 7 are shown in Fig. 15 in the projection to the plane orthogonal to the PBO^+ chain axis.

The estimate of the phosphate group number can be considered as realistic because the estimation from the X-ray data [6] gave the lower limit of 4 and the upper limit of 12 phosphate groups per PBO monomer for the PBO–PPA complexes. In order to calculate the PPA neutral molecule number in the complexes of Phase I by using these estimates, it is necessary to know the degree of the phosphoric acid polymerization (which is unknown) or to calculate the arrangement of the acid molecules with higher polymerization degrees at the polymer molecule surface. The calculations are in progress.

3.2.3. *Overcharged complexes (Phase II)*

The most important question is why the PBO chains are protonated in Phase II? As mentioned above, the transition from Phase I to Phase II occurs if some water is added, which leads to deprotonation of the neutral acid molecules existing in Phase I and to the formation of an excess amount of anions.

The AM1 calculations of the complexes with various excess anion numbers have demonstrated that the PBO chain in such complexes preserves its protonated state. As evident from Table 1, there is a minor difference between the partial charge distributions in the PBO chain in the neutral and overcharged complexes. According to AM1 calculations (which confirmed the MM calculations), the overcharged complex can include no more than one additional anion per PBO monomer and a further increase in anion number is energetically unfavorable. Therefore, it can be concluded that the presence of excess anions is responsible for preservation of the protonated PBO chain state in Phase II. Like in the MM calculations, the structures differing by the anion arrangement near the PBO chain were obtained (Fig. 16). The first structure with the anions localized on the opposite sides of the PBO^+ molecule (Fig. 16a) is more preferable in energy (4.2 kcal/mol) as compared with the second one (Fig. 16b). The distances between counterions and the PBO^+ molecule ($d1 = d4 = 1.76$, $d2 = d3 = 1.79$, and $d4 = d5 = 3.77$ Å) are very close to those obtained in the MM calculations.

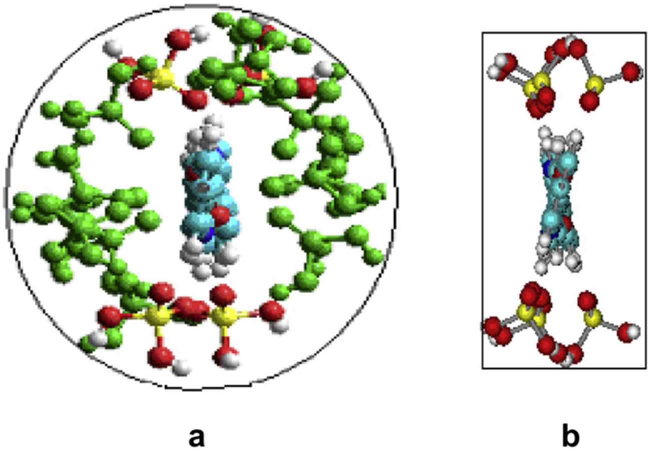

Fig. 17. Cross-sections of the (a) neutral (Phase I) and (b) overcharged (Phase II) complexes.

No doubt, the system in the aggregated state of Phase II is neutral as a whole. It includes the co-ions, i.e., water molecules with the protons captured from neutral acid molecules present in Phase I. To elucidate the co-ion distribution in Phase II, it is necessary to calculate the structure of this crystal-solvate phase. These calculations are in progress.

4. Conclusions

The complexes formed by the protonated olygomer molecules of the poly (p-phenylene benzobisoxazole), deprotonated molecules of the orthophosphoric acid, and neutral acid molecules were studied by the MM and quantum-chemical methods. Three types of the complexes as the models of the structures formed in solution and in two aggregated phases (Phase I and Phase II) were considered.

The experimentally observed increased PBO molecule flexibility was explained by local thermal deformations leading to a local chain bending [22]. The bending deformations of the PBO molecule generated by the electrostatic binding of one OPA anion with two positively charged heterocycles obtained in our study provides new hints into the molecular mechanisms of the PBO chain flexibility in solution. As shown by our calculations, i*n contrast to the equal* probability of TRANS and CIS rotational isomers, which is inherent in an isolated PBO^+ chain, only one type of the rotational isomers is preferable for the polymer chains in the complexes (in solution and in the aggregated phases). The CIS rotational isomer is energetically preferable for the PBO^+ chains in the complexes formed in solution (undercharged complexes). However, in the complexes of the aggregated phases the TRANS rotational isomer becomes energetically preferable in the PBO^+ chain.

The force that holds neutral acid molecules in the complexes of Phase I arises mainly due to their strong attractive interaction with their own anions and the PBO^+ molecule. The second interaction is weaker than the first one, but not so much weaker than the interaction between neutral acid molecules. This explains the PBO precipitation into the crystal-solvate Phase I in the form of the complexes that include not only anions but also neutral acid molecules. Moreover, the PBO molecules in the complexes of Phase I are protonated due to the presence of neutral acid molecules. The preservation of the protonated PBO molecule state in Phase II can be explained by the presence of excess acid anions in the complexes that form this crystal-solvate phase.

According to X-ray data [6], the crystal cell parameters in the cross section orthogonal to the PBO chain axis reduce by half at the transition from Phase I to Phase II (from $a = 1.26$ nm and $b = 1.16$ nm to $a = 0.7$ nm and $b = 0.58$ nm). The calculations for the PBO–OPA complexes have shown that the complex of Phase I can be represented by a cylinder with the PBO^+ molecule in its center and OPA charged and neutral molecules around it (see Fig. 17a). The geometry of the complex of Phase II is radically different (Fig. 17b) and assumes a more dense packing of the PBO chains in this aggregated state.

Since the PPA molecule polymerization degree is unknown [5,6], it is incorrect to compare directly the experimental data with the OPA calculations, but a qualitative agreement between the results obtained in the present study and future calculations for higher phosphoric acid polymerization degrees can be expected.

Similar structure transitions were observed for another high performance aromatic heterocyclic rigid-rod polymer – poly(p-phenylene benzobisthiasole) (PBZT) [4,5,7], but, in contrast to PBO, this polymer was deprotonated in Phase II [5]. The calculations in order to elucidate the mechanisms of the PBZT deprotonation are in progress.

Acknowledgments

This work was supported by the"Russian Foundation for Basic Research (project No. 08_03_00565).

Appendix

The partial atomic charges obtained from the AM1 and ab initio calculations for the PBO$^+$ and OPA$^-$ molecules are presented in Fig. A1 and A2, respectively.

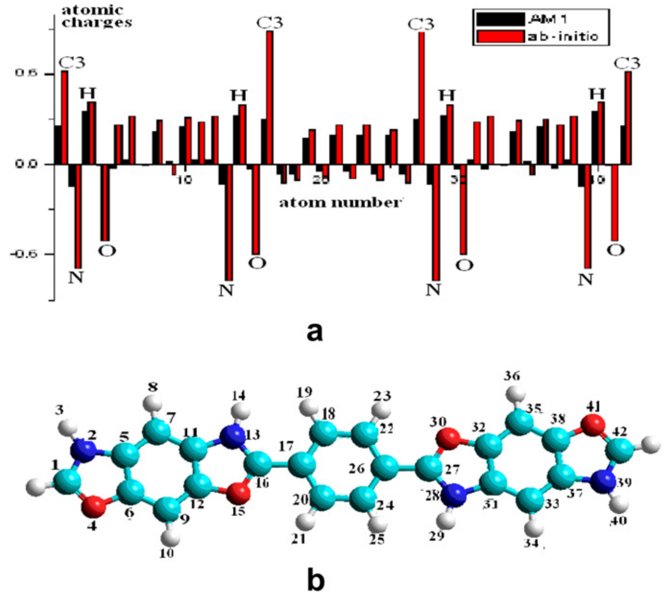

Fig. A1. (a) Comparison of charge distributions obtained from the AM1 and ab initio calculations. (b) Protonated PBO chain.

The results of the MM calculations of the undercharged, neutral, and overcharged complexes with the ab initio atomic charges in the PBO$^+$ and OPA$^-$ molecules are presented in Figs. A3–A5, respectively.

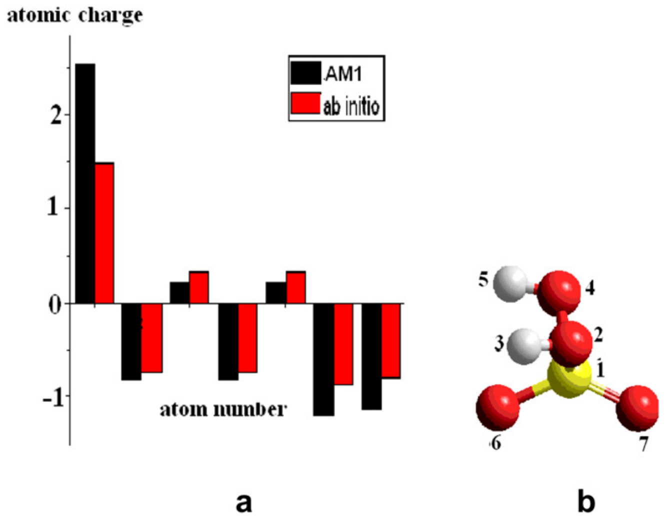

Fig. A2. (a) Comparison of charge distributions obtained from the AM1 and ab initio calculations. (b) Deprotonated OPA molecule.

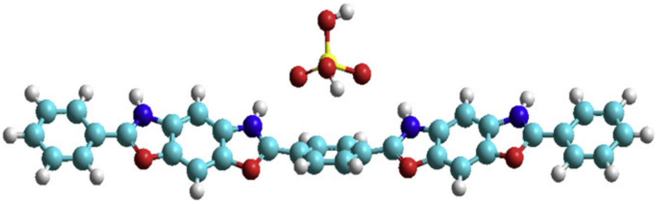

Fig. A3. Minimum energy structure of the PBO$^+$–OPA$^-$ undercharged complex with one counterion.

The PBO molecule in the complexes with a deficient amount of the OPA$^-$ anions gets a CIS rotational isomeric state and the bent structure generated by the electrostatic binding of one OPA anion with two positively charged heterocycles.

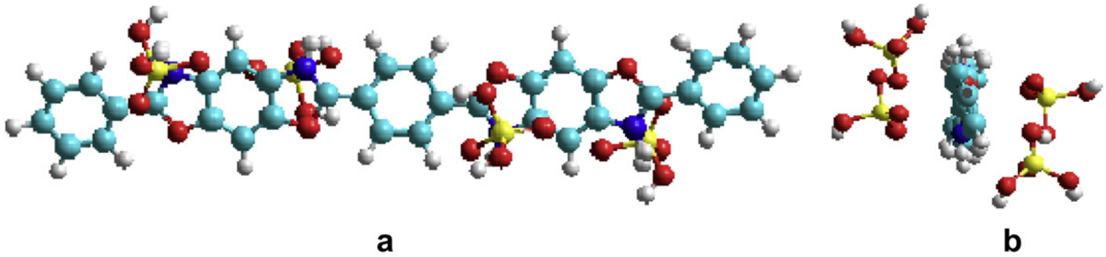

Fig. A4. . Minimum energy structure of the PBO$^+$–OPA$^-$ neutral complex displayed in two projections: (a) parallel and (b) orthogonal to the plane of the heterocycles.

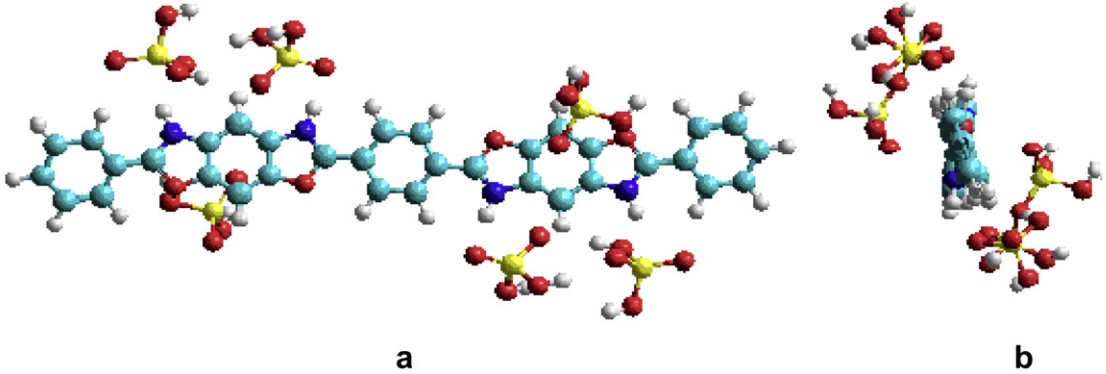

Fig. A5. Minimum energy structure of the PBO$^+$–OPA$^-$ overcharged complex displayed in two projections: (a) parallel and (b) orthogonal to the plane of the heterocycles.

The calculations have demonstrated that in spite of some differences in the structures of the neutral and overcharged complexes as compared with their structures obtained by using the AM1 charge sets, the main results are the same: the PBO^+ molecule in the neutral and overcharged complexes has a TRANS rotational isomeric composition; the integration of the PBO^+ and OPA^- molecules in the overcharged complex results in the energy gain which is higher than that of the neutral complex formation.

References

[1] Xiao-Dong Hu, Jenkins SE, Byung G, Polk MB, Kumar S. Macromol Mater Eng 2003;288(11):823–43.
[2] Wolf JF, Loo BH, Arnold FE. Macromolecules 1981;14:915–20.
[3] Choe EW, Kim SN. Macromolecules 1981;14:920–4.
[4] Cohen Y, Cohen E. Macromolecules 1995;28:3631–6.
[5] Cohen Y, Sarnyama Y, Thomas EL. Macromolecules 1991;24:1161–7.
[6] Cohen Y, Adams WW. Polymer 1996;37(13):2767–74.
[7] Lee CC, Chu SG, Berry GC. J Polym Sci Polym Phys Ed 1983;21:1573–97.
[8] Farmer BL, Dudis DS, Adams WW. Polymer 1994;36(17):3746–61.
[9] Roitman DB, McAlister J, McAdon M, Wessling RA. Polym Sci Polym Phys 1994;32(7):1157–62.
[10] Paton-Morales P, Talens-Alesson FI. Langmuir 2002;18:8295–301.
[11] Besteman K, Van Eiik K, Lemay SG. Nat Phys 2007;3:641–4.
[12] Besteman K, Zeverbergen MA, Heering HA, Lernay SG. Phys Rev Lett 2004;93:170802–900.
[13] Kramarenko EY, Erukhimovich IY, Khokhlov AR. Macromol Theory Simul 2002;11:462–81.
[14] Lukasheva NV, Darinskii AA. In: Proc. 12 International Conference on Composites Nano Engineering, Tenerife, Spain; 1–6 August 2005.
[15] Farmer BL, Wierschke SG, Adams WW. Polymer 1990;31:1637–48.
[16] Lukasheva NV, Darinskii AA. Polym Sci Ser A 2007;49:168–75.
[17] Dobrinin AV. Macromolecules 2006;39:9519–27.
[18] Munson RA. J Chem Phys 1963;40:2044–6.
[19] Yota Jiro. J Electrochem Soc 2009;156(11):G173–9.
[20] Kumar S. In: Lee SM, editor. International Encyclopedia of Composites, vol. 4. New York: VCH; 1990. p. 51.
[21] Chu S-G, Venkatraman S, Berry GC, Einaga Y. Macromolecules 1981;14:939–50.
[22] Farmer BL, Chapman BR, Dudis DS, Adams WW. Polymer 1992;34(8): 1588–601.
[23] Mansfield MI. Macromolecules 1986;19:854–9.
[24] Lewin Y. Rep Prog Phys 2002;65:1577–632.
[25] Messina R. J Phys Condens Matter 2009;21:18. 113102.